Crystallization of Carbonate and Sulfate Minerals in Organic Matrices: Examples from Biomimetic and Biological Polymer-Mineral Composites

by
Fitriana Nindiyasari

PhD Thesis
SUBMITTED IN PARTIAL FULFILLMENT
OF THE REQUIREMENT FOR THE DEGREE OF
Dr. rer. Nat.

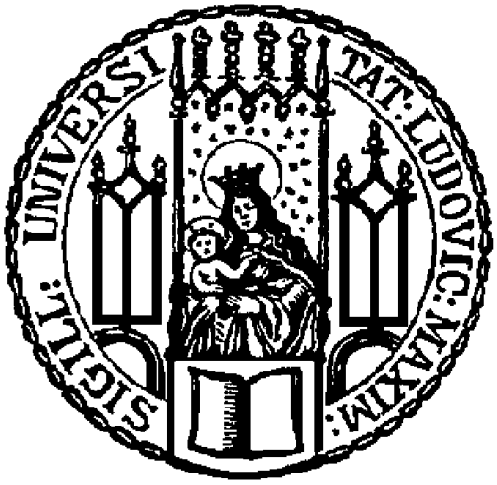

Fakultät für Geowissenschaften
Ludwig-Maximilian-Universität München

January, 2015

Supervisor : Prof. Dr. Wolfgang W. Schmahl

1. Reviewer : Prof. Dr. Wolfgang W. Schmahl

2. Reviewer : Prof. Dr. Lurdes Fernández-Díaz (External examiner)

Date of Oral Examination: 26.05.2015

----------For my parents----------

Nothing in life is to be feared, it is only to be understood.
Now is the time to understand more, so that we may fear less.

Marie Curie

Abstract

Biological carbonate hard tissues, such as the shell of the bivalve *Mytilus edulis,* are composites of biopolymers and minerals. *M. edulis* has two distinct layers, the outer layer consists of fibrous calcite and the inner layer is composed of nacreous aragonite. Close to the interface between nacreous aragonite and fibrous calcite, a 1-2 micrometer wide zone exists that consists of granular aragonite. Aragonite granules and tablets as well as calcite fibrous are embedded into matrix biopolymers.

In order to understand the composite nature of these hard tissues, biomimetic experiments using hydrogels were carried out. Hydrogels are able to model biogenic matrix environments due to their ability to confine space and to determine diffusion rates, local concentrations and supersaturation of the solutes. Hydrogels have local crystallization microenvironment that is distinguished from that in solution by confinement of solutes in the hydrogel pores. However, hydorgels only mimic biological extracellular matrices to some extent as the hydrogel fiber organization lacks any order, unlike it is in the case of the cholesteric liquid phase, e. g. chitin. The hydrogel strength is adjustable by changing its solid content. It further increases local hydrogel fiber co-aligments that to some extent will mimic organic matrices in biological hard tissues. Different kinds of hydrogels were used to study calcite crystallization (silica, agarose, gelatin). As each hydrogel has different characteristics, hydrogels can act differently in promoting or inhibiting crystallization. Hydrogels have an ability to mechanically impede the growth of a crystal depending on the strength of the hydrogel. Gelatin hydrogel is a poly-peptide material derived from natural collagen through hydrolytic degradation. The hyrolitic degradation breaks the triple-helix structure of collagen into single-strand molecules. Gelatin contains both acidic and basic amino acids with isoelectric point values near ~5 and with predominance of acidic moieties. Agarose hydrogel is a linear polysaccharide extracted from marine red algae. It consists of β-1,3 linked D-galactose and α-1,4 linked 3,6-anhydro-α-L-galactose residues. Gelatin and agarose hydrogels are composed of a fibrous structure that have varying mesh void dimensions depending on the hydrogel solid content. Hydrogel with 2.5 wt % gelatin solid content exerts less pressure against the growing calcite crystal aggregate than a hydrogel with 10 wt % gelatin solid content. Silica hydrogel does not exert strong pressure against the growing calcite crystal aggregate due to its nature as it is composed of minute (less than 20 nm) sized spherical particles that do not appear to form a network. The hydrogel strength together with the growth rate of the crystal defines the amount of incorporated hydrogel into the growing calcite crystal aggregate such that a strong hydrogel will incorporate more gel into the calcite crystal than a weak hydrogel.

Calcite grown in Mg-free silica hydrogels has a rhombohedral shape and is elongated on the c-axis. It grows as dumbbell-shaped aggregates in the presence of Mg. Silica hydrogel either Mg-free or Mg-bearing does not give a major influence on the co-orientation of the obtained crystal aggregate. Calcite grown in Mg-free agarose has two morphologies: rhombohedron-shaped calcite crystals and calcite radial aggregates. Calcite grown in Mg-bearing agarose has sheaf-like and peanut like morphologies. The presence of Mg in agarose influences the co-orientation of calcite crystals within calcite Mg-bearing agarose composites. The calcite/Mg-free agarose composite has several large crystal subunits while the calcite/Mg-bearing agarose composite shows a spherulitic microstructure. In the case of gelatin hydrogel, the precipitate consists of calcite aggregates that have a variety of features i.e. the formation of mosaic crystals

and mesocrystal-like subunits in one aggregate, the formation of aggregates with a fan-like distribution of the c-axis orientation and the formation of spherulitic aggregates. The formation of aggregates with different characteristic in the subunits can be explained as a result of a combination between local differences in gelatin matrix arrangement and physicochemical conditions such as the change in Mg/Ca ratio, pH, saturation, etc. The development of a fan-like distribution of the c-axes orientation in the calcite aggregate subunits can be explained as a result of Mg intrasectorial zoning. A different degree of Mg incorporation in different growth steps will accumulate misfit strain in the lattice. This misfit strain could be released through the formation of dislocations at regular intervals, such that small-angle boundaries develop. This growth further leads to the extreme split growth and the formation of fan-like and spherulitic crystal aggregates.

The etching experiments of calcite/hydrogel composites reveal the structure of the incorporated hydrogel within the calcite crystals and aggregates. In the case of Mg-bearing silica hydrogel more silica hydrogel is incorporated into the calcite crystal than in the case of Mg-free silica hydrogel. Thick hydrogel membranes are observed when Mg-free gelatin and agarose hydrogels are used. These membranes do not occur when Mg is present. The formation of these membranes in Mg-free gelatin and agarose hydrogels is a result of an accumulation of the hydrogel fibers that are driven back by growing crystals or aggregates. The stiffness of the gelatin and agarose hydrogel fibers increase as Mg is added into the hydrogel. The hydrogel becomes stiffer and exerts more pressure against the growing aggregates. No hydrogel membranes are observed in aggregates grown in Mg-bearing gelatin and in agarose hydrogels.

On the basis of biopolymer and mineral composites, gypsum ($CaSO_4$)/cellulose fiber composites were prepared. The purpose of the addition of cellulose fiber to gypsum was to create a composite with a high ecological value and interesting mechanical properties such as high Young's modulus, high bending strength and high compression strength. The cellulose fiber affects the mechanical property of the composites depending on the fiber characteristics, e.g. the nature of the cellulose (natural or synthetic), water retention value, degree of swelling, etc. Lyocell fiber, a synthetic fiber, is found to be able to increase the Young's modulus of the final composite.

Zusammenfassung

Biologisches Karbonat-Hartgewebe, wie das der Schale der Bivalve *Mytilus edulis*, ist ein Kompositmaterial aus Biopolymeren und Mineralen. Die Schale von *M. edulis* setzt sich aus zwei Lagen zusammen. Die Äußere besteht aus Faserkalzit, während die Innere aus perlmuttartigem Aragonit aufgebaut ist. Nahe am Übergang von Aragonit zu Kalzit befindet sich ein 1-2 μm dicker Bereich, der aus granularem Aragonit besteht. Die Minerale in der Schale sind in eine organische Matrix eingebettet.

Um den Kompositaufbau von biologischen Hartgeweben zu verstehen, wurde der Kristallisationsprozess von Karbonaten in biomimetischen Experimenten mit Hydrogelen untersucht. Aufgrund der Fähigkeit Raum zu limitieren und die Diffusionsrate, lokale Konzentration sowie die Übersättigung der gelösten Stoffe zu bestimmen, sind Hydrogele in der Lage eine biogene Matrixumwelt darzustellen. Hydrogele verfügen über eine lokale Kristallisationsmikroumgebung. Diese unterscheidet sich durch den Einschluss von gelösten Stoffen in den Hydrogel-Poren von der in Lösungen. Jedoch ahmen Hydrogele nur biologische extrazelluläre Matrizen ansatzweise nach, weil der Organisation der Hydrogelfasern, im Unterschied zur cholesterischer Flüssigphase (z. B. Chitin), jegliche Ordnung fehlt. Die Stärke des Hydrogels ist durch die Änderung seines Feststoffgehaltes einstellbar. Zusätzlich nimmt die lokale Co-Ausrichtung der Hydrogelfasern mit dem Feststoffgehalt zu, sodass im gewissen Maße die Matrizen in biologischen Hartgeweben nachgeahmt werden. Es gibt viele verschiedene Hydrogel-Arten, die für Untersuchungen von Kalzit-Kristallisation verwendet werden (z. B. Kieselerde, Agarosegel, Gelatine, Polyacrylamid, etc.). Da jedes Hydrogel über unterschiedliche Charakteristiken verfügt, verhalten sie sich unterschiedlich und können die Kristallisation unterstützen oder unterdrücken. Hydrogele haben die Eigenschaft das Wachstum eines Kristalls, abhängig von ihrer Stärke, mechanisch zu hindern. Gelatine-Hydrogel (GH) ist ein Polypeptidmaterial, das vom natürlichen Kollagen durch hydrolytische Zersetzung abgeleitet ist. Im Zuge von diesen Prozessen wird die Struktur der Dreifachhelix in einen Moleküleinzelstrang gebrochen. Gelatine enthält sowohl saure als auch basische Aminosäuren mit Werten des isoelektrischen Punktes nahe ~5. Zusätzlich sind saure funktionelle Gruppen dominant. Das Hydrogel von Agarosegel ist ein lineares Polysaccharid, das aus der marinen Rotalge extrahiert wird. Es besteht aus 1,3-β-D-Galactose und 1,4-α verbundener 3,6-Anhydro-α-L-Galactose-Resten. Hydrogele von Gelatine und Agarose bilden eine fibröse Struktur mit variierenden Netz-Lücke-Dimensionen. Dies ist abhängig vom Festkörpergehalt des Hydrogels. Das Gelatine-Hydrogel mit einem Gehalt von 2,5 Gew.-% übt weniger Druck auf das wachsende Kalzitkristall-Aggregat aus als ein Hydrogel mit 10 Gew.-%. Das Kieselerde-Hydrogel übt aufgrund seiner Natur, da es aus winzigen (kleiner als 20 nm) sphärischen Partikeln besteht und kein Netzwerk ausbildet, keinen starken Druck auf die wachsenden Kalzitkristall-Aggregate aus. Die Stärke des Hydrogels zusammen mit der Kristallwachstumsrate definiert die Menge des in das wachsende Kalzitkristall-Aggregat eingebauten Hydrogels. Dies bedeutet, dass bei einem starken Hydrogel mehr Gel in den Kalzitkristall einbaut wird als bei einem schwachen.

Ein im Mg-freien Kieselerde-Hydrogel (KH) wachsender Kalzit hat eine rhomboedrische Form, die entlang der c-Achse getreckt ist, während der Kalzit in der Anwesenheit von Mg als hantelförmiges Aggregat wächst. Das KH, egal ob Mg-frei oder Mg-haltig, hat keinen bedeutenden Einfluss auf die Koorientierung der erhaltenen Kristallaggregate. Ein in Mg-freier

Agarose gewachsener Kalzit verfügt über zwei Morphologhien: rhomboederförmige Kalzitkristalle und radiale Kalzitaggregate, während ein in Mg-haltiger Agarose wachsender Kalzit bündel- und erdnussförmige Morphologien aufweist. Die Anwesenheit von Mg in Agarose beeinflusst die Koorientierung der in diesen gewachsenen Kalzitkristallen. Der Kalzit/Mg-freie Agarose-Komposit besteht aus mehreren Untereinheiten, während der Kalzit/Mg-haltige Agarose-Komposit eine sphärulitische Mikrostruktur zeigt. Im Fall vom GH besteht die Ausfällung aus Kalzitaggregaten, die eine Vielzahl von Eigenschaften zeigen. Diese sind beispielsweise die Bildung von Mosaikkristallen und die Mesokristall-ähnlichen Untereinheiten in einem Aggregat, die Bildung der Aggregate mit einer fächerartigen Verteilung der c-Achsenorientierung und die Bildung von sphärulitischen Aggregaten. Die Bildung der Aggregate mit unterschiedlichen Charakteristiken in den Untereinheiten kann als Ergebnis einer Kombination aus lokalen Unterschieden in der Gelatinematrixanordnung und den physiochemischen Bedingungen, wie die Änderung im Mg/Ca-Verhältnis, pH, Sättigung, etc., erklärt werden. Die Entwicklung einer fächerartigen Verteilung der c-Achsenorientierung in den Untereinheiten der Kalzitaggregate kann als Ergebnis einer Zonierung erklärt werden. Ein anderer Grad von Mg-Einbau in anderen Wachstumsabschnitten führt zu verstärktem misfit strain. Dieser könnte durch die Bildung von Versetzungen in regelmäßigen Intervallen freigesetzt werden, sodass sich daraus Kleinwinkelkorngrenzen entwickeln. Dieses Wachstum führt ferner zu einem extremen, aufgespalteten Wachstum und zur Bildung von fächerartigen, sphärulitischen Kristallaggregaten.

Ätzexperimente an Kalzit/Hydrogel-Kompositen zeigen die Struktur des eingebauten Hydrogels innerhalb der Kalzitkristalle und -aggregate. Im Fall vom Mg-haltigen KH wird mehr KH in die Kalzitkristalle eingebaut als im Mg-freien KH. Dicke Hydrogelmembranen werden bei der Verwendung von Mg-freiem GH und AH beobachtet. Diese Membranen treten in Mg-haltigen GH und AH nicht auf. Die Bildung dieser Membranen, die in Mg-freien GH und AH vorkommen, ist ein Ergebnis der Ansammlung von Hydrogelfasern, welche von den wachsenden Kristallen oder Aggregaten zurückgedrängt werden. Die Steifigkeit der GH- und AH-Fasernansammlungen nehmen mit der Zugabe von Mg zu den Hydrogelen zu. Dadurch werden Hydrogele steifer und üben mehr Druck auf die wachsenden Mineral Aggregate aus. Folglich werden keine Hydrogel-Membranen in Aggregaten, die in Mg-haltigen GH und AH gewachsen sind, beobachtet.

Auf der Basis von Biopolymer/Mineral-Kompositen wurden Gips ($CaSO_4$)/Cellulose-Faserkomposite hergestellt. Der Zweck der Cellulosefasern im Gips ist es ein Komposit von hohem ökologischen Wert und besonderen mechanischen Eigenschaften, z. B. hohes E-Modul, hohe Biegefestigkeit und hohe Kompressionsstärke, zu erstellen. Abhängig von der Fasercharakteristik beeinflusst die Cellulosefaser die mechanische Eigenschaft der Komposite, z. B. die Natur der Cellulose (natürlich oder synthetisch), Flüssigkeitsansammlungswert, Grad der Schwellung, etc. Es wurde herausgefunden, dass die Lyocell-Faser, eine synthetische Faser, in der Lage ist das E-Modul des Komposites zu erhöhen.

List of Abbreviations

GH	Gelatine-Hydrogel
KH	Kieselerde-Hydrogel
ACC	amorphous calcium carbonate
VMHI	vickers nanohardness indentation
CPD	critical point drying
NFC	nanofibrillated cellulose
XRD	x-ray diffraction
SEM	scanning electron microscopy
SE	secondary electron
CRT	cathode-ray tube
TEM	transmission electron microscopy
BF	bright field
DF	dark field
EDX	energy dispersive x-ray
FE-SEM	field emission scanning electron microscopy
EBSD	electron backscatter diffraction
CCD	charge-coupled device
BSE	backscatter electron
PF	pole figure
ICP-OES	inductively coupled plasma-optic emission spectroscopy
TGA/DTA	thermogravimetry analyses/differential thermal analyses
FWHM	full width half maximum
FGD	flue gas desulfurization
FT-IR	fourier transform infrared spectroscopy
CP/MAS NMR	cross polarisation/magic angle spinning nuclear magnetic resonance
AFM	atomic force microscopy
STM	scanning tunneling microscopy

Table of Contents

1. Introduction

Carbonate biological hard tissues formed the inspiration for the scientific work in this thesis. These carbonate biological hard tissues are composites of biopolymers and carbonate minerals and are formed through biological mineralization. In order to understand the formation of carbonate biological hard tissues, it is essential to investigate the crystallization process in biomimetic systems. This yields a profound understanding of both, the biomimetic as well as the biological hard tissues.

1.1 Carbonate Biological Hard Tissue as Composite of Carbonate Minerals and Biopolymers

Biological mineralization or biomineralization refers to a process by which organisms form minerals. There are at least 60 different minerals in the biosphere that can be produced by organisms (Lowenstam & Weiner, 1989). Even though the majority of organisms do not form minerals, those which do form minerals in aquatic system, e.g. coccolith, bivalves, gastropods, echinoderms, play an important role in the formation of sedimentary sequences and exert major impacts on ocean chemistry. Biomineralization is also performed by vertebrates (Lowenstam & Weiner, 1989), bacteria (Winklhofer & Peterson, 2006) and plants (Lowenstam & Weiner, 1989). Vertebrates such as mammal biomineralizes calcium phosphate to produce bones and teeth and calcium oxalate as secretion product (kidney stone) (Lowenstam & Weiner, 1989). Calcium oxalate is also found in the skeleton of plant (chlorophyta) (Lowenstam & Weiner, 1989).

1.1.1 Biomineralization Processes of Carbonate Biological Hard Tissues

The process of biomineralization can be divided into two different mechanisms. Lowenstam (1988) proposed the concept of “biologically induced mineralization”. This refers to a process that occurs as a result of the metabolic activity of the organism. A second concept was introduced by Mann (1983). It is “biologically controlled mineralization”, a process that refers to the formation of minerals under the regulation of the organisms. The latter biomineralization process often produces minerals for environmental and metabolic specific purposes. Some organisms develop the ability to form hard tissues with functions that vary due to environmental purposes such as mobility in vertebrates; protection in bivalves, brachiopods and foraminifera; embryonic protection in the avian eggshell; balance in fish; detection of the Earth’s magnetic field in magnetotactic bacteria. Biologically controlled mineralization can be classified as extra-, inter- or intracellular process (Lowenstam & Weiner, 1989). In the case of extracellular mineralization the cell produces a macromolecular matrix outside of the cell in an area that will become the site of mineralization. The intercellular mineralization typically occurs in single-celled organisms that exist as a community (Weiner & Addadi, 2011). This type of mineralization is not widespread. The last type of mineralization, intracellular mineralization, occurs within specialized vesicles or vacuoles that direct the nucleation and growth of biominerals within the cell (Weiner & Dove, 2003).

The biomineralization process discussed in this dissertation focuses on extracellular mineralization. The extracellular mineralization is initiated by sequestering and concentrating ions from sea water or foods for mineralization (Figure 1.1a, b). The incorporated ions are then transported using the endoplasmic reticulum through membrane channels to the mineralization

sites (vesicles) (Figure 1.1c, d). In the case of mollusks (Watanabe et al., 1976), crustaceans (Levi-Kalisman et al., 2002) and echinoderms (Beniash, 1997), mineral-containing vesicles are found in the cells responsible for producing the mineralized tissues. Amorphous calcium phosphate (ACP)-containing vesicles in vertebrates are present in some cells that are responsible for cartilage and bone mineralization (Mahamid et al., 2010). The mechanism of transportation of the highly disordered mineral phase (Figure 1.1e) from the vesicle to the site of mineral deposition is characteristic for each organism such as dissolution and reprecipitation mechanism in limpet teeth where the highly disordered mineral is found in the vesicle while there is no evidence of mineral precursor phase in the extracellular matrix (Weiner & Addadi, 2011). A further example is the exocytosis mechanism in sea urchin larva where amorphous calcium carbonate (ACC)-containing vesicles are present in the extracellular matrix and are responsible for spicule formation (Weiner & Addadi, 2011).

The mechanisms between the introduction of the mineral into the extracellular environment and the formation of the extracellular matrix are synchronized. The highly disordered mineral is transported to the extracellular environment that contains the extracellular matrix prior to the introduction of the amorphous phase into the extracellular matrix (Figure 1.1f). In this extracellular matrix, the amorphous phase transforms into a more ordered phase (Figure 1.1g). The last process is the formation of the mature mineral. This mature mineral can remain within or can be exocytosed from the cell (Figure 1.1). In comparison to the geological counterparts, biominerals are usually less ordered (Griesshaber et al., 2013; Kim et al., 2014; Nindiyasari et al., 2014[b], Maier et al., 2014; Goetz et al., 2014). However, some organisms produce highly disordered minerals such as isopod cuticle (Seidl & Ziegler, 2012).

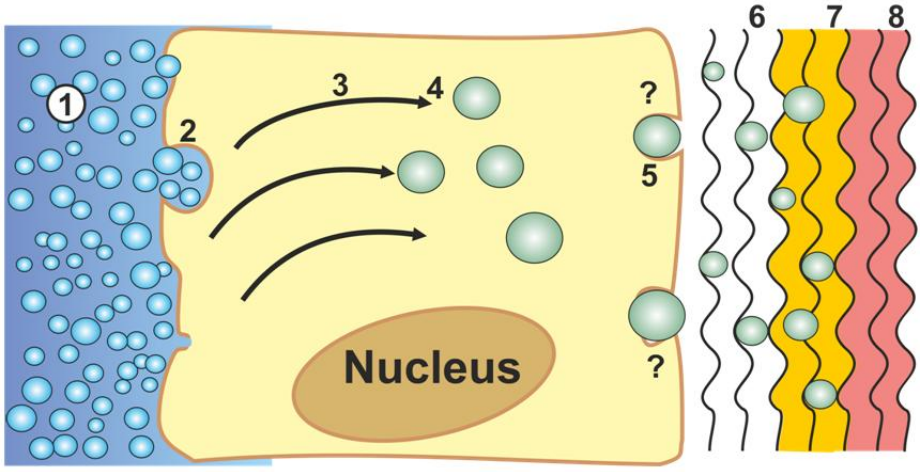

Figure 1.1. Schematic of extracellular mineralization showing (1) the medium from which the ions are derived, cell where the nucleus and vesicles are located inside and extracellular matrix (6, 7, and 8). The mineralization is commenced by an ion-sequestering process (2) and followed by ions transportation to the vesicle or mineralization sites (3, 4). The mineral-bearing vesicles are then transported to the extracellular matrix (5, 6) where the highly disordered phases are transformed into less disordered phase (7) and lastly into mature minerals (8). Modified after Weiner & Addadi (2011).

1.1.2 Phases in Carbonate Biological Hard Tissues

Calcium carbonate is one of the most abundant minerals on Earth (Lippmann, 1973). It has two hydrated forms, three anhydrous forms and amorphous forms (Cartwright et al., 2012). The hydrated forms are known as hexahydrate (ikaite) and monohydrate (Brooks et al., 1950). The anhydrous forms are calcite, vaterite and aragonite (Radha & Navrotsky, 2013). Calcite is the thermodynamically stable phase under Earth surface conditions and the most abundant phase among all calcium carbonate phases (Plummer & Busenberg, 1982). Aragonite is a less stable form and is mainly found as biosynthetic $CaCO_3$ in bivalve and gastropod shells and corals. Non-biological, geogenic, aragonite forms in caves and occurs generally in environments where Mg concentration is high. Finally, the most unstable carbonate polymorph, vaterite (Lippmann, 1973), rarely occurs in nature-made materials but plays an important role in calcium carbonate formation from solution (Sawada, 1997; Lippmann, 1973; Grasby, 2003). Vaterite is also found in environments that have high salinity and high sulfate concentration (Lippmann, 1973) and can act as transient phase (Lowenstam & Abbot, 1975; Rodriguez-Blanco et al., 2011).

Calcium carbonate in biominerals (Table 1.1) is found in brachiopod, gastropod and bivalve shells, corals, otolith, teeth and the exoskeleton of arthropods, decapods, etc (Mann, 2001). Some organisms, such as coccolithophores, foraminifera, mollusks, crustaceans, brachiopods and gastropods use calcium carbonate as an exoskeleton with several purposes such as protection of the soft tissue against predators, stabilization and facilitation of filtration in combination with the exclusion of sediment from the soft tissue, augmentation of respiration and dispersion of gametes and, if applicable, the brood of larvae (Alexander, 2001; Rudwick, 1970).

Table 1.1. Calcium carbonate biominerals in some organisms, summarized from Mann (2001).

Minerals	Formula	Organisms
Calcite	$CaCO_3$	Coccolithophores Foraminifera Trilobites Mollusks Crustaceans Birds Mammals
Mg-calcite	$(Mg, Ca)CO_3$	Octocorals Echinoderms
Aragonite	$CaCO_3$	Scleractinian corals Mollusks Gastropods Cephalopods Otolith
Vaterite	$CaCO_3$	Gastropods Ascidians
Amorphous	$CaCO_3\,nH_2O$	Crustacean Plants

Amorphous calcium carbonate (ACC) is a transient phase of calcium carbonate. It is believed that the transient ACC is a precursor of biological calcite and aragonite (Han & Aizenberg, 2008; Lam et al., 2007). The transient amorphous calcium carbonate was first identified, in the late 1960s, in chiton teeth (Towe & Lowestam, 1967). Amorphous calcium carbonate can be found in invertebrates and vertebrates with different functions. Some organisms such as arthropods (Cartwright et al., 2012) and earthworms (Gago-Duport et al., 2008) use amorphous calcium carbonate as storage for the future availability of calcium carbonate. Echinoderms (Beniash et al., 1997), crustaceans (Raz et al., 2002) and mollusks (Weiss et al., 2002) use amorphous calcium carbonate as a transient phase or a precursor in the formation of calcium carbonate crystals. Some crustacean species such as the crayfish *Procambarus clarkia* uses amorphous calcium carbonate (ACC) as a temporary storage before molting (Marin & Luquet, 2004). Gastropods transform ACC into aragonite and some calcite (Marxen et al., 2003), bivalves transform ACC into aragonite and brachiopods transform ACC into calcite. In a terebratalia brachiopod, *Megerlia truncata,* the amorphous calcium carbonate can be found between the organic membranes at the innermost of the secondary layer (Griesshaber et al., 2009). Gebauer et al. (2008) identified two different ACC based on solubility, ACC I and ACC II. ACC I is more stable and resembles the short-range structure of calcite while ACC II, the less stable ACC, is related to the less stable anhydrous calcium carbonate, vaterite. Recent study further introduced the notion of protocrystalline structuring in ACC, namely ACC I as proto-calcite ACC (pc-ACC) and ACC II as proto-vaterite ACC (pv-ACC) (Gebauer et al., 2010).

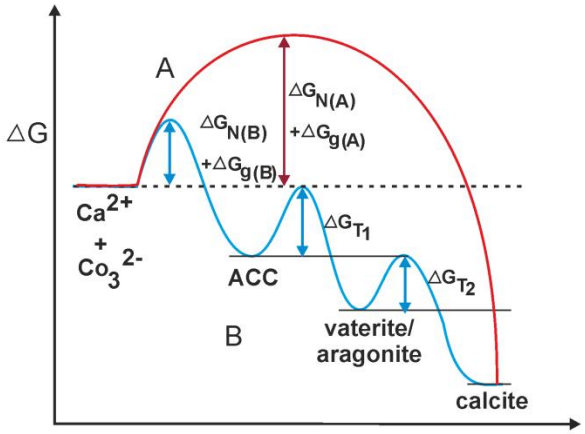

Figure 1.2. Reaction diagram that illustrates the energy barriers and the Gibbs free energy change associated to the formation of calcite. Two different pathways are depicted. Pathway A represents the classical crystallization pathway, where $\Delta G_{N(A)}$ is the activation-energy barrier associated with nucleation, $\Delta G_{g(A)}$ is the free energy of activation associated with growth and ΔG_T is the activation-energy barrier associated to the phase transformation. Pathway B involves a multi-step route towards the formation of calcite, with the formation of ACC, vaterite and/or aragonite in intermediate steps. This route is a manifestation of Ostwald's "step rule". Modified after Gower (2008).

Amorphous calcium carbonate as a metastable phase of calcium carbonate is found in some organisms as a stable form. However, the question on how to produce stable amorphous

calcium carbonate is still unanswered. There should be a controller that provokes the stabilization of amorphous calcium carbonate. Macromolecules, water, membranes, and ionic molecules are proposed to play the role (Politi et al., 2003; Huang et al., 2007; Guillemet et al., 2006; Loste et al., 2003; Xu et al., 2005). Inorganic phosphate, phosphoenol pyvurate and citrate have been demonstrated to control the stabilization of amorphous calcium carbonate in crustacean cuticles (Akiva-Tal et al., 2011; Sato et al., 2011).

The activation-energy barriers and the Gibbs free energy are associated to the formation of calcite from an aqueous solution and follow two reaction pathways (Figure 1.2). A one-step route, pathway A, requires overcoming a large energy barrier while the other reaction, pathway B, involves a sequence of steps with small energy barriers. The first step of pathway B leads to the formation of ACC, which eventually transforms into aragonite/vaterite and finally into calcite (Gower, 2008).

1.1.3 Biological Composites

One of the special characteristics that distinguish biological carbonate from geological carbonate minerals is that most of the former are composites or crystal aggregates whose inorganic units are separated by organic materials (Weiner & Dove, 2003). These organic materials are structured in a continuous sheet-like organic matrix that subdivides the space where mineralization occurs. In most organisms, organic matrices are usually constituted from a framework of macromolecules such as collagen (Rahman & Isa, 2005; Murayama et al., 2000), proteoglycans (Jolivet et al., 2008; Borelli et al., 2003) or chitin (Addadi & Weiner, 2003; Ponce & Evans, 2011; Al-Sawamih et al., 2008), etc. Organic matrices in combination with biominerals play an important role in the definition of some features required by the organism to facilitate specific functions. At unit cell level, organic matrices can influence the characteristics of biominerals by causing a so called anisotropic lattice distortion such as in the case of the orthorhombic unit cell of a mollusk-made aragonite that is anisotropically distorted as compared with that one of geological aragonite (Cusack & Freer, 2008; Pokroy et al., 2006).

Griesshaber et al. (2013) investigated the organic matrix structure in *Mytilus edulis*. Organic matrix in *M. edulis* is an occluded fabric-like network that constitutes of an open pore system. Both aragonite and calcite biominerals have an organic matrix surrounding the aragonitic nacre tablets and the calcitic fibers, respectively. The organic matrix layer is also found at the transition of aragonite to calcite with a layer thickness of 1-2 micrometers. Mollusk shells consist of 95 to 99% per weight calcium carbonate mineral while the remaining 1-5 % per weight is occupied by the organic matrix. The aragonite nacre contains a small amount of organic biopolymer. Therefore aragonite nacre exhibits a fracture toughness that is higher than that of aragonite from chemical precipitation (Jackson et al., 1988). One of the most popular nacreous materials is the mother-of-pearl that consists of an iridescent aragonite layer. The organic matrix of mollusk shells is a mixture of proteins, gylcoproteins, and chitin that controls the calcium carbonate polymorphs, the size, the shape of the crystallites, and the texture of the shells (Marin & Luquet, 2004).

In the case of brachiopods two shell forming principles are observed (Figure 1.3). One is

based on calcite mineral fibers embedded in ~2 wt % of organic biopolymer sheaths while in the second strategy the biopolymer fiber is reinforced by Ca-phosphate nanoparticles and forms a fibrous nanocomposite (Schmahl et al., 2008). The microstructure and micromechanics of brachiopods have been thoroughly studied. The calcitic brachiopod's valves consist of two major layers as seen in *Megerlia truncata* and *Terebratalia transversa*. The microhardness of a thin, nanocrystalline, hard outer protective layer exceeds the value of 200 HV as measured with Vickers nanohardness indentation (VMHI). The second layer, a much thicker layer, has two distinct layers, an outer part and a soft inner layer. The outer part, consists of transversely cut fibers, has a VMHI value between 100 and 140 HV; while the inner soft layer, consists of longitudinally cut fiber, has values between 70 and 110 HV (Griesshaber et al., 2007). The fibrous material is used to compose both, the outer and inner secondary layer that displays distinctly different hardness properties.

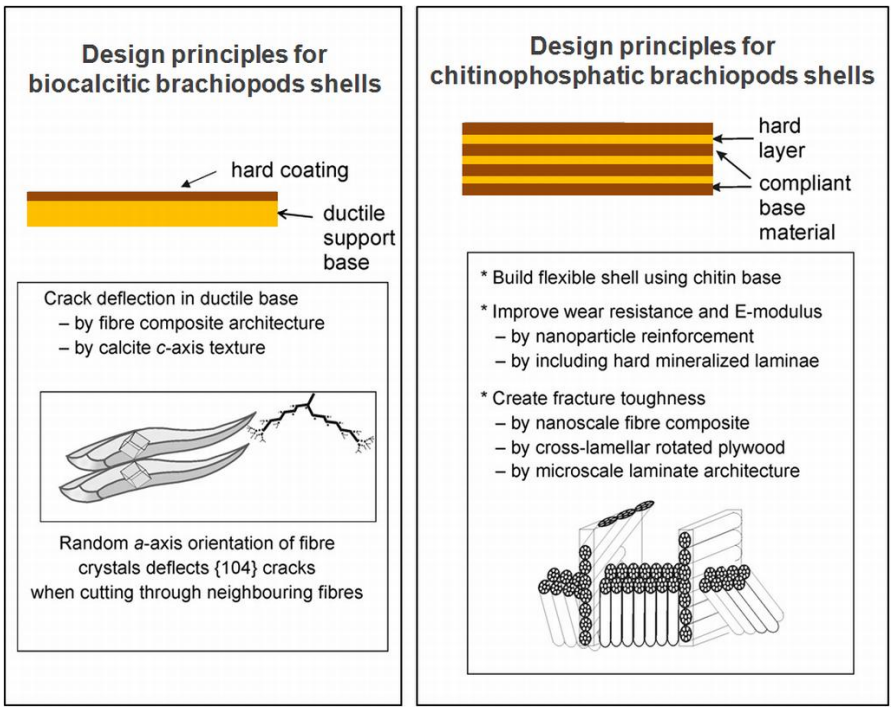

Figure 1.3. Design principles of calcitic (terebratalia) and chitinophosphatic (lingulid, discinid) brachiopod shells. Modified after Schmahl et al. (2008).

Nanoindentation measurements of the chitinophospatic brachiopod species such as *Lingula anatina* and *Discradisa stella* have an E-modulus in the range of 3 to 55 GPa and a nanohardness of 0.1 to 3 GPa as a result of the varying degree of mineralization. In comparison, the E-modulus of the calcitic brachiopod shell is 63±8 GPa and the nanohardness is 4±0.5 GPa. The chitinophosphatic layer is a laminated layer with a sequence of chitinous and mineralized chitinophosphatic layers.

1.2 Calcium Carbonate Biomimetic Composite Materials

Organic matrices in organisms such as mollusks, corals, and coccolithophorids play a

crucial role in biomineralization (Cusack & Freer, 2008; Kobayashi & Samata, 2006). It is well established that most biomineralization processes occur in confined environments within organic matrices (Levi-Kalisman et al., 2001). Those organic matrices show features strikingly similar to those of hydrogel systems (Table 1.2). It is possible to fine-tune the porosity and the chemical characteristics of hydrogels by using different hydrogel contents and additives in order to get better resemblance of the characteristics of organic matrices in organisms (Nindiyasari et al., 2014[a,b]). Thus, this dissertation focuses on the crystallization of calcium carbonate in hydrogel biomimetic counter-diffusion system.

Table 1.2. Applications of hydrogels as organic matrices for biomineralization, summarized from Asenath-Smith et al. (2012).

Mineral	Hydrogel matrix	Organism	Organic matrix
Aragonite	Silk fibroin-like hydrogel	Mollusks, nacre	Acidic protein
	Fibrillar, non-collagenous protein	Coral	Acidic (sulfonated) glycoprotein
	Short-chain meshwork-forming collagen	Otoliths	Glycoprotein Otoconins
Calcite	Short-chain meshwork-forming collagen	Otoconia	Glycoprotein Otoconins
		Otoliths	OMP-1
	α-chitin	Barnacles	Acidic protein
Vaterite	Short-chain meshwork-forming collagen	Otoconia	Glycoprotein Otoconins
Carbonate apatite	Amelogenin	Enamel	Glycoprotein
	Fibrillar collagen	Bone	Acidic glycoprotein, Proteogylcans

1.2.1 Classical and Nonclassical Concepts of Crystal Growth

Crystal growth processes mainly involve three important steps (Sunagawa, 2005). The first step is the generation of driving forces that allow the following steps to proceed. Such driving force arises when the system achieves a supersaturated or super cooled state. In a supersaturated system clusters are continuously forming and are being destroyed as a result of fluctuations (Chernov, 1984; Kashiev, 2000; Gebauer et al., 2008; Gebauer & Cölfen, 2011; Cölfen & Antonietti, 2005; Meldrum & Cölfen, 2008). According to the classical nucleation theory, clusters with a size smaller than a critical size of a nucleus are unstable and tend to disintegrate, while clusters that are larger than a critical size of the nucleus tend to grow. The formation of particles or clusters larger than the critical size of the nucleus is referred to as nucleation. As soon as nucleation occurs, the growth of crystals will occur (Sunagawa, 2005).

Nucleation can be classified as primary and secondary nucleation. Primary nucleation refers to the case when nucleation occurs without the intervention of previously existing crystals. There are two different pathways for primary nucleation, homogenous and heterogeneous nucleation. Homogenous primary nucleation is a spontaneous nucleation that occurs in the bulk of a uniform medium. Heterogeneous primary nucleation occurs when the formation of nuclei is facilitated by the presence of a preexisting surface. This surface can correspond to foreign

particles such as impurities, additives or crystals. The secondary nucleation pathway is followed when crystals of the crystallization phase are already present in the system and supercritical nuclei originate as a result of a number of phenomenon, among them attrition, collision, etc (Mullin, 2001).

When an atom or molecule arrives at the surface of a crystal, it is not immediately integrated into the crystal lattice but it is able to migrate on the crystal surface. The migrating units become integrated into the crystal after attachment at active sites on the surface (Chernov, 1984; Meldrum & Cölfen, 2008).These sites can be kinks, steps and terraces (Figure 1.4). The attachment energy of the growth unit to the crystal site decreases from terrace to kink sites. Thus, a solute molecule that reaches a crystal surface will preferentially incorporate into a kink site (Sunagawa, 2005).

In the classical model of crystal growth, three crystal growth mechanisms are contemplated:

a) Continuous or adhesive growth, which predominates at high supersaturations. The limiting process, i.e. the process that defines the growth rate, is the volume diffusion, the diffusion of growth units from the bulk medium (aqueous solution in the case of biomineralization and formation of most minerals on the Earth surface) to the surface of the growing crystal. Once crystal growth units reach the crystal surface, they readily incorporate into growth sites. For this mechanism to predominate, crystal surfaces need to be rough (show a high proportion of kink sites). There are crystals that have surfaces that are intrinsically rough (thermodynamic roughness). Other crystals have flat surfaces but these can become rougher with growing supersaturations (kinetic roughness) (Sunagawa, 2005).
b) Two-dimensional nucleation mechanism, which operates at intermediate supersaturations. For growth to occur, two-dimensional nuclei have to form on crystal surfaces. Two-dimensional nucleation has a energy barrier associated that can be overcome when supersaturation is high enough. As soon as a two-dimensional nucleus forms, it spreads on the surface. Consequently, two-dimensional nucleation leads to layer-by-layer growth (Sunagawa, 2005).
c) Spiral growth, which predominates at low supersaturations. It requires the existence of screw dislocations, which represent a continuous source of growth sites (kink site at the merging of the dislocation) (Mullin, 2001).

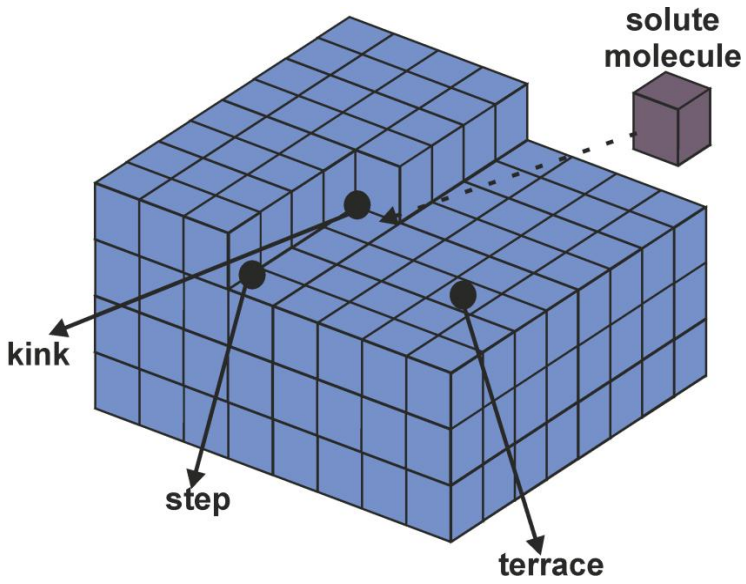

Figure 1.4. Kossel's model of layer-by-layer growth mode illustrating the kink site, step site, terrace site and solute molecule. The model is modified after Sunagawa (2005).

In thermodynamic equilibrium, the given temperature-pressure range determines the final stable phase. Moreover, thermodynamics predicts the nucleation of the stable phase in a single step and its immediate growth, which will continue as long as the system remains supersaturated with respect to this phase. Figure 1.5 illustrates the variation of the Gibbs free energy of a crystal nucleus as a function of the nucleus size, assumed the nucleus to be spherical. The total change in free energy ΔG accompanying this event is equal to the sum of the volume excess free energy (ΔG_v) such as the excess energy between a very large particle and the solute in solution and the surface excess free energy (ΔG_s) such as the excess free energy between the surface of the particle and the bulk of the particle. Thus, it can be expressed as:

$$\Delta G = \tfrac{4}{3}\pi r^3 \Delta G_v + 4\pi r^2 \gamma$$

where r is the radius of the nucleus, ΔG_v is the volume free energy change of the transformation, ΔG_s is surface free energy change and γ the specific interfacial energy, i. e. between the developing crystalline surface and the supersaturated solution in which it is located. While the first term of the sum, the volume excess free energy (ΔG_v), has a negative value if the phase to form is thermodynamically stable, the second one, the surface excess free energy (ΔG_s), is positive. The form of the function ΔG depends on the balance between the values of these two terms and is shown in Figure 1.4 as a function of the nucleus radius (Mullin, 2001).

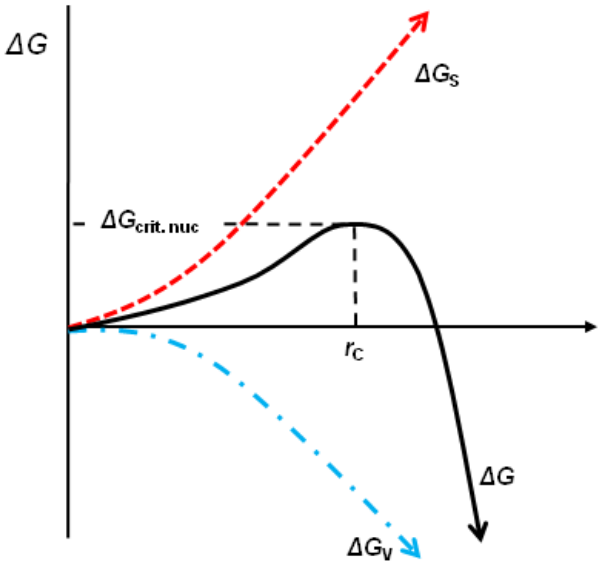

Figure 1.5. Gibbs free energy of the nucleation as a function of the nucleus radius. The critical nucleus radius is shown as r_c while ΔG is Gibbs free energy. Modified after Gower (2008).

The energy contribution resulting from the formation of the nucleus surface predominates when the nucleus is small, but is overbalanced by the energy contribution associated to the formation of the nucleus volume as soon as a certain size of the nucleus, the critical size, is reached (Mullin, 2001). Consequently, nuclei larger than the critical size will grow since them becoming larger leads to a reduction of the free energy (Mullin, 2001).

In classical crystallization (pathway A in Figure 1.1 and (a) in Figure 1.6) crystals are assumed to grow from primary building blocks such as atoms, ions or molecules that coalesce to form clusters (Niederberger & Cölfen, 2006). The clusters which reach the critical nucleus size will continue to grow through ion-by-ion attachment. However, long time overwhelming evidence has shown that classical crystallization does not always operate. In 2008, Meldrum & Cölfen summarized numerous examples in which the classical crystallization models cannot be applied and interpret them in the framework of non-classical crystallization. This non-classical crystallization includes the following crystallization mechanisms; (i) formation of an intermediary cluster or phase separation to liquid precursor as the primary building blocks (Gebauer & Cölfen, 2011; Gebauer et al., 2008), (ii) crystallization via amorphous intermediates involving transient amorphous building blocks, which can undergo mesoscopic transformations (Cölfen & Antonietti, 2005; Niederberger & Cölfen, 2006), (iii) oriented attachment of nanoparticle building blocks that transform into a single crystal upon fusion of the nanoparticles, and (iv) nanoparticles assembly through three-dimensional self-organization to produce mesocrystals (Meldrum & Cölfen, 2008).

Crystallization under kinetic control is generally the consequence of either occurring under high supersaturation conditions or a modification of the activation-energy barrier for nucleation, growth, and/or phase transformation. The presence of specific ions or molecules (additive) in the crystallization medium can lead to the predominance of the kinetic control (Meldrum & Cölfen, 2008). Kinetic control of the crystallization may result in the formation of

different polymorphs. However, the difference in polymorphs can also be a result of the passivation of the nuclei of the stable phase by an additive, which renders them unable to grow and leads to the formation of an alternative polymorph whose solubility is only slightly higher than that of the stable phase (Nindiyasari et al., 2014[b]). When kinetically controlled crystallization occurs at high supersaturation as a driving force, nanosized particles can form and subsequently aggregate.

Two of the non-classical crystallization pathways suggested in (iii) and (iv), are schematized in Figure 1.6. The first pathway (iii), pathway (b) in Figure 1.6 occurs through the formation of iso-oriented crystals that transform into a single crystal upon fusion of the nanoparticles. The second pathway, pathway (iv) or pathway (c) in Figure 1.6, applies when crystals are coated by some organic compounds. This pathway operates through the mesoscale assembly of nanoparticulate building blocks and leads to the formation of mesocrystals. An early definition of mesocrystal was suggested by Niederberger & Cölfen (2006) who describe mesocrystals as colloidal crystals composed of individual nanocrystals that are aligned in a common crystallographic fashion. Seto et al. (2012) then adapted the definition of mesocrystals as an ideal crystal that comprises a 3D array of isooriented single crystal particles with sizes in the range of 1-1000 nm.

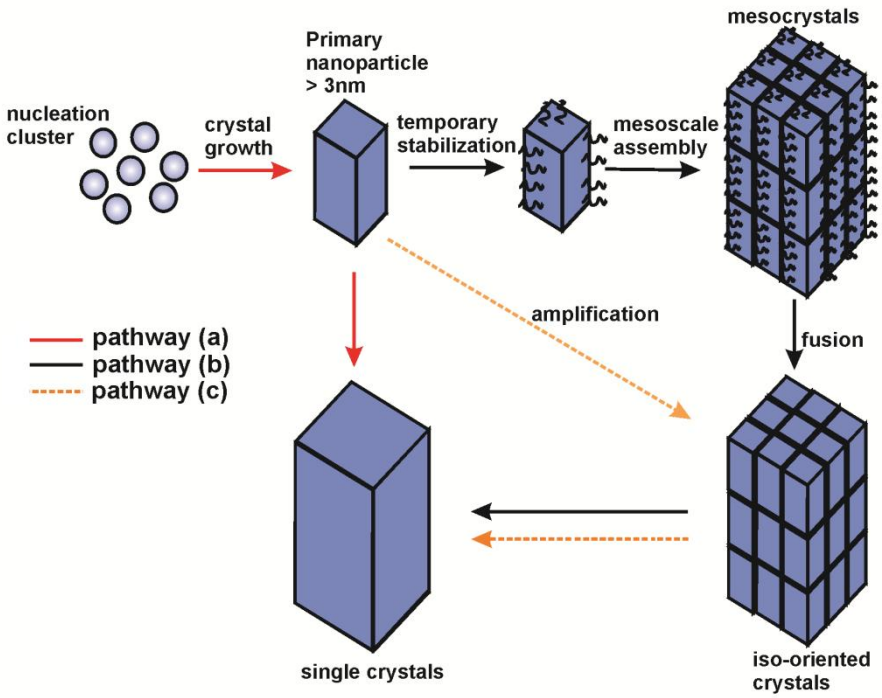

Figure 1.6. Schematic illustrating three different crystallization pathways including classical crystallization and non-classical crystallization routes that lead to the formation of mesocrystals. Modified after Cölfen & Antonietti (2005).

1.2.2 Hydrogel as Organic Matrix for Biomimetic Composite Material

There are several hydrogels that can be used to mimic the characteristics of organic

matrices, such as polyacrylamide, gelatin, silica, agarose gel, etc. An organic poly-acrylamide hydrogel was used by Grassmann et al. (2003) to synthesize calcite aggregates with a double diffusion system. The obtained aggregates have a pseudo-octahedral morphology and are built up by units with sizes in the range of hundreds of nanometers. The hydrogel incorporated in these calcite aggregates is about 0.7 mass %.

Apart from the counter-diffusion methods some other hydrogel-based methods can be applied to mimic biomineralization. Li & Esttroff (2009) applied a method based on the diffusion of CO_2 to grow calcite in hydrogels of two different agarose gel and explored the relationship between crystal growth rate, hydrogel strength, and organic matrix incorporated into a growing crystal. The mechanism through which calcite crystals incorporate the porous agarose hydrogel matrix during growth is proposed in Figure 1.7. The growth rate is related to the driving force, i.e. supersaturation with respect to calcite in this case. The schematic image illustrates the role of the growth rate and the hydrogel strength. During growth the crystal exerts a pressure against the hydrogel matrix. In the case of a weak hydrogel the crystal pushes it away unless the growth rate is slow. Thus, depending on how fast the crystal is growing, little or no hydrogel is incorporated into the growing crystal. The strong hydrogel, on the other hand, can resist the crystallization pressure and push back against the growing calcite crystal. In this case a significant amount of hydrogel is incorporated into the crystal during growth, even when the growth rate is slow. The combination of a strong hydrogel and a high growth rate will lead to a competition between the hydrogel and the grown crystal (Li & Esttroff, 2009; Asenath-Smith et al., 2012).

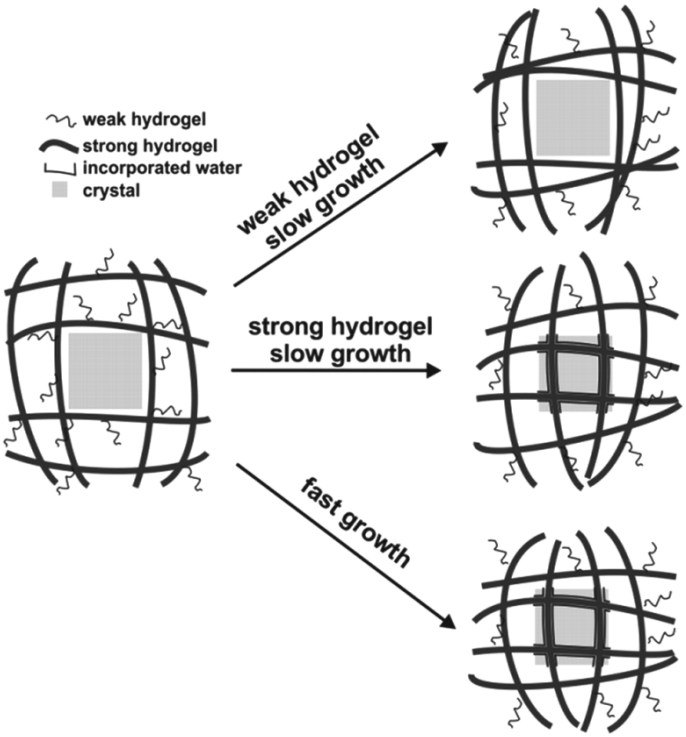

Figure 1.7. Illustration of calcite crystal grown in strong or weak hydrogels, respectively. The connection between hydrogel strength and fast growth results in crystals with high amounts of hydrogel matrix incorporated. Modified after Li & Esttroff (2009).

1.3 Biomimetic Gypsum/Cellulose Composites

Carbonate biological hard tissues are composites that have characteristic mechanical properties as a result of an intimate association between organic matrices and minerals. This idea is an inspiration to create gypsum/cellulose composites that have improvements in mechanical properties.

1.3.1 Gypsum

Calcium Sulfate System and Production

Gypsum is a useful material in industry that has been used for centuries. It readily loses its water when heated resulting in partially or totally calcined gypsum. When the water is added to the calcined gypsum, it reverts to its original dihydrate form. Gypsum is also found in antiquity as mortar and is called *gatch* in Persian language, *gypsos* in Greek and *gypsum* in Latin. There are four calcium sulfate phases that exit at room temperature: calcium sulfate dihydrate, calcium sulfate hemihydrate, calcium sulfate anhydrite III and calcium sulfate anhydrite II. The last phase of calcium sulfate, calcium sulfate anhydrite I, only exists above 1180 °C. Each phase of calcium sulfate has different and specific characteristics (Table 1.3).

Table 1.3. Calcium sulfate-water system and characterization, summarized from Wirsching (2005).

Formula	Molecular mass (g/mol)	Stages	Water of crystallization (wt %)	Density (g/cm^3)	Solubility*
$CaSO_4.2H_2O$	172.17	-	20.92	2.31	0.21
$CaSO_4.1/2H_2O$	145.15	α-form,	6.21	2.757	0.67
		β-form	6.21	2.619 – 2.637	0.88
$CaSO_4$ anhydrite III	136.14	α-anhydrite,	0.00	2.58	hydrates to hemihydrate
		β-anhydrite	0.00	2.58	
$CaSO_4$ anhydrite II	136.14	AII-s, slowly soluble anhydrite	0.00	2.93-2.97	-
		AII-u, insoluble anhydrite	0.00	2.93-2.97	-
		AII-E, *Estrichgips*	0.00	undetermined	-
$CaSO_4$ anhydrite I	136.14	-	0.00	undetermined	-

* Solubility in water at 20 °C, g $CaSO_4$ per 100g solution.

Calcium sulfate hemihydrate has two different morphologies, α-hemihydrate and β-hemihydrate. The calcium sulfate α-hemihydrate consists of compact, well-formed, transparent,

large primary particle and is obtained from the dehydration of calcium sulfate dihydrate at high water-vapor partial pressure, achieved above 45 °C in acid solutions or above 97.2 °C in water under certain pressure. The calcium sulfate β-hemihydrate is obtained from calcium sulfate dihydrate by heating it under low water-vapor partial pressure, such as in dry air or vacuum, between 45 °C and 200 °C. The calcium sulfate transformation and calcium sulfate anhydrite production are explained in Figure 1.8 (Wirsching, 2005).

The various gypsum and anhydrite deposits of calcium sulfate differ in purity, structure and color. Calcium carbonate (limestone), clay and dolomite are the major impurities followed by silica, bitumen, glauberite, syngenite and polyhalite. Gypsum is also produced from Flue Gas Desulfurization (FGD). The gypsum produced through this method is highly pure. The FGD gypsum is produced as follows;

(1) Desulfurization.

The flue gas is sprayed with limestone ($CaCO_3$) suspension. The reaction, occurred at pH 7-8, produces insoluble calcium sulfite ($CaSO_3$).

SO_2 (g) + $CaCO_3$ (s) + $1/2H_2O$ ⟶ $CaSO_3.1/2H_2O$ (s) + CO_2 (g)

(2) Forced oxidation.

The calcium sulphite ($CaSO_3$) reacts spontaneously with atmospheric oxygen (pH 5) and forms soluble calcium bisulfate which then is oxidized into calcium sulfate dihydrate.

$CaSO_3.1/2H_2O$ (s) + O_2 (g) + $3H_2O$ ⟶ $2CaSO_4.2H_2O$ (s)

(3) Gypsum separation.

The calcium sulfate dihydrate product is then separated and solid impurities are removed.

(4) Gypsum washing and dewatering

The calcium sulfate dihydrate crystals are filtered or centrifuged and washed with clean water.

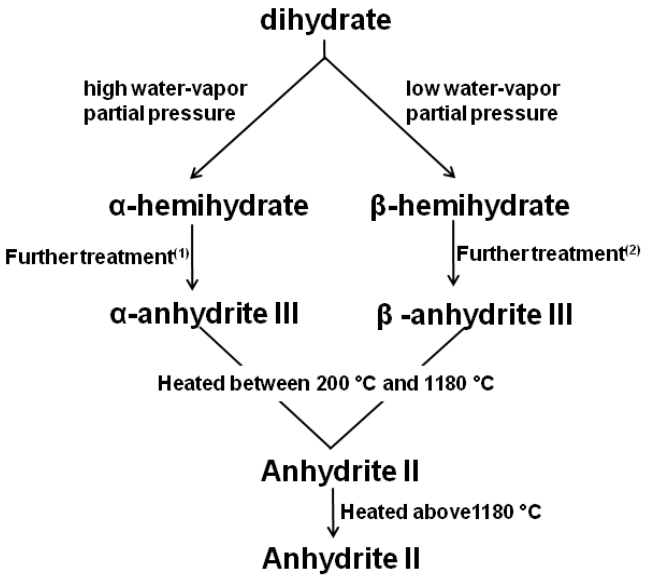

Figure 1.8. Calcium sulfate transformation from dihydrate (gypsum) to anhydrite. The dihydrate is transformed to hemihydrate and subsequently to several different anhydrite phases. The transformations are temperature and pressure dependent. The schematic is summarized from Wirsching (2005).

Calcium sulfate hemihydrate can be produced from both the natural gypsum and FGD gypsum. In the case of natural gypsum, the β-hemihydrate or plaster of Paris, that is mainly used as a building component and as a building plaster, is produced by calcination between 120 °C and 180 °C while α-hemihydrate is produced by a wet calcination process, either under elevated pressure in autoclaves or atmospheric pressure in acids or aqueous salt solutions between 80 °C and 150 °C. In the case of β-hemihydrate from FGD gypsum, the FGD gypsum must be dried before calcination. The drying procedure can be conducted in tube dryers heated indirectly with steam. The calcinations of β-hemihydrate takes place in kettles while the calcinations of α-hemihydrate is carried out using continuous autoclaves process (Wirsching, 2005).

Mechanical Properties of Calcium Sulfate Dihydrate ($CaSO4.2H_2O$) and Reinforced Calcium Sulfate Dihydrate ($CaSO4.2H_2O$)

The transformation of hemihydrate calcium sulfate into gypsum through hydration relies on several aspects, as follows (Padevet et al., 2011);

(1) Temperature during the gypsum slurry preparation.

The temperature during the gypsum slurry preparation affects the hydration time. The high gypsum slurry preparation temperature leads to a fast drying of the slurry before placed into the mould.

(2) Water/gypsum ratio.

The ratio of water/gypsum has influence on the physical characteristics of the hardened gypsum, such as its volume density and total porosity. Thus, it also influences the mechanical properties of the material, its moisture, thermal properties and sound insulation properties.

(3) Gypsum mixing method.

There are several methods of gypsum mixing, such as casting, pressing and vibrating. Casting method, simply placing the gypsum slurry into the mould, may lead to the entrapment of air bubbles that further produce high porosity. Pressing and vibrating can reduce the entrapment of air bubbles.

(4) The purity of initial hemihydrate or gypsum.

The purity of the gypsum is related to the different phases of calcium sulfate-water systems. Thus, the proportion between calcium sulfate hemihydrate, anhydrite and dihydrate and other impurities influences the hydration process.

(5) Addition of some other impurities/additives.

Singh et al. (2005) explains an effect of carboxylic acid on the hydration process of hemihydrates plaster. Adsorption of carboxyl acid on gypsum crystal surface is maximal resulting in maximum retardation of hemihydrate hydration.

In a recent study Chen et al. (2010) investigated the hierarchical mechanical properties of gypsum from single crystals to aggregates. For free standing single crystals a flexural strength of 2.2 GPa measured using nanoindentation was reported. The elastic modulus, tensile strength, and fracture toughness of monolithic gypsum consisting of interlocking needle-like microcrystals are also reported and strongly change as functions of porosity and accelerator (ground gypsum) addition (Chen et al., 2010). In addition to a reduction of porosity, a microstructure change from common radial needle aggregates to a single crystal made up of homogeneous, randomly oriented, crystals have improved the mechanical properties up to 50–100%.

The improvement of the mechanical properties of gypsum can be achieved by fiber reinforcement such as cellulose fiber, polyamide fiber, hemp fiber, etc. In industrial manufacturing, gypsum fiber board where gypsum is reinforced with e.g. cellulose fibers from recycled paper is a fairly novel material class which shows extreme fracture damage tolerance. Some researches already investigated the ability of fiber as reinforcement material. Eve et al. (2002) reported an increase in fracture toughness of the gypsum composite from 0.14 to 0.20 $MPam^{1/2}$. The increase in fracture toughness was achieved after porosity was reduced from 52% to 42% due to an addition of 2% polyamide fibers. Another research done by Dalmay et al. (2010) reported an increase in bending strength of gypsum composites from 3.2 MPa to 3.7 MPa by adding less than 10% flax fibers, and an increase from 3.2 MPa to 3.5 MPa by adding less than 10% hemp fibers. As a comparison the typical value for the compressive and bending strength of gypsum without any additive has been reported to be in the order of 8-15 MPa and 3-6 MPa, respectively.

1.3.2 Cellulose

Cellulose is a hydrophilic polymer, non-toxic, biodegradable (Goussé et al., 2004) and a renewable polymer with good process ability (Bochek, 2003). Cellulose is a polysaccharide built by the sequence of glucose repeating units. In plant, polysaccharide exits in the primary, secondary and tertiary walls. The primary wall consists of cellulose chains that run in all directions within the wall plane. In the other hand, in the secondary wall, the cellulose chains consist of microfibrils that are parallel to each other. Thus, the packaging is denser and aligned more or less with the fiber axis. The third wall has a low amount of cellulose and is mainly composed of xylan (O'Sullivan, 1997).

The first model of cellulose as the fringe micellar was proposed by Astbury (1933). The micellar model has completely ordered or crystalline regions that, without any distinctive boundary, change into disordered or amorphous regions. The crystalline region consists of microfibrils with size of 10 – 20 nm that combine into larger fibrils or lamellae and form fibers. The disordered cellulose molecules together with hemicelluloses and lignin are located in the spaces between the microfibrils. The amorphous region has the same alignment with the microfibrils. Another model about microfibril was proposed by Frey-Wyssling (1953). This model states that a microfibril with several aggregated elementary fibrils is called a micellar strand or unordered crystallized cellulose. Fengel (1971) proposed a model of ultrastructural wood cell wall (Figure 1.9) explaining that wood has several layers of hemicelluloses molecules between the fibrils and a monomolecular layer of hemicelluloses between elementary fibrils. The lignin is found to surround the total microfibrillar.

Cellulose has around six different polymorphs; cellulose Iα, cellulose Iβ, cellulose II, cellulose III_I, cellulose IV_I and cellulose IV_{II} (Table 1.4). The polymorphs of cellulose were studied during several years using several different techniques such as Fourier Transform Infrared Spectroscopy (FT-IR), Cross Polarization/Magic Angle Spinning Nuclear Magnetic Resonance (CP/MAS NMR), neutron and electron diffraction, raman spectroscopy, scanning electron spectroscopy (SEM), atomic force microscopy (AFM), transmission electron microscopy (TEM), scanning tunneling microscopy (STM) and some computer based modeling (O'Sullivan, 1997).

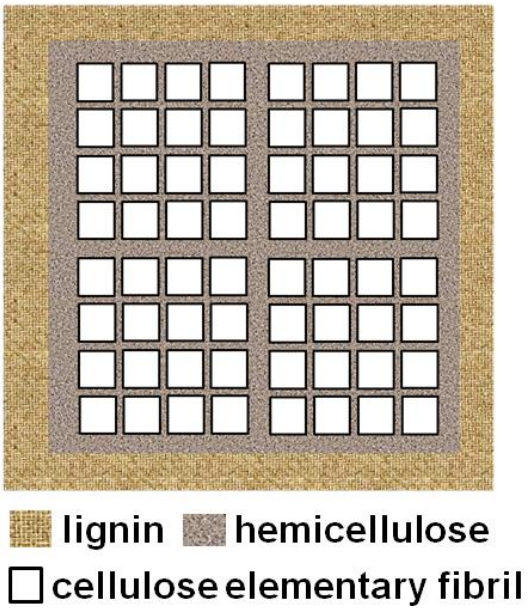

Figure 1.9. The cross-sectional model of ultra structural organization of the wood cell wall components. The wood cell wall is composed of lignin, hemicellulose and cellulose, modified after Fengel (1971).

Table 1.4. Different polymorphs of cellulose with crystallographic details.

Polymorph	Crystal system	Space group	Cell parameter
Cellulose Iα	Triclinic	P_1	a = 6.717 Å ; b = 5.962 Å; c = 10.4 Å α = 118.08 ° ; β = 114.80 ° ; γ = 80.37 °
Cellulose Iβ	Monoclinic	$P2_1$	a = 7.784 Å ; b = 8.201 Å; c = 10.38 Å α = β = 90 ° ; γ = 96.5 °
Cellulose II	Monoclinic	$P2_1$	a = 8.10 Å ; b = 9.03 Å; c = 10.31 Å α = β = 90 ° ; γ = 117 °
Cellulose III_I	Monoclinic	$P2_1$	a = 4.450 Å ; b = 7.850 Å; c = 10.31 Å α = β = 90 ° ; γ = 105.10 °
Cellulose IV_I	Orthorhombic	P_1	a = 8.03 Å ; b = 8.13 Å; c = 10.34 Å γ = 90 °
Cellulose IV_{II}	Orthorhombic	P_1	a = 7.99 Å ; b = 8.10 Å; c = 10.34 Å γ = 90 °

Cellulose I or native cellulose is a polymorph that is found in nature and mainly derived to the other cellulose polymorphs (Figure 1.10). Cellulose II can be obtained from cellulose I using two different methods. The first method is a regeneration method that uses the solubility of cellulose I in a solvent. The dissolved cellulose I is then reprecipitated in water to produce cellulose II. The second method, so called mercerization, is a swelling procedure where

cellulose I is swollen in a concentrated sodium hydroxide solution. The removal of swelling agent then produces cellulose II. Cellulose III_I and cellulose III_{II} are produced in a reversible process. Cellulose III_I is a reversibly product of cellulose I and cellulose III_{II} is the reversible product of cellulose II. The transformations of cellulose I to cellulose III_I and cellulose II to cellulose III_{II}, respectively are done by liquid ammonia treatment. The reversible reaction is achieved by evaporation of excess ammonia, while heating treatments of celluloses III_I and cellulose III_{II} up to 206 °C result in the formation of cellulose IV_I and cellulose IV_{II}, respectively.

Cellulose Iα and cellulose Iβ polymorphs have the same conformation of the heavy atom skeleton but differ in the hydrogen bonding patterns. Cellulose Iα is a metastable phase with a triclinic unit cell containing one chain while cellulose Iβ has two chains in its monoclinic unit cell. Cellulose II, derived from cellulose I, has a similar unit cell to the unit cell of cellulose I. The main difference to cellulose I is that cellulose II has two cellulose chains that lie antiparallel to one another. As produced from cellulose I and cellulose II, cellulose III_I and cellulose III_{II}, respectively have a cellulose chains polarity that resembles to that of the starting material. The transformation of cellulose III_I and III_{II} to cellulose IV_I and IV_{II}, changes the space group from monoclinic to orthogonal, respectively (Finkenstadt & Millane, 1998; O'Sullivan, 1997; Langan et al., 2001; Wada et al., 2006).

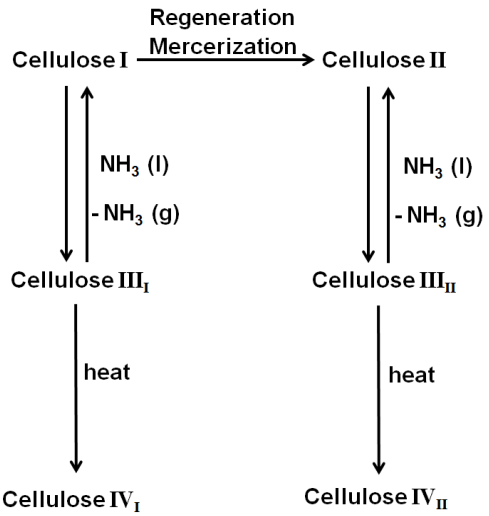

Figure 1.10. Transformation of six different cellulose polymorphs, from O'Sullivan (1997). The cellulose I is used as native cellulose. Other cellulose polymorphs are derived from cellulose I.

1.3.3 The Mechanical Characteristics of Fiber Reinforced Composites

On the basis of their diameter, fibers are divided into three major groups; whiskers, fibers and wires. Whiskers are very thin single crystals that have extremely large length-to-diameter ratios. Due to their small size, whiskers usually have a high degree of crystallinity. Materials that are categorized as fibers are either polycrystalline or amorphous and have a small diameter. Fine wires have a comparatively large diameter and are made of metals like steel, molybdenum and tungsten. The common use of fine wires can be found as a radial steel

reinforcement in automobile tires, in filament-wound rocket casings and in wire-wound high-pressure hoses (Callister, 2007).

The matrix phase of the fiber reinforced composites can be a metal, a polymer, a ceramic, gypsum or concrete (Callister, 2007; Eve et al., 2002). The matrix phase has several functions. First, it binds the fiber together. When the load is applied, the matrix will transmit and distribute the stress to the fiber and only sustain a small proportion of the applied load. Second, the matrix phase protects the individual fiber from surface damage as a result of chemical reaction with the environment or abrasion. Third, the matrix phase separates the fiber and prevents the propagation of brittle cracks from fiber to fiber that can result in catastrophic failure (Callister, 2007).

Mechanical characteristics of fiber reinforced composites depend on the fiber properties and the degree to which the applied load is transmitted to the fiber by the matrix phase (Figure 1.11). Thus, the magnitude of the interfacial bond between the fiber and the matrix phase is important.

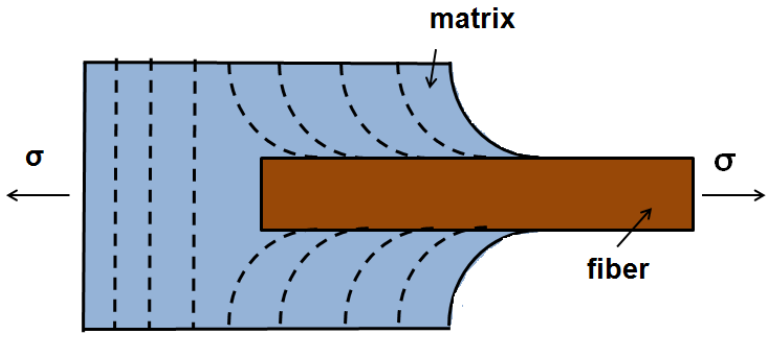

Figure 1.11. The pattern of matrix deformation where the matrix is surrounded by the fiber that is subjected to an applied tensile load (σ), from Callister (2007).

The critical fiber length plays an important role in the effectiveness of the strengthening and stiffening of the composite. The critical length of the fiber (l_c) depends on the fiber diameter (d), its ultimate (or tensile) strength (σ_f^*) and the fiber-matrix bond strength or the shear yield strength of the matrix (τ_c) according to $l_c = \frac{\sigma_f^* d}{2\tau_c}$. When the fiber length is bigger than the critical fiber length, the fiber becomes more effective as reinforcement. A fiber length that is smaller than the critical length will not be sufficient to hold the applied load (Callister, 2007).

Fiber alignment relative to one another also affects the mechanical properties of the composite. There are three different possibilities of fiber alignment. The continuous fiber is normally aligned while the discontinuous fiber can be totally aligned, partially aligned or totally misaligned (Figure 1.12).

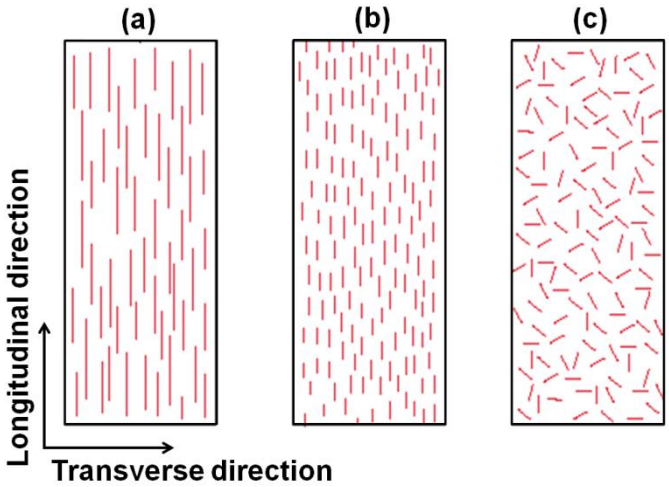

Figure 1.12. Schematic of fiber alignment on the fiber reinforced composite, from Callister (2007). Three types of fiber alignments are showed as (a) aligned and continuous, (b) aligned and discontinuous and (c) random and discontinuous.

The mechanical properties of the fiber reinforced composite with continuous and aligned fibers are highly anisotropic. They depend on the direction along which the load is applied either in longitudinal or transverse direction (Figure 1.12). The stress-strain curves are shown in Figure 1.13 where the fiber is totally brittle and the matrix is reasonably ductile. The fracture strength of the fiber and the matrix are σ_f^* and σ_m^*, respectively, and the fracture strain of the fiber and the matrix are ε_f^* and ε_m^*, respectively. Figure 1.13a shows a case of fiber and matrix stress-strain curve in which the $\varepsilon_m^* > \varepsilon_f^*$. There are two different stages that are received by the composite after the load is applied. At the initial stage (Stage I (Figure 1.13b)), both, the fiber and the matrix deform elastically. This portion of the curve is normally linear. The process then evolves to Stage II. During Stage II, the stress-strain curve is relatively linear with a diminished slope in comparison to that in Stage I. The composite failure begins when the fibers start to fracture that corresponds to a strain value of about that at ε_f^* (Figure 1.13) (Callister, 2007).

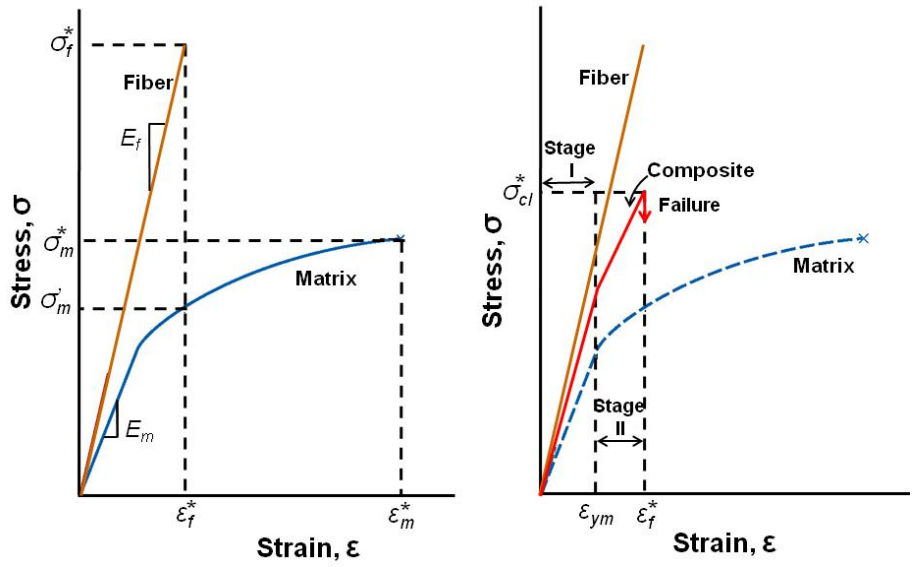

Figure 1.13. Stress-strain curves of two different behaviors of the fiber and the matrix, from Callister (2007). (a) Stress-strain curve for brittle and ductile matrix. (b) Stress-strain curve for an aligned fiber-reinforced composite that is exposed to a uniaxial stress applied in the direction of alignment. Curves for the fiber and matrix material shown in (a) are also superimposed.

When a longitudinal load is applied to the continuous and aligned fibrous composite, it is assumed that the deformation of both matrix and fibers is the same, $\varepsilon_c^* = \varepsilon_m^* = \varepsilon_f^*$ (*isostrain*), with ε_c^* being the fracture strain of the composite. Thus, the load carried by the composite is the total load carried by the fiber and the matrix, $F_c = F_m + F_f$. As the load is a stress that is multiplied by the surface area of the composite, $F = \sigma A$, the longitudinal deformation of the composite is then summarized as

$$\sigma_c A_c = \sigma_m A_m + \sigma_f A_f \tag{1.1}$$

The total cross-section of the matrix (A_m) and fiber (A_f) is then divided by the total matrix of the composite (A_c).

$$\sigma_c \frac{A_c}{A_c} = \sigma_m \frac{A_m}{A_c} + \sigma_f \frac{A_f}{A_c} \tag{1.2}$$

If $A_m / A_c = V_m$ (volume fraction of the matrix) and $A_f / A_c = V_f$ (volume fraction of the fiber) equation (1.2) can be summarized as,

$$\sigma_c = \sigma_m V_m + \sigma_f V_m \tag{1.3}$$

In order to calculate the Young's modulus ($E = \frac{\sigma}{\varepsilon}$) of the composite ($E_{cl}$), we simplified equation (1.1) and obtained the following equation,

$$E_{cl} = E_m V_m + E_f V_f \tag{1.4}$$

Since the composite is comprised only of the matrix and the fiber, $V_m + V_f = 1$, the equation can be simplified further as,

$$E_{cl} = E_m(1 - V_f) + E_f V_f \tag{1.5}$$

Based on the Figure 1.13, the longitudinal strength from equation (1.1) becomes

$$\sigma^*_{cl} = \sigma'_m(1 - V_f) + \sigma^*_f V_f \tag{1.6}$$

In the case of transverse loading, the load is applied at a 90° angle to the direction of fiber alignment and the stress (σ) to which the composite as well as the both phases are the same ($\sigma_c = \sigma_m = \sigma_f$). This term is called *isostress* state. The strain of the entire composite becomes $\varepsilon_c = \varepsilon_m V_m + \varepsilon_f V_f$. The Young's modulus is then derived into

$$\frac{1}{E_{ct}} = \frac{V_m}{E_m} + \frac{V_f}{E_f} \tag{1.7}$$

and simplified as

$$E_{ct} = \frac{E_m E_f}{V_m E_f + V_f E_m} = \frac{E_m E_f}{(1 - V_f)E_f + V_f E_m} \tag{1.8}$$

The discontinuous fiber composite usually has less reinforcement efficiency. The discontinuous fiber may have fiber length smaller than the critical fiber length ($l < lc$) or fiber length bigger than the critical fiber length ($l > lc$). For the $l < lc$, the longitudinal strength ($\sigma^*_{cd'}$) is given by

$$\sigma^*_{cd'} = \frac{l\tau_c}{d} V_f + \sigma'_m(1 - V_f) \tag{1.9}$$

And for the l > lc, the longitudinal strength (σ^*_{cd}) is given by

$$\sigma^*_{cd} = \sigma^*_f V_f \left(1 - \frac{l_c}{2l}\right) + \sigma'_m(1 - V_f) \tag{1.10}$$

When the fiber orientation is random and short fiber length is used, a 'rule-of-mixtures' expression is used for the Young's modulus, as show below

$$E_{cd} = KE_f V_f + E_m V_m \tag{1.11}$$

where K is a fiber efficiency parameter that depends on V_f and the E_f / E_m ratio.

In summary, the aligned fibrous composite is incoherently anisotropic and the maximum strength and reinforcement are achieved along the longitudinal direction. In the transverse direction, fracture usually occurs at relatively low tensile stresses.

2. Results and Discussion

2.1 Homoepitaxial meso- and microscale crystal co-orientation and organic matrix network structure in *Mytilus edulis* nacre and calcite

*Erika Griesshaber[a], Wolfgang W. Schmahl[a,d,e], Habinder Singh Ubhi[b], Julia Huber[c], **Fitriana Nindiyasari[a]**, Bernd Maier[a], Andreas Ziegler[c]*

[a] Ludwig Maximilian University Munich, GeoBioCenter and Department of Earth- and Environmental Sciences, Theresienstrasse 41, D-80333 Munich, Germany
[b] Oxford Instruments, Halifax Road, High Wycombe HP12 3SE, UK
[c] Central Facility for Electron Microscopy, University of Ulm, Albert Einstein Allee 11, D-89069 Ulm, Germany
[d] SNSB – Mineralogical State Collection, Theresienstrasse 41, D-80333 Munich, Germany
[e] GeoBioCenter, LMU, Richard Wagner Strasse 10, D-80333 Munich, Germany

Acta Biomaterialia **9**, 9492-9502 (2013)

https://www.sciencedirect.com/science/article/pii/S1742706113003681

Abstract:
New developments in high-resolution, low kV, electron backscatter diffraction (EBSD) enable us to resolve and quantify the co-orientation of nanocrystals constituting biological carbonate crystals with a step resolution between of 125 nm. This allows the investigation of internal structures in carbonate tablet and tower biocrystals in the nacre of mollusc shells, and it provides details on the calcite – aragonite polymorph interface in bivalves. Within the aragonite tablets of *Mytilus edulis* nacre we find a mesoscale crystallographic mosaic structure with a misorientation distribution of 2° FWHM. Selective etching techniques with critical point drying reveal an organic matrix network inside the nacre tables. The size scales of the visible aragonite tablet subunits and nanoparticles correspond to those of the open pore system in the organic matrix network. We further observe by EBSD that crystal co-orientation spans over tablet boundaries and forms composite crystal units of up to 20 stacked co-oriented tablets (tower crystals). Statistical evaluation of the misorientation data gives a probability distribution of grain boundary misorientations with two maxima: a dominant peak for very-small-angle grain boundaries and a small maximum near 64°, the latter corresponding to {110} twinning. Thus twin boundaries are between nacre tablets and not within them. We attribute this specific pattern of misorientation distribution to growth by particle accretion and subsequent semicoherent homoepitaxial crystallization. The semicoherent crystallization percolates between the tablets through mineral bridges and across matrix membranes surrounding the tablets.

Key words: mesocrystal, biomineralization, hybrid nanocomposite, hierarchical architecture, EBSD

Introduction
Bivalve and gastropod carbonate skeletons are major focus areas of biomineral research due to the extraordinary toughness of these hybrid composite materials [1-9]. The elaborate properties emerge from an intricate structural interrelation at several scale levels between an organic matrix and calcium carbonate fibres and tablets [6, 7, 10-12].
Bevelander and Nakahara [13] were the first to show that formation of bivalve nacre begins with the secretion of organic lamellar compartments enclosing a modified pallial fluid containing organic matrix components. Aragonite growth spreads laterally displacing organic material within the lamella and persists until neighbouring crystals abut against each other. In bivalve nacre this process leads to a few hundred nm thick and 4-5 micrometre sized tablets. These are assembled to Voronoi-polyhedral arrays [13-15] and have their c-axis oriented almost perpendicular to the tablets planar surface [8, 16-19]. Twinned microstructures are reported in the shells of

many mollusc species[18, 19] while they are not found yet in gastropod nacre [16]. Coppersmith et al. [20, 21] provide a model of aragonite c-axis orientation development for abalone shell and suggest that from an arbitrary orientation at the prismatic calcite – aragonite boundary the preferred orientation in nacre is achieved by differential growth rates that are a function of the misorientation between the angle of the c-axis of the growing crystal and the normal vector of the horizontal compartment membrane. From X-PEEM and TEM [8, 16, 22] studies it has been established that the crystallographic lattice in adjacent nacre tablets is frequently co-oriented, such that [001]-stacks of tablets in subsequent lamellae form "stack of coin" structures. Checa et al. [23] demonstrated that nacre rapidly grows in towers. This invokes the existence of a "mineral bridge" across interlamellar membranes which are regarded to be responsible for the continuation of crystal orientation [24]. In gastropods and *Nautilus* a mineral bridge runs through the centre of the tower, corresponding to 150-200 nm wide gaps in the interlamellar membrane by which the crystal continues to grow (38). In the terraced nacre of bivalves, these gaps are 100 nm wide and located near the edges of superposed tablets [17].

The variations in crystallographic orientation, the presence of twins and local misorientations raise questions about carbonate crystallite orientation distribution at the nanoscale. Electron backscatter diffraction (EBSD) has proved to be an ideal tool to investigate advanced material fabrics such as those present in biological hard tissues [25-31], since it combines the capabilities of the SEM with a diffraction method that is able to distinguish crystalline phase and orientation rapidly enough to map the microstructure of the sample [32-36]. Here we employ ultra-high resolution, low-acceleration voltage EBSD [30, 34, 37] and boost spatial resolution to such an extent that EBSD measurements reveal also the nanostructural crystallographic mosaic characteristics inside the composite crystals [38] of biological carbonate materials. Previously, an internal nanostructure has been reported, but only based on AFM, SEM or TEM pictures rather than measurements [9, 38-43]. We investigate the meso- and nanocrystalline architecture of aragonite nacre and the nature of the aragonite-calcite layer interface in *Mytilus edulis* shells. These shells are of particular

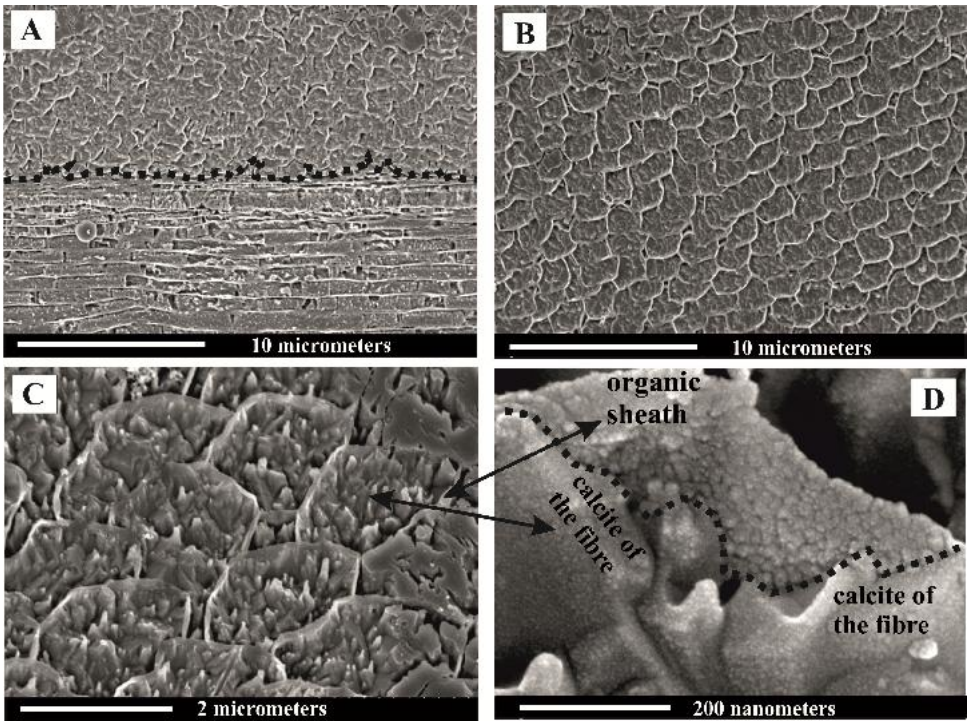

Fig.1 FE-SEM micrographs of a microtome polished, etched and critical point dried plane within the shell of *Mytilus edulis* revealing the organic matrix of the two carbonate shell layers. (A) View of both carbonate shell layers and the ragged interface zone between the polymorphs. (B) and (C) Micrographs of stacks of calcite fibres. (B), (C) and (D) Comparison of the structure of the organic sheath surrounding the fibres with the structure of the etched calcite.

interest because they contain both carbonate polymorphs and an extended polymorph interface zone.

Materials and methods

Specimens of *Mytilus edulis* were collected from Naples harbour, Italy, Mediterranean Sea. 300 µm thick wafers were cut out along the longest axis of the shell from the hinge to the commissure. The wafer surfaces were treated with several mechanical polishing steps. For thefinal step etch-polishing with colloidal silica in a vibratory polisher was applied. The samples were coated with 4 nm of carbon. For indexing the aragonite EBSD FEG-SEM equipped with an Oxford Instruments patterns we used the unit cell setting: a_0 = 4.97 Å, b_0 = 7.97 Å, c_0 = 5.75 Å. EBSD maps were obtained on an NordlysNano EBSD, X-Max 80 EDS detectors and AZtec software. An acceleration voltage of 8 kV was employed for SEM imaging and EBSD mapping. EBSD patterns were collected at 125 nm step resolution. For visualisation of the organic matrix shell samples were polished using an Ultracut ultramicrotome (Leica). First glass and diamond knifes (Diatome, Switzerland) were used to polish planes across the shell similar to the method described earlier [44]. The polished planes were then etched for 30, 60 and 90 seconds with an aqueous solution composed of 2.5% glutaraldehyde to stabilize organic components, and 0.01 mol/L MOPS buffer adjusted to a pH of 6.5. Etching was stopped by washing the samples three times with 100% isopropanol. After critical point drying (Bal-Tec CPD 030) samples were rotary shadowed with 3 – 4 nm platinum at an angle of 45° using a BAF 300 (Balzers, Liechtenstein and the exposed organic matrix was analysed with a Hitachi S-5200 Field emission SEM.

Results

SEM micrographs of Figures 1 to 6 and the images S1 to S4 of the supplementary section depict various characteristics of the micro- and nanostructure of *Mytilus edulis* calcite, aragonite, the calcite – aragonite interface and the organic matrix that envelopes the calcite fibres and aragonite tablets. The distribution pattern of the organic matrix is visualized on samples that were microtome cut, microtome polished and etched, while the internal structure of aragonite tablets and calcite fibres is shown on fracture surfaces and samples with highly polished surfaces prepared for EBSD. For comparison micrographs of non-biological calcite and aragonite equally treated to *Mytilus edulis* shell (thus microtome cut, microtome polished and etched) are presented with the images S3A and S3B in the supplementary material.

Figure 1A shows the microstructure of the calcitic and the aragonitic shell portions together with the interface zone between these sections. Figures 1B to 1D show the arrangement of the calcitic fibres (Fig. 1B), the thick organic sheaths lining each fibre (Fig. 1C) and differences in nanostructure between the organic sheath and the calcite of a fibre (Fig. 1D). The interface zone between the calcitic and the aragonitic shell layers is depicted in Figure 2A. The interface between the two carbonate polymorphs is ragged, narrow, and consists of two adjacent membranes: the organic sheath around the calcitic fibre and the organic layer that envelopes the aragonite tablets. The calcite - aragonite interface was traced in *Mytilus edulis* from the commissure to the hinge. Directly at the interface we always observe a few (one to three) thin and irregular aragonitic tablets (Figure 2A). These are bordered by a one to two micrometer thick non-platy layer, the so-called prismatic aragonite layer [45], which is highly enriched in mostly vertically oriented biopolymer fibrils (Figs. 2A, 2B). At their proximal side this layer is bordered by aragonite platelets, still not regularly shaped but thicker

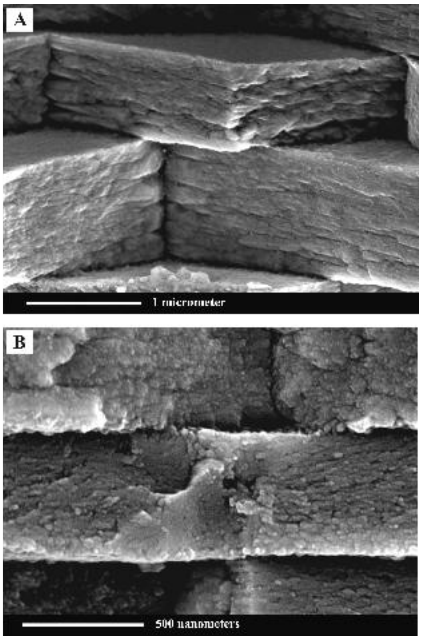

Fig.4. FE-SEM micrographs of fracture surfaces of the nacreous layer in *Mytilus edulis*. The 800-1000 nm thick tablets are internally structured into 200-220 nm thick subunits (A) which in turn are composed of 20 to 30 nm sized round nanoparticles (B). These appear to consist of even smaller primary particles.

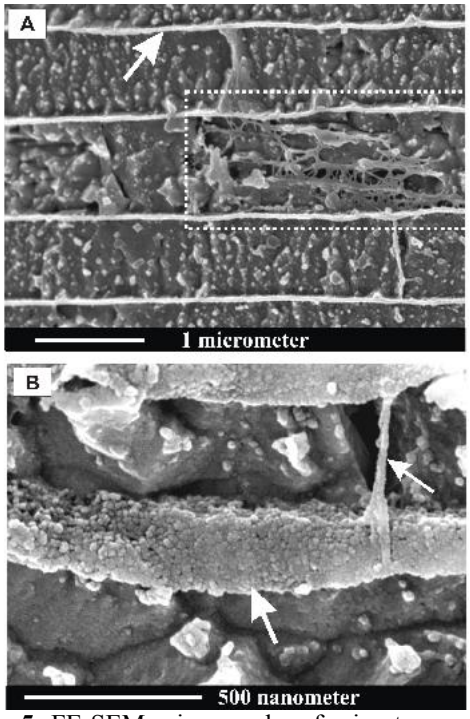

Fig.5. FE-SEM micrographs of microtome cut, microtome polished, etched and critical point dried surfaces of the nacreous shell portion of *Mytilus edulis*. We observe two distinct types of biopolymers in *Mytilus edulis* nacre: (A) and (B) thick boundary membranes (sheaths), indicated by arrows) which can be interconnected and (A) a sophisticated organic fibrous network within the platelets.

than those present in direct contact to the calcite – aragonite interface. Aragonite tablet layers are tied together by organic polymers present between the tablet layers (Figs. 3A, 3B). The 800-1000 nm thick aragonite tablets are internally structured into 200-220 nm thick and 300-350 nm wide subunits (Fig.3B, 4A, S4A) which in turn consist of 20 to 30 nm sized nanoparticles (Figs. 4B, S4b). Etched planes within the shell of *Mytilus edulis* reveal two

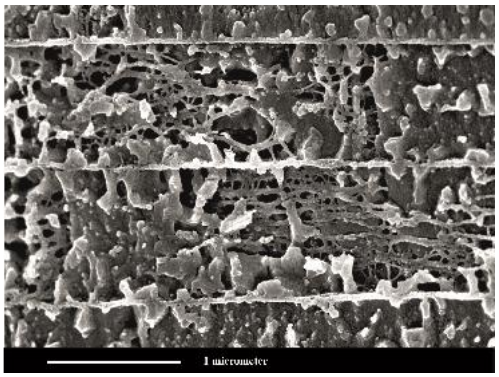

Fig.6. FE-SEM micrograph depicting the intra-platelet fibrous matrix network in *Mytilus edulis* nacre.

layer (sheath) of organic material around calcite fibres (Fig. 1D) and between aragonitec layers (Figs. 5A, 5B)and (b) a network of organic fibrils within aragonite tablets (Figs. 5A, tablet

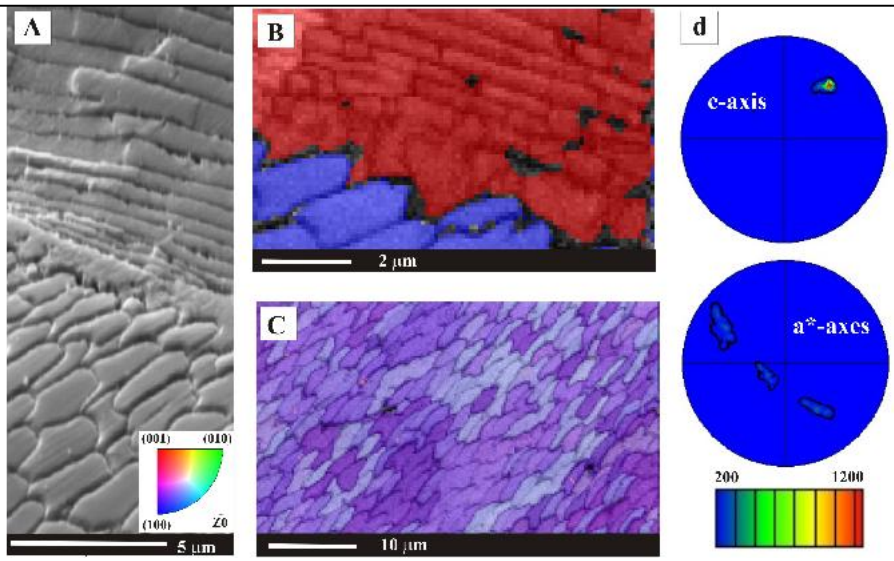

Fig. 7. SEM image, and EBSD phase map and calcite EBSD orientation map taken on highly polished surfaces of *Mytilus edulis*. (A) SEM image showing the transition zone between the calcitic fibrous shell layer to the aragonitic nacre tablet shell layers. Well observable in the SEM image is the disturbed microstructure at the polymorph transition zone. (B) The phase map taken at the calcite – aragonite transition proves that the prismatic band between the calcitic fibres and the nacre tablets is aragonite. (C) and (D) The presence of highly co-oriented calcite crystals within the fibrous, calcitic shell layer is well visible from the uniform magenta colour of the EBSD map (C) and the pole figures (D) . The alignment of calcite crystals comes close to that present in a calcite single crystal.

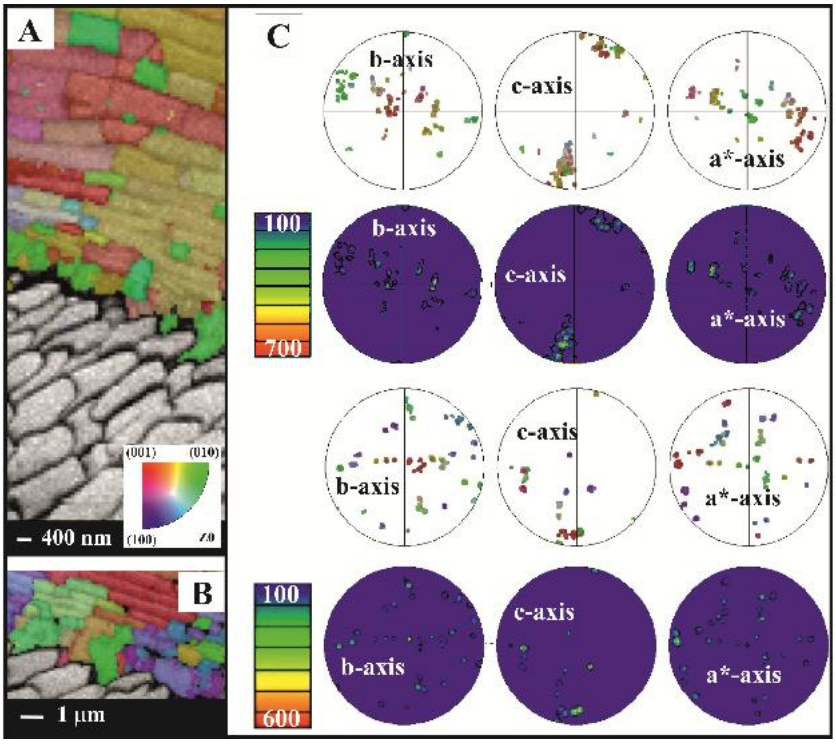

Fig. 8. EBSD aragonite crystal orientation patterns taken on highly polished surfaces at the interface of calcite and aragonite layers in *Mytilus edulis* and corresponding pole figures. Pole figures C correspond to map A, and pole figures D correspond to map B. Within the prismatic aragonite zone at the polymorph interface the degree of crystallographic preferred orientation of aragonite crystallites is low (best visible in the EBSD map B and the corresponding pole figures in D. The preferred orientation increases further away from the interface in shell portions where the stacks of platelets are well developed.

6, S4C) and within the prismatic aragonite layer at the calcite – aragonite interface (Fig. 2B). The organic network within the nacreoustablets is densely distributed throughout the tablets compartments and forms a substantial part of the tablet (Figs. 6, S4C). Calcite and aragonite orientation results obtained from EBSD are shown in Figures 7 to 12 and S5 of the supplementary section. Complementary SEM images of the mesoscale arrangements of the calcite fibres, aragonite tablets and prismatic aragonite at the calcite – aragonite interface were obtained on highly polished surfaces and are given in Figures 7A, S1 and S2 of the supplementary section. Well visible from the SEM image in Fig. 7A is the disturbed structure of platy aragonite at the calcite – aragonite interface. The phase map in Fig. 7B demonstrates that aragonite as the dominant phase of the prismatic layer at the polymorphinterface. Orientation patterns are shown in EBSD maps (Figs. 7C, 8A, 8B, 9A) and as axes density distributions given in pole figures (Fig. 7D, 8C and 9A). Crystallographic orientation patterns are given colour coded in an inverse pole figure colouring mode, which indicates which crystal axis is parallel to X, Y, or Z-axis, respectively, of the EBSD map. As it is well visible from Figs. 7C, 7D and S1 over large portions of the shells calcite in the fibres and the fibres themselves are highly co-oriented to an almost single crystalline degree.Aragonite crystal orientation pattern at the calcite – aragonite interface and in the prismatic aragonite layer is given in Figure 8. In comparison to the calcitic shell portions aragonite co-orientation is disturbed at the interface and is almost random within the prismatic layer (Fig. 8B, 8C). Aragonite co-orientation increases away from the interface zone and is well developed in the aragonite tablets (Figs. 9A, S2).

Fig. 9A shows an EBSD map of a cross-section through the nacreous portion of the shell of *Mytilus edulis*. The colours code for crystallographic orientation in an inverse pole figure colouring mode. Superimposed on the colour in the map is the EBSD band contrast (the signal strength in each individual EBSD pattern) as a grey scale component, from which the distribution of the organic matrix membranes between the aragonite tablets becomes visible as dark lines in the mapped area. The statistics of the crystallographic

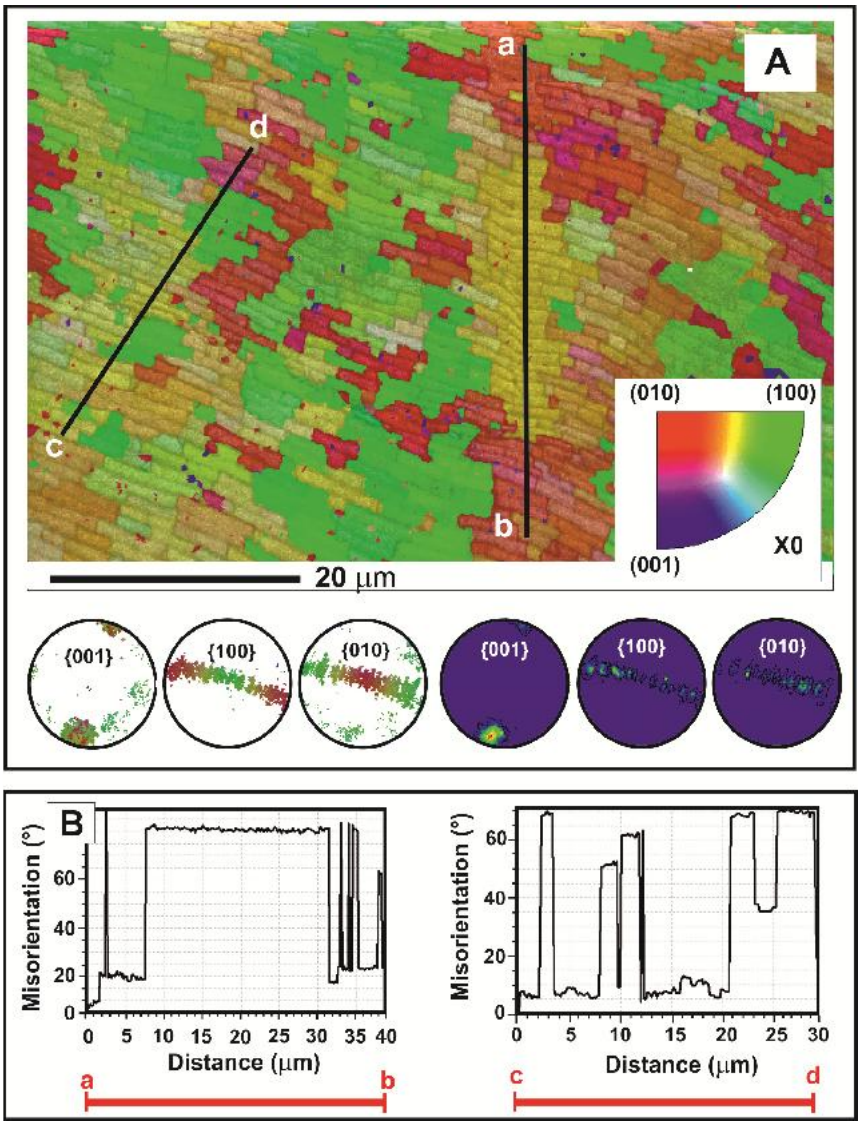

Fig. 9. (A) EBSD map of a cross-section through the shell of *Mytilus edulis* and corresponding pole figures. The colours code for crystallographic orientation in the inverse pole figure colouring mode defined in the insert: the colour indicates which axis of the crystal is parallel to the horizontal direction in the map (reference direction x_0). Superimposed on the colour in the map is the EBSD band contrast (Kikuchi band signal strength) as a grey scale component. From this contrast the distribution of the organic matrix membranes between the aragonite tablets becomes visible as dark lines. (B) Misorientation profiles along two trajectories in the map. Note the co-orientation of clusters of stacked tablets along the profiles.

orientation is visualized in Fig. 9A, in the pole figures below the EBSD map. As expected, the pole figures show that the crystallographic c-axis is nearly perpendicular to the tablets, while the a- and b-axes are distributed in a random occurrence of maxima on the circle around the c-axis (we use the Pmcn unit cell setting: a_0 = 4.97 Å, b_0 = 7.97 Å, c_0 =5.75 Å). Chateigner et al.[19] used XRD to determine the texture of neighbouring tablets frequently show similar orientation. This feature of the microstructure is highlighted in misorientation profile diagrams of Fig. 9A which clearly demonstrate the *Mytilus* shells, and report a distribution of {100} maxima every 60° on this circle. In our data (which are limited to a small "volume" compared to the XRD studies) there is only a very weak ~60° orientation correlation of {100} pole density peaks. It appears that the crystal orientation pattern shown in Fig. 9A evolves into an axial (cylindric) texture for an increased investigated area. In the EBSD map of Fig. 9A orientation correlation between neighbouring tablets for selected profiles "a-b" and "c-d" across the map in Fig. 9A. The stacks of co-oriented tablets form extended plateaus in the

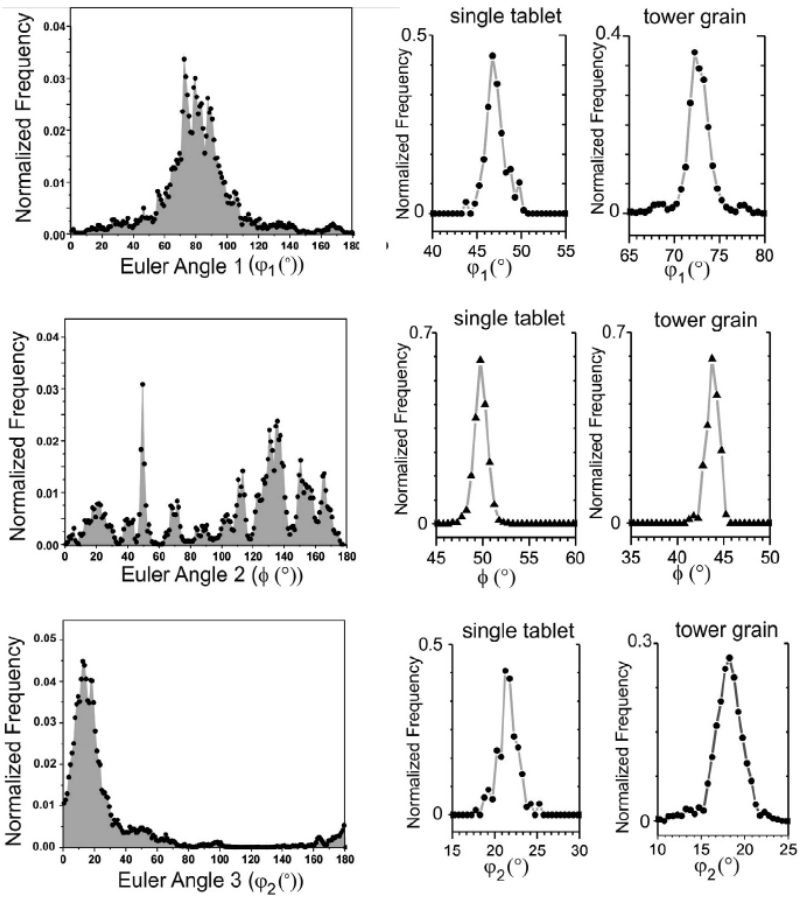

Fig. 10. Statistics of the orientation distribution displayed in the map of Fig. 9. The Euler angles 1 and 3 (φ_1 and φ_2 in Bunge[46] notation) display the overall orientation spread of the c-axes; it is a 2D near-Gaussian distribution of 25° (+/- 2°) FWHM. The Euler angle 2 (φ in Bunge[46] notation) reflects the distribution in the a-b-plane with its many different discrete peaks spread across the complete circle around the c-axis.

misorientation profiles (Fig. 9B). Most striking is the large column or "tower" of co-oriented tablets covered by the profile labelled "a-b" in Fig. 9A. Numerical data on the measured orientation distribution are presented in Fig. 10. The Euler angles 1 and 3 (φ_1 and φ_2 in Bunge[46] notation) display the overall orientation spread of the c-axes that is a 2D near-Gaussian distribution of 25° (+/- 2°) FWHM. The Euler angle 2 (φ_1 and φ_2 in Bunge[46] notation) reflects the distribution in the a-b-plane with its many different discrete peaks spread across the complete circle.

Discussion

Nanoparticle misorientation within single nacre tablets and composite tablet crystals

The two size scales observed in the morphological hierarchical substructure as visible in FE-SEM imaging (Figs. 4, S4A), i.e. the 200-220 nm thick subunits and the 20-30 nm round nanoparticles correspond to the two size scales of the pore system in the intra-tablet organic matrix network (Fig. 5A, Fig. 6 and Fig. S4B). Thus we conclude that the observed morphological substructures in the aragonite are created by the organic matrix. In systems with a lower degree of skeleton mineralization, such as e.g. the cuticle of crustaceans, the correlation of mineral particles and (chitin) matrix in a hierarchical structure is more obvious [47]. The high spatial resolution obtained with low kV EBSD allows us to investigate the orientational mosaic spread within a single nacre tablet and within composite crystals formed by co-oriented adjacent tablets. Fig. 11 highlights three examples. For the individual tablet labelled "a" and the "tower" of co-oriented tablets labelled "b" in Fig. 11 we show the profiles of the mosaic spread in the inserts in Fig. 10. For individual tablets such as "a" the spread is

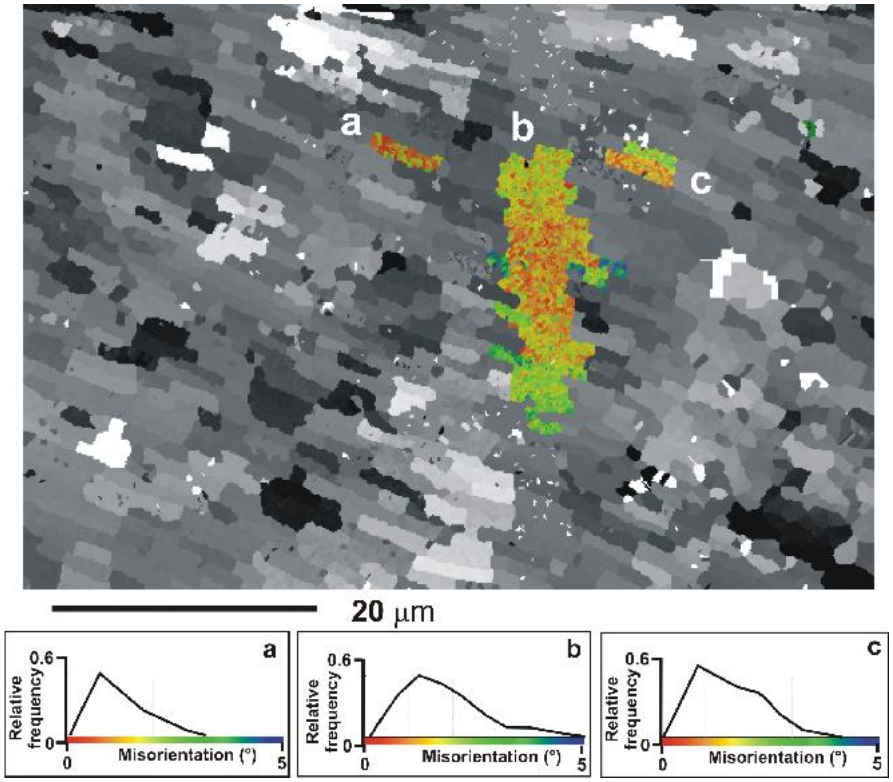

Fig. 11. Mosaic spread within aragonite tablets and composite crystals formed by co-oriented tablets with colour coding for misorientation with respect to the averaged orientation of each of the three entities: (a) single tablet, (b) a "tower grain" or composite crystal, and (c) a double tablet. The experimental uncertainty is +/- 0.3 degrees. The Euler1, Euler2 and Euler3 distributions for the single tablet (a) and the tower grain (b) are presented as inserts in Fig. 2. Gray-scale contrast in the background is Euler-angle 1 (φ_1).

typically in the order of 2° FWHM (compared to the experimental orientation resolution of +/- 0.3°). As shown in Figs. 4A, 4B, 6 and S4 nacre tablets are an accretion of (potentially membrane-separated) nanoparticles in the size range of 20-30 nm (also [48], [40], [49]). In addition these particles give the impression of being composed of even smaller primary particles. We attribute our observed intra-tablet mosaic spread observed by EBSD to small errors in the lattice co-orientation between these nanoparticles-agglomerates induced by the presence of the organic matrix network within the tablets (Fig. 6). The observed mesoscale architecture fits well the definition of a mesocrystal [50]. For the tower-like array of co-oriented tablets the mosaic spread is not much larger than that of a single tablet (inserts a, b, c in Fig. 11). In this hierarchical composite crystal [38] labelled b in Fig. 11 the organic matrix forms (at least) two hierarchical levels and is systematically occluded: the intra-tablet matrix network and potentially thin membranes between the nanoparticles (Fig. 6) and significantly thicker membranes lining the tablet compartments (Figs. 5A, 5B). From the map in Fig. 11 it can be observed that the hierarchical composite crystal labelled "b" has overall orientation gradients on the scale of micrometres. "c" in Fig. 11 marks a typical pair of contiguous co-oriented tablets with internal mosaic spread and with a small-angle misorientation between the tablets.

The quality of our EBSD map allows for the first time for biological aragonite a detailed investigation of grain boundary arrangements (Figs. 12 and S5). Fig. 12 displays a map of grain boundary misorientations in a section of the investigated map together with the overall statistics of grain boundary misorientations (for the full map see Fig. S5 in the supplementary material section). Corresponding to the mesocrystal-like constitution of the tablets the maximum of distribution is located at small-angle boundary misorientations at lowest angles. We expect the true maximum to be even below 1°, but our experimental resolution of +/- 0.3° led us to omit data below 1° from the statistics. From this low-angle maximum the misorientation probability density falls monotonously reaching out to about 30° before the distribution becomes level (Fig. 12B). This

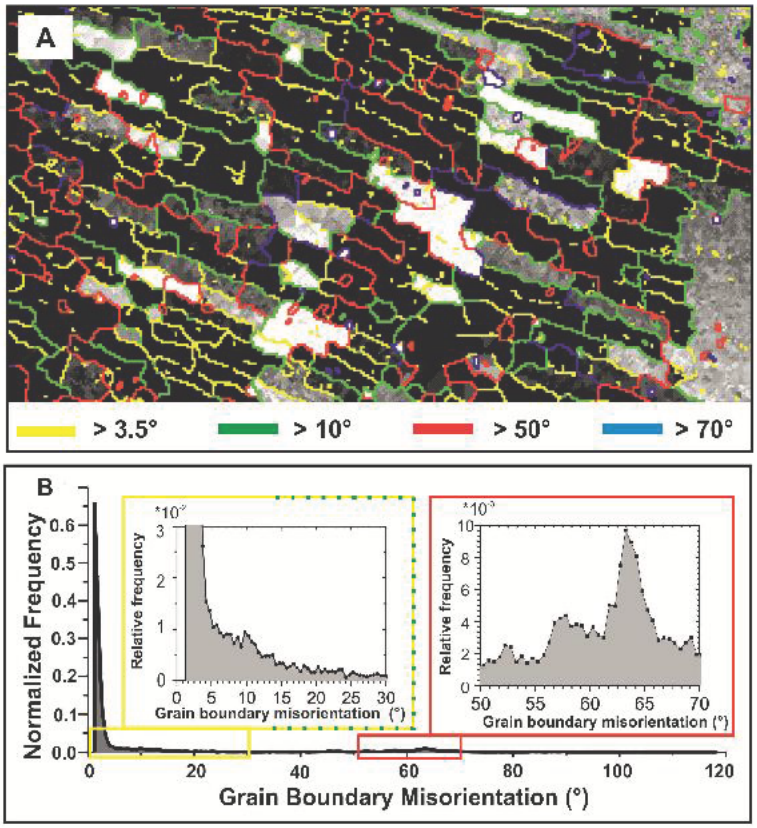

Fig. 12. (A) Distribution pattern of grain boundary misorientation shown for a selected area of the EBSD map of Fig. 9 (see Fig. 5 in supplementary material for the boundaries in the entire EBSD dataset). The grey-scale contrast in the background is the angular deviation from the mean c-axis orientation of the map from 0° (black) to 25° (white). (B) Statistics of grain boundary misorientation in the entire map (Figs. 9 and 3 supplementary section). Note the dominance of (very) low-angle boundaries and the peaks near 60° due to {110} twinning.

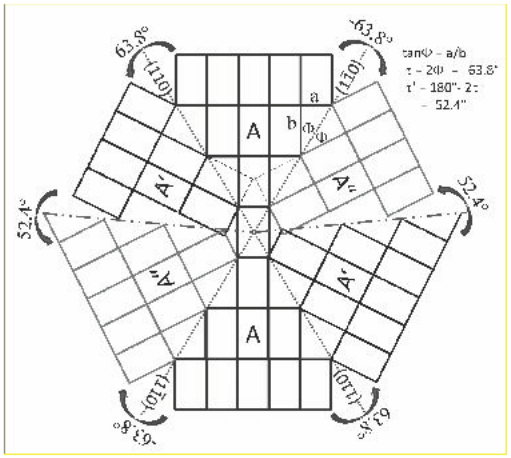

Fig. 13. Scheme displaying the {110} triple-twin geometry of aragonite. The twin angle arising from a (110) or $(1\bar{1}0)$ reflection twin operation, respectively is $s = 2U = 2\arctan(a_0/b_0) = 63.8°$. The angle between the A' and A'' twin domains is 2s, corresponding to a 52.4° misorientation.

type of distribution allows no objective criterion for the selection of a critical boundary misorientation in order to distinguish between "small-angle boundaries" within aragonite crystals and "grain boundaries" between the crystals. Empirically, by trial-and-error, we found that an arbitrary critical misorientation angle in the order of 3°-4° retraces most of the tablet boundaries in *Mytilus edulis* nacre (Fig. 12A, the location of the tablet boundaries is known from the band contrast shown in Fig. 9A). Visualization of grain boundaries with smaller values of critical misorientation creates a maze inside the tablets that is consistent with their internal mesoscale mosaic spread. Additional small but significant maxima in the misorientation distribution occur in the region between 50°-70°. The common {110} aragonite triplet-twinning [16, 51] leads to a misorientation rotation of $\tau = 2*\arctan(a_0/b_0) = 63.8°$ around [001] between two adjacent twin individuals A and A'. If grain A' is twinned on its second {110} plane with a third individual A", a misorientation of $\tau' = 180° - 2\tau = 52.4°$ around [001]) between the first grain (A) and the third grain (A") is the result. This cyclic

twinning can create pseudohexagonal shapes. However, since pseudohexagonal symmetry in aragonite is only approximate, a perfectly coherent closing of a {110} twinning cycle on the aragonite lattice is not possible. Thus, we must expect some small-angle misalignment in cyclic {110} twin arrangements and we, accordingly, attribute the maxima in the misorientation histogram at 50-70° (Fig. 12B) as due to twin orientations, which occur with a higher probability than random high-angle grain boundary orientations. In Fig. 12A the twin boundaries (grain boundary class with 50°-70° rotation around axes within +/- 10° of [001]) are coloured in red and show that twin boundaries in *Mytilus edulis* nacre are usually between the nacre tablets or the stacks of co-oriented tablets that form composite crystals, respectively, and NOT INSIDE the tablets. With XRD, the ~60° "twinning" orientation relationships can be observed frequently as peaks in the pole-figures of texture studies[18, 19] which average over at least millimetres of material. In their comprehensive table of shell biocarbonate textures Chateigner et al.[19] list the *Mytilus edulis* nacre as *double twinned* corresponding to the existence of both the (110) and the $(1\bar{1}0)$ twin-related orientations. However, twin orientation relationship and twin interface orientation are not necessarily the same: as our grain boundary orientation data shows, most interfaces between {110}-twin-orientation-related aragonite units are the organic-matrix-interfaced ~{001} oriented tablet boundaries and not {110} interfaces as one might have expected. We cannot rule out that during crystallization from nanoparticle to nanoparticle the {110}-type-twin-misorientations nucleate somewhere at a common {110}-lattice plane interface on the nano-scale or unit-cell scale since the crystal growth mechanism in nacre is guided by the organic matrix and proceeds by occlusion of organic matrix membranes into composite crystals. On the microscale the organic matrix-lined interfaces dominate over crystallographic {110} interfaces in the hierarchical hybrid composite and the theoretical expectation of 64° and 53° {110}-twin misorientations apply only to a coherent direct contact of twin-related lattices on {110} twin planes. The spread around ~60° misorientation as observed here also correlates with the fact that {110} is not the true interface, and that matrix membrane interfaced {001} contacts are by far more frequent.

Aragonite growth in *Mytilus edulis* nacre

From the observed mosaic spread within the tablets and its continuation into adjacent tablets we suggest the following scenario of aragonite growth in *Mytilus edulis* nacre:

First, the organic matrix membrane defining tablet layers are formed and the compartments are filled subsequently with mineral [13]. The mineral is originally produced as nanogranules of amorphous calcium carbonate [2, 3, 5, 40, 48, 49, 52-54] which are possibly coated by organic vesicle membranes. The nanogranules attach to the growing aragonite tablets [14, 15, 49], crystallize and thus promote tablet growth. As suggested by Baronnet et al. [39] for mollusc calcite, by Weiner and Addadi for sea urchin spines [53, 55] by Goetz et al. [30] for brachiopod calcite, and by Nouet et al. [41] for crossed-lamellar gastropod aragonite, crystallization percolates from nanoparticle to nanoparticle. The EBSD results show that each nanoparticle inherits the lattice orientation of the tablet to which it has been attached, incorporating small-angle lattice-misalignments during the homoepitaxial percolation of crystallization. We attribute this misorientation to the stresses and strains imposed by the occlusion of the organic matrix that is present as fibre networks, and as organic additives stabilizing the ACC nanoparticles. The growth by particle attachment spreads laterally in a tablet layer until the tablets impinge on each other in order to form the Voronoi-polyhedral array [14, 15]. Growth also spreads continuously into adjacent layers via bridges at tablet triple junctions[5, 14, 15] where the matrix membranes between the tablet compartments are absent or have been disrupted [23]. TEM work of Checa et al. [17] leaves little doubt about the communication of crystalline orientation to adjacent tablet compartments in the c-direction via mineral bridges through the matrix membranes. Hence the process of amorphous particle attachment and semicoherent homoepitaxial percolation of crystallization with the occlusion of organic matrix in the crystallized material explains the formation of the nacre structure in *Mytilus edulis*. These two mechanisms are manifested in the characteristic frequency distribution of grain misorientation angles: we observe with probabilities falling monotonously and smoothly a dominant peak for very-small-angle misorientations (misorientations within a tablet) and a second, much smaller, peak for twin-oriented epitaxy (Figs. 9, 12, twin-related misorientations between clusters of differently oriented stacks of tablets). Nudelman et al.[5] showed that the tablets also grow in thickness

inside the maturing nacre at the expense of the width of the organic matrix layer. This implies that an additional crystal growth mechanism through their [5] proposed proteinaceous gel-like matrix substance is active. Such a secondary growth and crystallization mode is also necessary to fill pores between the nanoparticles and weld them together to yield a dense structure. To obtain the quasi-axial c-axis texture with the 25° FWHM orientational spread of the c-axes (Fig. 10), that is an order of magnitude larger than the mosaic spread in the mesocrystal tablets or towers, a competition between the semicoherent homoepitaxial growth through the bridges and occasional independent nucleation must exist.

Conclusions

1. Biocarbonate crystals of *Mytilus edulis* contain an occluded fabric-like network of organic matrix which constitutes an open pore system with two length scales, one of 200-220 nm thickness, the other of 20-30 nm pores. The aragonite tablet crystal is substructured by the matrix network.
2. High-resolution, low kV, EBSD provides both the required spatial resolution to enable the mesoscale study of individual aragonite tablets and the efficiency to scan large sample areas in order to obtain a good statistical overview of the microstructure.
3. In the aragonite-calcite polymorph interface zone a 1-2 micrometer wide “prismatic” aragonite layer exists, which shows a high density of organic matrix and a comparatively low degree of crystallographic preferred orientation.
4. The crystallographic constitution of the *Mytilus edulis* aragonite tablets shows an internal orientational mosaic spread which we attribute to misorientations induced by the intra-tablet organic matrix network.
5. In *Mytilus edulis* nacre the crystallographic lattice orientation clearly spreads from tablet to tablet and across interlamellar matrix sheaths. Most frequently, for *Mytilus edulis* the co-orientation comprises at least two adjacent tablets. We also find co-oriented tower-like stacks of up to 20 tablets along the c-axis and covering the area of 1-2 tablets in the a-b-plane. This indicates that the organic matrix membranes in nacre usually become occluded into a growing *hierarchical composite crystal*.
6. The interlamellar membranes are associated with a small-angle misorientation or a twin-misorientation rather than with a large-angle grain boundary.
7. {110} twin orientation relationships are frequently observed between adjacent nacre tablets. However, {110}type twin interface planes are rare. The contact planes between the {110} twin domains are typically the membrane-lined flat {001} faces of the tablets.

Acknowledgements

Financial support by the German Science Foundation DFG (GR 1235/9-1) is gratefully acknowledged. We thank A. Immenhauser, S. Hahn, E. Kessler, and J. Dettmer, Ruhr-Universität Bochum, for providing well-prepared sections of *Mytilus edulis*.

References

[1] Currey JD, Zioupos P, Davies P. Mechanical properties of nacre and highly mineralized bone. Proc Royal Soc London Series b 2001;268:107-12.

[2] Addadi L, Joester D, Nudelman F, Weiner S. Mollusk shell formation: a source of new concepts for understanding biomineralization processes. Chemistry 2006;12:980-7.

[3] Nudelman F, Gotliv BA, Addadi L, Weiner S. Mollusk shell formation: Mapping the distribution of organic matrix components underlying a single aragonitic tablet in nacre. J Struct Biol 2006;153:176-87.

[4] Barthelat F, Espinosa HD. An Experimental Investigation of Deformation and Fracture of Nacre–Mother of Pearl. Exp Mechanics 2007;47:311-24.

[5] Nudelman F, Shimoni E, Klein E, Rousseau M, Bourrat X, Lopez E, et al. Forming nacreous layer of the shells of the bivalves *Atrina rigida* and *Pinctada margaritifera*: an environmental-and cryo-scanning electron microscopy study. J Struct Biol 2008;162:290-300.

[6] Wang R, Gupta HS. Deformation and Fracture Mechanisms of Bone and Nacre. Ann Rev Mater Res 2011;41:41-73.

[7] Wang RZ, Suo Z, Evans aG, Yao N, Aksay Ia. Deformation mechanisms in nacre. J Mater Res 2011;16:2485-93.

[8] Gries K, Kroger R, Kubel C, Schowalter M, Fritz M, Rosenauer A. Correlation of the orientation of stacked aragonite platelets in nacre and their connection via mineral bridges. Ultramicroscopy 2009;109:230-6.

[9] Li X, Xu Z-H, Wang R. In situ observation of nanograin rotation and deformation in nacre. Nano letters 2006;6:2301-4.

[10] Mayer G, Sarikaya M. Rigid biological composite materials: structural examples for biomimetic design. Exp Mechanics

2002;42:395-403.
[11] Dunlop JWC, Fratzl P. Biological Composites. Ann Rev Mater Res 2010;40:1-24.
[12] Dunlop JWC, Weinkamer R, Fratzl P. Artful interfaces within biological materials. Materials Today 2011;14:70-8.
[13] Bevelander G, Nakahara H. An electron microscope study of formation of the nacreous layer in the shell of certain bivalve molluscs. Calc Tissue Res 1969;3:84-&.
[14] Rousseau M, Lopez E, Coute A, Mascarel G, Smith DC, Naslain R, et al. Sheet nacre growth mechanism: a Voronoi model. J Struct Biol 2005;149:149-57.
[15] Rousseau M, Meibom A, Gèze M, Bourrat X, Angellier M, Lopez E. Dynamics of sheet nacre formation in bivalves. J Struct Biol 2009;165:190-5.
[16] Mukai H, Saruwatari K, Nagasawa H, Kogure T. Aragonite twinning in gastropod nacre. J Cryst Growth 2010;312:3014-9.
[17] Checa AG, Cartwright JHE, Willinger M-G. Mineral bridges in nacre. J Struct Biol 2011;176:330-9.
[18] Chateigner D, Hedegaard C, Wenk H-R. Mollusc shell microstructures and crystallographic textures. J Struct Geol 2000;22:1723-35.
[19] Chateigner D, Ouhenia S, Krauss C, Hedegaard C, Gil O, Morales M, et al. Voyaging around nacre with the X-ray shuttle: From bio-mineralisation to prosthetics via mollusc phylogeny. Mater Sci & Eng A 2010;528:37-51.
[20] Coppersmith SN, Gilbert PUPA, Metzler RA. Theoretical characterization of a model of aragonite crystal orientation in red abalone nacre. J Phys A 2009;42:125101.
[21] Gilbert PUPA, Metzler RA, Zhou D, Scholl A, Doran A, Young A, et al. Gradual ordering in red abalone nacre. JACS 2008;130:17519-27.
[22] Gries K, Kröger R, Kubel C, Fritz M, Rosenauer A. Investigations of voids in the aragonite platelets of nacre. Acta Biomat 2009;5:3038-44.
[23] Checa AG, Cartwright JHE, Willinger M-G. The key role of the surface membrane in why gastropod nacre grows in towers. Proc Nat Acad Sci USA 2009;106:38-43.
[24] Schäffer TE, Ionescu-Zanetti C, Proksch R, Fritz M, Walters DA, Almqvist N, et al. Does abalone nacre form by heteroepitaxial nucleation or by growth through mineral bridges? Chem Mater 1997;9:1731-40.
[25] Schmahl WW, Griesshaber E, Neuser R, Lenze A, Job R, Brand U. The microstructure of the fibrous layer of terebratulide brachiopod shell calcite. Europ J Mineral 2004;16:693-7.
[26] Dalbeck P, England J, Cusack M, Lee MR, Fallick AE. Crystallography and chemistry of the calcium carbonate polymorph switch in M. edulis shells. Europ J Mineral 2006;18:601-9.
[27] Griesshaber E, Schmahl WW, Neuser R, Pettke T, Blum M, Mutterlose J, et al. Crystallographic texture and microstructure of terebratulide brachiopod shell calcite: An optimized materials design with hierarchical architecture. Americ Mineralog 2007;92:722-34.
[28] Checa AG, Esteban-Delgado FJ, Ramirez-Rico J, Rodriguez-Navarro AB. Crystallographic reorganization of the calcitic prismatic layer of oysters. J Struct Biol 2009;167:261-70.
[29] Suzuki M, Kameda J, Sasaki T, Saruwatari K, Nagasawa H, Kogure T. Characterization of the multilayered shell of a limpet, *Lottia kogamogai* (Mollusca: Patellogastropoda), using SEM-EBSD and FIB-TEM techniques. J Struct Biol 2010;171:223-30.
[30] Goetz AJ, Steinmetz DR, Griesshaber E, Zaefferer S, Raabe D, Kelm K, et al. Interdigitating biocalcite dendrites form a 3-D jigsaw structure in brachiopod shells. Acta Biomat 2011;7:2237-43.
[31] Goetz AJ, Griesshaber E, Neuser RD, Luter C, Huhner M, Harper E, et al. Calcite morphology, texture and hardness in the distinct layers of rhynchonelliform brachiopod shells. Europ J Mineral 2009;21:303-15.
[32] Dingley D. Progressive steps in the development of electron backscatter diffraction and orientation imaging microscopy. J Microsc (Oxford) 2004;213:214-24.
[33] Zaefferer S. On the formation mechanisms, spatial resolution and intensity of backscatter Kikuchi patterns. Ultramicroscopy 2007;107:254-66.
[34] Steinmetz DR, Zaefferer S. Towards ultrahigh resolution EBSD by low accelerating voltage. Materials Science and Technology 2010;26:640-5.
[35] Seidl BHM, Reisecker C, Hild S, Griesshaber E, Ziegler A. Calcite distribution and orientation in the tergite exocuticle of the isopods *Porcellio scaber* and *Armadillidium vulgare* (Oniscidea, Crustacea) – a combined FE-SEM, polarized SCμ-RSI and EBSD study Zeitschrift für Kristallographie 2012;227:812-9.
[36] Hahn S, Rodolfo-Metalpa R, Griesshaber E, Schmahl WW, Buhl D, Hall-Spencer JM, et al. Marine bivalve shell geochemistry and ultrastructure from modern low pH environments: environmental effect versus experimental bias. Biogeosciences 2012;9:1897-914.
[37] Griesshaber E, Ubhi HS, Schmahl WW. Nanometer scale microstructure and

microtexture of biological materials revealed by high spatial resolution (15 to 5 kV) EBSD. In: Tewari A, Suwas S, Srivastava D, Samajdar I, Haldar A, editors. Textures of Materials, Pts 1 and 22012. p. 924-7.
[38] Schmahl WW, Griesshaber E, Kelm K, Ball A, Goetz A, Xu DY, et al. Towards systematics of calcite biocrystals: insight from the inside. Zeitschrift für Kristallographie 2012;227:604-11.
[39] Baronnet A, Cuif JP, Dauphin Y, Farre F, Nouet J. Crystallization of biogenic Ca-carbonate within organo-mineral micro-domains. Structure of the calcite prisms of the Pelecypod *Pinctada margaritifera* (Mollusca) at the submicron to nanometre ranges. Mineralogical Magazine 2008;72:617-26.
[40] Rousseau M, Lopez E, Stempfle P, Brendle M, Franke L, Guette A, et al. Multiscale structure of sheet nacre. Biomaterials 2005;26:6254-62.
[41] Nouet J, Baronnet A, Howard L. Crystallization in organo-mineral micro-domains in the crossed-lamellar layer of *Nerita undata* (Gastropoda, Neritopsina). Micron 2012;43:456-62.
[42] Schmahl WW, Griesshaber E, Kelm K, Goetz A, Jordan G, Ball A, et al. Hierarchical structure of marine shell biomaterials: biomechanical functionalization of calcite by brachiopods. Zeitschrift Fur Kristallographie 2012;227:793-804.
[43] Kelm K, Goetz A, Sehrbrock A, Irsen S, Hoffmann R, Schmahl WW, et al. Mosaic structure in the spines of *Holopneustes porossisimus*. Zeitschrift Fur Kristallographie 2012;227:758-65.
[44] Fabritius H, Walther P, Ziegler A. Architecture of the organic matrix in the sternal CaCO3 deposits of *Porcellio scaber* (Crustacea, Isopoda). J Struct Biol 2005;150:190-9.
[45] Feng QL, Li HB, Pu G, Zhang DM, Cui FZ, Li HD, et al. Crystallographic alignment of calcite prisms in the oblique prismatic layer of *Mytilus edulis* shell. Journal of Materials Science 2000;35:3337-40.
[46] Bunge HJ. Texture Analysis in Materials Science: Mathematical Methods. London: Butterworths; 1982.
[47] Fabritius HO, Karsten ES, Balasundaram K, Hild S, Huemer K, Raabe D. Correlation of structure, composition and local mechanical properties in the dorsal carapace of the edible crab *Cancer pagurus*. Zeitschrift Fur Kristallographie 2012;227:766-76.
[48] Neff JM. Ultrastructure of the outer epithelium of mantle in clam mercenaria-mercenaria in relation to calcification of shell. Tissue & Cell 1972;4:591-600.
[49] Jacob D, Soldati a, Wirth R, Huth J, Wehrmeister U, Hofmeister W. Nanostructure, composition and mechanisms of bivalve shell growth. Geochim Cosmochim Acta 2008;72:5401-15.
[50] Seto J, Ma Y, Davis SA, Meldrum F, Gourrier A, Kim Y-y, et al. Structure-property relationships of a biological mesocrystal in the adult sea urchin spine. Proc Nat Acad Sci USA 2011:3700-4.
[51] Marsh ME, Sass RL. Aragonite twinning in the molluscan bivalve hinge ligament. Science 1980;208:1262-3.
[52] Weiss IM, Tuross N, Addadi L, Weiner S. Mollusc larval shell formation: Amorphous calcium carbonate is a precursor phase for aragonite. Journal of Experimental Zoology 2002;293:478-91.
[53] Addadi L, Vidavsky N, Weiner S. Transient precursor amorphous phases in biomineralization. In the footsteps of Heinz A. Lowenstam. Zeitschrift Fur Kristallographie 2012;227:711-7.
[54] Weiss IM. Species-specific shells: Chitin synthases and cell mechanics in molluscs. Zeitschrift Fur Kristallographie 2012;227:723-38.
[55] Weiner S, Addadi L. Crystallization Pathways in Biomineralization. Ann Rev Mater Res 2011;41:21-40.

Supplementary Figures

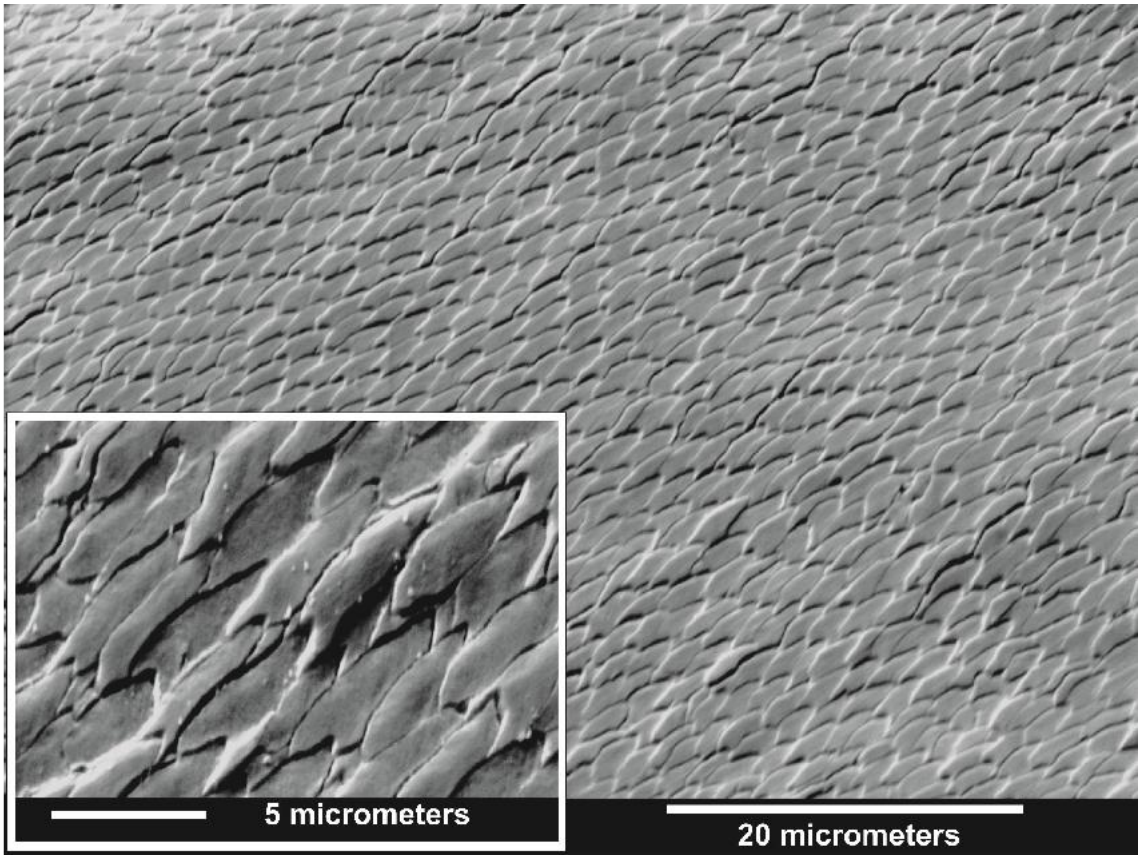

Fig. S1 FE-SEM image on a polished surface of a cross section through the calcitic shell layer of *Mytilus edulis* away from the calcite – aragonite interface zone.

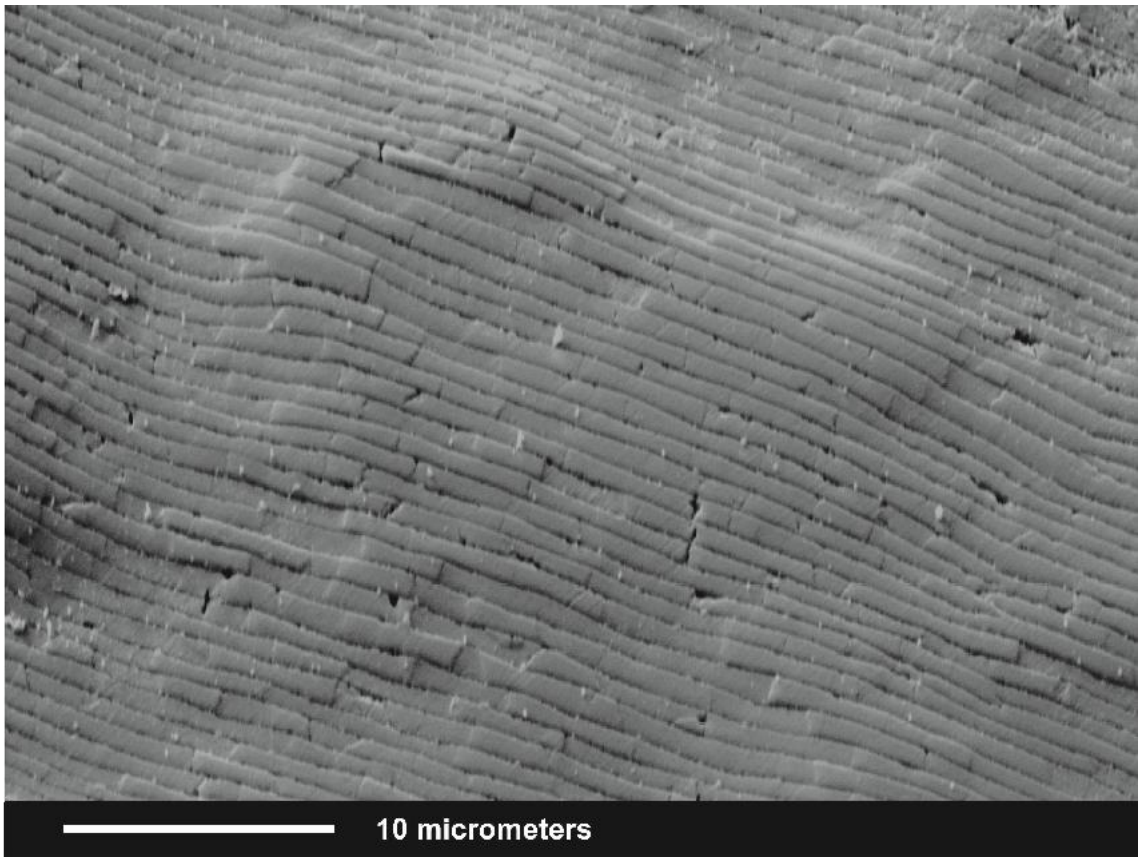

Fig. S2. FE-SEM image of well developed tablet layers of aragonite in the nacre shell layer of *Mytilus edulis*.

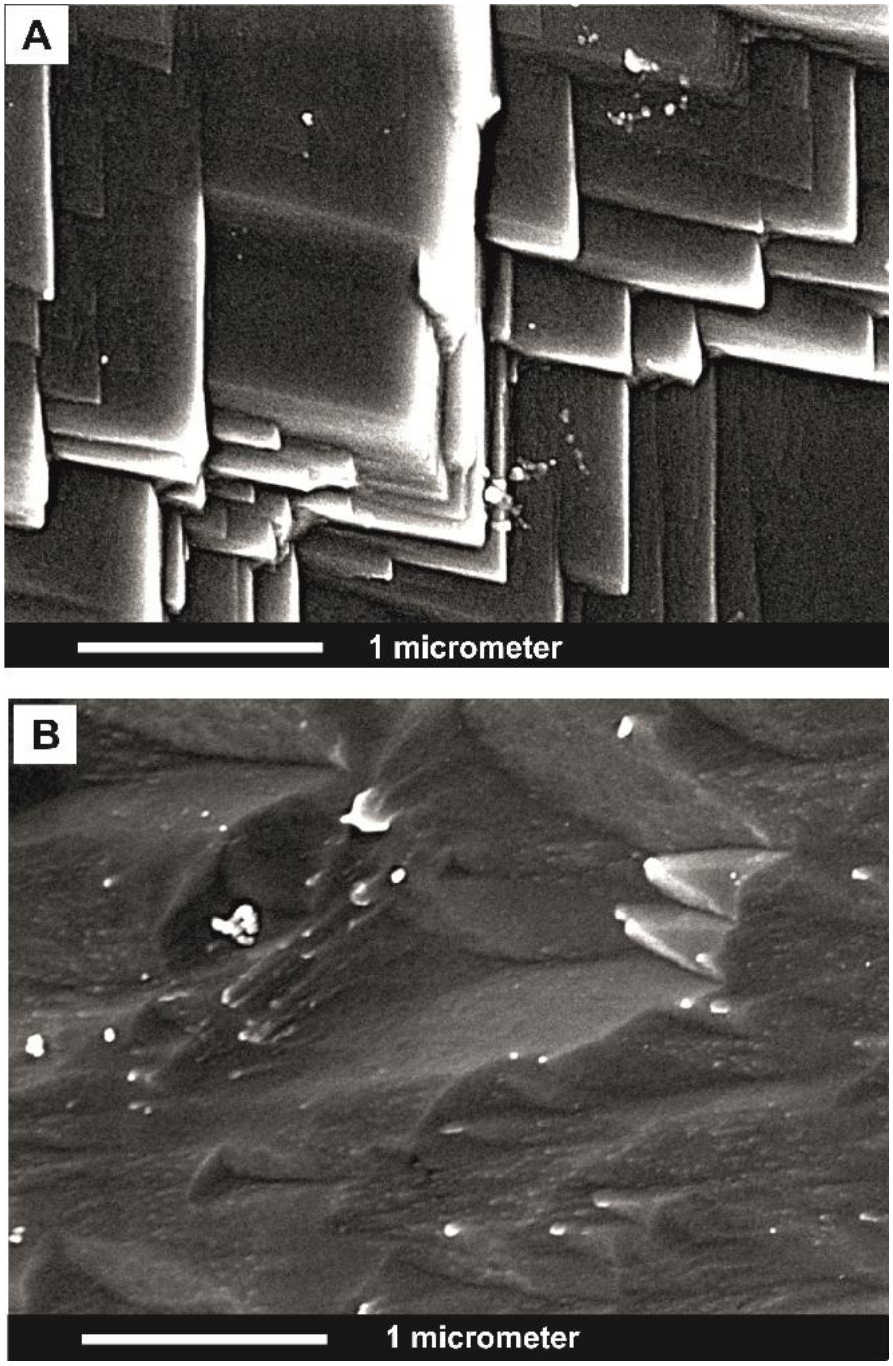

Fig. S3. Non-biological, geologic, calcite (A) and aragonite (B) crystal reference treated similarly to *Mytilus edulis* calcite and aragonite: microtome cut, microtome polished, etched and critical point dried.

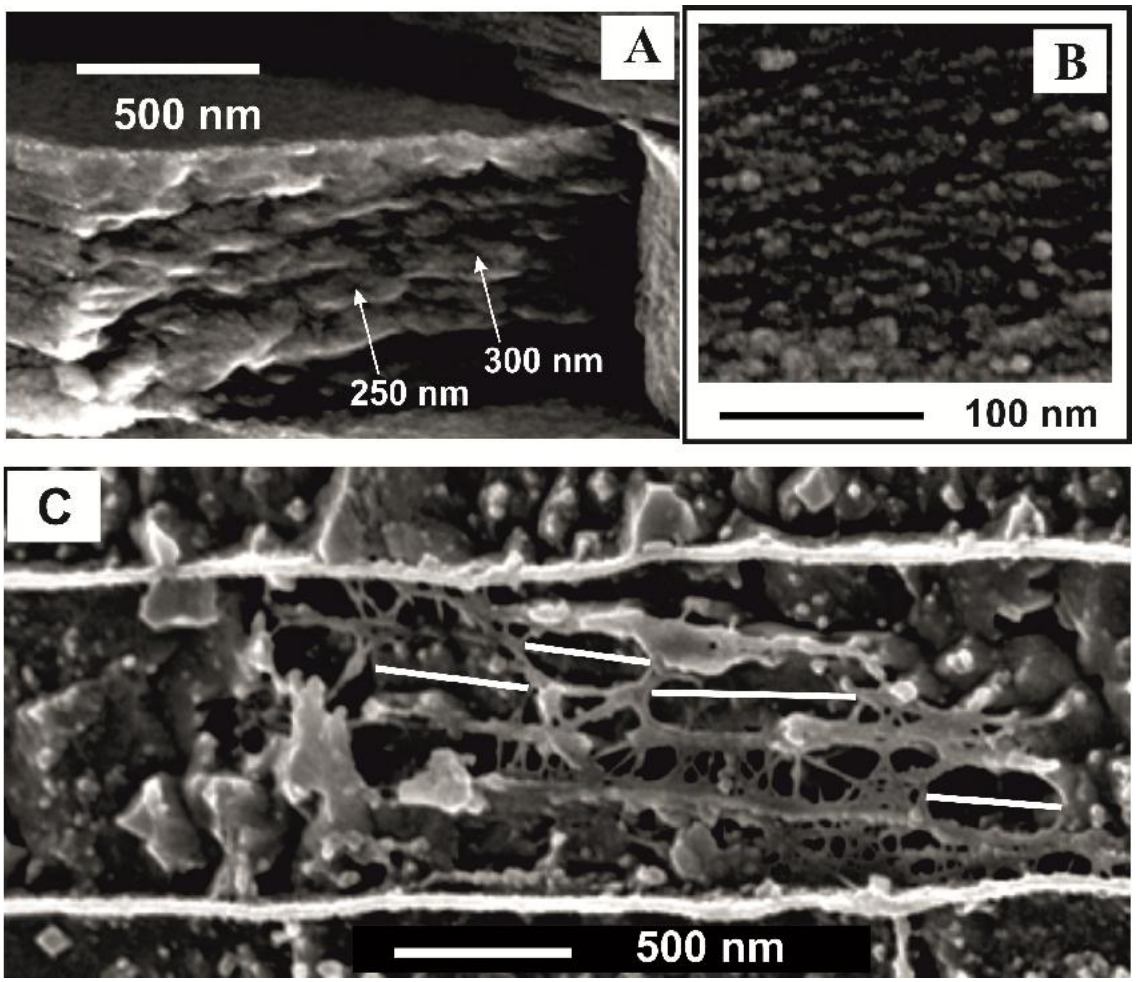

Fig. S4. Direct comparison of size scales of (A) subunits in the aragonite tablets, (B) nanoparticles constituting the aragonite, and (C) open pores in the intra-tablet organic matrix network.

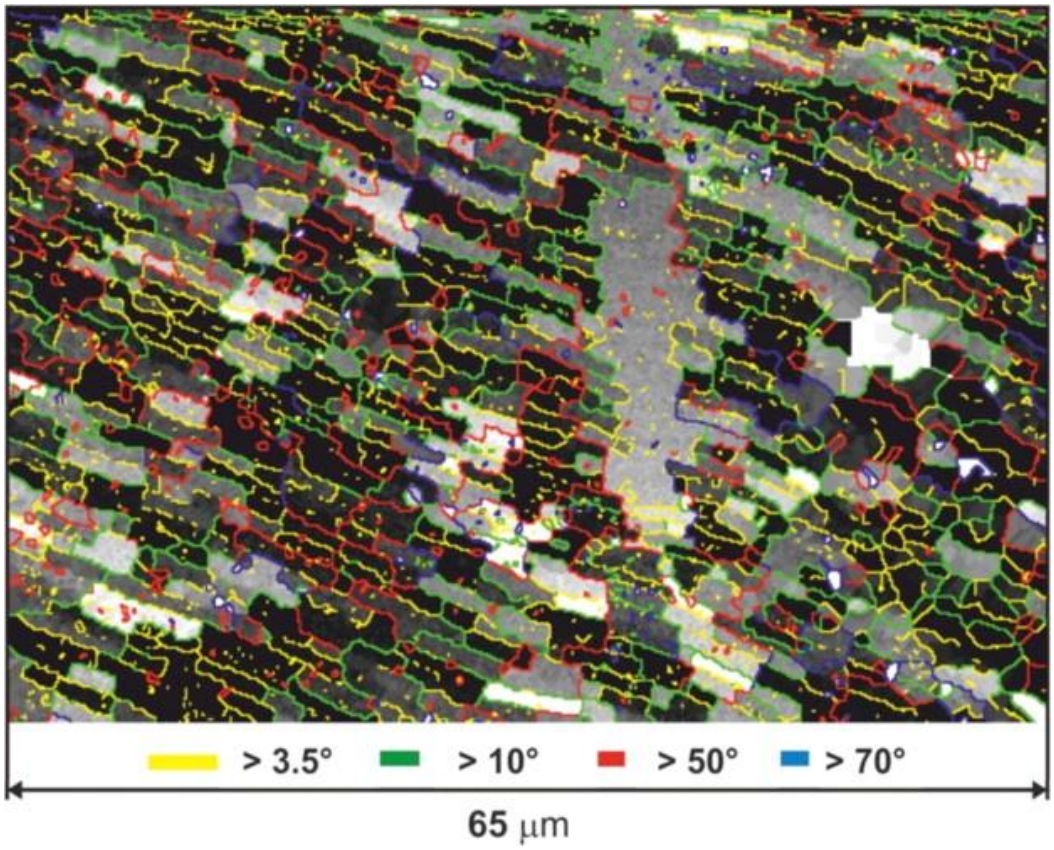

Fig. S5. Grain boundary misorientation map for the entire EBSD data set shown in Fig. 12. Gray-scale contrast is the angular deviation from the mean c-axis orientation of the map from 0° (black) to 25° (white).

2.2 The influence of gelatin hydrogel porosity on the crystallization of $CaCO_3$

Fitriana Nindiyasari,†, Lurdes Fernández-Díaz*,§,‡, Erika Griesshaber†, José Manuel Astilleros§,‡, Nuria Sánchez-Pastor§ and Wolfgang W. Schmahl†*

†Department of Earth- and Environmental Sciences, Ludwig-Maximilians-Universität, 80333 Munich, Germany.
§Departamento de Cristalografía y Mineralogía, Universidad Complutense de Madrid, 28040 Madrid, Spain.
‡Instituto de Geociencias (UCM, CSIC). C/ José Antonio Novais 2, 28040 Madrid, Spain.

Journal of Crystal Growth and Design 14, 1531-1542 (2014)

https://pubs.acs.org/doi/abs/10.1021/cg401056t

ABSTRACT: We investigated the influence of the porosity of the growth medium on the crystallization of calcium carbonate in hydrogels with different gelatin solid contents (2.5, 5, and 10 wt %). In all experiments the precipitate consisted of calcite with occasional occurrences of some vaterite and aragonite. The calcite grew as compact radial intergrowths of crystals that show rhombohedral external faces. The crystal surfaces consist of identical 1-10 micrometer-sized rhombohedral sub-blocks. Electron backscatter diffraction (EBSD) uncovered the radial intergrowth structure of the aggregates. EBSD also documented the internal microscale mosaicity and mesocrystal-like constitution of the gel-grown calcite. Raman spectroscopy and Thermogravimetric Analysis confirmed the presence of gelatin within the crystals. It reached up to ~2 mass % in the calcite-gelatin composites that formed in hydrogels with 10 wt % gelatin content. Calcite morphology and mosaicity varied with the gelatin content of the hydrogel, such that an increase in gelatin content initiated the growth of smaller crystal aggregates having progressively rougher surfaces, increasing amounts of incorporated gel, and increasing degrees of misorientation in the internal mosaic structure. Apart from biospecific morphology the gel growth experiment successfully mimics many characteristics of calcite biomineralization such as formation of a hierarchical hybrid composite, crystal mosaicity and mesocrystal-like constitution.

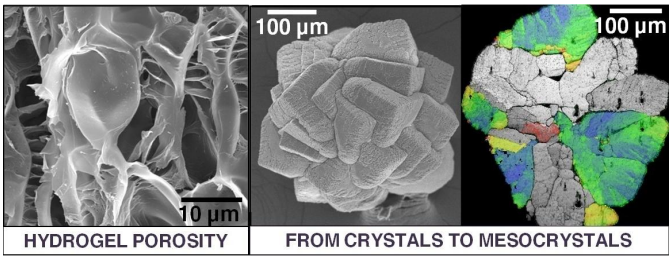

Introduction

Crystal growth in hydrogel matrices is a long-stated method, and its advantages to model biomineralization become increasingly evident.[1-2] Numerous authors have emphasized the role of organic matrices in the biomineralization processes in a variety of organisms (molluscs, corals, coccolithophorids, etc).[3-5] Such matrices consist of assemblies of polysaccharides, proteins and glycoproteins and show different active groups as well as different porosities. Moreover, it is well established that most biomineralization processes occur in confined environments within organic matrices.[6-7] These natural organic matrices show features strikingly similar to those of hydrogel-systems. The possibility of fine-tuning the porosity and the chemical characteristics of hydrogels by using different solid gel contents and additives in their preparation constitutes a further advantage of hydrogels for modeling biomineralization processes.[8-11]

Numerous authors have studied the crystallization of $CaCO_3$ in a variety of hydrogels (silica, agar, gelatin, polyacrylamide, etc).[12-17] In many cases, experiments yielded calcite crystals that exhibited a wide range of unexpected shapes (octahedron, cuboctahedron, dodecahedron, etc.). Such crystals were built up by nanometric to micrometric rhombohedral sub-blocks that are slightly tilted relative to each other. These crystals entities often incorporate small amounts (1-3 wt %) of the hydrogel matrix that is present at the contact between the building sub-blocks.[15-

[19] For these objects descriptive terms such as "hybrid structure of calcite crystalline assemblies"[15] or "single-crystalline nanoclustered calcite of semicoherent domains"[18] have been coined. More recently these objects are described as "mesocrystals".[1,20-23] The definition of a mesocrystal evolved to the statement of Seto et al.[22] "a mesocrystal ideally comprises a 3D array of isooriented single crystal particles of size 1-1000nm" (with no reference to hybrid composite structure). Song and Cölfen[24] assign mesocrystal formation in gels to nanoparticle alignment along an organic matrix, based on work by Grassmann and coworkers[15-18] and Huang et al.[19] Nanoparticle assembly processes or so-called non classical crystallization becomes an increasingly important concept in the crystallization of mesocrystals and in nucleation and growth of calcium carbonate.[1,25-30] Carbonate biominerals in skeletons and teeth typically have characteristics of a hybrid (organic-inorganic) mesocrystalline assembly and a hierarchical architecture over several length scales.[31-36] Grassmann et al.[16] already described nanoparticle assembly as a non-classical growth mode of calcite forming at high supersaturation in gels, a notion which has been suggested for general systems with very low molecular solubility or high supersaturation by Colfen and Antonietti.[23]

Over the last decade the influence on carbonate crystallization of both, the hydrogel types as well as the organic and inorganic additives to the growth medium have been extensively explored.[2,37-41] To the knowledge of the authors, only Helbig (2008)[42] has studied the effect of the solid gel concentration of polyacrylamide hydrogels on the polymorph selectivity and morphology of $CaCO_3$ crystals. It has been concluded that the solid content of the hydrogel has little to no effect on polymorph selectivity.[42] However, it strongly affects the morphology of calcite crystals, which upon growth, evolves from rhombohedron to octahedron-shaped single crystals and crystal aggregates composed of oriented sub-blocks.

Gelatin is an interesting hydrogel, since its porosity can easily be modified by changing the solid content of the gel. In this study gelatin hydrogels were used to conduct $CaCO_3$ crystal growth experiments by using a double diffusion set-up. The gels were prepared with three different gelatin contents: 2.5, 5 and 10 wt %. One major aim of this work was to explore the influence of gelatin content on the nucleation of $CaCO_3$ and to investigate the variation in experimental waiting time of the first optically visible crystal, the position of the first precipitate, the number of nuclei and the type of polymorph formed. A further aim was to study the effect of gelatin content on the growth morphology of calcite crystals, focusing on possible differences in their mosaicity. The final goal of this work was to relate changes of $CaCO_3$ precipitates to changes in porosity and diffusivity of the crystallization medium relative to the gelatin content of the hydrogel.

Experimental procedures

Crystal growth experiments. $CaCO_3$ crystal growth experiments were conducted at 15 °C in a double-diffusion system consisting of two vertical branches separated by a horizontal column of hydrogel. At this temperature the hydrogels remain rigid. Also, this temperature is within the range of common temperatures in shallow sea waters[43], the living-environment for a variety of organisms.[44-46]

The reagents, aqueous solutions of calcium chloride (0.5M $CaCl_2$; Sigma Aldrich) and sodium carbonate (0.5M Na_2CO_3; Sigma Aldrich), filled the vertical branches, from where they counter-diffused through the porous structure of the hydrogel. The hydrogel was prepared by dissolving porcine gelatin (Sigma Aldrich; Type A, Bioreagent) in high purity deionized (MilliQ) water (18.2 MΩ) heated at 60 ºC. The gelification was carried out at 4 ºC for an hour and the hydrogels were subsequently set at 15 ºC for 24 hours before pouring the reagent solutions in the vertical branches. The hydrogels were prepared using three different contents of gelatin: 2.5, 5 and 10 wt %. The hydrogel column was 70 mm long and had a diameter of 9 mm in all the cases. Upon starting the experiments, the counter-diffusion of the reagents determined that eventually $CaCO_3$ nucleation and growth occurred in a narrow region of the hydrogel column. The time (t_w) that elapsed between the start of experiments and the occurrence of the first crystals that were detected with 400x magnification was measured as a mean to determine differences in physicochemical conditions in the experiments during early crystallization stages. It is important to note that, although the experimental waiting time for the first optically visible crystal is always longer than the actual nucleation time and is influenced by the method used to detect the first nuclei, the error involved in its measurement is identical in all experiments, which makes this parameter (t_w) suitable for comparison between the different experiments. Crystal growth was monitored by optical microscopy. One week after the

observation of the first optically visible crystals, the experiments were stopped and the crystals were extracted by dissolving the gel in hot water and filtering the precipitate through a 1-µm pore size membrane. The crystals were subsequently washed 3 times with Milli-Q water heated at 60 ºC to remove any impurity and dried in air at room temperature. The entire extraction/washing procedure lasted ~ 15 minutes. In order to ensure that this procedure does not influence the morphological characteristics nor the surface features of crystals, we have conducted the following experiments:

Reference crystals with rhombohedral faces were prepared (i) by crushing a Spar quality calcite single crystal and sieving to select small fragments of the desired size, (ii) by growing calcite rhombohedra in water by the gas-diffusion method. SEM images of the crushed crystals without further treatment and water-grown crystals which were washed in alcohol and rapidly dried were obtained. The gel extraction procedure (washing at 60 °C for 15 minutes) was then applied to the reference crystals, and those sample were SEM imaged similarly. The crushed calcite crystals were bounded by flat (104) faces, the calcite cleavage plane, as expected. The only feature that could be distinguished by SEM on their surface, irrespective their having been in contact with the hot water or not, was the presence of cleavage steps that formed during the crushing. Calcite crystals obtained by gas-diffusion in (ii) showed the typical rhombohedral habit, with flat (104) faces and straight edges. No differences were detected by SEM between crystals that had been in contact with hot water and those which had not. In summary, no SEM-visible etch pits formed on the crystal surface of calcite as a result of their being in contact with 60°C water for 15 minutes (Figure S1 of the Supporting Information Section).

Qualitative analysis of the gel porosity. In order to obtain qualitative information on the porosity of the hydrogel as a function of its gelatin content, small volumes (30 mL) of hydrogel with different gelatin contents were prepared following the procedure described for the growth experiments. Hydrogel samples were frozen with liquid nitrogen and subsequently lyophilized during 24 hours in a lyophiliser (Lyoquest-55 Eco, Telstar) to eliminate all the water trapped in the gel pores. Fragments of the dried samples were double coated using firstly carbon and subsequently gold. Scanning electron microscope images were obtained with a JEOL JSM 6400 operated at 20 kV. Since it is expected that the lyophillization process alters the porosity of the samples, these observation are exclusively used for comparison purposes.

Reagent concentrations at nucleation time and location. In order to obtain information on the concentration of the reagents at the experimental waiting time of the first optically visible crystal in the region of the hydrogel column where the first crystals formed, two sets of independent experiments were conducted. In both cases, one of the vertical branches of the experimental set up was filled with water, while the other was filled with one of the reagent solutions. Independent runs were conducted for each content of solid gelatin in the hydrogel. The experiments were stopped after times that equal to the time delayed between the beginning of the corresponding growth experiment and the observation of the first crystals: ~24 hours for the hydrogel with a 2.5 wt % solid content; ~84 hours for the hydrogel with a 5 wt %; and a ~120 hours for the hydrogel with 10 wt % gelatin content. The gelatin column was then recovered and the region of this column corresponding to the location of the first nuclei was cut, dissolved in water and analyzed. Ca analyses were conducted by Inductive Coupled Plasma-Optic Emission spectrometry (ICP-OES) using an ICP-Arcos (spectrolab). The concentration of carbonate ions was determined by potentiometry, using a pH-meter Orion 710A. The information obtained in this way allowed us to estimate the relative supersaturation at experimental waiting time of the first optically visible crystal in the region of the hydrogel column where the first nuclei were detected and correlate it to the gelatin solid content of each hydrogel. This calculation was conducted using the geochemical speciation code PHREEQC[47] and the PHREEQC.DAT database.

$CaCO_3$ crystals characterization. The crystals obtained were coated with carbon and imaged using a FEG-SEM (JEOL JSM 6400) operated at 20 kV. Selected crystals were characterized using X-ray powder diffraction (XRD). The XRD analyses were carried out on a Philips X'Pert Pro X-ray diffractometer in the 2θ angle range between 5° and 80° in steps of 0.02° using Cu-Kα radiation. Raman spectra of the samples were obtained using a confocal Thermo Fischer DXR Raman Microscope. It allowed us to establish the correlation between a given crystal morphology and a specific $CaCO_3$ polymorph. The objective selected was of 10x together with a laser source 780 nm at 10mV in a laser mode power at 100 %. The average spectral resolution of the Raman shift ranging from 70 to 3000 cm^{-1} was 2-4 cm^{-1}, i.e., grating 400 lines/mm. Operated under OMNIC 1.0 software with a

pinhole aperture of 50 µm and a bleaching time of 1-2 s, 4 to 8 exposures of 10 to 15 s were averaged, depending on the sample. Thermogravimetric and differential thermal analyses (TGA-DTA) were performed using a SDT-Q600 apparatus on calcite samples to detect the possible incorporation of the different amounts of gelatin as a function of the gelatin solid content in the hydrogel. The weight loss between room temperature and 150 ºC was considered the consequence of drying. The weight loss corresponding to the loss of gelatin was considered to start at 200 ºC.

EBSD measurements were performed on embedded and highly polished crystal surfaces. The required highly even surface of the samples was achieved by a final etch-polishing with colloidal silica in a vibratory polisher. The samples were coated with 4 nm of carbon. EBSD maps were obtained at 20 kV on an FEG-SEM (JEOL JSM 6400) equipped with an Oxford Instruments NordlysNano EBSD detector.

Results

Hydrogel porosity. During their preparation for SEM imaging the hydrogels undergo a certain shrinkage associated to the elimination of the water trapped in their porous structure. This shrinkage was similar in all samples (~17 wt % volume reduction) and affected mainly their outer region. In order to guarantee a minimum effect of this shrinkage with the porous structure of the hydrogels, all the SEM images were collected on fresh fracture surfaces on the core of the samples. The comparison between SEM images obtained on samples with different gelatin content clearly indicates that the concentration of gelatin strongly influences the porosity structure of the hydrogels. This influence is reflected by a progressively more complex porosity as the gelatin content increases and is also evidenced by changes in both, the pore sizes and pore wall thickness (Figure 1). Thus, hydrogels with 2.5 wt % gelatin show pore sizes >10 µm (Figure 1a, d), whereas in hydrogels with solid-gel contents of 5 and 10 wt % pore sizes are ≤ 5µm (Figures 1b, c, e, f). Moreover, the thickness of the pore walls clearly increases with higher gelatin content in the hydrogel. These walls are very thin and show a spider web-like structure (see areas within the square frames in Figure 1d) in hydrogels with 2.5 wt % gelatin content. Pore walls in hydrogels with 5 wt % gelatin content are thicker. Although in this case the spider web-like structure shows a poorer development, each pore seems to contain several sub-pores of smaller sizes (see areas within the square frames in Figure 1e), which appear located on the walls separating bigger pores. Finally, pore walls in hydrogels with 10 wt % solid gel content are significantly thicker and show no development of a spider-web-like structure. It is important to note that in this case a complicated arrangement of thinner walls develops within the pores. These thinner walls connect opposite sides of bounding-pore walls and subdivide the bigger pores in cages with sizes in the range between 1-2 µm (see areas within the square frames in Figure 1f).

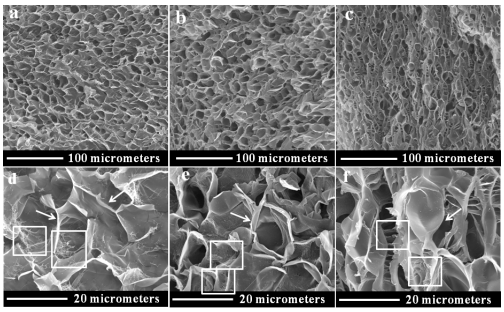

Figure 1. SEM images illustrating the variation of the porosity of gelatin hydrogels as a function of their solid content. Images (a), (b) and (c) show a general overview of this porosity when the gelatin content was 2.5 wt %, 5 wt % and 10 wt %, respectively. Images (d), (e) and (f) show close-up of the pores in (a), (b) and (c), respectively. A progressive reduction of the pores size with increasing gelatin content in the hydrogel is observed. This reduction correlates with a thickening of the walls separating the pores and an increase of the complexity of the porosity structure. White squares in images (d), (e) and (f) highlight the existence of small pores on the walls interconnecting larger pores. White arrows highlight the thickness of the inter-pore walls.

Influence of the gelatin content on the early stages of crystallization and polymorph selectivity. Table 1 summarizes the experimental waiting time of the first optically visible crystal (t_w), the location of these crystals in the hydrogel column (distance measured from $CaCl_2$ reservoir), the number of crystals (NC) and the type of polymorph observed. The experimental waiting time of the first optically visible crystal progressively increased with the gelatin content in the hydrogel, being ~24 hours for 2.5 wt % gelatin content; ~84 hours for 5 wt % gelatin content; and ~120 hours for 10 wt % gelatin content, respectively. In all experiments the crystals first appeared in a narrow, central region (~5 mm) of the hydrogel column. An increase in gelatin content caused the displacement of the location of the first optically visible crystals towards the calcium reservoir. With increased

gelatin concentration the number of crystals in the first visible precipitate decreased. In our experiments the hydrogel column remained transparent and did not show any shade change before the observation of the first crystals. The first optically visible crystals always were calcite irrespective of the gelatin content of the hydrogel. Moreover, in all experiments calcite remained the main component of the precipitate. In the final stages of crystallization some vaterite was also present. We could observe a distinct negative correlation between the amount of vaterite and the gelatin content of the hydrogel. This strongly implies that gelatin inhibits the crystallization of vaterite. While vaterite represented ~10 % of the precipitate in the experiments conducted using hydrogels with a 10 wt % gelatin content, its amount increased up to ~ 40 % when the hydrogel contained 2.5 wt % gelatin (see Table 1). Aragonite was not observed in the experiments conducted with 2.5 wt % gelatin hydrogel. It was detected as a minor phase when the gelatin content in the hydrogel was 5 and 10 wt %.

Table 1. Experimental waiting time of first optically visible crystal (t_w), location of the first crystals in the gel column (distance measured from $CaCl_2$ reservoir) and total number of crystals (NC) of calcite (Cal), vaterite (Vtr) and aragonite (Arg) individuals measured 24 hours after the observation of the first crystal.

wt % gelatin	t_w (hours)	Position (mm)	NC		
			Cal	Vtr	Arg
2.5	~24	32-35	70	28	0
5	~84	37-39	32	6	1
10	~120	38-41	17	3	1

Influence of the gelatin content on crystal size and morphology. The size of the crystals was measured 7 days after their first observation. Vaterite grew as spherulitic aggregates with a mean size of ~ 100 ± 20 μm. These aggregates consisted of small lens-shaped individuals (~ 10 μm x 1 μm) in a rosette-like arrangement (Figure 2a). The gelatin content of the hydrogel did not affect the size of the vaterite crystals. Aragonite grew as aggregates consisting of radiating, fibrous crystals (Figure 2b). In the case of calcite, both, the morphology and the size of the crystal changed significantly with the gelatin content of the hydrogel. Calcite grew in hydrogels with 2.5 wt % gelatin content as blocks formed by several sub-parallel crystals bounded by flat, terraced (104) surfaces (Figures 3a, b) and had a mean size of 220 ± 70 μm. Calcite grown in hydrogels with 5 wt % gelatin content appeared as both, blocks as above, and as radial aggregates composed of small and blocky rhombohedra. These crystals were bounded by strongly terraced (104) as well as rough, rounded vicinal surfaces

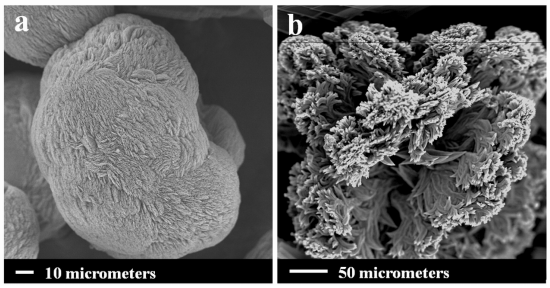

Figure 2. (a) Spherulitic aggregates of vaterite and (b) radially growing fibrous aragonite.

(Figures 3c, d). The mean size of the calcite aggregates was 400 ± 50 μm. Single crystals that were elongated parallel to their c-axis were also observed (Figure 3e). These crystals also showed flat (104) but also rough, curved surfaces that seem to belong to the prism region. In these rough surfaces, crystalline sub-blocks were present (Figure 3f) that were slightly tilted relative to each other. Calcite grown in hydrogels with 10 wt % gelatin content formed crystal aggregates of numerous individuals. The mean size of these aggregates was ~500 μm. Their constituting individuals had sizes around 100 μm and were bounded by rough (104) faces with curved, rough edges and corners (Figure 3g). The increased roughness in regions near the crystal edges is depicted in Figure 3h, where the presence of the tilted crystalline sub-blocks can be observed. Each sub-block, ranging from less than 1 μm to over 5 μm in size, shows the typical morphology of the calcite rhombohedron (Figure 4a). An interesting example of the rhombohedral sub-blocks forming the calcite crystal aggregates grown in a hydrogel with 10 wt % gelatin is shown in Figure 4b. The rhombohedron-shaped sub-blocks seem to be hierarchically arranged, with their dimensions covering several size ranges. A comparison of crystallite size determined from XRD and the Scherrer equation (without corrections for stress) to selected h k l reflections with the pixel-step of the EBSD measurements is shown in the Supporting Information in Table S1.

Influence of hydrogel gelatin content on crystal morphology and mosaicity. Figures 5 and 6 show EBSD (Electron Backscatterorientation) maps and corresponding

pole figures of crystal aggregates that grew in hydrogels with different gelatin content. Figures 5a and 6a show crystals obtained from hydrogels containing 2.5 wt % gelatin, Figures 5b and 6b display crystals that were obtained from hydrogels with 10 wt % gelatin content. Crystallographic calcitethe EBSD band contrast (Figures 5a, b). This is a grey scale component that gives the signal strength in each individual EBSD-Kikuchi diffraction pattern. Where carbonate mineral is present, the strength of the EBSD pattern is high, while in pores and gel inclusions the strength of the EBSD pattern is low. The band contrast signal thus indicates the distribution of incorporated gelatin within the crystal. Also shown in Figure 5 is the mean calcite orientation for all crystals composing the investigated aggregates. For crystal aggregates grown in hydrogels with 10 wt % gelatin the orientation of the constituting crystals shows random scatter (Figure 5b), while for the crystal aggregates grown in hydrogels with 2.5 wt % gelatin (Figure 5a) some degree of mutual co-orientation of the constituting crystals is present. This correlates with the vaguely rhombohedral overall shape of the aggregates grown in hydrogels with 2.5 wt % gelatin.

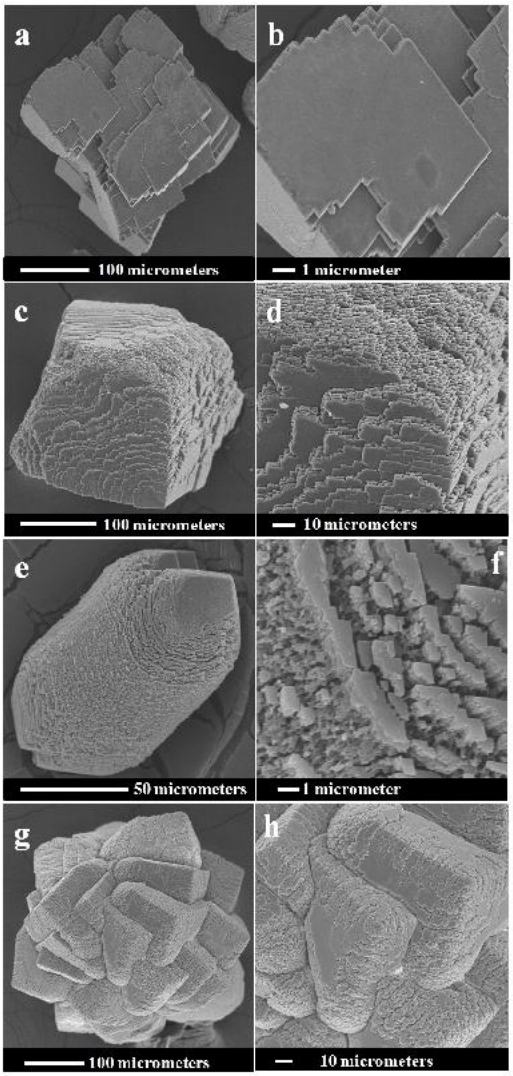

Figure 3. (a) Blocky calcite bounded by (104) surface grown in a hydrogel with 2.5 wt % gelatin content. (b) Detail of the surface, with flat appearance. (c) Calcite crystal grown in a hydrogel with 5 wt % gelatin content, bounded by (104) surfaces and non-singular surfaces. (d) Detail showing the formation of curved surfaces due to the accumulation of rough steps. Note that, while (104) surfaces are relatively flat, other surfaces are very rough. (e) Calcite crystal grown in a hydrogel with 5 wt % gelatin content. The crystal is elongated along the c axis. (f) Detail showing the high roughness of the curved surfaces. (g) Calcite crystal aggregate grown in a hydrogel with 10 wt % gelatin content. (h) Close up of (g) showing the higher roughness of the surfaces near the edges.

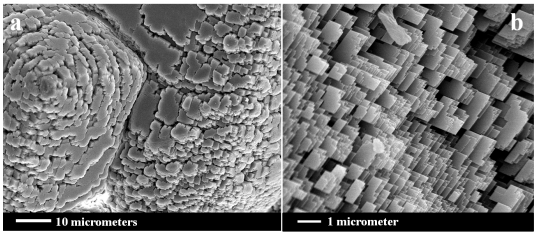

Figure 4. Images of the surface of calcite crystals grown in a hydrogel with 10 wt % gelatin content. An increased surface roughness is present and indicates that the crystal aggregates consist of rhombohedral sub-blocks arranged in an approximately equal orientation. Near the edges of the crystal surface roughness is increased (4a). The size of the rhombohedral sub-blocks varies between 1 to 5 µm (4b).

We observe significant differences in the morphology of the crystal aggregates grown in the two different media. An increase in hydrogel gelatin content causes rounded crystal surfaces (Figure 6b) and a pronounced internal mosaic structure of each crystal in the aggregate, i.e. each crystal is composed of several microscale subcrystals.

Incorporation of gelatin into calcite crystals during growth and mesocrystallinity. In order to study the incorporation of gelatin into the calcite crystals during their growth Raman spectra were collected on three selected calcite samples. The spectra are shown in Figure 7. The Raman spectrum of calcite is characterized by

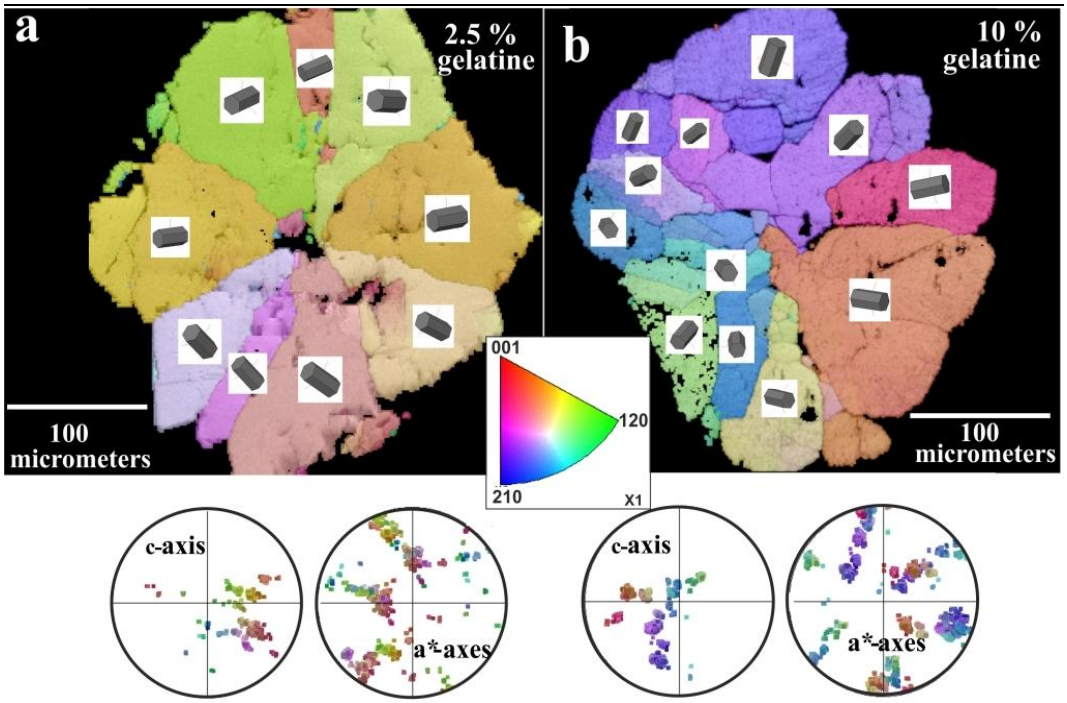

Figure 5. The influence of hydrogel gelatin content on the morphology of crystal aggregates. Figure 5a: crystal aggregate grown in a hydrogel with 2.5 wt % gelatin, Figure 5b: crystal aggregate grown in a hydrogel with 10 wt % gelatin content. Crystal orientation patterns are given color-coded, in both, the EBSD maps as well as in the corresponding pole figures.

two low frequency bands at 155 and 281 cm^{-1} which arise from external vibrations and three higher frequency bands at 711, 1085 and 1435,resulting from the CO_3^{2-} group's internal vibrations.[48-51] All these bands are clearly identifiable and show identical characteristics in the spectra of the three studied calcite samples. Most interesting is the presence of weak bands around 488, 1016, 1341, 1748 and 2952 cm^{-1} in all three spectra. Although the band at 1748 cm^{-1} may be interpreted as resulting from the combination of calcite bands ν_1 and ν_4[52], the other bands cannot be assigned to any vibration in the calcite structure. However, some of these bands occur at wavelengths that indicate gelatin in the calcite crystals. The Raman spectrum that was collected on the powdered porcine gelatin that was used to prepare the hydrogels is shown with Figure S2 in Supporting Information. For example, the sharper band around 2900 cm^{-1}, present in the spectrum of the powdered gelatin, is commonly assigned to the CH stretching mode and is considered indicative of the presence of organic material.[53] Most significant is the band located around 1016 cm^{-1}, that is present in both, the calcite crystals and the powdered porcine gelatin spectra. Bands in the region between 1005–1020 cm^{-1} occur in the spectra of different gelatins.[54] They have also been found in the shells of some marine mollusks[55], lobster shell pigments[56], birds feathers[57] and are indicative of the presence of methyl groups, either as a CH out-of-plane[58] or as the deformation-activated CH=CH wagging modes[53]. The increasingly stronger intensity of the 1016 cm^{-1} band in the calcite spectra (see inset in Figure 7) supports the interpretation that gelatin is incorporated into calcite crystals and that this incorporation is much more marked as the hydrogel gets heavier.

Thermogravimetric analyses (TGA) and differential analyses (DTA) of calcite samples grown in hydrogels with different gelatin solid content also supported the incorporation of small amounts of organic hydrogel into the calcite crystal aggregates (Figure S3). This amount varied as a function of the gelatin concentration in the hydrogel, being extremely small, around 0.2 mass %, for crystals grown in hydrogels with 2.5 wt % gelatin. It increased to 0.9 and 1.5 mass % for crystals formed in hydrogels with 5 and 10 wt % gelatin contents, respectively. These values are consistent with the 1.9 mass % of gelatin content determined by TGA in calcite mesocrystals grown at 25 ºC in a gelatin hydrogel with a 10 wt % gelatin solid content[19(19)] and are similar to the estimated amount of organic hydrogel network (0.7 mass %) incorporated into calcite grown in a poly-acrylamide hydrogel[16].

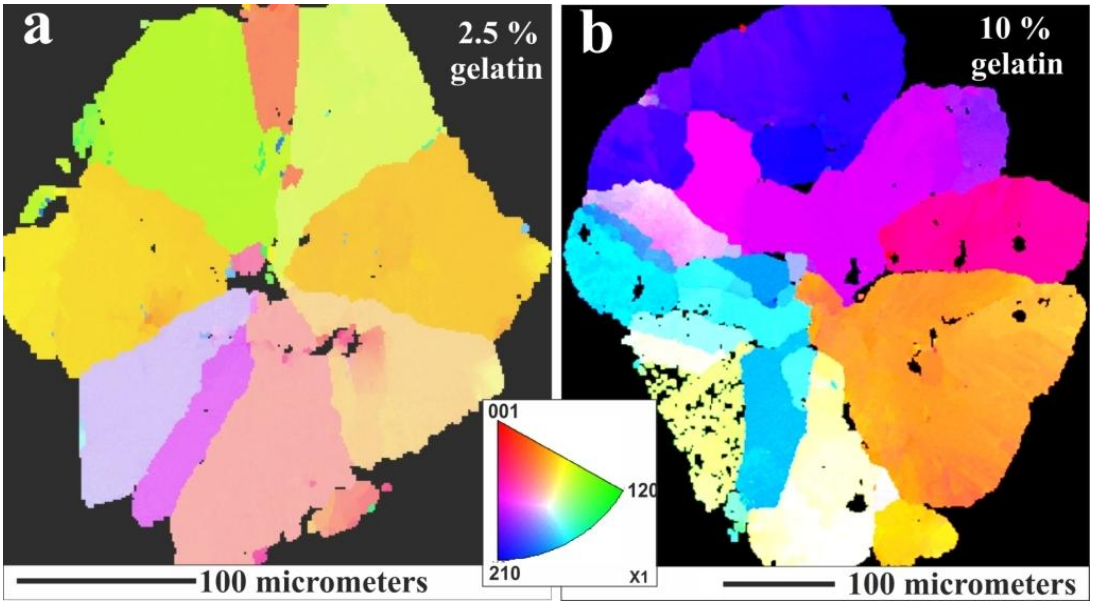

Figure 6. Difference in the degree of mosaicity of crystals composing a crystal aggregate grown in hydrogels with 2.5 wt % and 10 wt % gelatin solid contents. While the ~ 100 µm sized crystals composing the aggregate grown with 2.5 wt % gelatin content show very little internal structuring (6a), all crystals composing the aggregate grown with a gelatin content of 10 wt % (6b) display an increased internal substructuring (mosaic structure).

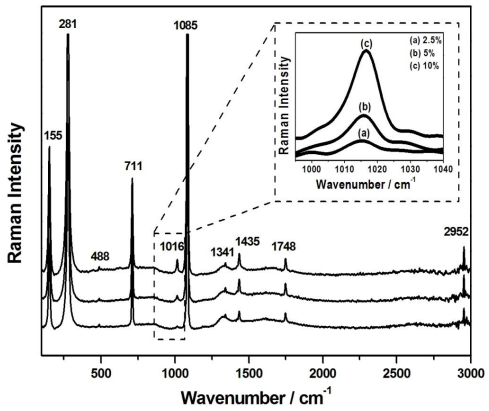

Figure 7. Raman spectra of three calcite samples grown in gelatin hydrogels with different gelatin solid content. The inset highlights the increasing intensity of the band at 1016 cm^{-1} as the gelatin solid content in the hydrogel increases. Raman spectrum of the powdered skin pork gelatin used to prepare the hydrogels is provided as Supporting Information, Figure S2.

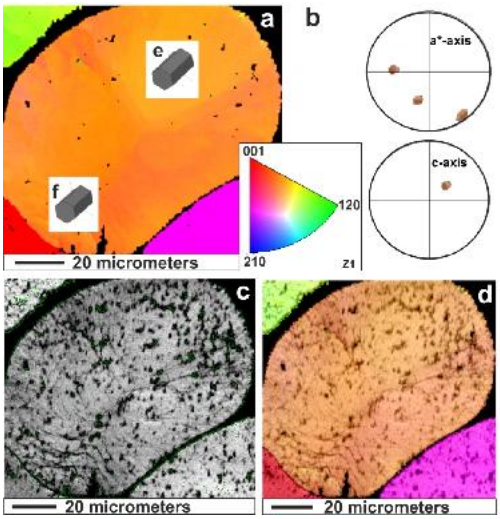

Figure 8. The mosaicity and hybrid composite constitution of a crystal in an aggregate grown from a hydrogel with 10 wt % gelatin. Figure 8a color coded EBSD map and corresponding pole figure (8b). The band contrast image (Figure 8c) of the crystal highlights the incorporation of gelatin. Map 8d shows superimposed color coded orientation and band contrast. Figures 8e and 8f show the difference in the two major orientations that are encountered in this crystal.

Details on the characteristics of TGA/DTA analyses of the different calcite samples can be found in Supporting Information, Figure S3.High-resolution EBSD allows the investigation of crystallite and particle arrangement with a spatial resolution in the sub-micrometer scale range.[59-60] Figure 8 shows one crystal in an aggregate grown in a hydrogel with 10 wt % gelatin. Well visible in the band contrast map of Figure 8c are traces of incorporated gelatin. These appear as grey lines and green and black dots within the crystal. The variation of

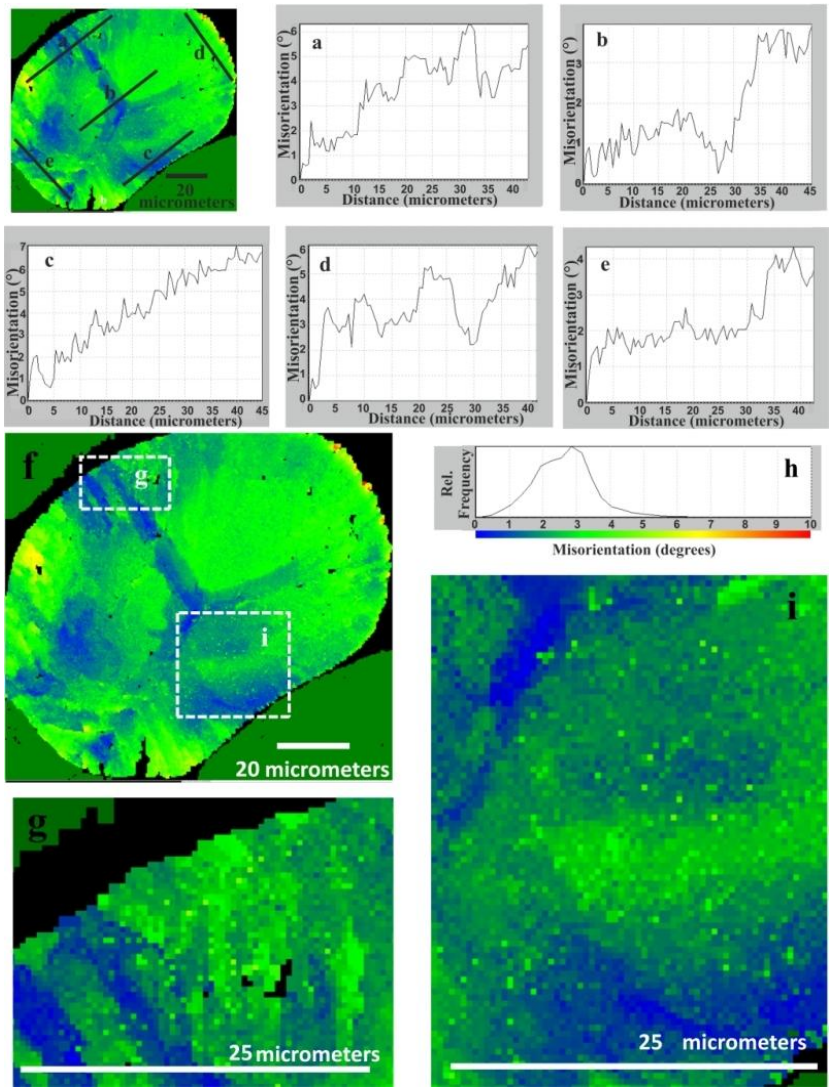

Figure 9. Profile lines showing local misorientation versus position within a crystal in a crystal aggregate grown in a hydrogel with 10 wt % gelatin content (Figures 9a to 9e). In figure 9f-i internal misorientation is displayed as color coded maps and overall statistics (histogram h) over the complete crystal shown in f. The misorientation between microscale mosaic blocks composing the crystal reaches up to 6 degrees. Note also the mesocrystal-like constitution indicated by the pixel-to-pixel misorientation shown in the enlarged regions g and i; EBSD pixel (step) size is 400 nm, experimental orientation resolution ± 0.3°.

colors (which code for crystal orientation) in Figure 8a and 8d clearly indicates that the crystal is composed of a multitude of mosaic blocks, each having a slightly different orientation (Figures 8a, e, f). For the same crystal Figure 9 highlights calcite misorientation variations along five trajectories within the crystal (Figure 9a-e) and displays the overall statistics of internal misorientation of all measured EBSD pixels with respect to the average orientation of this particular crystal (Figure 9h). The misorientation in degrees also defines the color scale of the maps. Misorientation in the crystal ranges up to 6 (Figure 9h). It is not evenly distributed. In the center of the crystal, the orientation happens to be identitcal to the average orientation (blue colors), while misorientation generally increases towards the rims. The misorientation profiles (Figure 9a-e) indicate that misoriented mosaic blocks exist on the scale of tens of micrometers down to one micrometer or below. The microscale mosaic blocks are usually separated by sharp small-angle boundaries associated with steps in the misorientation profiles. Moreover, a close inspection by zooming into local areas of the map (e.g. 9g, i) reveals a misorientation mosaic structure on the length scale of the 400 nm step-size of the present EBSD measurement (i.e. the pixel size in the maps of Figure 9f, g, i). Accordingly, the crystal is constituted of an array

of nanocrystallites which are imperfectly co-oriented. We may speculate that the imperfect co-orientation of the nano-building-blocks is related to the presence of incorporated gel matrix not only - as visible in Figure 8 - on the microscale but also on the nanoscale (Figure 9). Such a structure has been described as mesocrystalline (cf. Seto et al.[22] for the definition of a mesocrystal). The mesocrystal architecture allows continuous orientation gradients as can be seen in Figure 9c. Crystallite size estimation from XRD line broadening is given in Table S1 and it supports the mesoscale structure on a length scale consistent with the EBSD observation.

Figure 10 compares the internal microscale mosaicity within the crystals composing a crystal aggregate grown in a hydrogel with 2.5 wt % and 10 wt % gelatin content, respectively. Well visible is the difference in internal structuring as well as internal misorientation. In the calcite grown in a hydrogel matrix with 10 wt % gelatin the overall mosaic spread is more than three times as high (up to 6 degrees) as the internal misorientation (about 1 degree) within the calcite of a crystal aggregate grown in a hydrogel with 2.5 wt % gelatin. These results clearly show the effect of gelatin content of the hydrogel matrix on $CaCO_3$ crystallization and crystal aggregate formation. Note the almost dendrite-like, branching mosaic structure in the sample from the gel with 10 wt % gelatin.

Physicochemical conditions at early crystallization stages. Table 2 summarizes the measured pH, Ca^{2+} and CO_3^{2-} concentrations for the diffusion experiments conducted with only one ion species for the estimation of the supersaturation at the experimental waiting time in the portion of the gel column where the first optically visible crystals were detected. Table 2 gives the calculated activities and nominal supersaturation levels with respect to calcite. The nominal supersaturation is based on the assumption that no crystals or solid precursor phases are present. It is expressed in terms of the saturation index (SI) according to: $SI = \log(\Omega) = \log (IAP/K_{sp})$, where ion activity product (IAP) is the product of the activities of the reacting ions (in this case, Ca^{2+} and CO_3^{2-}) powered to their stoichiometric number in the solid formula, K_{sp} (thermodynamic solubility product) is the value of IAP at thermodynamic equilibrium, and $\Omega = IAP/K_{sp}$ is the saturation state. The saturation indexes were calculated from pH and analytical chemical data of the aqueous solutions using PHREEQC3.0 and the PHREEQC.DAT database, in which the K_{sp} for calcite at 15 ºC is 10^{-8} [3].

As it can be seen from Table 2, at the early stages of crystallization, increasing levels of supersaturation of the aqueous solution in the pores must be expected with increasing concentrations of gelatin in the hydrogel unless an invisible precursor forms and buffers the supersaturation. Even though for all three cases the calculated nominal supersaturation is very high compared to situations where calcite forms in free solutions, it becomes extreme when the gelatin content in the hydrogel is 5 and 10 wt %, respectively. At these stages the nominal saturation state values are more than ten times higher than in hydrogels with 2.5 wt % gelatin at the time when the first, optically visible calcite crystals are detected.

Discussion

Our results show that the solid content of the gelatin hydrogel has a slight influence on $CaCO_3$ polymorph selection, with calcite being the main component of the precipitate in all the cases and vaterite representing about 40 % of the precipitate in 2.5 wt % gelatin hydrogels and only 10 % in 10 wt % gelatin hydrogels. Since the crystals grow against the hydrogel structure, the influence of the solid content of the gel becomes obvious from the size and morphology of the obtained crystals. The crystals become progressively smaller and have rougher surfaces as the solid content in the hydrogel increases. Moreover, higher solid contents in the hydrogel correlate with increasing imperfection in crystalline constitution on (at least) three length scales: (i) a mesocrystal architecture with increasing imperfection in the precise co-alignment of the constituting nanoscale units, (ii) a microscale intra-crystalline mosaic structure with subgrains separated by small-angle boundaries or - occasionally - smooth continuous orientation gradients, and (iii) the formation of radial aggregates of crystals on the scale of tens to hundreds of micrometers. For the gel with 2.5 wt % gelatin the ~ 100 µm sized crystals constituting the aggregate still show some degree of mutual co-alignment, while for the gel with 10 wt % gelatin a co-orientation can no longer beobserved. In order to understand these findings it is necessary to investigate how an increase in the solid content of the hydrogel affects the physicochemical conditions of the fluid where crystallization occurs.

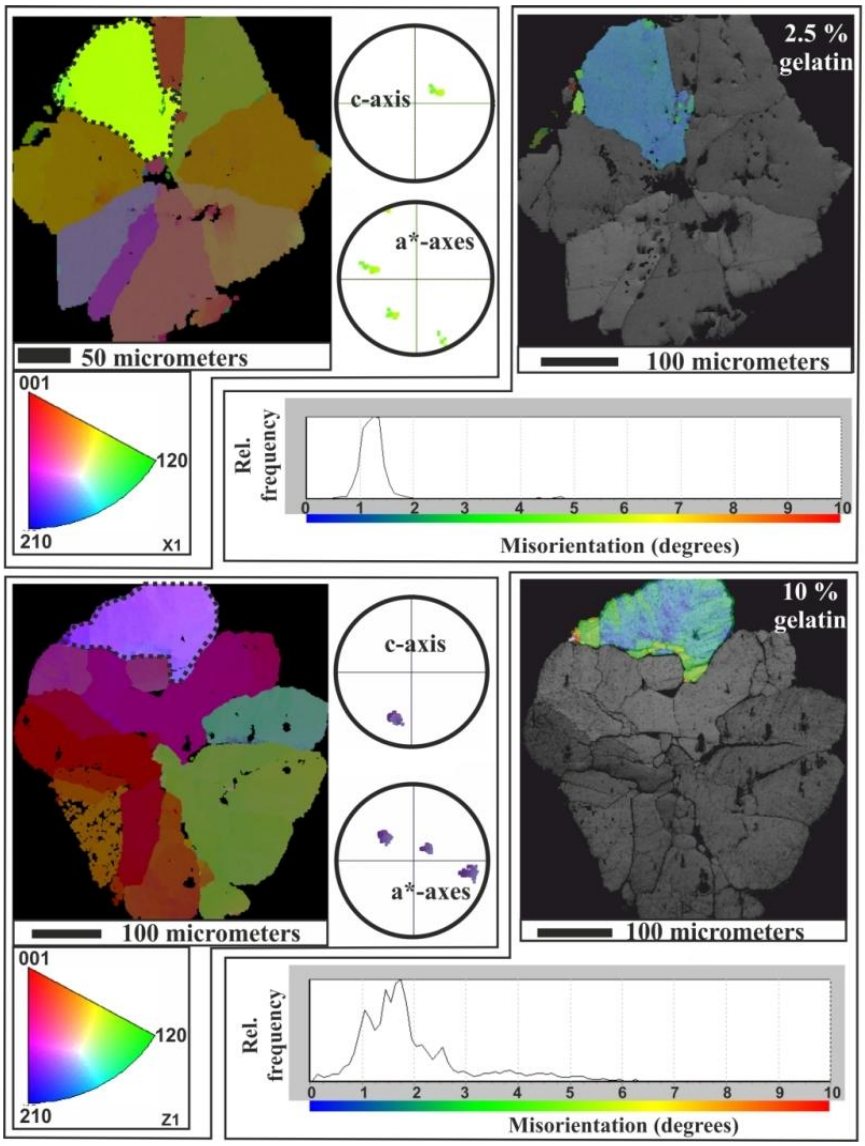

Figure 10. The effect of hydrogel gelatin content on the degree of calcite misorientation in the crystals composing a crystal aggregate grown in a hydrogel with 2.5 wt % and 10 wt % gelatin content, respectively. The mosaic spread (misorientation) in the crystals composing a crystal aggregate that grew in a hydrogel with 10 wt % gelatin is more than three times as high as that of crystals composing a crystal aggregate that grew in a hydrogel with 2.5 wt % gelatin. Note the branching, almost dendrite-like mosaic blocks which are separated by small angle grain boundaries in the misorientation map.

Table 2. Summary of the fluid chemistry in the hydrogel pores at experimental waiting time of the first visible crystal: pH, total concentration of calcium and carbonate ($[Ca^{2+}]$, $[CO_3^2]$) in mmol/L, activity of calcium and carbonate ions (aCa^{2+}, aCO_3^{2-}), and saturation index and saturation state with respect to calcite (SI_{Cal} and Ω_{Cal}, respectively).

Gelatin Solid wt %	Content	pH	$[Ca^{2+}]$ mmol/L	$[CO_3^2]$ mmol/L	aCa^{2+} (x10^{-4})	aCO_3^{2-} (x10^{-2})	SI_{Cal}	Ω_{Cal}
2.5 %		9.64	5.10	42.47	2.66	1.137	2.9	794
5 %		9.84	48.02	97.24	17.03	2.022	3.9	7943
10 %		10.01	50.31	116.25	15.96	2.365	4.0	10000

Physicochemical conditions at early stages of crystallization. In hydrogels, nucleation and early stages of crystallization occur in confined solutions, within the volume of a pore. In this type of systems the concentration of the reagents, the pH and the supersaturation continuously evolve in time and space It has been demonstrated that this evolution depends on the boundary conditions[61-62], i.e. the initial concentration of the reagents in the deposits and the length of the diffusion column. Furthermore, it has been stated that the characteristics of this evolution control the supersaturation at which nucleation (of whichever phase) occurs.[54-55] This supersaturation is referred to as the threshold supersaturation. While in the case of crystallization from free aqueous solution the critical supersaturation, i.e. the supersaturation at which nucleation rate reaches 1 $cm^{-3}s^{-1}$, has a single value for a given system,[63] the threshold supersaturation, which applies to systems where supersaturation is a function dependent on both time and space, has different values depending on the supersaturation rate (R_β), i.e. the rate at which the system moves from equilibrium.[64] It has been demonstrated that higher concentrations of the counter-diffusing reagents and shorter lengths of the diffusion column result in nucleation occurring under higher supersaturation levels, i.e. lead to higher values of the threshold supersaturation.[65-66] The reason underlying this behavior is a faster change in the concentration profiles along the gel column and, consequently, a higher supersaturation rate.

In the crystal growth experiments conducted in this study, both, the concentration of the reagents and the length of the gel column were identical. The optically first visible crystals corresponded to calcite, and the time needed to form them increased significantly with increasing concentration of gelatin in the gel.

A possible explanation for the increase of waiting time by a factor of five between the 2.5% and the 10% gelatin gel may be a reduced diffusion rate in the denser gels. The diffusion coefficient in the gel (D_g) relates to the diffusion coefficient in water (D_w) by the expression:

$$D_g = D_w (\varphi/\tau^2) \qquad (1)$$

where φ and τ are the porosity and the effective tortuosity of the hydrogel, respectively.[67] An increase in the solid content of a hydrogel correlates with a decrease of its total porosity and necessarily induces a decrease of the diffusion coefficients compared to those in water. This effect can be enhanced if higher solid contents also determine more complex porosity structures and, consequently, higher tortuosity, for instance, by generating isolated pores, dead-end pore paths, etc. This is the case in gelatin hydrogels, where a more complexly organized porosity appears as the gelatin content in the hydrogel increases. Both, the lower percentage of porosity and the more complex structure of the porosity will lead to lower diffusion coefficients. Consequently, the counter-diffusion of the reagents must occur at lower rates in hydrogels with higher gelatin contents and, as a result, longer diffusion times should be required to reach identical supersaturation (of whichever phase) in the different gels. To test this hypothesis we conducted the single-component diffusion experiments (with either Ca^{2+} or HCO_3^-, respectively) in the different gels. The result, however, clearly contradicts the hypothesis of a diffusion-related delay. Given the measured waiting times, the diffusion through the gel column clearly delivered much larger amounts of Ca^{2+} and HCO_3^- to the location of crystallization at early stages of calcite formation, than in the gel with less gelatin. For the denser gels, the calculated calcite nominal supersaturation from the ionic concentrations at the early stage of calcite crystallization is even more than ten times higher than for the gel with 2.5% gelatin (Table 2). None of the gels showed any sign of turbidity. Turbidity would have been a clear sign for the formation of a finely dispersed precursor[48-50] which, if present, would provide a sink for the calcium carbonate in solution. The absence of turbidity, however, does also not rule out the presence of dilute nanoscale precursor particles,

The experiments with higher gelatin contents lead to much more disordered structures of the calcite aggregates (with respect to a perfect single crystal). According to the nominal supersaturation data, the early stages of calcite crystallization take place significantly farer away from equilibrium conditions as the gelatin content in the hydrogel increases. Therefore an important influence of the gel structure on the nucleation and growth of the calcite must be concluded. Either, the denser gel structure leads to a dramatical increase of the critical supersaturation for calcite formation, and/or it induces a dramatical increase in the formation of a nanometric solid precursor. For the latter, however, we see no evidence so far.

In order to explain the potential effect of the gel solid content on supersaturation at early crystallization stages other characteristics of the porosity than its complexity and influence in diffusivity have to be considered. A most relevant feature of porosity is the size of the pores. In

gelatin hydrogels this size clearly decreases as the solid content increases, mainly due to the increase of the pore wall thickness and the formation of sub-pores within bigger pores. Nucleation and early crystallization stages in gels occur in the bulk of aqueous solutions confined in the volume of pores. It has been demonstrated that diminishing the pore size in silica gel and gelatin lowers the nucleation probability.[65,68-69] This can be easily explained considering that nucleation occurs as a result of fluctuations that bring together a sufficiently large number of ions to exceed the critical size.[70] In the case of sparingly soluble phases such as calcium carbonate polymorphs, the number of ions in a given volume is small even if supersaturation is high. Diminishing the volume of solution cells makes this number smaller and, consequently, nucleation less probable. This consideration is further supported by the fact that the number of visible crystals at the waiting times specified in Table 1 decreases significantly with increasing gelatin content of the hydrogels. We thus conclude that higher supersaturation levels are required for crystallization from solutions confined to smaller pores. An increase of the supersaturation increases the number of ions available in the volume of a small pore, facilitating the nucleation process.

Crystallization process. As explained above, higher gelatin contents in the hydrogels correlate with a lower number of calcite crystals per volume of hydrogel, smaller crystal sizes and a predominance of spherulitic aggregates with respect to single crystals in the precipitates. Crystallization occurring at significantly higher supersaturation can explain the variation in the crystal sizes and the predominance of aggregates as the hydrogel gets heavier.

It is notorious that crystallization in hydrogels always occurs under high (at least nominal) supersaturations.[40,42,65-66,71] Under these conditions neither nucleation nor growth follows classical paths. Non-classical nucleation can lead to the formation of amorphous or metastable phases.[72] Although the formation of a nanometric phase prior to calcite in these experiments cannot be confirmed nor discarded by our experiment, calcite, the stable $CaCO_3$ polymorph at 15 ºC, was always the main component of the precipitate and the first phase that was optically detected. Moreover, the amount of vaterite found was higher in the precipitate formed in the hydrogel with the lower gelatin content, i.e. where nominal supersaturation at early crystallization stages should be lower. The reason for the formation of this higher amount of vaterite in the later stages of crystallization in lighter gelatin hydrogels and its inhibition in heavier hydrogels are unclear and cannot be connected to an effect of the supersaturation parameter.

The classical layer by layer growth mechanism, which involves the integration of atoms or molecules onto energetically favorable sites on crystal surfaces,[73-74] is not likely to be efficient when mass transfer is limited, the aqueous solution is confined in the small volume of pores and supersaturation is very high. Moreover, the peculiar characteristics of the calcite crystals grown in hydrogels with high gelatin content cannot really be explained by a layer by layer growth mechanism. In this case an alternative scenario can be contemplated. It is generally accepted[1,16,25,27] that under these conditions (solution confined in small pores and high supersaturation) crystal growth occurs through a specific mechanism involving the oriented attachment of short-range ordered (subcritical) clusters due to dipolar forces.[75-78] The presence of large amounts of these clusters would also reduce the activity of the calcium and carbonate ions and hence the supersaturation compared to the nominal supersaturation which we calculated from the results of the single-component diffusion experiments. The driving force for, particle attachment would be the reduction of the surface free energy that results from the crystallographic fusion of aggregated nanoparticles.[1,16-19,23,37] This aggregation mechanism leads to the formation of an assembly of nanometric basically equally-oriented sub-blocks. This mechanism can therefore explain the characteristics of the calcite crystals obtained in this work in hydrogels with gelatin contents ≥ 5 wt %. During the aggregation process a small amount of hydrogel is incorporated in between the assembled nanoparticles. This amount directly relates to the concentration of gelatin solid in the hydrogel and the increased thickness of the hydrogel pore walls. Larger incorporations may also be favored by both higher viscosities and supersaturations in the growth medium. The characteristics of calcite crystals formed in hydrogels with 2.5 wt % gelatin content does not support the idea that aggregation played a dominant role in their growth. These crystals also grew under high supersaturation, although it is not as high as that for the crystals formed in hydrogels with gelatin contents ≥ 5 wt %, and incorporated some gelatin. Our results point to the switch from classical to non-classical growth mechanisms depending on subtle relationships between supersaturation, growth medium viscosity and hydrogel incorporation during

growth.

It is important to know that the dipolar forces involved in the oriented attachment of crystal sub-blocks strongly vary with distance. Consequently, mesocrystals formed in more viscous, thicker wall-pored hydrogels should show a less perfect co-orientation of their nanometric building blocks. This is consistent with our EBSD observations, which show that the mosaic spread within calcite crystal individuals grown in hydrogels with 10 wt % gelatin content is almost twice as high as that measured in calcite crystals formed in hydrogels with 2.5 wt % gelatin.

It is also interesting that the mosaic spread measured within crystal individuals grown in 10 wt % gelatin hydrogels is not homogeneous but increases from core to rim. To attain a perfect co-alignment of the nanoparticles the hydrogel has to be expelled from in between the particles. This process will necessarily involve the deformation of the hydrogel pore walls as they are squeezed by the attaching particles and it will give an increase of the viscosity of the growth medium at the front of the growing mesocrystal aggregate, as the hydrogel is expelled from inner to outer regions. The direct consequence is a higher hydrogel incorporation in the rim region of the crystal aggregates, which in turn leads to the higher particle misorientation in the rim in comparison to that in the core of the mesocrystals, as evidenced by the EBSD measurements.

Conclusions

$CaCO_3$ was crystallized in gelatin hydrogels with different solid contents. Our results show that this parameter strongly influences the crystallization of carbonate crystals. Regarding early stages of crystallization, the nominal supersaturation markedly increased with the gelatin content of the hydrogel. However, this parameter had little effect on the $CaCO_3$ polymorphic selection, with the precipitate always consisting of mainly calcite. Regarding the characteristics of calcite crystals, we observed that with increasing gelatin concentrations in the hydrogel the calcite (1) showed smaller crystals sizes, rougher surfaces, more complex growth morphologies and a tendency to develop as crystal aggregates rather than as single crystals, (2) incorporated increasing amounts of gelatin during their growth, and (3) showed an increasing degree of internal structuring with an orientational mosaic spread that increases rapidly with increasing gelatin concentration of the hydrogel. For low gelatin concentrations we find a certain degree of mutual co-alignment of the ~ 100 μm sized crystals forming the macroscopic (submillimeter) aggregates, while for 10 wt % gelatin concentration in the gel a spherulite-like radial configuration of the macroscopic aggregates prevails. The internal mosaic structure within the individual crystals of the aggregates comprises both microscale mosaic blocks separated by small-angle boundaries as well as an underlying mesocrystalline structure: the microcrystals are built of imperfectly co-aligned nanoscale units.

The influence of the hydrogel solid content on the crystallization process and the characteristics of calcite crystals arises from changes in hydrogel porosity characteristics. The changes in porosity (1) induce changes in the diffusivity and, in turn, in the evolution of the physicochemical conditions of the gel during counterdiffusion, (2) they affect the early stages of crystallization by varying the volume of aqueous solution available within the hydrogel pores, (3) they induce the transition from a classical layer-by-layer crystal growth mechanism to an aggregation mechanism as the hydrogel becomes more viscous, thereby promoting the formation of mesocrystals.

Acknowledgements. This research is part of the German-Spanish joint Acciones Integradas program (AIB2010 DE-0008), DAAD-50749739. F.N. is grateful for a stipendium by KAAD. E.G. is supported by Deutsche Forschungsgemeinschaft, DFG grant number GR-1235/9-1. This research was partially funded by project CGL2010-20134-C02-01 (MECC-Spain). We are indebted to Sabino Veintemillas-Verdaguer (ICMM, CSIC) for his advice and help in the characterization of the hydrogel porosity. We sincerely thank Eugenio Baldonedo from the National Microscopy Centre (ICTS), Emilio Matesanz from the X-ray Diffraction Central Service, and the staff from the Laboratory of Geochemistry and Environmental Analysis of the Complutense University (UCM) for technical support and assistance. We are also grateful to Laura Tormo and Cristina Paradela for enabling Raman measurements at the MNCN, CSIC (Madrid, Spain).

References

(1) Meldrum, F.; Cölfen, H. *Chem. Rev.* **2008**, *108*, 4332-4432.
(2) Asenath-Smith, E.; Li, H.; Keene, E. C.; Seh, Z. W.; Estroff, L. A. *Adv. Funct. Mater.* **2012**, *22*, 2891-2914.

(3) Kobayashi, I.; Samata, T. *Mater. Sci. Eng.* **2006**, *26*, 692-698.
(4) Falini, G.; Albeck, S.; Weiner, S.; Addadi, L.; *Science* **1996**, *271*, 67-69.
(5) Cusack, M.; Freer, A. *Chem. Rev.* **2008**, *108*, 4434-4454.
(6) Griesshaber, E.; Schmahl, W. W.; Neuser, R.; Pettke, T.; Blüm, M.; Mutterlose, J.; Brand, U. *Am. Mineral.* **2007**, *92*, 722-734.
(7) Levi-Kalisman, Y.; Fallini, G.; Addadi, L.; Weiner, S. *J. Struc. Biol.* **2001**, 135, 8-17.
(8) Zhou, J.; Zhou, M.; Caruso, R. A. *Langmuir* **2006**, *22*, 3332-3336.
(9) Kim, U.; Park, J.; Li, C.; Jin, H.; Valluzzi, R.; Kaplan, D. L. *Biomacromolecules* **2004**, *5*, 786-792.
(10) Xie, M.; Olderøy, M. Ø.; Andreassen, J. P.; Selbach, S. M.; Strand, B. L.; Sikorski, P. *Acta Biomaterialia* **2010**, *6*, 3665-3675.
(11) Annabi, N.; Nichol, J. W.; Zhong, X.; Ji, C.; Koshy, S.; Khademhosseini, A.; Dehghani, F. *Tissue Eng.* **2010**, *16*, 371-383.
(12) McCauley, J. W.; Roy, R. *Am. Mineral.* **1974**, *59*, 947-963.
(13) García-Ruíz, J. M.; Amorós, J. L. *J. Cryst. Growth* **1981**, *55*, 379-383.
(14) Fernández-Diaz, L.; Putnis, A.; Prieto, M.; Putnis, C. V. *J. Sediment. Res.* **1996**, *66*, 482-491.
(15) Grassmann, O.; Muller, G.; Löbmann, P. *Chem. Mater.* **2002**, *14*, 4530-4535.
(16) Grassmann, O.; Neder, R. B.; Putnis, A.; Löbmann, P. *Am. Mineral.* **2003**, *88*, 647-652.
(17) Grassmann, O.; Löbmann, P. *Chem. Eur. J.* **2003**, *9*, 1310-1316.
(18) Sethmann, I.; Putnis, A.; Grassmann, O; Löbmann, P. *Am. Mineral.* **2005**, 90, 1213-1217.
(19) Huang, Y.; Buder, J.; Cardoso-Gil, R.; Prots, Y.; Carrillo-Cabrera, W.; Simon, P.; Kniep, R. *Angew. Chem. Int. Ed.* **2008**, *47*, 8280-8284.
(20) Yuwono, V. M.; Burrows, N. D.; Soltis, J. A.; Penn, R. L. *J. Am. Chem. Soc.* **2010**, 132, 2163–2165.
(21) Song, R.-Q.; Cölfen, H. *Adv. Mater.* **2010**, 22: 1301–1330
(22) Seto, J.; Ma, Y.; Davis, S. A.; Meldrum, F.; Gourrier, A.; Kim, Y-Y.; Schilde, U.; Sztucki, M.; Brughammer, M.; Maltsev, S.; Jäger, C.; Cölfen, H. *PNAS* **2012**, 109, 3699-3704.
(23) Cölfen, H.; Antonietti, M. *Angew. Chem. Int. Ed.* **2008**, 44, 5576-5591.
(24) Song, R-Q.; Cölfen, H. *Cryst. Eng. Comm*. **2011**, 13, 1249-1276.
(25) Gebauer, D.; Coelfen, H. *Nano Today* **2011**, 6, 564-584.
(26) Gebauer, D.; Völkel, A.; Cölfen, H. *Science* **2008**, 322, 1819-1822.
(27) Cölfen, H. *Nature Materials* **2010**, 9, 960-961.
(28) Dey, A.; Bomans, P. H. H.; Müller, F. A.; Will, J.; Frederik, P. M.; de With, G.; Sommerdijk, N. A. J. M. *Nature Material* **2010**, 9, 1010-1014.
(29) Demichelis, F.; Raiteri, P.; Gale, J. D.; Quigley, D.; Gebauer, D. *Nature Comm.* **2011**, 2, 1-8.
(30) Picker, A.; Matthias, K.; Seto, J.; Gebauer, D.; Cölfen, H. *Z. Kristallogr.* **2012**, 227, 744-757.
(31) Vielzeuf, D; Floquet, N; Chatain, D.; Bonneté, F.; Ferry, D; Garrabou, J.; Stolper, E. M. *Am. Mineral.* **2010**, 95, 242-248.
(32) Floquet, N.; Vielzeuf, D. *Cryst. Growth Des.* **2012**, 12, 4805–4820.
(33) Seidl, B. H**.;** Reisecker, C.; Hild, S.; Griesshaber, E.; Ziegler, A. *Z. Kristallogr.* **2012**, 227, 777-792.
(34) Kelm, K.; Goetz, A.; Sehrbrock, A.; Irsen, S.; Hoffmann, R.; Schmahl, W. W. *Z. Kristallogr.* **2012**, 227, 758-765.
(35) Schmahl, W. W.; Griesshaber, E.; Kelm, K.; Ball, A.; Goetz, A.; Xu, D.-Y. *Z. Kristallogr.* **2012**, 227, 604-611.
(36) Schmahl, W. W.; Griesshaber, E.; Kelm, K.; Goetz, A.; Guntram, J.; Ball, A. *Z. Kristallogr.* **2012**, 227, 793-804.
(37) Grassmann, O.; Löbmann, P. *Biomaterials* **2004**, 25, 277-282.
(38) Fernández-Díaz, L.; Astilleros, J. M. Pina, C.M. *Chem. Geol.* **2006**, *225*, 314-321.
(39) Hanying, L.; Estroff, L. A. *J. Am. Chem. Soc.* **2007**, *129*, 5480-5483.
(40) Sánchez-Pastor, N.; Gigler, A. M.; Cruz, J. A.; Park, S.-H.; Jordan, G.; Fernández-Díaz, L. *Cryst. Growth Des.* **2011**, *11*, 3081-3089.
(41) Dorwee, J. R.; Boskey, A. L.; Estroff, L. A. *Cryst. Eng. Comm. 2012*, *14*, 5681-5700.
(42) Helbig, U. *J. Cryst. Growth* **2008**, *310*, 2863-2870.
(43) Minchin, D. *Marine Biology* **1987**, *95*, 139-145.
(44) Hahn, S.; Rodolfo-Metalpa, R.; Griesshaber, E.; Schmahl, W. W.; Buhl, D.; Hall-Spencer, J. M.; Baggini, C.; Fehr. K. T.; Immenhauser, A. *Biogeosciences* **2012**, *9*, 1897-1914,
(45) Rijssel, M.; Giesken, W. W. C. *J. Sea Res.* **2002**, *48*, 17-27.
(46) Schouten, S.; Ossebaar, J.; Schreiber, K.; Kienhuis, M. V. M.; Langer, G.; Benthien, A.; Bijma, *J. Biogeosciences* **2006**, *3*, 113–119.
(47) Parkhurst D. L.; Appelo C. A. J. In User's Guide to PHREEQC, US Geological Survey Water Resources Investigations Report 99-

4259, US Geological Survey, Washington, DC. **1999**
(48) Wang, Y.-W.; Kim, Y.-Y.; Stephens, C. J.; Meldrum, F. C.; Christenson, H. K. *Cryst. Growth Des.* **2012**, 12, 1212−1217.
(49) Huang, S.-C.; Naka, K.; Chujo, Y. *Langmuir* **2007**, 23, 12086-12095.
(50) Loste, E.; Wilson, R. M; Seshadri, R.; Meldrum, F. C. *J. Cryst. Growth* **2003**, 254, 206–218.
(51) Rutt, H. N; Nicola, J. H. *J. Phys. C: Solid State Phys.* **1974**, *7*, 4522-4528.
(52) Gunasekaran, S.; Anbalagan, G.; Pandi, S. *J. Raman Spectrosc.* **2006**, *37*, 892-899.
(53) Soldati, A. L.; Jacob, D. E.; Wehrmeister, U.; Häger, T.; Hofmeister, W. *J. Raman Spectrosc.* **2006**, *39*, 525-536.
(54) Vandenabeele, P.; Moens, L.; Edwards, H. G. M.; Dams. R. *J. Raman Spectrosc.* **2000**, *31*, 509-517.
(55) Barnard, W.; Waal, D. *J. Raman Spectrosc.* **2006**, *37*, 342-352.
(56) Nelson, W. H.; Carey, P. R. *J. Raman Spectrosc.* **1981**, *31*, 326-328.
(57) Veronelli, M.; Zerbi, G.; Stradi, R. *J. Raman Spectrosc.* **1995**, *26*, 683.
(58) Fujimori, K.; Sakamoto, A.; Tasumi, M. *Macromol. Symp.* **2004**, *205*, 33-46.
(59) Goetz, A. J.; Steinmetz, D. R.; Griesshaber, E.; Zaefferer, S.; Raabe, D.; Kelm, K.; Irsen, S.; Sehrbrock, A.; Schamhl, W. W. *Acta Biomaterialia* **2011**, *7*, 2237–2243.
(60) Griesshaber, E.; Schmahl, W. W.; Ubhi, H. S.; Huber, J.; Nindiyasari, F.; Maier, B.; Ziegler, A. *Acta Biomaterialia* **2013**, in press.
(61) Henisch, H. K.; Garcia-Ruiz, J. M. *J. Cryst. Growth* **1986**, *75*, 195-202.
(62) Henisch, H. K.; Garcia-Ruiz, J. M. *J. Cryst. Growth* **1986**, *75*, 203-211.
(63) Walton, A.G. *Nucleation in liquids and solutions*; in Zettlemoyer, A.C., ed., Nucleation.; Marcel Dekker, 1969 pp. 225-307.
(64) Prieto, M.; Fernández-Díaz, L.; López-Andrés, S. *J. Cryst. Growth* **1991**, *108*, 770-778.
(65) Putnis, A.; Prieto, M.; Fernández-Díaz, L. *Geol. Mag.* **1995**, *132*, 1-13.
(66) Prieto, M.; Putnis, A.; Fernández-Díaz, L.; López-Andrés, S. *J. Cryst. Growth* **1994**, *142*, 225-235.
(67) Oelkers, E. H. *Rev. Mineral.* **1996**, *34*, 131-191.
(68) Halberstadt, E. S.; Henisch, H. K.; Nickl, J.; White, E.W. *J. Colloid Interfacial Sci.* **1969**, *29*, 469-471.
(69) Henisch, H. K. *Crystals in Gels and Liesegang Rings*; Cambridge University Press: Cambridge, 1988.
(70) De Yoreo, J. J.; Vekilov, P. G. *Rev. Mineral. Geochem.* **2003**, *54*, 57-93.
(71) Prieto, M.; Fernández-Díaz, L.; López-Andrés, S. *J. Cryst. Growth* **1989**, *98*, 447-460.
(72) Chernov, A. A. *Modern Crystallography III: Crystal Growth.* Springer: Berlin, Heidelberg, New York, Tokyo, 1984.
(73) Kossel, W. *Nachr. Ges. Wiss Göttingen, Math.-Physik. Kl.* **1927**, 135-143
(74) Burton, W. K.; Cabrera, N.; Frank, F. C. *Phil. Trans. Roy. Soc. London A* **1951**, 2*43*, 299-358.
(75) Niederberger, M.; Cölfen, H. *J. Phys. Chem.* **2006**, 8, 3271-3287.
(76) Lee, E. J. H.; Ribeiro, C.; Longo, E.; Leite, E. R. *J. Phys. Chem. B* **2005**, 109, 20842-20846.
(77) Zhang, Q.; Liu, S. H.; Yu, S. H. *J. Mat. Chem.* **2009**, 19, 191-207.
(78) Yao, Q. Z.; Guan, Y. B.; Fu, S. Q. *Eur J Mineral.* **2012**, 24, 519-526.

Supporting Informations

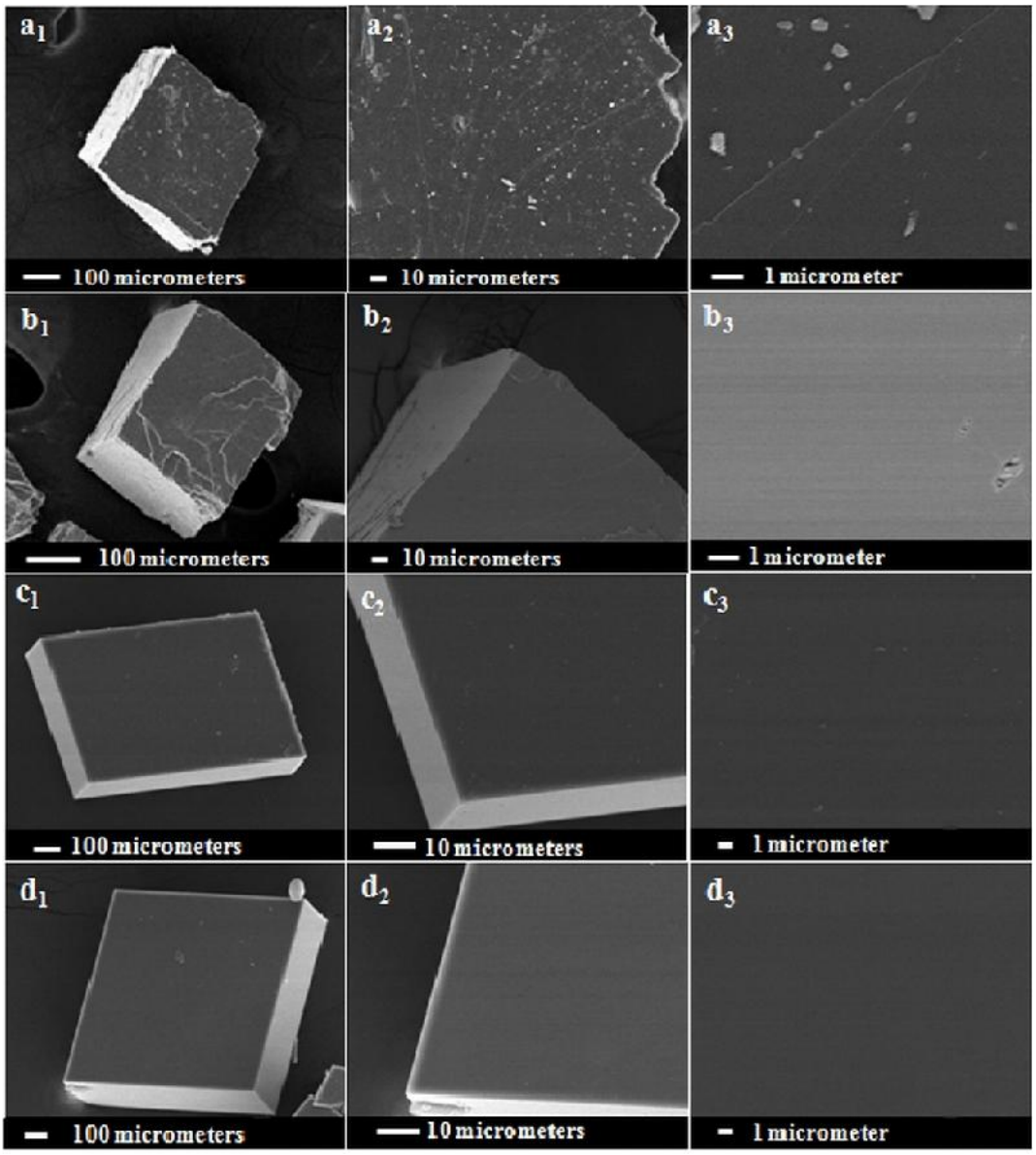

Figure S1. SEM images of crushed calcite crystals (a and b) and calcite crystals grown using the gas diffusion method (c and d). Figure a shows crushed calcite without any further treatment. Crushed calcite treated with hot water (60 °C) for 15 minutes is shown in Figure b. The calcite crystal grown by using the gas diffusion method (without any further treatment) can be seen in Figure c and with treatment (using hot water 60 °C) in Figure d. The treatment with hot water (60 °C) does not affect the dissolution of the crystal surface neither in the case of the crushed crystal nor when calcite is grown using the gas diffusion method.

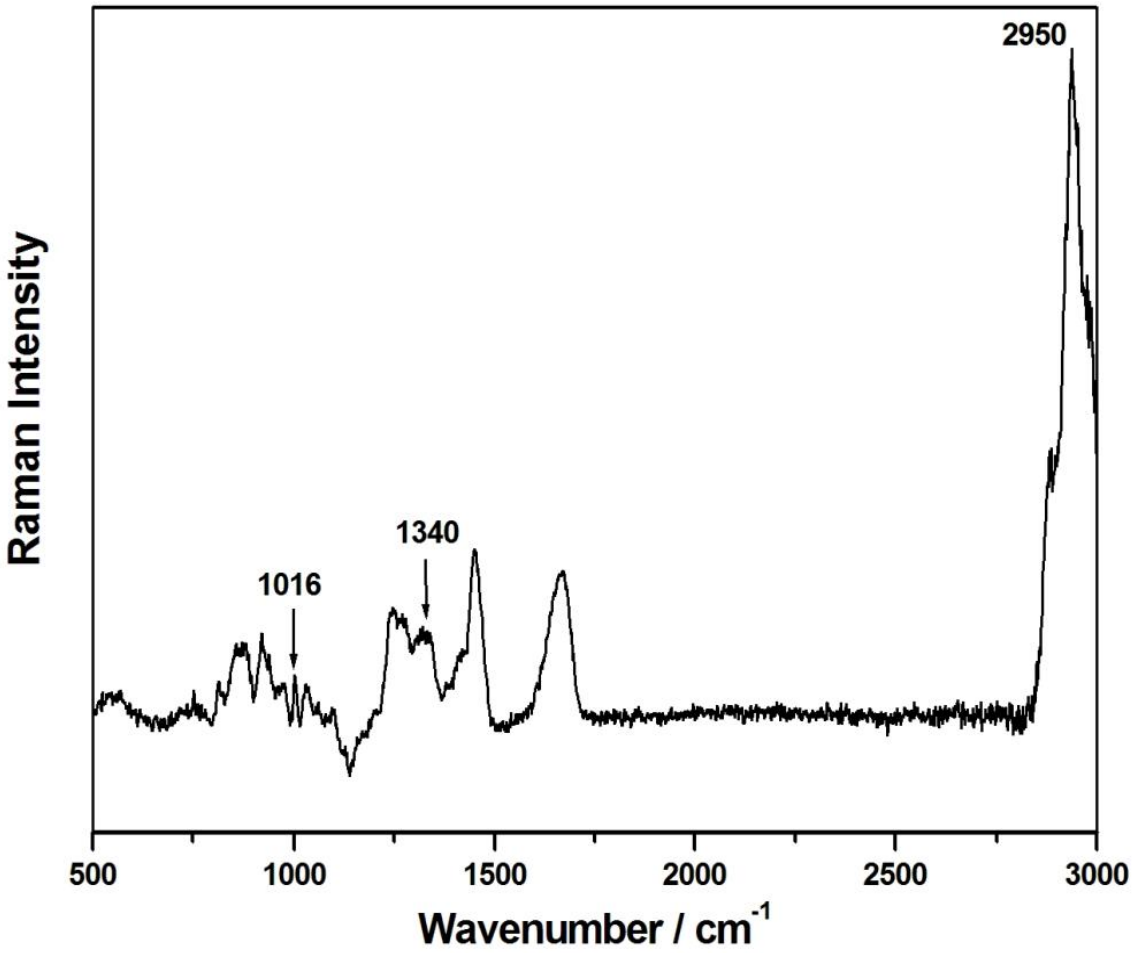

Figure S2. Raman spectrum of the powdered skin pork gelatin used to prepare the hydrogels.

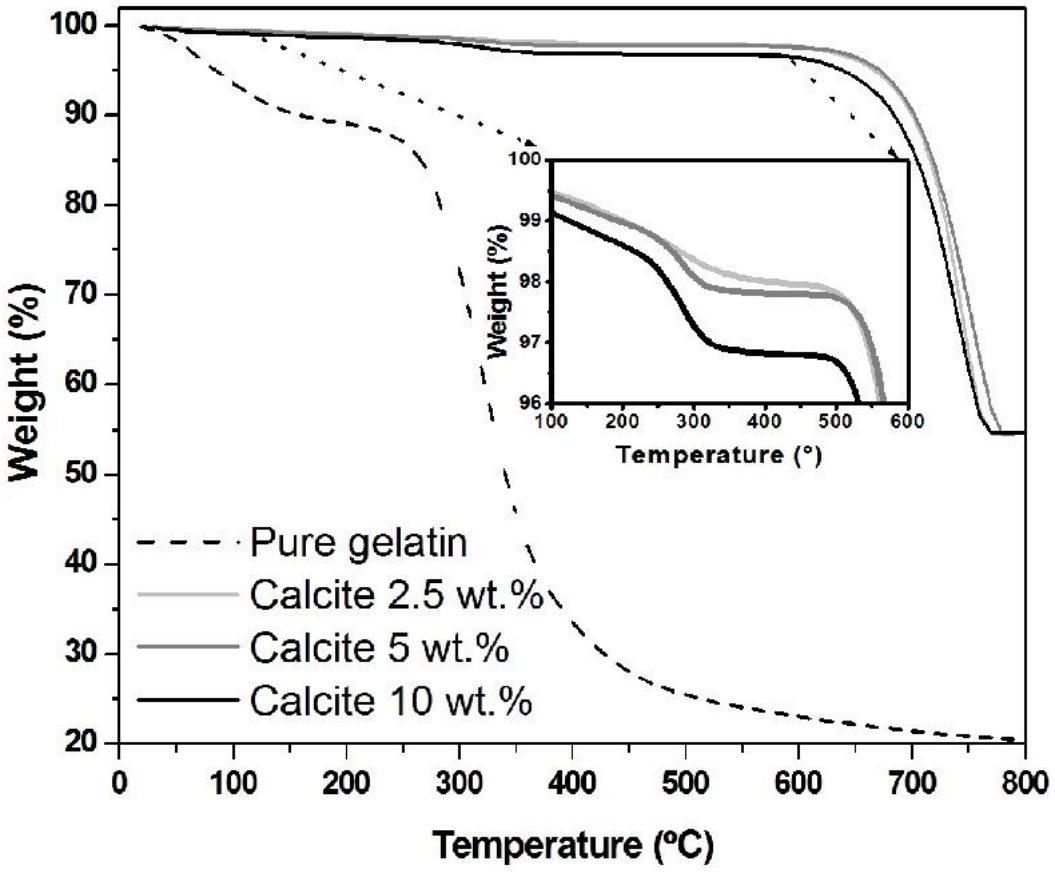

Figure S3. TGA curves of calcite aggregates grown in hydrogels with 2.5, 5 and 10 wt % gelatin content and the powdered skin pork gelatin used to prepare the hydrogels.

Table S1. A comparison of crystallite size determined from XRD and the Scherrer equation (without corrections for stress) to selected h k l reflections with the pixel-step of the EBSD measurement.

Gelatin 2.5 wt %	Pixel size measured with **EBSD**	Crystallite size determined from the **Scherrer equation**	FWHM (°)	Crystal plane
	1.2 µm	324 nm	0.025	(0 1 2)
		456 nm	0.018	(1 0 4)
		412 nm	0.02	(0 0 6)
		261 nm	0.032	(1 1 0)
		272 nm	0.031	(1 1 3)
Gelatin 10 wt %	Pixel size measured with **EBSD**	Crystallite size determined from the **Scherrer equation**	FWHM (°)	Crystal plane
	0.4 µm	238 nm	0.034	(0 1 2)
		228 nm	0.036	(1 0 4)
		201 nm	0.041	(0 0 6)
		238 nm	0.035	(1 1 0)
		196 nm	0.043	(1 1 3)

2.3 The effect of Mg and the hydrogel solid content on the crystallization of calcium carbonate in biomimetic counter-diffusion systems

Fitriana Nindiyasari[a], Erika Griesshaber[a], Lurdes Fernández-Díaz*[b,c], José Manuel Astilleros[b,c], Nuria Sánchez-Pastor[b], Andreas Ziegler[d], Wolfgang W. Schmahl[a]*

[a]Department für Geo- und Umweltwissenschaften, Ludwig-Maximilians-Universität, 80333 Munich, Germany.
[b]Departamento de Cristalografía y Mineralogía, Universidad Complutense de Madrid, 28040 Madrid, Spain.
[c]Instituto de Geociencias (UCM, CSIC). C/ José Antonio Novais 2, 28040 Madrid, Spain.
[d]Central Facility for Electron Microscopy, University of Ulm, Ulm, Germany.

Journal of Crystal Growth and Design 14, 4790-4802 (2014)

https://pubs.acs.org/doi/abs/10.1021/cg500938k

ABSTRACT: Carbonate biominerals are nanocomposites with an intimate association of organic and mineral components. Here we investigate the crystallization of $CaCO_3$ in gelatin hydrogels (2.5 and 10 wt % solid content) in the presence of Mg (0.01 M) in the growth medium. The precipitate consisted mainly of calcite in all experiments. A wide variety of morphologies and incorporated Mg contents (up to 26 mol % in sphere-like aggregates grown in 10 wt % gelatin) was observed. Etching experiments uncovered an intimate relation between the inorganic component and a polymeric network in the calcite crystal aggregates. The characteristics of this network varied for hydrogels with different solid contents. When Mg was not present in the growth medium, then we obtained 200nm – 1µm thick intercalations that were bordered at their two sides by a delicate gelatin network. Was Mg was added, then the intercalations became thin (about 50 -60nm) and the gelatin network at the side of the intercalation became compact. Electron backscatter diffraction (EBSD) evidenced that the calcite usually consists of aggregates of mutually misoriented crystals with internal mosaic spread. Crystals with high lattice co-orientation occur rather rarely, these are terminated by regular rhombohedral (104)-type faces. The irregular shaped and mosaic structured aggregates occasionally have a rim of such rhombohedral crystallites. In the experiment with 10 wt % solid gelatin content and Mg in the growth medium, the calcite consists of crystallites with fan-like small-angle misorientations (split growth), leading to spherulitic microstructures. We attribute these frequent and characteristic small-angle boundaries to dislocations relaxing misfit strain, which is associated with selective Mg-incorporation at acute growth steps. We ascribe our observations to the acidic functional groups of the gelatin promoting the desolvation of the hydrated Mg^{2+}-ions, leading to an increased incorporation of Mg into calcite, and a reduced inhibition of calcite nucleation and growth.

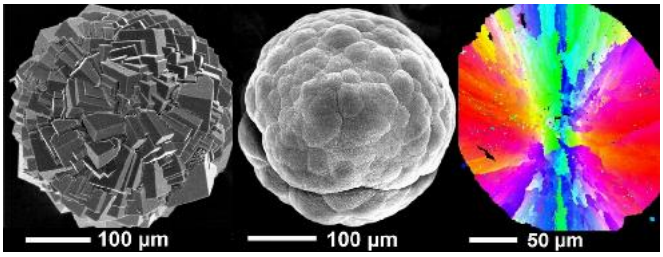

INTRODUCTION

Calcite, the stable $CaCO_3$ polymorph at Earth surface conditions, is one of the most abundant mineral constituents of mineralized tissues in both, fossil and modern organisms.[1-3] Magnesium is a very common additive to calcium carbonate biological hard tissues and occurs in a wide range of concentrations. Most common concentrations vary from about 0 to 23 mol % $MgCO_3$,[4] although magnesium contents as high 45 mol % $MgCO_3$ are found in the hard tissues of some organisms like sea urchin teeth.[5] Since different phyla incorporate Mg to a variable extent into their hard tissues [6-10], they are ranked into two major groups: low and high Mg carbonate producing organisms.[4] Echinoderms, corals and neritic benthic foraminifera belong to the high-Mg group, while planktonic foraminifera and brachiopods represent low-Mg biocarbonates, respectively. Mg in echinoderm skeletons shows the highest variation in Mg concentrations (4.8 to 15.9 mol % $MgCO_3$), oktocorals and neritic benthic

foraminifera have more or less comparable amounts of Mg in their skeletons (13.0 to 15.6 mol % MgCO, and 13.4 to 15.2 mol % $MgCO_3$, respectively), while planktonic foraminifera and brachiopods contain only between 0.23 to 0.96 mol % $MgCO_3$ and 0.69 to 9.4 mol % MgCO3, respectively.[4]

Hydrogel matrices are popular crystallization substrates for biomimetic crystallization since they can be fine tuned to adequately reproduce a wide range of biomineralization conditions.[2,11-14] Hydrogels have successfully been used to obtain synthetic mesocrystals of a variety of phases that are relevant to biological hard materials.[15-17] Major characteristics of hydrogel matrices such as diffusivity, composition of the aqueous phase filling the gel pores, presence of functional groups on pore walls are strongly variable and depend on the hydrogel in use [2,18-20] and the mode of hydrogel preparation. In a recent study we investigated the effect of hydrogels with varying gelatin contents on hydrogel porosity and crystallization of $CaCO_3$.[21] As the gelatin content was increased smaller-sized calcite crystal aggregates were obtained; these had progressively rougher surfaces and an increasing degree of misorientation in the mosaic structure of the mineral aggregate.[21]Numerous experimental results indicate that even low concentrations of magnesium in the growth medium strongly influence carbonate crystallization, inhibiting crystal nucleation, reducing the growth rate and modifying crystal morphology.[12-13,22-24] Moreover, high concentrations of magnesium in the growth medium lead to the switch of $CaCO_3$ polymorph selection from calcite to aragonite.[7,8,25] These effects have been partially explained as resulting from the hydration characteristics of magnesium and its preferential incorporation onto specific sites on the carbonate crystal surface.[26-32]

In the study presented here we aim to investigate the influence of magnesium-bearing gelatin hydrogels on carbonate crystallization with special attention to compositional, morphological and textural characteristics of the crystals, as well as the amount and mode of gelatin that is incorporated within the crystal aggregates and its crystal subunits. In the course of our experiments the content of Mg was kept constant to 0.01M Mg while the composition of the hydrogel was varied. We used hydrogels with 2.5 and 10 wt % gelatin contents, respectively. In order to highlight differences and similarities we juxtapose the observed morphologies, the organic-inorganic composite nature of aggregates, mode of aggregation and crystal orientation patterns of calcite grown in the two different gels, in the presence and absence of magnesium.

EXPERIMENTAL PROCEDURES

Crystal growth. Crystallization experiments were performed in a double diffusion system. The experimental set-up consists of two vertical branches separated by a 70 mm long column of gelatin hydrogel (diameter = 9 mm). The vertical branches were filled with 5 ml of the reagents, aqueous solutions of calcium chloride (0.5M $CaCl_2$; Sigma Aldrich) and sodium carbonate (0.5M Na_2CO_3; Sigma Aldrich), which were brought together by counter-diffusion through the porous structure of the hydrogel. The hydrogel was prepared by dissolving porcine gelatin (Sigma Aldrich; Type A, Bioreagent) in high purity deionized (MilliQ) water (18.2 MΩ) heated at 60 ºC. To prevent micro organisms' growth in the hydrogel prior to use all the glasswares were soaked in a 10 % (v/v) HCl solution for minimum 2 hours and then rinsed three times with deionized water. The hydrogels were prepared using two different contents of gelatin (2.5 and 10 wt %) and two solvents: water and an aqueous solution of 0.01 M $MgCl_2$. The gelification was carried out at 4 ºC during an hour. Subsequently, the hydrogels were set at 15 ºC for 24 hours before pouring the reagent solutions in the vertical branches. Crystallization of $CaCO_3$ eventually occurred within the gelatin hydrogel. The formation of the first crystals was detected optically by inspecting the hydrogel column under 400 x magnifications. The time that elapsed between the start of experiments and the detection of the first crystals is referred to as the experimental waiting time for first optically visible crystal (t_w). Table 1 summarizes the concentration of gelatin and Mg in the hydrogel, the composition of the counter-diffusing reagents, the experimental waiting time for the observation of the first optically visible crystal (t_w), the location of the first crystals in the column (distance measured from the $CaCl_2$ reservoir), the total number of crystals formed (NC) and the $CaCO_3$ polymorph (Cc = calcite), V = vaterite, A = aragonite) that was detected in each set of experiments. The number of crystals was measured 24 hours after the observation of the first visible crystal and corresponds to the crystals/aggregates observable with 400x magnification. Crystal growth was monitored by optical microscopy. The experiments were stopped one week after the first crystals were optically observed. The crystals were extracted

Table 1. Experimental waiting time for the first visible crystal (t_w), location of the first crystals in the gel column (distance measured from $CaCl_2$ reservoir), the total number of crystals (NC) measured 24 hours after the observation of the first crystal, and the $CaCO_3$ polymorphs detected in the experiment.

	wt% gelatin	[$MgCl_2$]	[$CaCl_2$]	[Na_2CO_3]	t_w (hours)	position (mm)	NC	Phases
E1	**2.5**	-	0.5 M	0.5 M	~24	32-35	98	Cc, V
E2	**2.5**	0.01 M	0.5 M	0.5 M	~76	35-38	62	Cc, A
E3	**10**	-	0.5 M	0.5 M	~120	38-41	21	Cc, V,A
E4	**10**	0.01 M	0.5 M	0.5 M	~148	37-40	16	Cc

by dissolving the slice of hydrogel where the precipitate was located in hot water (60 ºC). The precipitate was then filtered through a 1-µm pore size membrane, washed 3 times with hot Milli-Q water and dried at room temperature. The whole extraction procedure took ~ 15 minutes. The percentage of crystal aggregates corresponding to a given polymorph among the total forming the precipitate was determined after confirming the correspondence between mineral phase and morphology using Raman spectroscopy. The experiments were conducted at 15 °C in order to ensure the rigidity of the hydrogel columns during the experiments. This temperature within the range of common temperatures in shallow sea waters and therefore relevant to biomineralization processes.

Morphological and structural characterization of the crystals. The characteristics of the different phases obtained in the experiments were studied by Raman spectroscopy. Raman spectra of the samples were collected using a confocal Raman microscope (WITec alpha 300 R) equipped with a SHG Nd:YAG laser (532 nm, max. power 22.5 mW) and a lens-based spectrometer. Elastically scattered photons were rejected by a long pass filter, i.e. only the Stokes shifts were recorded. Using 600 mm^{-1} and 1800 mm^{-1} diffraction gratings, the spectral resolution was 3.5 and 1.2 cm^{-1} per CCD-pixel, respectively. Spectra were recorded at selected positions with an integration time of 1, 5, and 10 seconds and ten-fold averaging at 5 mW. A 100x microscope objective (working distance 0.26 mm, NA 0.90) was used for the measurements. On the samples, two areas were selected under the microscope and 2-3 spots were analyzed from each area.

Preparation of the crystals for SEM imaging, EDX and EBSD. The morphology and composition of the different phases were studied using a JEOL JSM 6400 Scanning Electron Microscope (SEM), equipped with an Oxford Instrument Energy Dispersive X-ray (EDX) detector. SEM imaging and EDX analysis of cut samples were performed using a Hitachi S5200 FE-SEM at 4 kV. The crystals were first embedded in EPON and were subsequently cut and polished with glass and diamond knives using a Leica Ultracut ultra-microtome. The incorporated gelatin matrices were exposed by etching the even crystal surfaces for 90 seconds with a HEPES (pH of 6.5) and a 2.5% glutaraldehyde solution. Etching was stopped by washing the samples 3 times for 10 minutes with 100% isopropanol. Subsequently the samples were critical point dried, coated with platinum nad imaged. EBSD measurements were performed on conventionally prepared sample surfaces. The crystals were embedded into epoxy-resin and were treated with several sequential mechanical grinding and polishing steps down to a grain size of 1 µm. The final step was etch-polishing with colloidal silica (particle size ~ 0.06 µm) in a vibratory polisher.

RESULTS

The influence of Mg on the crystallization process. In all experiments the first crystals were detected in the central, narrow region (3-5 mm wide) of the gel column. The amount of Mg in the growth medium strongly increased the experimental waiting time for the detection of the first visible crystals (t_w) but decreased the number of crystals formed (NC). The experimental waiting time varied from ~24 hours (E1) and ~120 hours (E3) in the blank experiments to 76 hours (E2) and 148 hours (E4) in the experiments conducted with Mg in the growth medium.

The number of crystals in the experiments 24 hours after the optical observation of the first crystals was around 30% smaller when Mg was present in the growth medium. It is important to note that, although no change in color shade was observed in the hydrogel column prior to the observation of the first crystals, in experiments conducted with a Mg-bearing hydrogel (E2 and E4) a 2 mm wide region of the gel column,

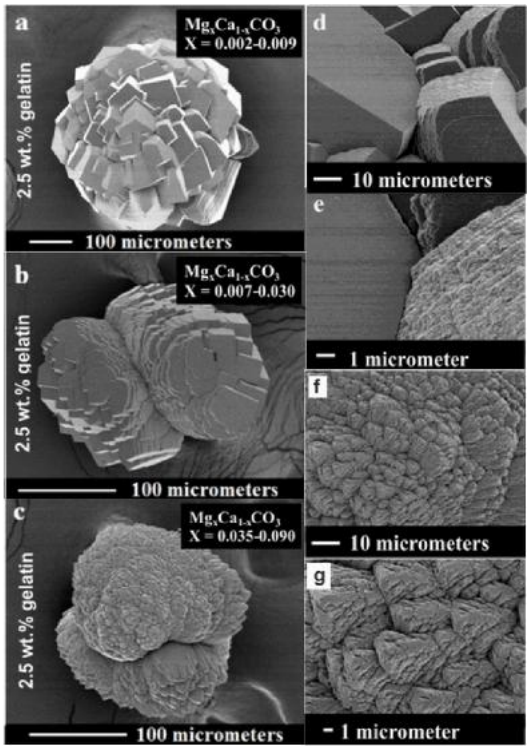

Figure 1. SEM images showing the variety of morphologies of calcite aggregates that grew in hydrogels with 2.5 wt % gelatin content and Mg in the growth medium. (a) Radial aggregate consisting of rombohedron-like calcite subunits. The habit of the subunits is controlled by (104) faces. The close-up in Figures d and e show the very different roughness of the different faces that reflect the crystallographic non-equivalency of parallel edges bounding (104). (b) Aggregate consisting of rombohedron-like subunits aligned pseudo-parallel to each other. Note the equatorial cleft in the center of the aggregate that is a consequence of the deviant growth kinetics of the parallel edges bounding the (104) surfaces. (c) Aggregate with highly rough surfaces of the subunits. The close-up (f and g) shows that the subunits consist of rombohedron-like sub-blocks with sizes smaller than 1 micron.

located adjacent to the right hand side of the precipitation region, i.e. closer to the carbonate deposit, turned tenuously cloudy when the first crystals were observed. After 24 hours, the cloudy appearance became more pronounced, with this region showing a whitish color and thus indicating the presence of very small particles. The cloudiness of the Mg-bearing hydrogel was positively correlated to its gelatin content. As time passed by, even though its width remained constant, the cloudy region moved rightwards, towards the carbonate deposit. Simultaneously, the region occupied by

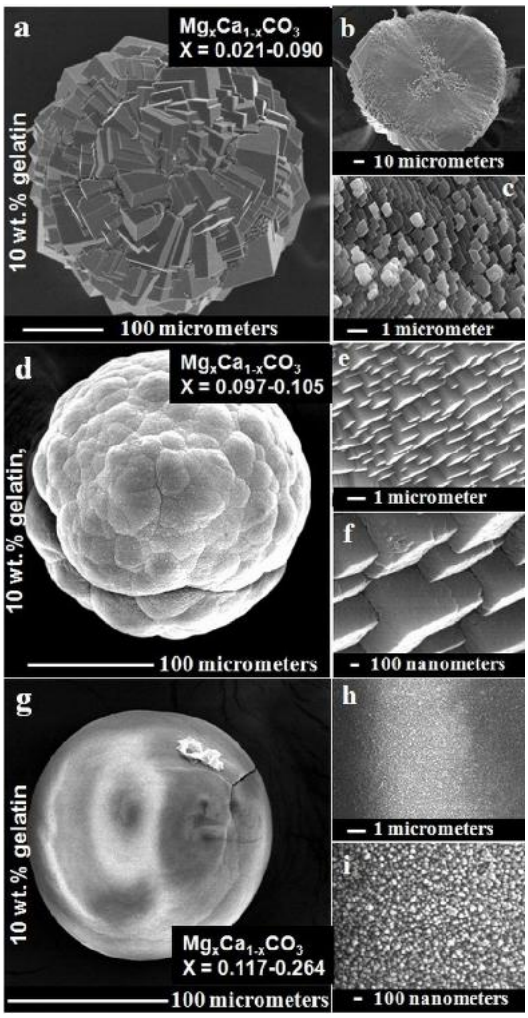

Figure 2. SEM images showing calcite aggregates that grew in hydrogels with 10 wt % gelatin and Mg in the growth medium. (a) Radial aggregate similar in habit to the aggregate that grew in 2.5 wt % gelatin (Figure 1a). The close-ups in Figures b and c highlight the roughness of the crystal in the core where the size of the crystallites is on the order of 1 micrometer. (d) Calcite aggregate with a cauliflower-like appearance. The close ups (e and f) show that the crystal is composed of small rhombohedron like blocks with sizes in the order of hundreds of nanometers. (g) Round shaped calcite crystal has the highest Mg-incorporation content. Figures h and i show the presence of small rounded particles within the blocks that have sizes in the order of tens of nanometers.

crystals increased its width, widening both rightward and leftward. The rightward widening (towards the carbonate deposit) occurred simultaneously with the dissolution of the whitish precipitate. The extremely small size of the particles constituting this precipitate and its

rapid dissolution made it impossible to recover them from the hydrogel and also prevented their characterization. When the experiments were stopped the width of the precipitation region was 10 - 12 mm in both, the experiments with and without Mg in the growth medium.

The role of Mg in polymorph selectivity and crystal morphology. In all experiments the precipitate mainly consisted of calcite, irrespective of the Mg content in the hydrogel. However, both, the gelatin concentration and the absence/presence of Mg influenced the $CaCO_3$ polymorph selection. Thus, while in blank experiments using hydrogels with 2.5 wt % gelatin (E1) the precipitate contained ~ 30% vaterite, in hydrogels containing Mg (E2) no vaterite was observed. In experiment E2 around 25% of the precipitate consisted of aragonite aggregates (Figure S1). In the blank experiments using 10 wt % gelatin (E3) the precipitate contained ~ 15% vaterite and 5% aragonite, while calcite was the only detected crystal phase in the precipitate when the hydrogel also contained Mg (E4). The presence of Mg in the growth medium had a strong effect on the morphology of the calcite crystals. In blank experiments using hydrogels with 2.5 wt % gelatin content (E1) calcite grew as blocks consisting of several sub-parallel crystals bounded by flat (104) faces. In the equivalent experiments using Mg-bearing hydrogels (E2), crystal aggregates showed a variety of morphologies. SEM micrographs in Figure 1 illustrate the morphological characteristics of these aggregates that ranged from radial crystal aggregates of numerous individuals bounded by (104) faces (Figure 1a) to dumbbell-like aggregates of sub-parallel crystals (Figure 1b) and dumbbell-like aggregates of progressively diverging crystals with highly rough surfaces (Figure 1c). EDX analyses taken on the surface and in cross-sections (Figure S2) of these crystal aggregates, taken from experiment E4, evidenced that all of them incorporated Mg: up to 0.9 mol % $MgCO_3$ in the radial aggregates (Figure 1a), up to 3 mol % $MgCO_3$ in the aggregates shown in Figure 1b and up to 9 mol % $MgCO_3$ in the aggregates shown in Figure 1c. Similarly, in blank experiments using hydrogels with 10 wt % gelatin content (E3) calcite grew as radial aggregates consisting of numerous individuals bounded by rough (104) surfaces, while when Mg was present in the growth medium (E4) the calcite aggregates had a wide variety of morphologies, including radial aggregates (Figure 2a), cauliflower-like aggregates (Figure 2d) and sphere-like aggregates (Figure 2g). EDX analyses on the surface of these aggregates also evidenced a correlation between crystal aggregate morphology and Mg content, with around 2 mol % $MgCO_3$ in the radial aggregates (Figure 2a), up to 10 mol % $MgCO_3$ incorporated in the cauliflower-like aggregates (Figure 2d) and up to 26 mol % $MgCO_3$ in the sphere-like aggregates (Figure 2g). All Raman spectra collected on samples of the different aggregates (Figure S3) show the typical features of a calcite spectrum,[33-34] although some variations in band half widths and positions can be detected when comparing spectra corresponding to samples grown in the absence of Mg (E1 and E3) to samples formed in the presence of Mg in the growth medium (E2 and E4) (see spectra labeled a to d in the insert of Figure S3). The spectrum of calcite aggregates obtained in experiments E1 and E3 shows a strong band at 1085 cm^{-1}, corresponding to CO_3^{2-} symmetric stretching mode (υ_1), another well-defined band at 711 cm^{-1}, assigned to the CO_3^{2-} in-plane bending mode (υ_4), a weak band at 1437 cm^{-1}, corresponding to CO_3^{2-} asymmetric stretching mode (υ_3), another weak band at 1748 cm^{-1}, regarded as the combination band of $\upsilon_1 + \upsilon_4$, and other two bands located at 153 and 280 cm^{-1}, which correspond to lattice modes. All these bands can be identified in the Raman spectra of the crystal aggregates obtained in the experiments E2 and E4. However, in those spectra, the bands show a clear broadening and appear to be shifted towards higher frequencies (see insert in Figure S3). Band broadening and band shifting becomes more apparent as the Mg content of the aggregate increases. For example, the strong band corresponding to the CO_3^{2-} symmetric stretching mode (υ_1) appears at 1085 cm^{-1} and has a half width of 9.6 cm^{-1} in the spectrum of crystal aggregates that grew in the absence of Mg (E1 and E3), while it appears to be shifted to 1089 cm^{-1} and has a half width of 15.74 cm^{-1} in the spectrum of the aggregates with the highest Mg content (sphere-like aggregates in experiment E4). Similarly, the band corresponding to the CO_3^{2-} in-plane bending mode (υ_4) shifts from 711 cm^{-1} in the spectrum of aggregates without Mg to 715 cm^{-1} in the aggregates with the highest Mg content and shows an increase of its half width from 11.23 to 25 cm^{-1}. Detailed information on the characteristics of the Raman spectra of crystal aggregates with different Mg contents is supplied as supplementary information in Figure S3 and Table S1.

The combined influence of Mg and the gelatin content of the hydrogel on the fabric of the incorporated gelatin, crystal morphology and surface characteristics. Figure 3 shows etched surfaces of crystals grown in 2.5 wt % gelatin hydrogels, with and without Mg. While Mg exerts only a small effect on the fabric of the incorporated hydrogel, the gelatin content of the hydrogel imposes the major effect. The gelatin that is incorporated into the crystal aggregates that grew in hydrogels with 2.5 wt % gelatin has a delicate spider-web like fabric (black arrow in Figure 3a). The incorporated gelatin network becomes thicker (black arrows in Figure 3c) when Mg is added to the 2.5 wt % gelatin hydrogel.

In crystal aggregates that grew in hydrogels with 10 wt % gelatin (Figure 4), in aggregates without Mg, we observe thick (200 nm – 1 μm in width) gelatin intercalations (black arrows in Figures 4a, b) that are bordered at two sides by a thin network of gelatin (white arrows in Figure 4a). With the addition of Mg to the 10 wt % gelatin hydrogel the thick intercalations become thinner (about 50-60 nm in width) and are less pronounced (black arrows in Figure 4c). The bordering gelatin network increases in thickness and is highly pronounced at the sides of the solid intercalations as well as within the carbonate mineral (white arrows in Figures 4c, d). Calcite crystal surface morphology is mainly influenced by the amount of gelatin in the hydrogel (Figures 3 and 4). While calcite that grew in a hydrogel with 10 wt % gelatin has a granular surface and fabric (Figures 4b, d), calcite crystals that formed in a hydrogel with 2.5 wt % gelatin have a blocky appearance and resemble to solid mineral (Figures 3b, d). In addition, the typical dissolution steps of calcite are well visible (Figure 3b), while this cannot be observed when the amount of incorporated gelatin becomes higher (Figures 4b, d). If Mg is added to the hydrogel (Figure 3d), then, in the case of low gelatin content hydrogels, crystal surfaces become facetted while in the case of hydrogels with high gelatin contents the size of the individual granules and that of the granular aggregates becomes smaller (Figure 4d).

The influence of Mg and the hydrogel gelatin content on crystal orientation patterns. Electron Backscatter Diffraction (EBSD) allows the investigation of crystallite and particle arrangement in microstructures with a spatial resolution in the sub-micrometer scale range.[35-36] Information obtained from EBSD measurements is presented in this study: (1) as band contrast images, (2) as color-coded crystal orientation images and (3) as pole density distributions for calcite c-axes (<001>-poles) and a*-axes ({100}-poles). We use the hexagonal setting of calcite. EBSD band

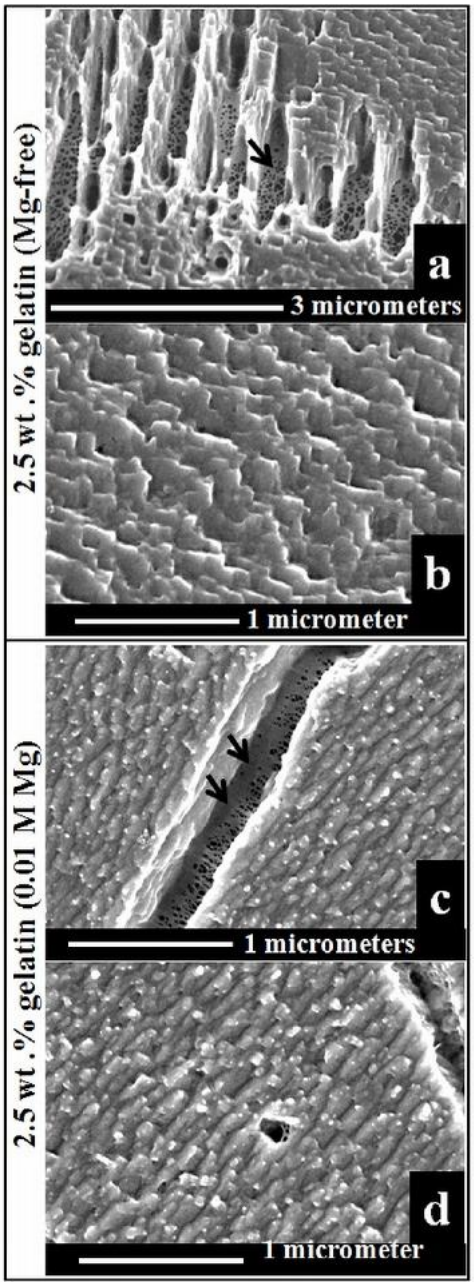

Figure 3. SEM images of calcite aggregates grown in hydrogels with 2.5 wt % gelatin. Figures 3a and 3b show the gelatin fabric and surface morphology of crystals that grew in hydrogels without Mg, while images in Figures 3c and 3d are from aggregates that were obtained in the presence of Mg in the growth medium. Black arrows in Figures 3a and 3c highlight the incorporated gelatin in the aggregates.

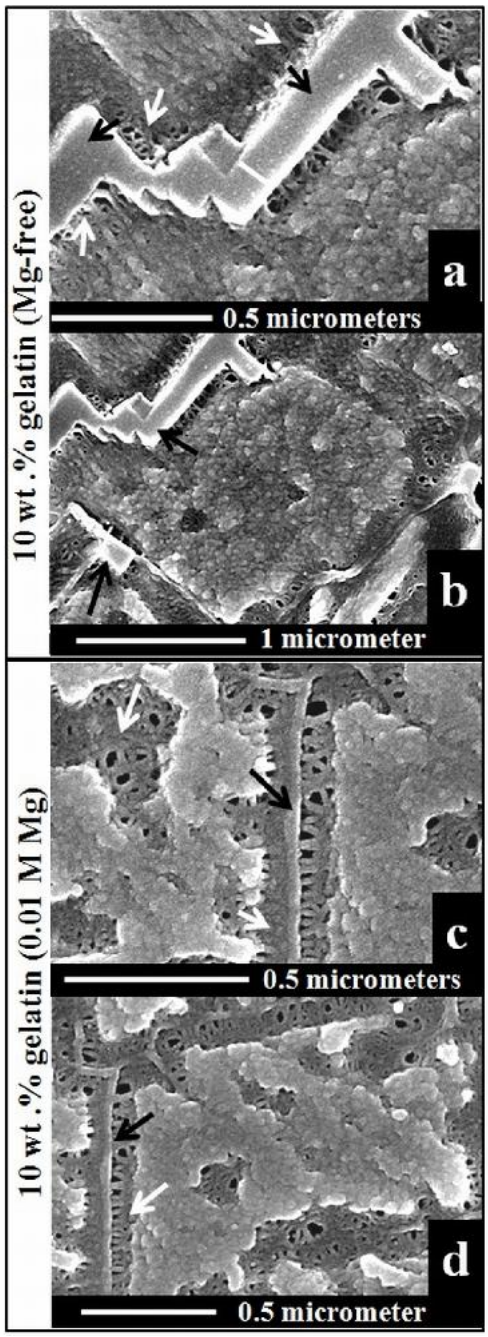

Figure 4. SEM images of calcite aggregates grown in hydrogels with 10 wt % gelatin content. Figures 4a and 4b grew in Mg-free solutions, while Figures 4c and 4d were obtained from a growth medium that contained Mg. White arrows point to the gelatin fabric that is present within the aggregate; black arrows highlight the intercalations of gelatin within the mineral. Note the granular appearance of calcite visible in all images.

contrast gives the signal strength of the EBSD-Kikuchi diffraction pattern. The strength of the EBSD signal is high when a mineral is detected, while it is weak or absent when a polymer or an amorphous phase is scanned. Thus, the band contrast highlights the distribution patterns of the mineral and the gelatin, respectively. Results for the 2.5 wt % gelatin experiment are shown in Figures 5 to 7 and S4 to S6. Figure 5 shows characteristic examples of crystals and crystal aggregates that grew in a hydrogel with a low (2.5 wt %) gelatin content. Some of those crystallization products are almost single-crystal like (Figure 5a), while most are radial aggregates consisting of a small number of individual subunits (Figure 5b, 5c). In Figure 5 we also show a radial aggregate which grew under similar conditions (2.5 wt % gelatin) but without Mg in the growth medium (Figure 5c).[21] Note from the stereograms in Figure 5 that the c-axes and the a*-axes of the constituting crystals are not randomly distributed across orientational space – instead they cluster around particular orientations, i.e. there is a certain, but vague, co-orientation between the constituting subunits. Note also, that the c-axes are not simply radially aligned (Figures 5e, 5f). To have some numerical measure of the degree of co-orientation we use the MUD value (multiple times random distribution) of the measured orientational distribution of the calcite within the object in question. Comparing the radial aggregates of the Mg-bearing and the Mg-free growth experiments, we can see that the MUD values are quite similar (Figure 5, S5). For the Mg-bearing experiment the surfaces of the aggregates are rounded, while in the Mg-free experiment we had more planar crystal faces and distinct vertices.

Figure 6 investigates the crystallographic co-orientation or mosaic structure within the near-single-crystal object of Figure 5a. This is both shown as an orientation map (Figure 6a) and as a misorientation profile (Figure 6b). The color in the map is chosen on a scale from 0 to 10 ° misorientation with respect to the mean orientation (Figure 6c); Figure 6d displays the misorientation spread of a reference crystal grown from pure hydrous solution. This spread is only about 0.5 ° and basically corresponds to the uncertainty of the individual EBSD spot measurements, that are in the order of sigma = 0.3°. The MUD value obtained from 735 EBSD data points of the tiny reference crystal is 725.[37] As it has almost no mosaic spread all data points plot on the same spot in the pole figures. Note that the gelatin-grown crystal shows a spotty appearance in the EBSD map (Figure 6a) and a slight broadening of the misorientation spread (Figure 6c) compared to the reference crystal.

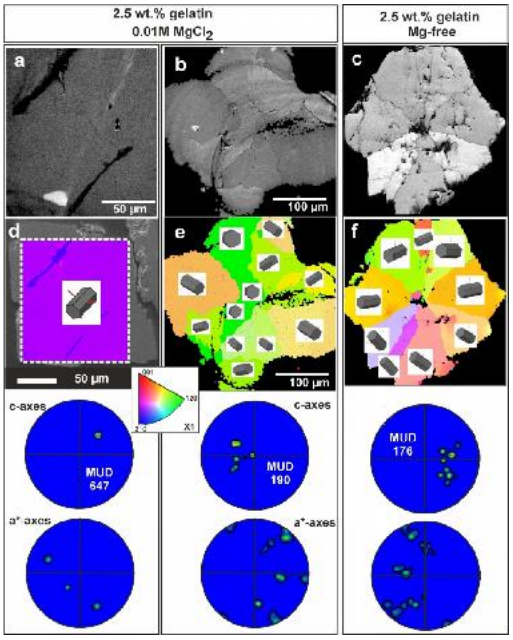

Figure 5. EBSD band contrast (a, b, c) and crystallographic orientation results (d, e, f) for crystals and crystal aggregates grown in a hydrogel with 2.5 wt % gelatin content; a, b, d, e display crystals that grew in the presence of 0.01M $MgCl_2$ in the growth medium; c, f display a crystal that was grown in a Mg-free environment.[21] Crystal orientation patterns are shown color-coded, the mean orientation of a specific subunit is visualized with the orientation of a sketched crystal. Pole-orientation density distributions show orientation patterns of calcite c- and a-axes. The strength of crystal co-orientation is depicted with the MUD values presented for each EBSD data set. The MUD value of an EBSD map is defined as the multiple of a random distribution.

Also, the misorientation profile (Figure 6b) shows some scatter larger than the ~ 0.3° random scatter of the orientation measurement procedure.

Figure 7 investigates the crystallographic constitution of the aggregate in Figure 5b. This aggregate is composed of three different types of subunits: near single crystals (e. g. crystal 1, Figures 7e, b, f), mesocrystals (crystal 2, Figures 7e, g), and mosaic crystals (crystal 3, Figure 7e, 7h). Misorientation within the near single crystal (1) scatters between 0.5 - 1.5 ° (profile A-B in Figures 7a, 7b). The tilt between two different subunits is between 40 and 45 ° (profile C-D in Figures 7a, 7c). Crystal 1 displays small-scale orientational scatter just exceeding what we would expect from the reference measurement (Figure 6c). The corresponding histogram for crystal 1 (Figure 7f) indicates a mosaic spread of up to 1.5 to 2 ° misorientation. The profile C-D (Fig 7c) crosses the sharp large angle grain boundary of 42°. The profile E-F (Figure 7d) cuts across a crystal grain which contains four mosaic blocks, which are separated by sharp small-angle boundaries (1- 4°) (Figure 7d). In the misorientation map (Figure 7e) these mosaic blocks occur in different colors according to the color scale defined in the histogram in Figure 7h, which also clearly displays the different blocks as maxima. Each subunit of the mosaic crystal is a mesocrystal (Figure S6a to S6c). The mosaic spread in all subunits of the radial aggregate as well as in the subunits of the mosaic crystal varies between 1.5 to 2 °. The patchiness of the mesocrystal subunit (crystal 2) shown in Figure 7e is not uniform throughout the unit. In comparison to the core, it is patchier at the rim of the crystal (Figures 7e, S5b). We relate this to a higher incorporation of gelatin at the rim of the mesocrystal unit relative to its core.

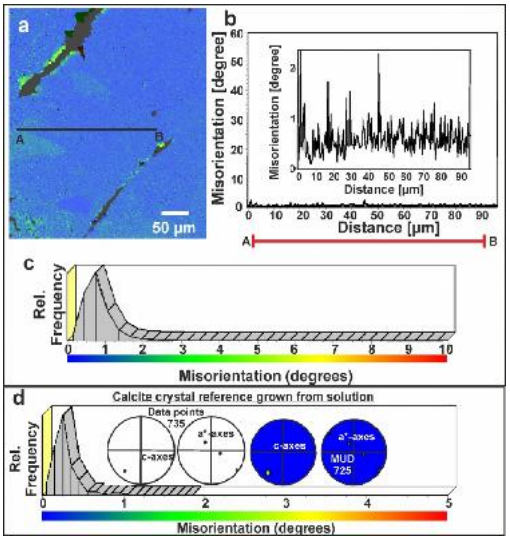

Figure 6. Misorientation mosaic spread (crystallographic co-orientation) of the crystal shown in Figure 5a. The spatial distribution of misorientation is shown with a color scale (Figure 6c) and corresponds to the misorientation versus distance histogram in Figure 6b with the location and the length of the investigated misorientation profile (A to B) shown in Figure 6a. For comparison, the mosaic spread, pole figures and MUD value of a calcite reference crystal that grew from solution is given in Figure 6d.[37]

MUD values (see supplementary Figure S5) of the crystals constituting the radial aggregates of Figure 5 are between 614 and 695, which indicates a relatively high crystallographic long-range register within the crystals. By

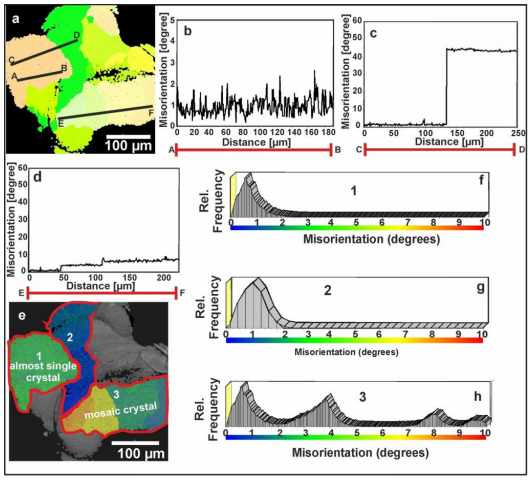

Figure 7. Analysis of crystallographic misorientation in the radial aggregate shown in Figure 5b. Inserts (b), (c), and (d) give characteristic misorientation profiles: profile A to B (Figure 7b) within a subunit of the aggregate, profile C to D (Figure 7c) from one subunit to the other and profile E to F (Figure 7d within a crystal with a prototype mosaic structure, with the mosaicity being based on sharp small-angle grain boundaries (Figures 7e, 7d). Misorientation in the almost single crystalline subunits 1 and 2 (Figure 7e) scatter between 1.5 and 2 (Figures 7f, 7g), while the degree of misorientation in the mosaic crystal is about 10 °s (Figure 7h).

comparison, our solution-grown reference crystal reaches an MUD of 725 (Figure 6d), which can be taken as optimal with respect to our instrumental angular resolution. Crystal 3 of Figure 7, which consists of four classical mosaic blocks, reaches an MUD value of 424, while the individual blocks reach MUD values between 652 to 702 (Figure S6). In summary, crystallization in 2.5 wt % gelatin gel leads to radial crystal aggregates, in which the constituting crystals show a vague co-orientation among each other. Inside the constituting crystals there is only a slight imperfection in crystallographic register. This imperfection is not only due to sharp small-angle grain boundaries, but also to some local orientation fluctuations.

Crystal aggregates that grew in hydrogels with 10 wt % gelatin are reduced in size, and, depending on the concentration of Mg, vary in morphology between radial aggregates and spherulites (Figure 8). The different morphologies incorporate a different Mg content. Radial aggregates of a small number of 50 - 100 micrometer large subunits incorporate 2 - 9 mol % $MgCO_3$. They resemble the aggregates grown in the Mg-bearing hydrogels with 2.5 wt % gelatin content (Figure 7a) and those obtained in 10 wt % gelatin hydrogel without Mg (Figure 8d). However, the aggregate of Figure 8a shows a certain degree of co-orientation of the constituting crystals: the c-axes form a cluster in the pole density in Figure 8a. Note that in the centre of the aggregate the c-axes are predominantly parallel to the axis of view, while they fan out towards the rim, where they form a small-circle on the stereographic projection sphere with 40 - 60 ° out-of planes. In the aggregates grown in Mg-free systems (Figure 8d) the c-axes are much more widely scattered in orientation.

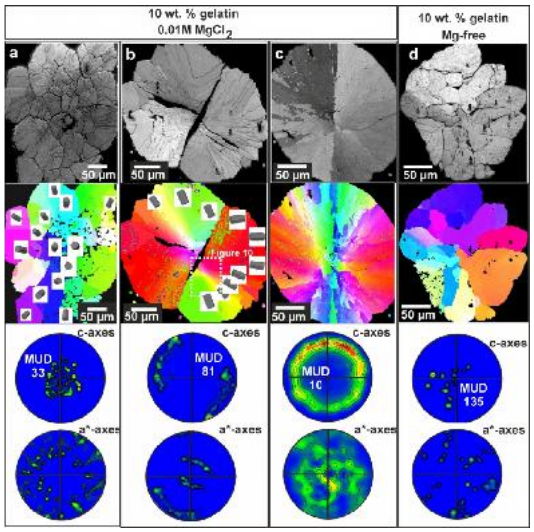

Figure 8. EBSD band contrast and crystallographic orientation results for crystal aggregates grown in a hydrogel with 10 wt % gelatin content and Mg in the growth medium. Orientation patterns are given color-coded and are shown in EBSD maps and pole figures that depict pole density distributions of calcite c- and a*-axes. The morphology of the aggregates changes from (a) to (c) due the difference in the content of Mg-incorporation. For comparison we show an example crystal morphology and orientation pattern of a calcite aggregate that also grew in a hydrogel with 10 wt % gelatin content but in an Mg-free environment.[21]

Prototypic spherulites (Figure 8c) are the most characteristic crystallization products in the 10 wt % gelatin gels with Mg in the growth medium. As expected for a prototypic spherulite, the aggregate is composed of a multitude of subunits. The c-axes of these crystals form a very distinct small-circle in the pole figures. As the EBSD measurement probes only a planar cut through the sphere, the azimuthal angle of this small circle will depend

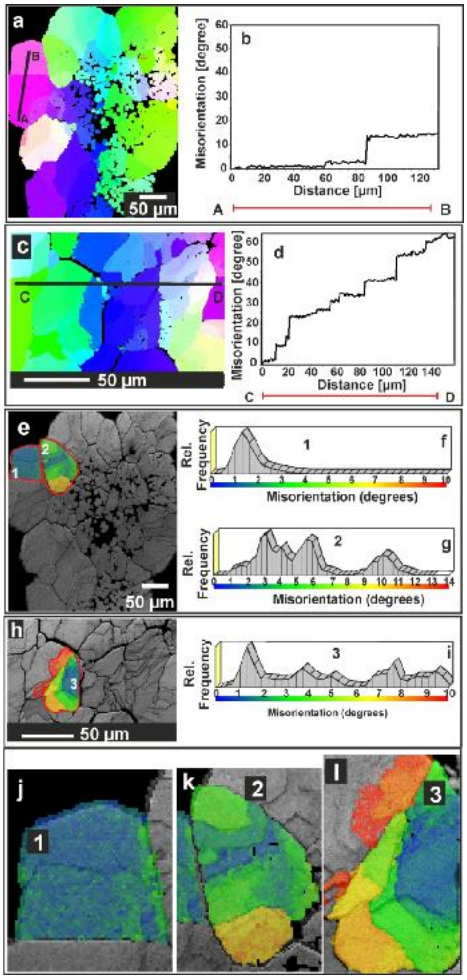

Figure 9. Misorientation analysis of an aggregate grown in a hydrogel with 10 wt % gelatin and about 2 mol % $MgCO_3$ incorporated into the crystals. Misorientation profiles over several subunits A-B (Figures 9 a, b) and C-D (Figures 9c, d) show the difference in calcite co-orientation between the rim and the center of the aggregate. Figures 9e to 9i show co-orientation patterns in three different subunits: subunit 1 (Figures 9e, 9j) is close to a single crystal with a misorientation of about 3 °, subunits 2 and 3 (Figures 9e, h, k, l) are mosaic crystals with prominent small angle boundaries between the individual blocks of the crystal (Figures 9k, 9l). Misorientation in the subunits 2 and 3 is about 10 °. Note the patchy appearance of subunit 1 (Figure 9j) that can be attributed to the incorporation of gelatin into the crystal.

on exactly where the sphere has been cut during specimen preparation. Aggregates as that shown in Figure 8b are an intermediate between the aggregate shown in Figure 8a, and the spherulites in Figure 8c. These aggregates consist of a small number of subunits (four in the case of the aggregate shown in Figure 8a),

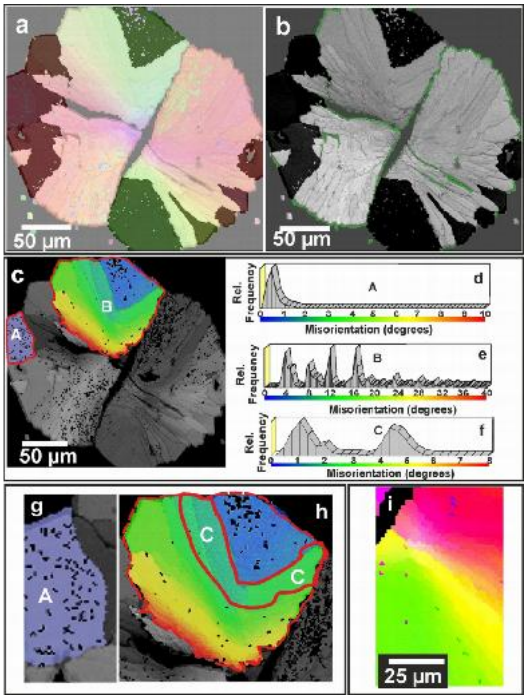

Figure 10. Misorientation analysis of an aggregate grown in a hydrogel with 10 wt % gelatin, in the presence of Mg in the growth medium. This aggregate shows a mixture of both: almost single crystalline subunits but also spherulitic regions. The rim of the aggregate is seamed by highly co-oriented calcite crystals (Figure 10a, 10g), while towards its center spherulitic subunits (Figure 10b, 10i) prevail. The degree of misorientation in the subunits at the rim of the aggregate scatters between 1 and 2 ° (Figure 10d), while in the spherulitic portions of the aggregate (subunit B, Figure 10c) the degree of misorientation reaches almost 40 ° (Figure 10e). In the spherulitic regions of the aggregate a cross-section towards its center shows that the size of the spherulitic subunits become smaller (Figure 10h, i). This is accompanied by an increase in the degree of misorientation (Figures 10e, f).

but in contrast to the aggregates in Figure 8a or d, the subunits are not single crystals. Instead, each subunit has a fan like spherulitic microstructure due to the presenceof numerous small-angle grain boundaries. The MUD value of the aggregate increases to 81, in comparison to the aggregate in Figure 8a, essentiallybecause the number of subunits is reduced. The object has been cut through a nearly equatorial plane, and thus the c-axes point only about 10 ° out of the plane of view, forming a small-circle on the pole figure. The corresponding crystal orientation pattern is hierarchical, its analysis is given in a section further below. Figure 9

analyses the mosaic structure of the constituting crystals of the aggregate of Figure 8a. In comparison to the subunits of the aggregate that grew in the hydrogel with 2.5 wt % gelatin content, for the 10 wt % gelatin experiment the subunits are smaller in size, have rounded outer shapes and, as profiles A-B and C-D show, are connected by small-angle boundaries with misorientations between 5 to 15 ° (Figures 9a to d). In comparison to the rim, subunit sizes are smaller in the center of the aggregate (Figures 9e, h). The subunits of the aggregate shown in Figure 9 can be addressed either as mesocrystals or as mosaic crystals composed of mesocrystals. Figure 9e-h display characteristic misorientation maps; the color scale is shown along with the misorientation histograms for the selected crystals. An example of a mesocrystal is shown in Figure 9e with crystal 1. It does not contain the otherwise ubiquitous small-angle sub-grain boundaries. Due to the absence of these imperfections, a submicron (mesoscale) variation in orientation becomes visible, which produces an orientational spread in the order of 3 ° (Figure 9f). The other two highlighted crystals contain mesocrystalline sub-grains bordered by sharp small-angle boundaries (Figures 9e, h, k, l). The overall mosaic spread of both units is around 10 - 12° (Figures 9g, i). The mosaic spread of individual mesocrystalline units of the mosaic crystals is about 2 ° (Figures 9g and 9i).

The aggregate analyzed in Figures 10 and 11 has morphological and crystal orientation characteristics intermediate between the radial aggregate of Figure 8a and the spherulite of Figure 8c. It is subdivided into four multicrystal sectors (Figure 8b). At its outer rim relatively large (~25 micrometer) subunits are developed (Figure 10a), with measured mosaic spreads below 1° (crystal A in Figures 10c, d and g). In addition to the almost single crystals at the rim, the aggregate contains fibrous crystals in a spherulite-like arrangement (see the grey scale band contrast map in Figure 10b). These spherulite crystals (e.g. the v-shaped unit labeled C in Figure 10h) show increased mosaic spreads in the order of 1.5 - 2 ° due to the mesoscale scatter (Figure 10f). The entire segment (e.g. the segment marked B in Figure 10c) contains numerous sharp small angle-boundaries which are associated with a stepwise but monotonically increasing misorientation relative to the initial reference orientation and give the object a mosaicity of almost 40 ° (Figure 10e). Towards the center of the aggregate the size of coherent crystals decreases dramatically and gives way to a continuous change of orientation down to the size of individual 800 nm steps of EBSD measurement (Figure 10c, i).

Figure 11 shows misorientation versus distance images taken from 5 different parts of the aggregate. Profile A-B shows the high co-orientation of calcite within an almost single crystalline subunit (Figure 11b); the profile essentially reflects the angular experimental resolution. Note that in all other profiles the misorientations increase monotonically, indicating a fan-like orientational spread. Towards the rim of the aggregate the crystals are larger, and thus the misorientation profile displays a step-like behavior (Figures 11c, f). The steps occur at sharp small-angle boundaries with misorientations between 10 to 15 °. The entire tilt range spanned by the profiles at the rim of the aggregate is between 40 to 50 °. In contrast to the rim, in the center of the aggregate, the coherent crystals are smaller and the profiles display an almost continuous increase of misorientation, corresponding to small steps of smaller sized crystals (Figure 11d, e), which accumulate to total misorientations of up to 60 °.

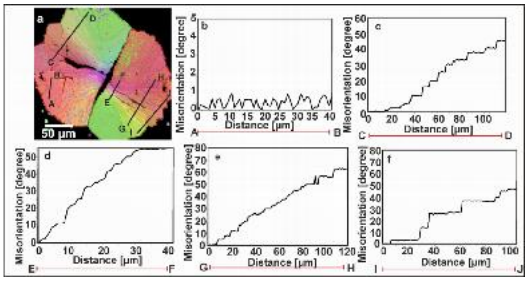

Figure 11. Misorientation versus distance results for selected profiles on a radial aggregate grown in a hydrogel with 10 wt % gelatin and 0.01M $MgCl_2$ in the growth medium (Figure 11a). Within a highly co-oriented (almost single crystalline) subunit (profile A to B) the degree of misorientation of calcite crystallites scatters around 0.5 degrees (Figure 11b). Along the rim of the aggregate (profiles C-D, I-J) the degree of misorientation is between 40 to 50 ° (Figures 11c, f). Well visible is the presence of small angle boundaries (the kincks in the graphs shown in Figures 11c and 11f) between the almost crystalline large subunits along the rim of the aggregate. Figures 11d, e show the degree of misorientation in the spherulitic regions, where it scatters between 50 to 60 ° with the tilt between the co-oriented blocks being on the order of 2-3 °.

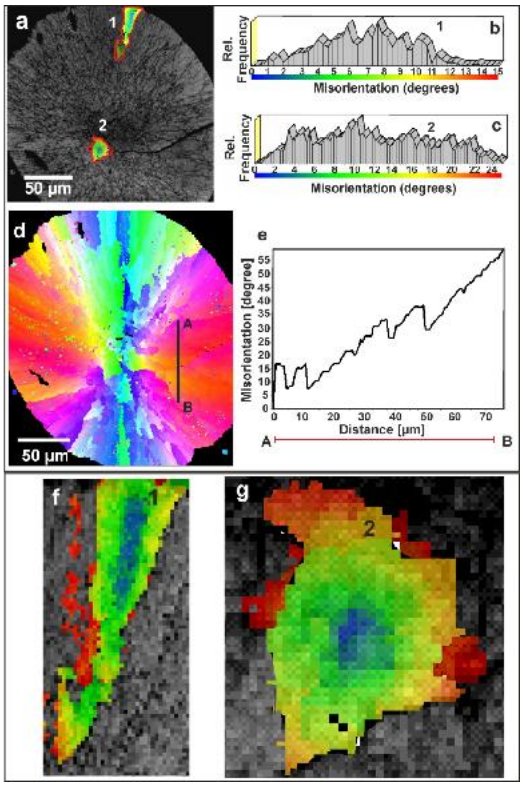

Figure 12. Misorientation analysis of a radial aggregate grown in a hydrogel with 10 wt % gelatin, in the presence of Mg in the growth medium. This aggregate is a spherulite, where the size of the subunits is larger in comparison to the size of the subunits in the center of the aggregate (Figure 12a). Misorientation in a subunit at the rim of the spherulite scatters between 12 to 15 ° (Figure 12b), while in the center of the aggregate misorientation in a subunit is on the order of 25 to 30 °. Note the mesocrystal-like constitution of the subunits that compose the spherulite visualized by the pixel-to-pixel misorientation shown in Figures 12f, g. The EBSD pixel step size is 800 nm and the experimental orientation resolution is +/- 0.3 °.

The prototype spherulite represents the cauliflower-like crystal in Figure 2d and is further analyzed in Figure 12. It is composed of a vast amount of minute conical fibrous crystallites, which are co-oriented and bundled with their neighbors (Figures 12a, d, f, and g). The size of these individual cone-shaped fibrous crystals is higher at the rim of the aggregate in comparison to its center. Misorientation histograms (Figure 12b, c) for the two selected cone-shaped crystals 1 and 2 show that the mosaic spread in crystals at the rim of the aggregate is about 12 °, while in the crystal in its center it is about 25 °, thus twice as high. The enlargements Figure 12f and g show that the misorientation changes almost on a pixel by pixel scale, reflecting a mesoscale internal structure. According to crystal co-orientation, the spherulitic aggregate is divided into four sectors, shown with red and blue-green colors (Figure 12d), which are in a nearly centro-symmetric arrangement.

DISCUSSION

Early stage of $CaCO_3$ crystallization and polymorph selection in the presence of Mg in hydrogels as a function of gelatin solid content. The present study complements on our recent study[21] of $CaCO_3$ crystallization in hydrogels with different gelatin contents, which was conducted without the presence of Mg. Nucleation and early stages of crystallization in hydrogels occur within the confined volume of pores.[21,38] It is well known that nucleation in gels takes place under high supersaturation conditions.[39-40] In the experimental setup used in this study the solution trapped in the hydrogel pores becomes supersaturated as a result of the reagents counter-diffusion from the reservoirs.[41-42] The actual supersaturation value when crystallization starts, designated as threshold supersaturation, depends on theboundary conditions of the system, i.e. the initial concentration of the reagents, the length of the diffusion column and the hydrogel used.[40,43] For equal boundary conditions, the threshold supersaturation can change as a result of changes in physical properties of the hydrogel, mainly porosity. Differences in threshold supersaturation between experiments can be qualitatively estimated considering changes in the waiting time for the first visible crystal (t_w).[12,44] Since the longer the mass transfer operates, higher amounts of reagent are delivered to the region of the hydrogel where crystallization takes place, higher t_w values amount to higher threshold supersaturations. Nindiyasari et al. (2014) have shown that an increase in the solid content of gelatin hydrogels results in a more complex porosity, with smaller pores and thicker pore-walls, and leads to higher threshold supersaturation values.[21] Such an influence of the hydrogel solid content on threshold supersaturation relies on the stochastic character of nucleation. Since nucleation results from fluctuations bringing together a number of ions large enough to exceed the critical nucleus size, the smaller the hydrogel pores are the lower the nucleation probability becomes.[19,38-40] Consequently, a higher supersaturation is required for the nucleation to occur.[21] This explains the results shown in Table 1 where the t_w values are significantly longer in

hydrogels with 10 wt % gelatin than those where the gelatin values are 2.5 wt %, both, in the absence (24 hours in E1 vs. 120 in E3) and the presence of Mg (76 hours in E2 vs. 148 in E4).

The results shown in Table 1 also show that the presence of Mg in the crystallization medium adds up to the inhibitory effect of the solid content of the hydrogel. The Mg inhibitory effect does not only result in longer t_w values but also in a significant reduction of the number of crystal aggregates observed 24 hours after the detection of the first visible crystals. Although both effects related to Mg are clear for the two gelatin contents in the hydrogel considered, stronger deviations from the blank are observed in experiments with a lower gelatin content.

Many researchers have reported the inhibiting effect of Mg on the formation of calcite, the stable $CaCO_3$ polymorph under Earth surface conditions.[11,25,45] This effect has traditionally been related to the poisoning of calcite surfaces by solvated Mg^{2+},[46] as a result of its much higher hydration energy in comparison to that of Ca^{2+}.[47] On the basis of in-situ AFM observations a thermodynamic alternative explanation that relates the inhibition of calcite crystallization to an increase in calcite solubility due to the lattice strain induced by Mg incorporation into the calcite structure has been proposed.[28,48] The combination of in-situ AFM observations and thermodynamic analysis of solid solution-aqueous solution systems or computer simulation studies have led other authors to relate this inhibition to kinetic factors rather than to a Mg-related increased calcite solubility.[49]

High Mg/Ca ratios in the growth medium are considered to promote the formation of aragonite, as an alternative $CaCO_3$ polymorph which does not substitute Mg^{2+} for Ca^{2+}.[46,50] Indeed, we observe a promotion of aragonite formation in experiment E2 (Mg-bearing hydrogel with 2.5 wt % gelatin) in comparison to experiment E1 (blank experiment, hydrogel with 2.5 wt % gelatin). However, Mg does not seem to promote the formation of aragonite when hydrogels with 10 wt % gelatin are used. On the contrary, while the three polymorphs calcite, aragonite and vaterite form in experiment E3 (blank experiment, hydrogel with 2.5 wt % gelatin), only calcite is detected in experiment E4 (Mg-bearing hydrogel with 10 wt % gelatin). Two explanations might rationalize the absence of aragonite in E4: (1) Since Mg is added to the hydrogel during its preparation, Mg concentration can be assumed to be basically constant in the region of the gel column where crystallization occurs. On the contrary, Ca diffusion from the Ca-reservoir leads to a progressive increase of the Ca concentration in the crystallization region as time passes, until crystallization occurs. Therefore considering identical boundary conditions, an increase in t_w correlates with a decrease in Mg/Ca ratio, implying that the Mg/Ca ratio at early stages of crystallization is lower in hydrogels with 10 wt % gelatin than with 2.5 wt % gelatin. However, the decrease in diffusivity through heavier hydrogels makes it very unlikely that an increase in t_w will lead to much smaller Mg/Ca ratios in E4 than in E2. More importantly, this explanation is in contradiction with the Mg contents detected in the aggregates obtained in experiment E4. Therefore, we conclude that this explanation can be discarded. (2) A second explanation would involve an active role of the gelatin matrix in the crystallization of $CaCO_3$. It has been reported that acidic amino acids, peptides, and full proteins accelerate calcite growth rate most likely by facilitating the desolvation of the solutes.[51] Gelatin consists of a mixture of peptides and proteins with isoelectric point values around 5, i.e. with predominance of acidic moieties.[52,53] An increase of the gelatin content of the hydrogel could help Mg desolvation, thereby partially reducing its inhibitory effect on calcite crystallization. It stands to reason that such an effect must also have an influence in Mg incorporation into calcite. This issue is discussed below.

Morphology of the calcite crystal aggregates. As explained above calcite aggregates grown in gelatin hydrogels with 0.01M Mg incorporate amounts of Mg that vary within wide ranges. This variation arises between growth media with the same Mg content but different gelatin solid contents. It also arises between aggregates of different morphology which grew in the same medium.

Furthermore, wide differences in $MgCO_3$ content are also detected in different areas of an aggregate. $MgCO_3$ in aggregates grown in hydrogels with 2.5 wt % gelatin varies between 2 and 9 mol %. Similar and even slightly higher Mg contents are found in radial and cauliflower-like aggregates formed in 10 wt % gelatin hydrogels. Finally, Mg contents up to 26 mol % $MgCO_3$ are found in sphere-like aggregates grown in 10 wt % gelatin hydrogels (Figure 2g). Evidence that the Mg is incorporated into calcite by substituting Ca can be found in the

characteristics of the Raman spectra collected on the different aggregates. Bands corresponding to vibrations of the CO_3^{2-} groups in these spectra show progressive band broadening and shift towards higher frequencies with increasing Mg content. Both features are characteristic of Mg-calcites and are interpreted to reflect the static positional disordering of the planar CO_3^{2-} groups associated to their tilting out of the basal plane to accommodate the shorter Mg-O bonds.[33,34] This disorder increases with the Mg content of Mg-calcites, thereby explaining the observed correlation between the Mg content of the different aggregates and the position and half width of carbonate bands in their Raman spectra.[33,34]

The Mg contents found in radial and cauliflower-like aggregates formed in 10 wt % gelatin hydrogels are significantly higher than those commonly found in synthetic Mg-calcites precipitated from bulk aqueous solutions, which are commonly in the range 1-3 mol % $MgCO_3$.[54] It is striking that the Mg contents (up to 26 mol % $MgCO_3$) found in sphere-like aggregates grown in 10 wt % gelatin hydrogels are in the range of those common in high Mg-calcites of biogenic origin. Indeed, biogenic calcites with more than 30 mol % are very rare.[5] It can be argued that an enhancement of Mg incorporation into the calcite structure can be promoted by the physicochemical conditions that are present in hydrogel systems, where, as explained above, crystallization occurs from highly supersaturated solutions in the confined volume of pores, and in the presence of acidic matrix. In fact, the higher Mg contents found in aggregates from hydrogels with 10 wt % gelatin could be related to the smaller porosity of the heavier hydrogel and the concomitant higher supersaturations at early stages of crystallization. However, these Mg contents still stand as very high when compared to the 1.8 to 5.7 mol % reported for Mg-calcites grown in silica hydrogels with Mg concentrations up to 5 times those used in the experiments described in this study.[11] As described above, in order to explain the absence of aragonite in the precipitate in experiments with Mg-bearing 10 wt % gelatin hydrogels, an active role of the acidic gelatin matrix in the incorporation of Mg would explain the high amount of Mg that is incorporated in the calcite aggregates. A significant enhancement of Mg in calcite due to hydrophilic peptides was detected by Stephenson et al. [55], who proposed that acid biomolecules create a lower-energy alternative pathway for Mg desolvation and thus facilitate its incorporation into the calcite structure. It cannot be left out that a transient amorphous calcium carbonate (ACC) precursor could also play a role in the formation of high Mg-calcite aggregates, especially in the case of the sphere-like aggregates with Mg contents above 25 mol %. This is supported by the observation, that the detection of the first visible crystals is accompanied by a whitish fine-grained precipitate present in a region of the hydrogel that is adjacent to that where the first crystals form. There is abundant evidence that high Mg/Ca ratios in the precipitating solution promote the formation of ACC[7,55] and that carbonates formed from Mg-ACC have Mg concentrations that are higher when the transformation occurs in the presence of organic acids or polyelectrolytes.[56-58] A pathway involving an ACC precursor for sphere-like aggregates (Figure 2g) with Mg contents is supported by the characteristics of their Raman spectrum (Figure S3). Furthermore, it is also consistent with SEM observations that these aggregates on the surface consist of spherical particles with sizes around tens of nanometers. Technical difficulties related to the extreme fragility and small size of these sphere-like aggregates has prevented the EBDS analysis of their internal microstructure.

Influence of gelatin solid content on the crystal co-orientation patterns in the presence of Mg. The different characteristics of both, the polymeric network fabric and intercalations between and within the subunits of the calcite aggregates, depending on the absence or presence of Mg in the growth medium (Figure 3 and 4), point to the existence of specific interactions between the gelatin matrix and the Mg^{2+} ions. The existence of these interactions is also supported by the much higher incorporation of Mg into calcite crystals grown in gelatin hydrogels in comparison to calcite crystals grown in other types of hydrogels whose pores contain solutions with similar to significantly higher Mg concentration. A more detailed explanation of this can be found in the previous section.

The incorporation of a polymeric matrix into crystals and crystal aggregates that grow in gelatin hydrogels results from a balance between the mechanical properties of the hydrogel and the characteristics of the growth process.[18] Crystals that are growing in the gelatin matrix exert a pressure against their surroundings.[18] This crystallization pressure determines rearrangements in the gelatin network. Most likely these rearrangements will

involve local changes in both, the pore sizes and the pore walls thickness. Since it is generally accepted that crystallization in hydrogels occur under high supersaturation conditions, fast growth rates can be expected, at least during the early stages of the crystallization process.[21,40] As shown by Uhlmann et al.[59] the faster the growth proceeds the more gelatin is incorporated into the crystals. It is important to keep in mind that physicochemical conditions continuously change in the gel column with time due to mass transfer from the reservoirs. As a result the reagents concentration, the pH, and supersaturation gradients change.[21,44,60] Moreover, the Mg/Ca ratio is not homogeneous but it varies from low values closer to the calcium reservoir to progressively higher values towards the carbonate reservoir as explained in the results section. Crystallization occurs in a small region within the hydrogel column. This region is also affected by changing physicochemical conditions and becomes locally altered once crystallization starts as a result of the consumption of reagents by growing crystals. The development of diffusion gradients around these growing crystals leads to physicochemical scenarios that can greatly differ locally. The combination of local differences in both, physicochemical conditions and the gelatin matrix arrangements could explain the differences observed in the characteristics of aggregates and their subunits, such as described for the aggregate shown in Figure 7e. EBSD results evidence that a variety of calcite aggregates are constituted by subunits with a fan-like orientational spread of the c-axis. The degree of c-axis tilting greatly varies within the same aggregate, as shown in Figure 11, where the orientational spread is limited to 10 to 15 ° in the central part of the aggregate and spans up to 45° at the rim. EDX analyses of these aggregates provided Mg contents between 2 and 9 mol %. The development of a fan-like distribution of the c-axis orientation in the calcite aggregates subunits can be explained as arising from Mg intrasectorial zoning.[29] On the basis of molecular scale in-situ AFM observations Davis et al.[29] proposed a differential incorporation of Mg into kink sites on parallel $\langle \bar{4}41 \rangle$ growth steps on calcite (104) surfaces that would arise from the different geometry of obtuse "+" (opener) step edges and acute "-" (closer) step edges depending on their advancement direction[61-63], following the idea that acute step edges provide more favorable coordination geometries for smaller ions.[62] Mg intrasectorial zoning in calcite was earlier concluded by Paquette & Reader[62] from cathodoluminescence microscopy and electron probe microanalyses. A different degree of Mg incorporation in the different growth steps will accumulate misfit strain in the lattice. This misfit strain could be released through the formation of dislocations at regular intervals, thus forming a small angle boundary. It is well known that dislocations associated to impurity incorporation play an important role in the development of split growth phenomena through the generation of small angle boundaries. When taken to the extreme split growth would lead to the formation of spherulites such as those structures shown in Figure 13.[64-67] The spherulite in Figure 8c corresponds to Figure 13 d, while the aggregate of Figure 8 b corresponds to Figure 13 c. The crystals with no incorporated Mg do not show small-angle boundaries (Figure 6), while those with smaller amounts of incorporated Mg show significantly fewer small-angle boundaries (Figure 7 and Figure 9).

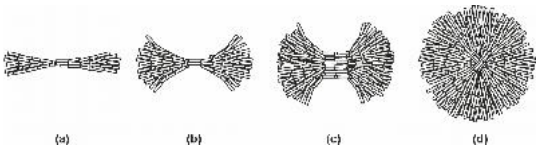

Figure 13. Schematic model proposed for the formation of spherulitic calcite aggregates through angle branching driven by the release of misfit strain induced by differential Mg-incorporation by arrays of dislocations corresponding to small angle boundaries.[64-67]

Conclusion

$CaCO_3$ was crystallized in gelatin hydrogels with two different solid contents (2.5 and 10 wt % gelatin), with and without Mg in the aqueous solution filling the hydrogel pores. Our results show that the combination of these two parameters, solid gelatin content and Mg absence/presence in the growth medium, strongly influence the characteristics of the $CaCO_3$ precipitate. The waiting time for the first optically observed crystals increases with the solid content of the hydrogel and additionally when Mg is present in the growth medium. Although calcite is the predominant phase forming the precipitate irrespective the solid content of the hydrogel or the presence of Mg in the growth medium, the combination influences the $CaCO_3$ polymorphic selection in a complex way. Thus, while Mg promotes the formation of aragonite in less concentrated gelatin hydrogels, calcite is the only phase detected in Mg-bearing

hydrogels with higher gelatin content. Regarding the characteristics of obtained calcite crystal aggregates, a wider variety of morphologies is obtained in Mg-bearing hydrogels compared to Mg-free hydrogels. The aggregates incorporate significantly higher Mg contents (up to 26 mol %) in hydrogels with higher solid contents. Moreover, with increasing incorporated Mg, the obtained aggregates develop more and more small-angle boundaries with the c-axis showing a fan-like orientational spread, up to the formation of spherulites. These small angle boundaries are most likely formed as a way of releasing misfit strain associated with the growth-step-specific incorporation of Mg into the calcite structure. Any type of intermediate situation between single crystals (virtually Mg-free) to prototype spherulites can be found. We attribute the simultaneous presence of quite different precipitate morphologies to differences in local supersaturation, with spherulites growing from highly supersaturated gels and more ideal rhombohedral crystals growing at lower supersaturation, the latter happening frequently on the surface of more irregular aggregates. Etching experiments uncovered an intimate relation between the inorganic component and a polymeric network in the calcite crystal aggregates. The characteristics of this network varied for hydrogels with different solid contents and when Mg was present in the growth medium. In the latter case the network is more nanofibrillar and intracrystalline, while without Mg it is found more compacted on crystallite boundaries. Due to the predominantly acidic hydrophilic functional groups of the gelatin we are lead to conclude that increased gelatin content of the hydrogel helps Mg desolvation, thereby partially reducing its inhibitory effect on calcite crystallization.

Acknowledgements. This research is part of the German-Spanish joint Acciones Integradas program (AIB2010 DE-0008), DAAD-50749739. F.N. is grateful for a stipendium by KAAD. E.G. is supported by Deutsche Forschungsgemeinschaft, DFG grant number GR-1235/9-1. This research was partially funded by project CGL2010-20134-C02-01 (MECC-Spain). We sincerely thank the staff of the National Microscopy Centre (ICTS) and the X-ray Diffraction Central Service of the Complutense University (UCM) and of the Raman spectroscopy laboratory of the MNCN, CSIC (Madrid, Spain) for technical support and assistance.

REFERENCES

1. Meldrum, F.; Cölfen, H. *Chem. Rev*. 2008, *108*, 4332-4432.
2. Asenath-Smith, E.; Li, H.; Keene, E. C.; She, Z. W.; Estroff, L. A. *Adv. Funct. Mater*. 2012, *22*, 2891-2914.
3. Falini, G.; Albeck, S.; Weiner, S.; Addadi, L. *Science* 1996, *271*, 67-69.
4. Carpenter, S .J.; Lohmann, K.C. *Geochim. Cosmochim. Ac.* 1992, *56*, 1837-1849.
5. Ma, Y.; Aichmayer, B.; Paris, O.; Fratzl, P.; Meibom, A.; Metzler, R. A.; Politi, Y.; Addadi, L.; Gilbert, P. U. P. A.; Weiner, S. *Proc. Natl. Acad. Sci. U.S.A.* 2009, *106*, 6048–6053.
6. Bentoz, S.; Erez, J. *Geochem. Geophy. Geosy*. 2006, *7*, 1-11.
7. Raz, S.; Weiner, S.; Addadi, L. *Adv. Mater*. 2000, *12*, 38-42.
8. Lenders, J. J. M.; Dey, A.; Bomans, P. H. H.; Spielmann, J.; Hendrix, M. M. R. M.; de With, G.; Meldrum F. C.; Harder, S.; Sommerdijk, N. A. J. M. *J. Am. Chem. Soc*. 2011, *134*, 1367-1373.
9. Cusack, M.; Freer, A. *Chem. Rev*. 2008, *108*, 4433-4454.
10. Griesshaber, E.; Schmahl, W. W.; Neuser, R.; Pettke, T.; Blüm, M.; Mutterlose, J.; Brand, U. *Am. Mineral*. 2007, *92*, 722-734.
11. Fernández-Diaz, L.; Putnis, A.; Prieto, M.; Putnis, C. V. *J. Sediment Res*. 1996, *66*, 482-491.
12. Sancho-Thomas, M.; Fermani, S.; Durán-Olivencisa, M. A.; Otálora, F.; Gómez-Morales, J.; Falini, G.; García-Ruiz, J. M. *Cryst. Growth Des.* 2013, *13*, 3884-3891.
13. Sancho-Thomas, M.; Fermani, S.; GOffredo, S.; Dubinsky, Z.; García-Ruiz, J. M.; Gómez-Morales, J.; Falini, G.; *Cryst. Eng. Comm.* 2014, *16*, 12571267.
14. Kosanovíc, C.; Falini, G.; Kralj, D. *Cryst. Growth Des.* 2011, *11*, 269-277.
15. Cölfen, H. *Macromol. Rapid Commun*. 2001, *22*, 219-252.
16. Sugawara, A.; Ishii, T.; Kato, T. *Angew. Chem. Int. Ed*. 2003, *42*, 5299-5303.
17. Kulak, A. N.; Iddon, P.; Li, Y.; Armes, S. P.; Cölfen, H.; Paris, O.; Wilson, R. M.; Meldrum, F. *J. Am. Chem. Soc*. 2007, *129*, 3729-3736.
18. Li, H.; Estroff, L. A. Adv. Mat. 2009, *21*, 470-473.
19. Halberstadt, E. S.; Henisch, H. K.; Nickl, J.; White, E.W. *J. Colloid Interfacial Sci*. 1969, *29*, 469-471.
20. Grassmann, O.; Löbmann, P. *Biomaterials* 2004, *25*, 277-282.
21. Nindiyasari, F.; Fernández-Díaz, L.;

Griesshaber, E.; Astilleros, J. M; Sánchez-Pastor, N.; Schmahl, W. W. *Cryst. Growth Des*. 2014, 14, 1531-1542.
22. García-Ruíz, J. M.; Amorós, J. L. *J. Cryst. Growth* 1981, *55*, 379-383.
23. Grassmann, O.; Müller, G.; Löbmann, P. *Chem. Mater*. 2002, *14*, 4530-4535.
24. Huang, Y.; Buder, J.; Cardoso-Gil, R.; Prots, Y.; Carrillo-Cabrera, W.; Simon, P.; Kniep, R. *Angew. Chem. Int. Ed.* 2008, *47*, 8280-8284.
25. Mucci, A.; Morse, J. W. *Geochim Cosmochim Ac*. 1983, *47*, 217-233.
26. Astilleros, J. M.; Fernández-Díaz, L.; Putnis, A. *Chem. Geol.* 2010, *271*, 52–58.
27. Davis, K. J.; Dove, P. M.; De Yoreo J. J. *Mat. Res. Soc. Symp*. 2000, *620*, M9.5.1-M9.5.7.
28. Davis, K. J.; Dove, P. M.; De Yoreo, J. J. *Science* 2000, *290*, 1134–1137.
29. Davis, K. J.; Dove, P. M.; Wasylenki, L.E.; De Yoreo, J. J. *Am.Min.* 2004, *89*, 714–720.
30. Nielsen, L.C.; De Yoreo, J. J.; De Paolo, D. J. *Geochim Cosmochim Ac.* 2013, *115*, 100-114.
31. Saldi G.D., Jordan G., Schott J., Oelkers E.H. *Geochim. Cosmochim. Ac.* 2009, 73, 5646-5657.
32. Jordan G., Pokrovsky O. S., Guichet X., Schmahl, W. W. *Chem. Geol*. 2007, 242, 484-496.
33. Bischoff, W.D.; Sharma, S.K .; Mackenzie, F.T. *Am. Min.* 1985, *70*, 581-589.
34. Urmos, J.; Sharma, S. K., Mackenzie F. T. *Am. Min.* 1991, *76*, 641-646.
35. Goetz, A. J.; Steinmetz, D. R.; Griesshaber, E.; Zaefferer, S.; Raabe, D.; Kelm, K.; Irsen, S.; Sehrbrock, A.; Schamhl, W. W. *Acta Biomaterialia* 2011, *7*, 2237-2243.
36. Griesshaber, E.; Schmahl, W. W.; Ubhi, H. S.; Huber, J.; Nindiyasari, F.; Maier, B.; Ziegler, A. *Acta Biomaterialia* 2013, *9*, 9492-9502.
37. Kim, Y.-Y.; Schenk, A. S.; Ihli, J.; Kulak, A. N.; Hetherington, N. B. J.; Tang, C. C.; Schmahl, W.; Griesshaber, E.; Hyett, G. Meldrum, F. C. *Nat. Comms*. 2014, *5*, 1-14.
38. Henisch, H. K. *Crystals in Gels and Liesegang Rings*; Cambridge University Press: Cambridge, 1988.
39. De Yoreo, J. J.; Vekilov, P. G. *Rev. Mineral. Geochem.* 2003, *54*, 57−93.
40. Putnis, A.; Prieto, M.; Fernández-Díaz, L. *Geol. Mag.* 1995, *132*, 1−13.
41. Henisch, H. K.; Garcia-Ruiz, J. M. *J. Cryst. Growth* 1986, *75*, 195-202.
42. Henisch, H. K.; Garcia-Ruiz, J. M. *J. Cryst. Growth* 1986, *75*, 203-211.
43. Prieto, M.; Putnis, A.; Fernández-Díaz, L.; López-Andrés, S. *J. Cryst. Growth* 1994, *142*, 225−235.
44. Prieto, M.; Fernández-Díaz, L.; López-Andrés, S. *J. Cryst. Growth* 1989, *98*, 447−460.
45. Reddy, M. M.; Wang, K. K. *J. Cryst. Growth* 1980, *50*, 470.
46. Lippmann, F. *Sedimentary Carbonate Minerals;* Springer-Verlag: New York, 1973. pp 228.
47. Huheey, J. E. *Inorganic Chemistry: Principles of Structure and Reactivity*; Harper and Row: New York, ed. 3, 1983.
48. Wasylenki, L. E.; Dove, P. M.; De Yoreo, J. J. *Geochim. Cosmochim. Acta* 2005, *69*, 4227-4236.
49. Astilleros, J. M.; Pina, C. M.; Fernández-Díaz, L. Putnis, A. *Surf. Sci.* 2003, *545*, 767-773.
50. Sand, K. K.; Rodriguez-Blanco, J. D.; Makovicky, E.; Benning, L. G.; Stipp, S. L. S. *Cryst. Growth Des.* 2012, *12*, 842–853.
51. Elhadj, S.; De Yoreo, J. J.; Hoyer, J. R.; Dove, P. M. *Proc. Natl. Acad. Sci. U.S.A.* 2006, *103*, 19237.
52. Boedtker, H.; Doty, P. *J. Phys. Chem*. 1954, *58*, 968–983.
53. Zhang, Z. K.; Li, G. Y.; Shi, B. J. *Soc. Leath. Tech. Ch.* 2006, *90*, 23-28.
54. Politi, Y.; Batchelor, D. R.; Zaslansky, P.; Chmelka, B. F.; Weaver, J. C.; Sagi, I.; Weiner, S.; Addadi, L. *Chem. Mater.* 2010, 22, 161-166.
55. Stephenson, A. E.; De Yoreo, J. J.; Wu, L.; Wu, K. J.; Hoyer, J.; Dove, P. M. *Science*, 2008, *322*, 724-726
56. Loste, E.; Wilson, R. M; Seshadri, R.; Meldrum, F. C. *J. Cryst. Growth* 2003, *254*, 206-218.
57. Cheng, X; Varona, P. L.; Olszta, M. J.; Gower, L. B. *J. Cryst. Growth* 2007, *307*, 395-404.
58. Han, H.; Blue, C. R.; De Yoreo, J. J.; Dove, P. M. *Procedia Earth and Planetary Science* 2013, *7*, 223-227.
59. Uhlmann, D. R.; Chalmers, B.; Jackson, K. A. J. Appl. Phys. 1964, 35, 2968-2993.
60. Sánchez-Pastor, N.; Gigler, A.M.; Cruz, J.A.; Park, S.-H.; Jordan, G.; Fernández-Díaz, L. *Cryst. Growth Des.* 2011, *11*, 3081-3089.
61. Staudt, W.J.; Reeder, R.J.; Schoonen, W. A. A. *Geochim. Cosmochim. Ac.* 1994, *58*, 2087-2098.
62. Paquette, J.; Reeder, R. J. *Geochim. Cosmochim. Ac.* 1995*, 59*, 735-749.
63. Jordan, G.; Rammensee, W. *Geochim.*

Cosmochim. Ac. 1998, *62*, 941-947.
64. Gránásy, L.; Pusztai, T.; Tegze, G.; Warren, J. A.; Douglas, J. F. *Phys. Rev. E* 2005, *72*, 011605.
65. Busch, S.; Dolhaine, H.; DuChesne, A.; Heinz, S; Hochrein, O.; Laeri, F. Podebrad, O.; Vietze, U.; Weiland, T.; Kniep, R. Eur. *J. Inorg. Chem.*1999, *10*, 1643-1653.
66. Busch, S.; Schwarz, U.; Kniep, R. *Adv. Func. Mat.* 2004, *13*, 189-198.
67. Simon, P.; Carrillo-Cabrera, W.; Formánek, P.; Göbel, C.; Geiger, D.; Ramlau, R.; Tlatlik, H.; Buder, J.; Kniep, R. *J. Mater. Chem.* 2004. *14*, 2218-2224.

Supporting Information

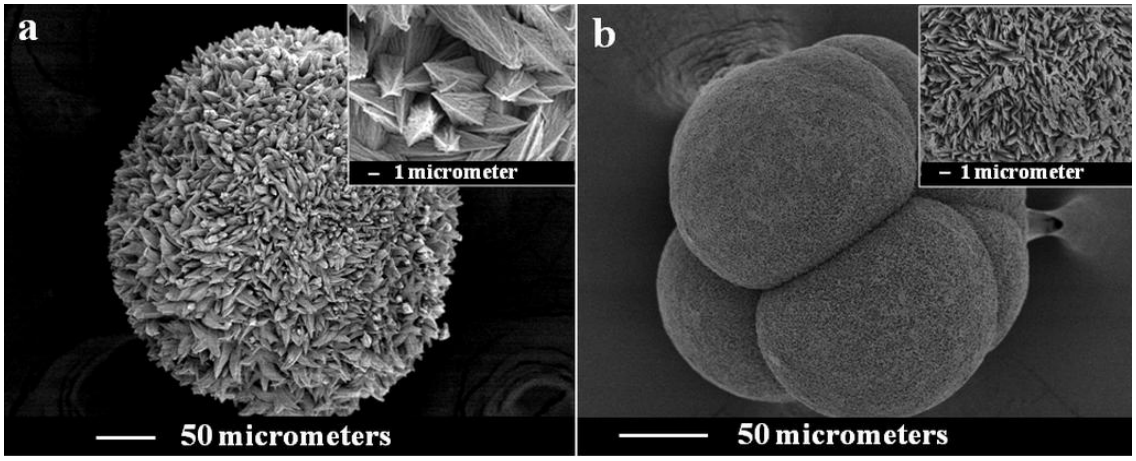

Figure S1. Aragonite aggregates obtained in hydrogels with 2.5 wt % gelatin in the presence of Mg in the growth medium. (a) Fibrous-radial aggregate consisting of elongated dendritic crystals. The close-up shows the high surface roughness of these dendrites (b) Sphere-like aggregate. The close-up shows that the aggregate consists of small platey crystals.

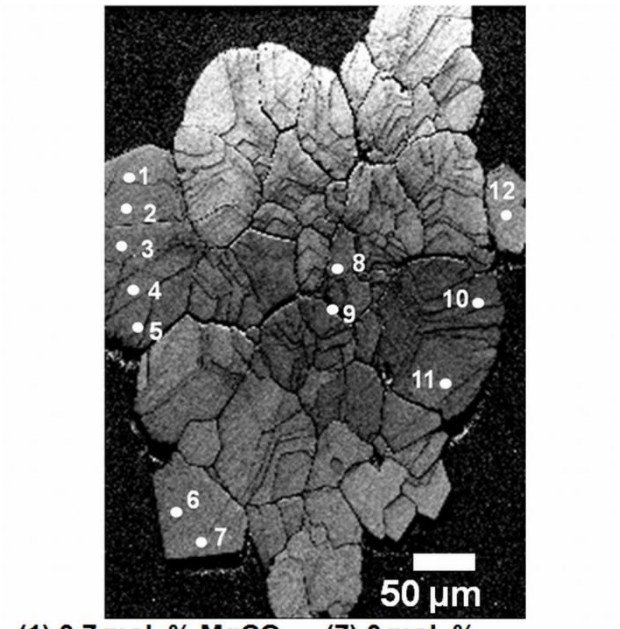

Figure S2. Representative list of EDX point analysis results for the Mg-content of the calcite taken on the cross-section of an precipitate (aggregate in Figure 8a). Here slightly higher Mg contents are found in the center of the aggregate compared to its rim of well-developed rhombohedral crystals.

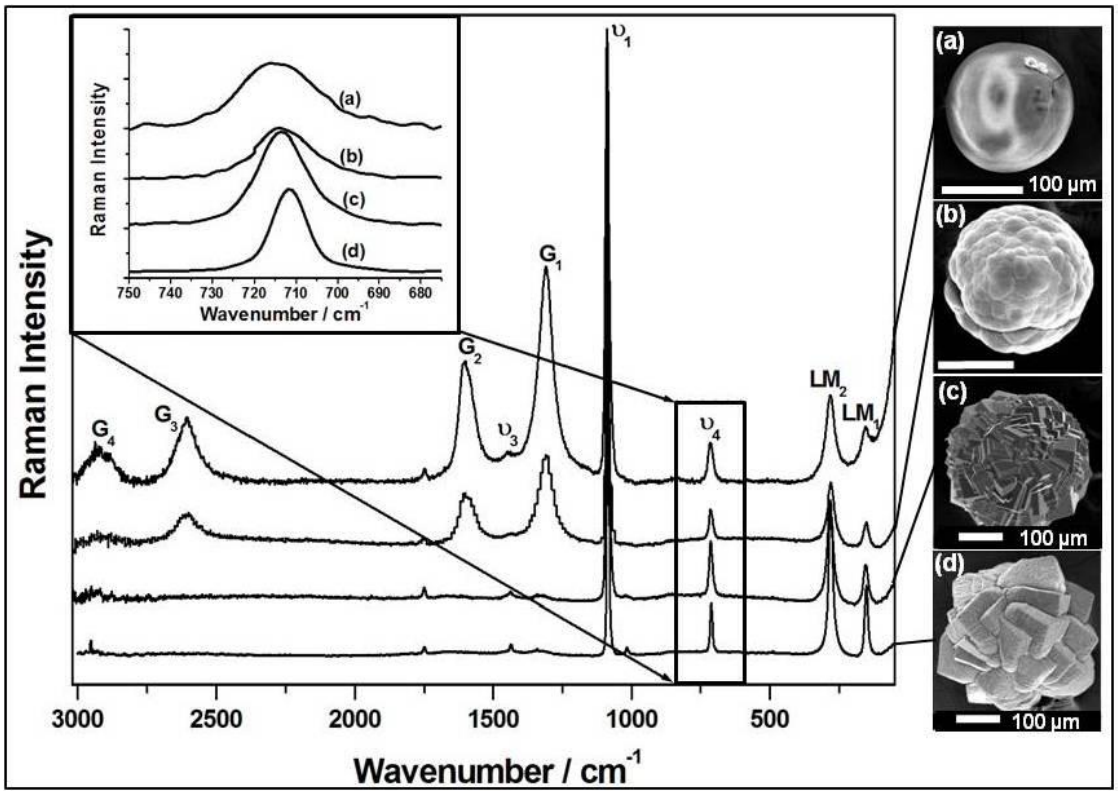

Figure S3. Raman spectra of 10 wt % gelatin-grown crystals: (d) without Mg, (a), (b), (c) with Mg. We observe three different morphologies depending on the amount of incorporated magnesium into the crystals (a) around 26 mol % $MgCO_3$, (b) around 10 mol % $MgCO_3$, and (c) with 2 mol % $MgCO_3$. Bands indicated by LM and G correspond to the lattice mode of calcite and gelatin, respectively. Bands marked by υ_1, υ_3 and υ_4 correspond to the CO_3^{2-} symmetric stretching mode, the CO_3^{2-} asymmetric stretching mode and the CO_3^{2-} in-plane bending mode. The inset highlights the correlation between the location and broadening of the υ_4 band and the amount of incorporated Mg into a specific aggregate. (a), (b), (c), (d) alludes to the investigated crystal morphologies.

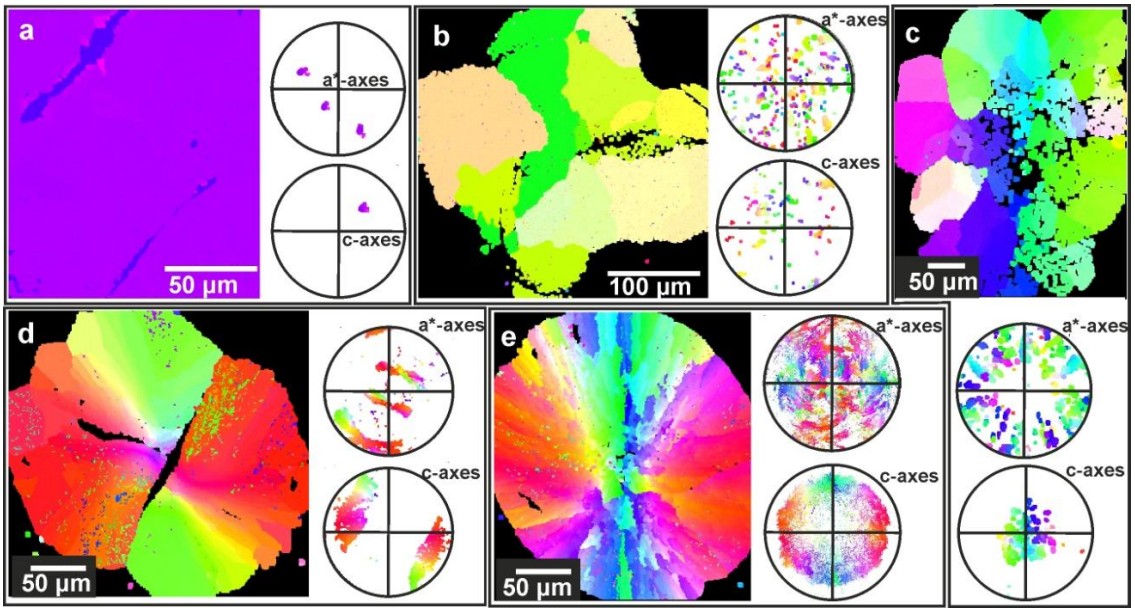

Figure S4. The pole figure of EBSD maps of gelatin-hydrogel grown calcite crystals/aggregates with 0.01M Mg in the growth medium. Crystals a, b: 2.5 wt % gelatin in the hydrogel; crystals c, d, e: 10 wt % gelatin in the hydrogel.

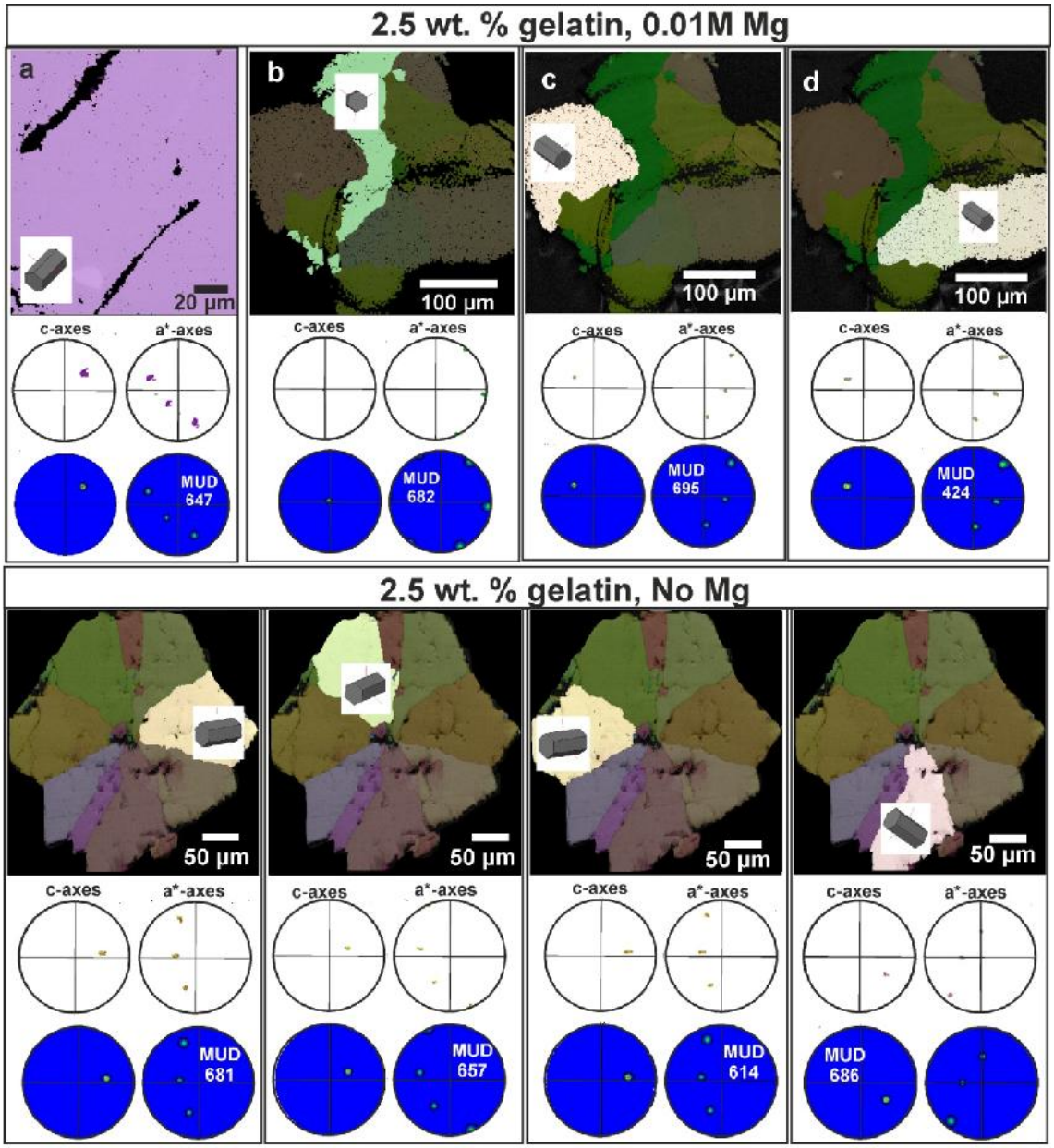

Figure S5. MUD (multiple times random) values for the orientational distributions in calcite crystals/subunits/aggregates grown from a hydrogel with 2.5 wt % gelatin. Top row: gels containing 0.01M Mg. Bottom row: no Mg. The crystal highlighted in (d) consists of three mosaic blocks (cf. Figure 7).

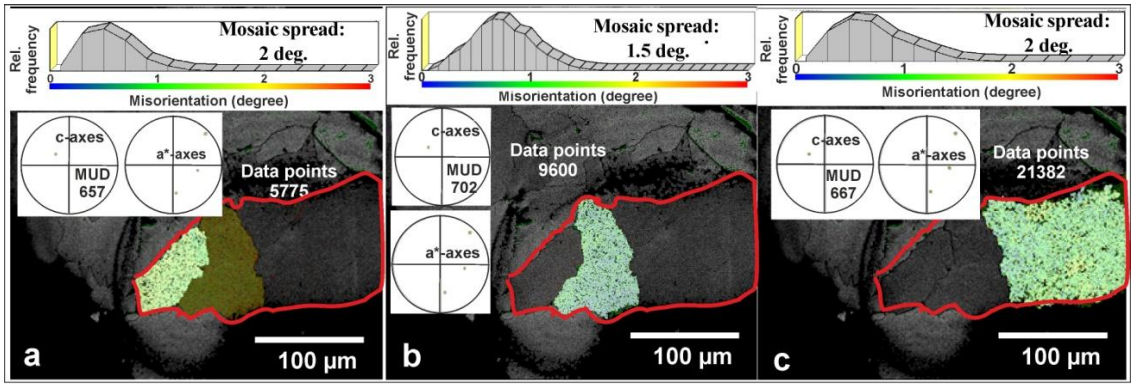

Figure S6. Crystal 3 of Figure 7e (2.5 wt % gelatin, 0.01M Mg), corresponding to Figure S5d, consists of four mosaic blocks. Two of those can hardly be separated as individual grains by our software; hence they are shown together in (c). Each of the blocks has an internal misorientation spread in the order of 1.5 °, indicating a mesocrystalline structure.

Table S1. Corresponding Raman bands (c f. Figure S3) of 10 wt % gelatin-grown crystal without Mg (E3) and three different morphologies of 10 wt % gelatin-grown crystals (E4). Bands indicated by LM correspond to lattice mode of calcite and G to gelatin. Bands indicated by υ_1, υ_3 and υ_4 correspond to the CO_3^{2-} symmetric stretching mode, the CO_3^{2-} asymmetric stretching mode and the CO_3^{2-} in-plane bending mode, respectively.

samples	**LM1**	**LM2**	**ν_4**	**ν 1**	**ν 3**	**ν 1+ ν 4**	**G1**	**G2**	**G3**	**G4**	**FHWM ν 1**	**FHWM ν4**
E3	153	280	711	1085	1434	**1748**	1320	-	-	2950	9.6	11.23
E4: ~ 2 mol % of $MgCO_3$	156	281	713	1087	1437	**1749**	1320	-	-	2950	11.6	16.5
E4: ~10 mol % of $MgCO_3$	156	281	714	1088	1442	**1750**	1320	1607	2617	2950	13.76	17
E4: ~26 mol % of $MgCO_3$	157	282	715	1089	1448	**1750**	1310	1603	2610	2950	15.74	25

2.4 The effect of hydrogel matrices on calcite crystal morphology, aggregate formation, and co-orientation in biomimetic experiments and biomineralization environments

Fitriana Nindiyasari[a], Andreas Ziegler[b], Erika Griesshaber[a], Lurdes Fernández-Díaz[*c,d], Julia Huber[b], Paul Walther[b] Wolfgang W. Schmahl[a]*

[a]Department für Geo- und Umweltwissenschaften and GeoBioCenter, Ludwig-Maximilians-Universität, 80333 Munich, Germany. [b]Central Facility for Electron Microscopy, University of Ulm, Ulm, Germany.
[c]Departamento de Cristalografía y Mineralogía, Universidad Complutense de Madrid, 28040 Madrid, Spain.
[d]Instituto de Geociencias (UCM, CSIC). C/ José Antonio Novais 2, 28040 Madrid, Spain.

Journal of Crystal Growth and Design 15, 2667-2685 (2015)

http://pubs.acs.org/doi/pdf/10.1021/cg5018483

ABSTRACT: The current interest in hydrogel systems is enhanced by their comparability to hydrous biological matrices of mineralizing tissues rendering these artificial model systems suitable for the investigation of the biological control of mineral formation.

In this study we investigate the effect of gelatin, agarose and silica hydrogels with and without magnesium in the growth medium, on calcite single crystal and aggregate formation. We characterize both components of the system, the hydrogel as well as the mineral by cryo-SEM, high-resolution SEM and electron backscatter diffraction (EBSD). We image the pristine hydrogel fabric and determine the way and the amount of hydrogel that is incorporated into the mineral. We further visualize the hydrogel-mineral interface and investigate the effect of the three hydrogels on patterns of calcite co-orientation and organization in the calcite-hydrogel composite aggregate. We finally compare hydrogel fabrics of biomimetic aggregates with the proteinaceous matrices and networks present in carbonate biological hard tissues.

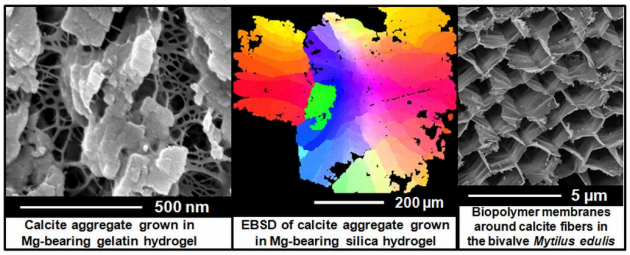

Our studies show, that in Mg-free environments, silica gel has very little effect on crystal co-orientation and mineral organization, in contrast to gelatin and agarose hydrogels, the calcite-silica gel composite that forms is a calcite single crystal. Agarose and gelatin hydrogels cause the formation of aggregates consisting of very few subunits which are bounded by hydrogel membranes. In contrast to aggregates grown in agarose, the subunits of aggregates that form in gelatin hydrogels are higher in number and more variable in sub-structure. When Mg is added to the medium, the subunits growing in silica gels form mesocrystals. In general, we see an increase of large and small angle boundaries in the aggregates when Mg is added to the growth medium and attribute this growth feature to a differential, accumulative split growth process, provoked by magnesium incorporation.

INTRODUCTION

Calcite is one of the two major carbonate mineral components in biological mineralized hard tissues and is produced by numerous organisms, such as foraminifera, echinoderms, mollusks, brachiopods, isopods and decapods.[1,2] In most cases calcite crystals are highly co-oriented in the hard tissue, however, except for echinoderm teeth, calcite co-orientation is never as high as it is in calcite that is precipitated from solution.[3-11] Biogenic carbonates incorporate Mg into their structure in proportions that can vary widely depending on the organism and the specific part of the hard tissue.[7, 12-14] Mg contents in hard tissues varies between 0 and 0.23 mol % $MgCO_3$ in planktonic foraminifera and reaches values close to 10 mol % $MgCO_3$ in brachiopods, while concentrations as high as 45 mol % $MgCO_3$ are found in the polycrystalline matrix filling the space between the needles and

the plates (10-15 mol% $MgCO_3$) in sea urchin. teeth.[7, 10, 15-17]

Hydrogels share characteristics with gelatinous environments where biogenic minerals are formed.[18] Important properties of hydrogels for crystal growth experiments are the possibility of fine tuning[19-22] some of their characteristics such as the solid content, porosity, composition of aqueous solutions filling the pores[23-26] and functionalization with specific active groups.[27-29] This renders hydrogels as relevant model systems that mimic to some degree formation processes in biological regimes.[30-31] Agarose is a linear polysaccharide extracted from marine red algae. It consists of β-1,3 linked D-galactose and α-1,4 linked 3,6-anhydro-αL-galactose residues. The polymer chains form single and double helices that bundle together to a three-dimensional, porous network with fibrous characteristics when it is in gel form.[31,32] Gelatin is a poly-peptide material derived from natural collagen through hydrolytic degradation, which breaks the triple-helix structure of collagen into single-strand molecules.[33,34] Gelatin contains both acidic and basic amino acids.[31,35] A variety of gelatins can be obtained depending on the origin of collagen and the production method.[35] Aqueous solutions of agarose (~ 0.1% w/v) and gelatin (~ 5% w/v) form hydrogels on cooling below 27 ºC.[35] The gelling process involves a helix-coil transition. Both agarose and gelatin hydrogels can be described as "reversible" or "physical" gels.[36] This means that the gelling process is reversible and their networks are held together through physical interactions between biopolymer chains, including, among others, molecular entanglements, H-bonding and Coulombic forces.[31,36] Silica hydrogel, on the other hand, is a "chemical" gel. It can be prepared by acidification of aqueous solutions of sodium metasilicate, the method used in this work, or by the hydrolysis of siloxanes.[19] In the case of silica hydrogel, gelling is an irreversible process. It involves the formation of a three-dimensional network of SiO links through the polymerization of, mainly, monosilicic acid (H_4SiO_4) and, to a lesser extent, other silicic species ($H_3SiO_4^-$ and H_2SiO_4) [3,37] The structural network in silica hydrogels is established predominantly by covalent interactions.[31,38] Both silica and agarose hydrogels are chemically relatively inert crystal growth media due to the absence of strongly interacting chemical functionalities within their matrixes, which makes them highly suitable for the investigation of the influence of physical factors on crystal nucleation and growth.[31] In contrast, it can be expected that gelatin hydrogels play a chemically active role in crystallization due to the presence of both acidic (carboxylic acid) and basic (amine) groups.[31,39]

Different studies have revealed that agarose hydrogel-grown calcite single-crystals show most of the typical features of biogenic calcite crystals, such as occluded, roughly intact hydrogels.[40-43] A recent study on the formation of calcite aggregates in gelatin hydrogels has shown that the aggregates incorporate gelatin in various amounts and proved that an increase in gelatin incorporation results in an increasing degree of internal structuring of the hydrogel-mineral aggregate.[44] Further studies have emphasized the active role of gelatin as a promoter of Mg incorporation into calcite [39,45-47] and described the cooperative influence of hydrogel porosity and Mg incorporation on an increasing internal structuring of the aggregates.[39]

In this study we complement our previous findings[39,44] with the investigation of carbonate aggregate formation in all three major hydrogels: gelatin, agarose and silica. We explore calcite growth and co-orientation in Mg-free and Mg-bearing hydrogel environments and investigate the influence of different hydrogel chemistries and hydrogel porosities on the internal constitution of the obtained mineral aggregates. Our aim is to record and juxtapose the influence of the different hydrogels on biomimetic calcite formation. We investigate the relation between hydrogel incorporation and calcite crystal organization in nanometer-sized entities, micrometer-sized subunits and macrometer-sized crystal aggregates. We end with a comparison between the findings obtained from the incorporated hydrogels and their influence on mineral nucleation and growth and the biopolymer distribution patterns and biopolymer fabrics present in modern marine carbonate biological hard tissues.

EXPERIMENTAL PROCEDURES

Crystal growth. Crystallization experiments were carried out using double diffusion system with a hydrogel column length of 120 mm and diameter of 9 mm. The vertical branches were filled with 5 mL of the aqueous solution of 0.5M $CaCl_2$ (Sigma Aldrich) and 5 mL of aqueous solution 0.5M Na_2CO_3 (Sigma Aldrich) that were brought together by counter diffusion through the porous structure of the hydrogel. Three different types of hydrogels were used.

Gelatin and agarose hydrogels were prepared by respectively dissolving porcine gelatin (Sigma Aldrich; Type A, Bioreagent) and agarose (Sigma Aldrich; Purified; Plant Cell Culture), in two solvents, water and an aqueous solution of 0.1 M $MgCl_2$, previously heated at 60 °C. The concentration of gelatin and agarose was 10 wt % and 1 wt %, respectively. The gelation was carried out at 4 °C during an hour. Silica hydrogel was prepared by acidification of a sodium silicate solution (Merck, sp. gr.: 1.509 g/cm3; pH = 11.2) with 1N HCl to a pH = 5.5. The silica hydrogel contains ~ 96.5wt% water filling its interconnecting pores. All hydrogels were set at 15 °C for 24 hours before the reagents were poured to the branches. All solutions were prepared using high purity deionized (MiliQ) water (18.2 MΩ). Experiments were conducted at 15 ºC.

Crystallization of $CaCO_3$ occurred within the hydrogels. In the case of gelatin and agarose, the crystals were extracted by dissolving the slice of hydrogel where the precipitate was located in hot water (60 ºC). The precipitate was then filtered through a 1-μm pore size membrane, washed 3 times with hot Milli-Q water and dried at room temperature. The whole extraction procedure took ~ 15 minutes. The crystals grown in the silica hydrogel were extracted by dissolving the slice of hydrogel in a 1 M NaOH solution during 20 minutes. Afterwards, the precipitate was thoroughly rinsed and introduced in an ultrasonic bath during 10 minutes to get rid of possible rests of silica hydrogel. Subsequently, the crystals were again carefully cleaned with Milli-Q water and dried at room temperature.

Morphological characterization of crystal aggregates. Crystal aggregates grown in the three different hydrogels were selected under a binocular stereomicroscope and picked using a fine painting brush. After being mounted on holders, the samples were coated with gold and studied using scanning electron microscopy (JEOL JSM6400, 40 kV; JEOL JSM335F, 30 kV) equipped with an energy dispersive spectrometer (LINK Ex1; Oxford Instruments 80 mm^2 X-Max SDD). Due to the difficulty of removing all rests of hydrogel without producing any crystal surface alteration, the surface of crystals grown in silica hydrogel occasionally appeared unclean. It has affected the quality of the SEM micrographs and has required double coating, with gold and carbon, of those samples.

Preparation for SEM imaging the etched crystal-hydrogel composites. The obtained crystals grown in the hydrogel were embedded in EPON resin. The samples were first cut using an Ultracut ultramicrotome (Leica) and with glass knifes to obtain plane surfaces within the material that were then polished with a diamond knife (Diatome) by stepwise removal of material in a series of sections with successively decreasing thicknesses (90 nm, 70 nm, 40 nm, 20 nm, 10 nm and 5 nm, each step was repeated 15 times).[48] The polished crystals were etched for 90 seconds using 0.1M HEPES (pH = 6.5) containing 2.5 % glutaraldehyde as a fixation solution. The etching procedure was followed by dehydration in 100 % isopropanol 3 times for 10 seconds each, before the specimens were critical point dried in a BAL-TEC CPD 030 (Liechtenstein). The dried samples were rotary coated with 3 nm platinum and imaged using a Hitachi S5200 FE-SEM at 4 kV.

Preparation of the crystals for Electron backscatter (EBSD) analysis. EBSD measurements were performed on conventionally prepared sample surfaces. The crystals were embedded into EPON resin and were treated with several sequential mechanical grinding and polishing steps down to a grain size of 1 μm. The final step was etch-polishing with colloidal silica (particle size ~ 0.06 μm) in a vibratory polisher.

Investigation of hydrogel porosity using high-pressure freezing and cryo-SEM. High-pressure freezing is a method that prevents or minimizes damage of the structure of a material caused by ice crystal formation.[49-50] The hydrogel samples, 10 wt % gelatin and 1 wt % agarose, were prepared by dropping a small portion of the hydrogel into the cavity of aluminum planchettes, having a total diameter of 3 mm, and a central cavity 2 mm wide and 300 μm deep.[49] The silica hydrogel was prepared in a Petri dish following the procedure described above. After settling, a small slice of silica hydrogel was sampled and placed into the aluminum planchettes and both, the planchettes and the hydrogels, were immersed in hexadecane solution to fill cavities between the hydrogel and the planchettes. Subsequently the sample was covered with the flat side of another aluminum planchette. In order to assess demage to the gel fabric induced by ice crystal formation, hydrogels were either high-pressure frozen without further treatment or after treatment with 30 % isopropanole for 30 minutes. We observed no shrinkage of the samples after isopropanol treatment. High-

pressure freezing was carried out in a HPF Compact 01 (Wohlwend GmbH, Sennwald, Switzerland) at 230 MPa.[51,52] The pressure and freezing temperature was reached within 30 ms. Planchettes with the frozen samples were then mounted on a holder in a cryo-chamber above liquid nitrogen and cryo-transferred to a BAF 300 freeze-etching device (Baltec, Balzers, Liechtenstein). Samples were warmed up to -93° C and the sample surface was freeze-dried for 30 min by sublimation of water. Then the frozen samples were coated with 3 nm of platinum at an angle of 45° and with 20 nm of carbon at an angle of 90°. The coated frozen samples were mounted onto the Gatan cryo-holder 626 (Gatan, Inc., Pleasanton, CA, U.S.A.) and cryo-transferred to the Hitachi S5200 FE-SEM.[53] The samples were investigated at a temperature of -100 °C and an accelerating voltage of 10 kV. Imaging was performed by using analysis mode and the backscattered electron signal.

RESULTS

Hydrogel fabric and pore structure and mode of incorporation into calcite during aggregate formation growth. The fabric and pore structure of the three investigated hydrogels were determined with cryo-scanning electron microscopy of high-pressure frozen samples treated with and without isopropanol (Figures 1, S1). This analytical approach[9,45,46-50] ensures that the intrinsic hydrogel structure is not destroyed by ice crystal formation, and, more importantly, the observed fabric is inherent to a specific hydrogel.

Figures 1 and S1 visualize characteristics of the hydrogels such as their specific fabric, pore sizes and fiber dimensions. Mg-free gelatin and agarose hydrogels have a fibrous structure with highly varying pore dimensions. In comparison to agarose, the fiber structure of gelatin hydrogel is more compact (Figure 1e). In the 2D section of Figure 1e and f, a characteristic mesh size in the order of 60 nm is visible, with occasional pores in the 150 nm size range. Smaller mesh sizes are very frequent, but they also might result from non-equatorial sectioning of large pores. While fiber thickness in agarose hydrogel (Figure 1c) is similar to that in gelatin, pore dimensions with 100-200 nm pore sizes of agarose hydrogel (Figure 1d) are wider than those of gelatin hydrogel (Figures 1f). Silica hydrogel has an entirely different structure (Figures 1a, b). It is composed of minute (less than 20 nm) spherical particles that do not appear to form a network. Figures 2 to 4 and S1 highlight the interlinkeage between a particular hydrogel and the calcite mineral. Figure 2a shows the rhombohedral morphology of calcite

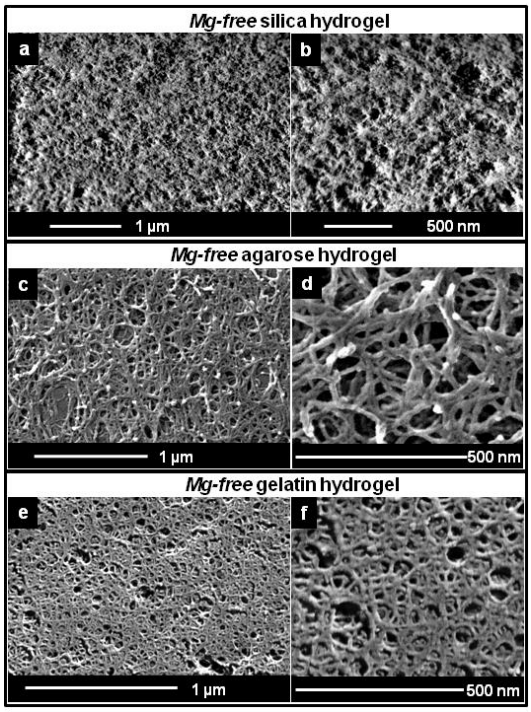

Figure 1. Cryo-FE-SEM images of high-pressure frozen hydrogels showing the fabric of Mg-free hydrogels: (a, b) Silica, (c, d) Agarose, (e, f) Gelatin. For the different hydrogels distinct fabrics and pore dimensions are observed. Silica hydrogel is an assemblage of interconnected nanometric silica spheres (a, b). Agarose hydrogel exhibits a network of fibers (c) with big pores sized (d). In comparison to agarose hydrogel, gelatin hydrogel is slightly denser (e, f).

grown in Mg-free silica hydrogel. The particulate character of silica hydrogel is apparent in all SEM images as well as the disruption of the incorporated hydrogel porosity structure due to broken pore walls at interfaces with the mineral part of the composite (Figures 2b, 2c). In calcite-Mg-free agarose (Figure 3) and calcite-Mg-free gelatin (Figure 4) composites we observe, in addition to the hydrogel network, the incorporation of compact hydrogel membranes of 100 nm thickness (white arrows in Figure 3b and white stars in Figures 4b and Figure S1b, c). In Mg-free agarose the intra-crystalline hydrogel network is a very pronounced characteristic of the composite structure (Figure 3c), the occluded hydrogel network (stars in Figure 3b) is found within the subunits of the aggregate. The

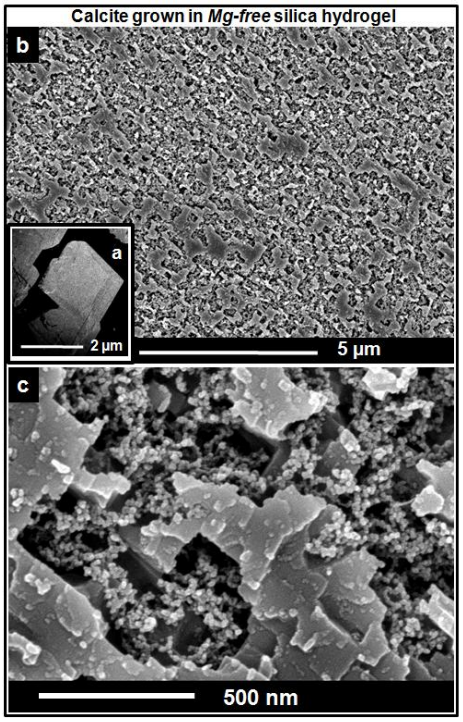

Figure 2. FE-SEM image of microtome cut, polished, etched and critical point dried surface showing the morphology of the crystal grown in Mg-free silica hydrogel, a rhombohedral shaped calcite single crystal (a). (b) highlights the mineral-hydrogel interconnection and overall fabric of the composite on a large scale. Silica hydrogel consists of an assembly of nanometer sized silica spheres and is occluded by mineral (calcite) entities (c). Silica hydrogel does not impose a major influence, neither on the overall microstructure of the composite nor on the co-orientation of calcite crystals or aggregates.

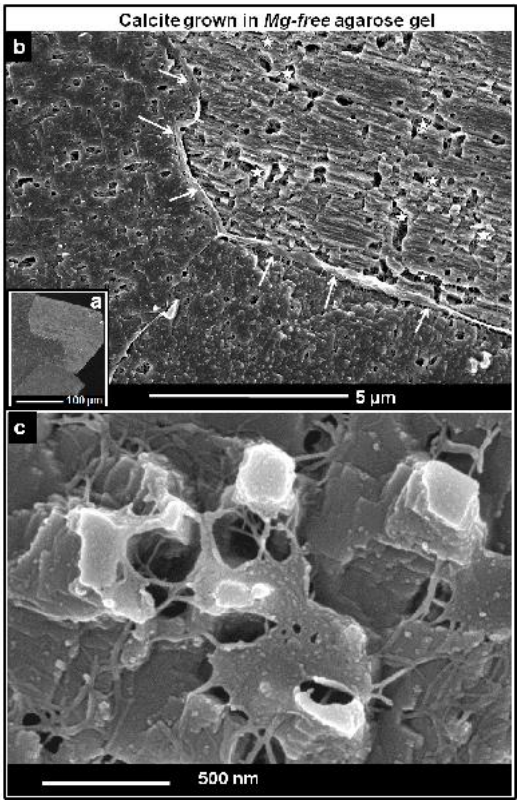

Figure 3. FE-SEM image of the surface of a microtome cut, polished, etched and critical point dried aggregate showing the interlinkeage of subunits in the aggregate that formed in Mg-free agarose hydrogel. (a). Large interlaced subunits can be distinguished within the aggregate. (b). These are separated from each other by agarose membranes (white arrows in b). Within the subunits of the aggregate, agarose hydrogel is developed as an evenly distributed occluded network (stars in b). The internal structure of calcite-Mg-free agarose composites, where calcite crystals are intimately surrounded by agarose network (c).

incorporation of Mg-free gelatin into calcite aggregates is not uniform. In subunit I and II (Figure 4b) we observe more patches of minerals connected by a delicate gelatin network, while in subunit III (Figure 4b) a highly pronounced network occluded between the mineral is visible. A thick gelatin membrane with a thickness of around 100 nm is also present (Figure 4c).

The presence of Mg in silica hydrogel does not induce a major influence on the fabric of calcite-Mg-bearing silica hydrogel (Figures 5, S1d) composites. On the other hand, the presence of Mg in agarose and gelatin hydrogels exerts a major influence on the structure of the composite materials. In all investigated calcite-Mg-bearing gelatin and calcite - Mg-bearing agarose aggregates the compact hydrogel membranes are missing (Figures 6b, c, S1e and 7b, c, S1f). In calcite-Mg-bearing agarose composites the hydrogel structure is delicate (Figure 6c) while in calcite-Mg-bearing gelatin composites the hydrogel network is highly pronounced (Figure 7c). Calcite that grows in Mg-bearing gelatin has a blocky appearance with the mineral entities having distinct dimensions (Figure 7c and black star in Figure S1f) in comparison to calcite that forms in gelatin hydrogels without the addition of Mg. In Mg-bearing agarose calcite entities have a columnar structure with rounded outer shapes (Figure 6b and black star in Figure S1e).

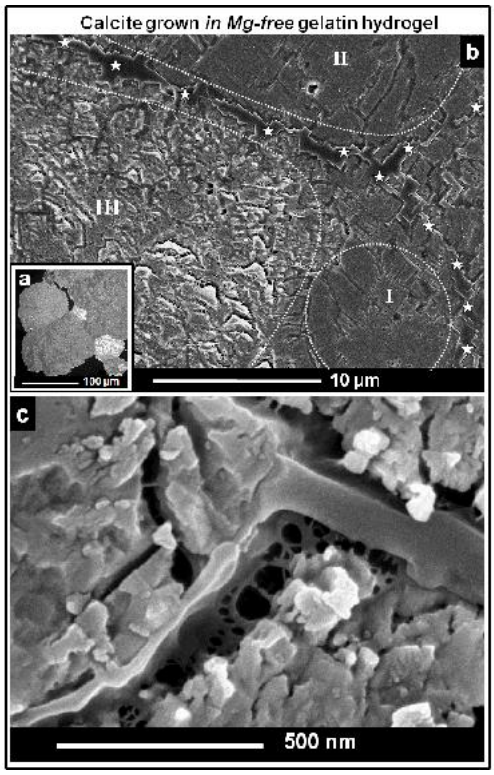

Figure 4. FE-SEM image of a microtome cut, polished, etched and critical point dried surface of a calcite-Mg-free gelatin hydrogel aggregate showing its morphology and internal structure (a, c). Large quantities of hydrogel are incorporated into the aggregate, either as thick gelatin membranes separating one subunit from each other (white stars in b) or as a highly pronounced network occluded between the mineral (subunit III in b) as well as connecting patches of mineral (subunits I and II in b). Gelatin incorporation into the aggregate is not uniform. In some subunits we observe more hydrogel (subunit III) while in others we see more mineral (subunits I, II). Gelatin hydrogel highly influences the pattern of crystal orientation and, thus, the overall microstructure of a subunit. High magnification of thick agarose hydrogel membrane is shown in (c).

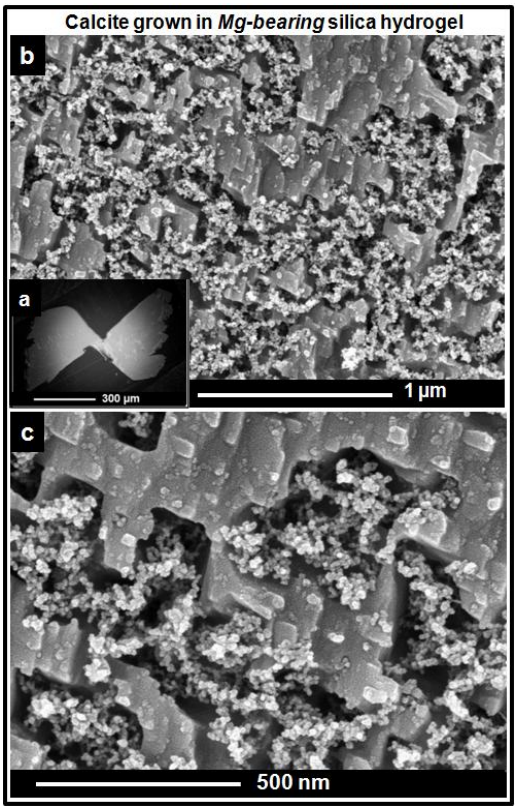

Figure 5. FE-SEM image of microtome cut, polished, etched and critical point dried surface showing the morphology of the crystal grown in Mg-bearing silica hydrogel. (a) The aggregates are dumbbell-shaped. (b) and (c) highlight the mineral-hydrogel interconnection and overall fabric of the composite. The addition of Mg in silica hydrogel has no influence in overall microstructure and orientation pattern of the aggregate.

Morphological characteristics of calcite crystal aggregates grown in Mg-free hydrogels. Calcite forms the main component in the precipitates of our experiments with Mg-free growth media, irrespective of the type of hydrogels that was used. However, depending on the hydrogel, we observed significant morphological differences between the calcite aggregates (Figure 8, 9 and S2).Calcite crystals grown in Mg-free silica hydrogel appear as single crystals which either have hopper habit[40-42] or show poorly developed dendritic branches (Figure 8a, b). Their habit is dominated by strongly terraced (104) faces and variably developed rough, blocky surfaces without a well-defined orientation. Edges bounding (104) faces are sharp for those converging in the three-fold axis, and curved and rough for those not converging in the three-fold axis (Figure 8b). The high roughness of the latter is depicted in Figure 8c, where both, their jagged appearance and the high porosity of flat (104) surfaces become evident.

Calcite that grows in Mg-free agarose hydrogel shows a wide variety of morphologies, ranging from rhombohedral single crystals (Figure 8d) to crystal aggregates (Figure 8e). Single crystals are bounded by flat (104) faces; with only those edges converging in the three-fold axis that appear smooth and straight (Figure 8d). Crystal aggregates consist of numerous individuals in an apparently radial arrangement. These constituting individuals are bounded by

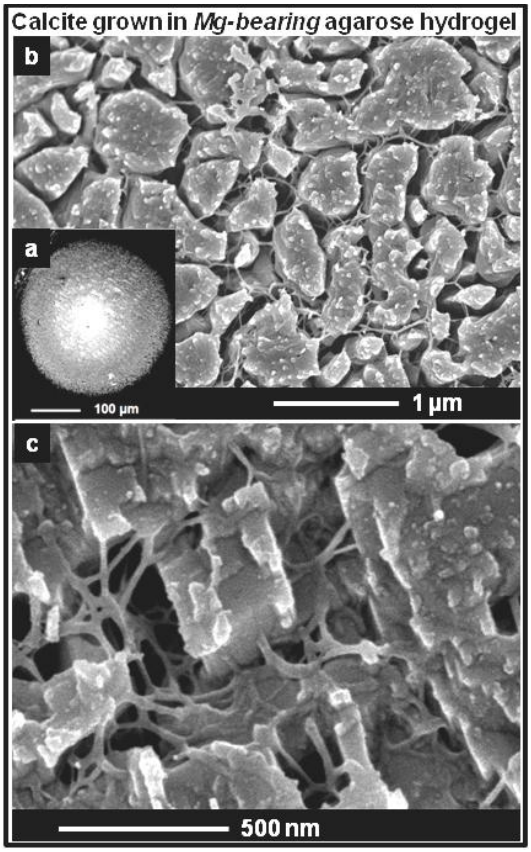

Figure 6. FE-SEM image of the surface of a microtome cut, polished, etched and critical point dried of calcite aggregate grown in Mg-bearing agarose hydrogel showing a spherical aggregate (a) and internal interconnection between agarose-mineral (b). Agarose hydrogel appears as a thin fibrous hydrogel interconnecting every subunits (c).

flat (104) faces with straight edges converging in the c-axis (Figure 8e). A detailed inspection of the (104) faces reveals that the crystals are highly porous as indicated by originally hydrogel-filled pores (Figure 8f).

Calcite that grows in Mg-free gelatin hydrogel appears as aggregates with very rough surfaces. The shape of these aggregates varies from approximately spherical (Figure 8g) to dumbbell-like structures (Figure 8h) and they consist of subunits with very slightly diverging crystallographic orientation. Detailed imaging of both aggregates and subunits reveals a surface structure consisting of isolated sub-micrometer blocks or pillars (size < 1 micron), which are separated by hydrogels designing their growth, and which appear to be only slightly misoriented relative to each other (Figure 8i).

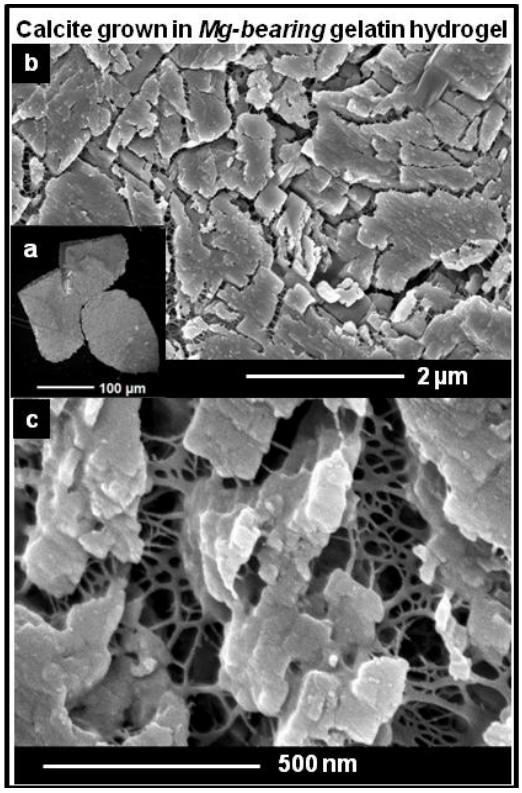

Figure 7. FE-SEM image of the surface of a microtome cut, polished, etched and critical point dried of calcite aggregate grown in Mg-bearing gelatin hydrogel showing its morphology (a) and internal interconnection between gelatin-mineral (b, c). Gelatin fibers have an intimate interconnection with mineral in subunit level (c).

Morphological and compositional characteristics of calcite crystal aggregates grown in high-Mg hydrogels. The characteristics of calcite crystal aggregates that grew in Mg-bearing gelatin, agarose and silica hydrogel are significantly different from aggregates that formed in Mg-free media (Figure 8, 9 and S2). These differences involve both, morphological and compositional features. Calcite grown in Mg-bearing silica hydrogel appears as bundled sheaf-like aggregates. These aggregates show an equatorial cleft and either consist of flat-surfaced similarly oriented units or numerous radially arranged, rough surfaced units (Figure 9a, c). In both cases, the units that compose the aggregates are bounded by rhombohedron faces (Figure 9b, d). Detailed inspection of the aggregates' surface show roughly defined sub-blocks that grow together and leave nanometric sized pores in between. EDX analyses collected on the surface of these aggregates yield Mg contents that range from 0 to 3 mol% $MgCO_3$.

Calcite crystal aggregates grown in Mg-bearing agarose hydrogel show two characteristic morphologies: sheaf-like and spherical aggregates. Figure 9e depicts a sheaf-like aggregate with a marked equatorial cleft. At the surface this type of aggregate displays (104) terraced faces of its subunits which are sub-parallel (Figure 9f). These aggregates have sizes in the range from 50 to 100 micrometers. EDX analyses collected on the surface of these aggregates provide Mg contents that vary between 2 and 5 mol% $MgCO_3$. Spherical aggregates show numerous sub-blocks in a radial arrangement (Figure 9g). These sub-blocks are bounded by rombohedron faces, although (104) faces can occasionally be distinguished (Figure 9h). The size of these aggregates is in the 50-150 micrometer range. The Mg content detected by EDX on the surface of these aggregates varies between 4 and 10 mol% $MgCO_3$.

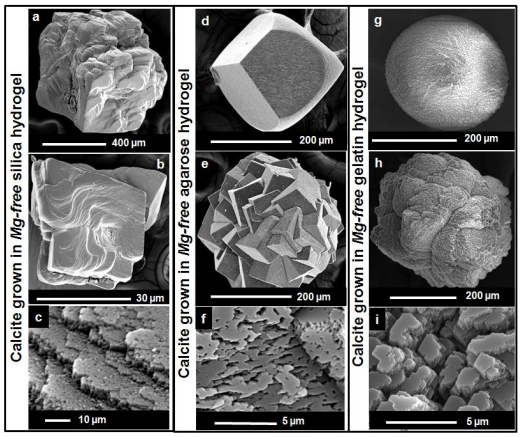

Figure 8. Calcite aggregates grown in Mg-free gelatin, agarose and silica hydrogels. (a, b) Hopper calcite crystal aggregate bounded by strongly terraced (104) faces and rough, blocky surfaces in the blocky surface without a well-defined orientation. The jagged character of the terrace edges is depicted in the close up of image (c). (d) Rhombohedron-shaped calcite crystal bounded by flat (104) and curved vicinal surfaces (e) Calcite radial aggregate consisting of rombohedron-like crystals. The close-up (f) shows the high porosity of the flat (104) surfaces. (g, h) Aggregates grown in gelatin hydrogel showing rough surfaces caused by slightly misoriented, submicron sized sub-blocks with (originally hydrogel-filled) channels between them (i).

Calcite formed in Mg-bearing gelatin hydrogel grows to sphere-like aggregates with small rombohedron-like sub-blocks at the surface (Figure 9 i-l). Two different types of aggregates

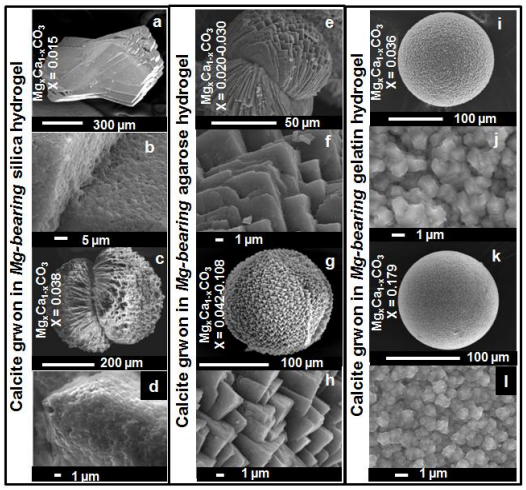

Figure 9. Calcite crystal aggregates grown in gelatin, agarose and silica hydrogels containing an initial Mg concentration of 0.1M. (a, c) Dumbbell-shaped aggregates grown in silica hydrogel. The characteristics of the flat porous surfaces of these aggregates are depicted in (b) and (d). The Mg content detected by EDX analyses on the surface of the aggregates is 1.5 (a) and 3.8 (c) mol % $MgCO_3$, respectively. (e) Sheaf-like shaped aggregate obtained from agarose hydrogel. The aggregate has two major subunits that consist of platy crystals in a sub-parallel arrangement (f). EDX analyses on the surface of this aggregate yield Mg contents between 2 and 3 mol % $MgCO_3$. (g, h) The rounded aggregate that was obtained in agarose hydrogel consists of numerous platy crystals in a radial arrangement. EDX analyses on the surface of the aggregates shown in (e) and (g) yielded 2.5 and 5 mol % $MgCO_3$ values, respectively. (i, k) Spherical aggregates obtained in gelatin hydrogel characterized by nanometric sub-blocks (j, i). The Mg content detected by EDX on the surface of these aggregates is 3.6 (i) and 17.9 mol % $MgCO_3$ (k), respectively.

can be distinguished regarding their size and composition. The first type consists of aggregates with sizes between 150 and 200 micrometers. These show ~ 0.8-1 micrometer sized sub-blocks on the surface. EDX analyses performed on the surface of these aggregates yield Mg contents that range from 3 to 10 mol% $MgCO_3$ (Figure 9i, j). The second type of precipitates includes aggregates with sizes < 100 micrometers. Their surface consists of rhombohedron-shaped sub-blocks. Mg concentrations derived from EDX measurements conducted on the surface of these aggregates vary between 13 and 28 mol% $MgCO_3$ (Figure 9k, l).

Characteristics of calcite crystal co-orientation patterns in mineral-hydrogel composites and their subunits. Calcite crystal co-orientation results were determined with high-resolution Electron Backscatter Diffraction (EBSD). Orientation results are presented in Figures 10 to 14. Crystal orientation is shown with color-coded EBSD maps and corresponding pole figures and pole density distributions of calcite c- and a*-axes. Microstructural characteristics of the aggregates and their subunits are visualized with EBSD band contrast images (Figures S3). EBSD band contrast gives the signal strength of the EBSD-Kikuchi diffraction pattern. This signal is high when a mineral is detected, while it is weak or absent when a polymer or an amorphous phase is scanned. Thus, the band contrast highlights well the distributions of the mineral and the hydrogel, respectively.

Misorientation of calcite within a subunit as well as between the subunits of the aggregates grown in Mg-free hydrogels is presented in Figures 10c, d, f, g, 11c, d, g, h and 12g, h, j, k. As the increased degree of misorientation shows, all aggregates have occluded a certain amount of hydrogel. While in calcite precipitated from solution (without any hydrogel in the structure) misorientation is only about 0.5 degrees corresponding approximately to the ±0.3° experimentalreproducibility of our EBSD experiment (Figure 10e), misorientation in the Mg-free silica hydrogel grown aggregate (Figure 10d) and in the two major subunits of the aggregate grown in Mg-free agarose (Figure 11d) is up to two degrees. As Figures 10f, g and 11g, h show, misorientation in the subunits of the Mg-free agarose grown aggregates is lower than that in the Mg-free silica hydrogel grown crystals. The degree of misorientation in the Mg-free silica hydrogel grown crystals goes up to two degrees, we even observe a stepping of the misorientation versus distance curves (Figures 10f, g) that indicates that the crystal does contain different parts, however, these are only very slightly misoriented to each other. In each of the two subunits of the aggregate that grew in agarose hydrogel calcite misorientation is about 0.5 degrees. While the aggregate that formed in Mg-free silica hydrogel is close to a single crystal (Figure 10a), the aggregate that grew in Mg-free agarose hydrogel is mainly composed of distinct subunits (Figure 11a). These subunits are separated from each other by hydrogel membranes (Figure 3b).

Misorientation in the aggregate that formed in gelatin hydrogel highly contrasts to that

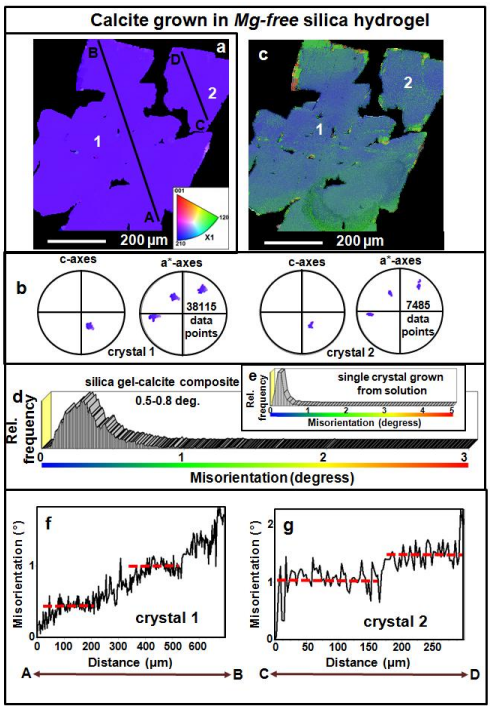

Figure 10. EBSD crystallographic co-orientation results of two calcite crystals (crystal 1 and crystal 2) grown in silica in a Mg-free environment: (a) Color-coded EBSD orientation map, (b) Corresponding pole figures showing the crystallographic orientation data crystal 1 and crystal 2. The corresponding band contrast image is shown in Figure S3a. The internal misorientation of (c) is shown in (d) in comparison to the internal misorientation of single crystal grown from solution (e), In local misorientation versus distance diagrams (f, g) taken over the profiles A-B and C-D (shown in a) the overall high co-orientation of the calcite c- and a*-axes is well visible. Note the profiles are almost 700 micrometers for crystal 1 and 300 micrometers for crystal 2, respectively. We observe steps in the local misorientation curves (marked by red dashed lines in images f and g) with a jump in misorientation of about 0.5 degrees. This proves an internal mosaicity that is present in the two crystals, thus, these two calcite-Mg-free silica hydrogel composite crystals are not perfect single crystals.

observed in aggregates obtained in silica and agarose hydrogels. The aggregate that formed in Mg-free gelatin hydrogel (Figure 12) is a radial, mosaic aggregate and is composed of distinctly sized and substructured subunits (Figure 12a). Calcite in all subentities of the subunits of this aggregate shows a mesocrystalline arrangement (Figures 12c, d, e), the degree of misorientation within a subunit is up to 2 degrees. The subentities of subunit 2 (Figure 12a, f) show a

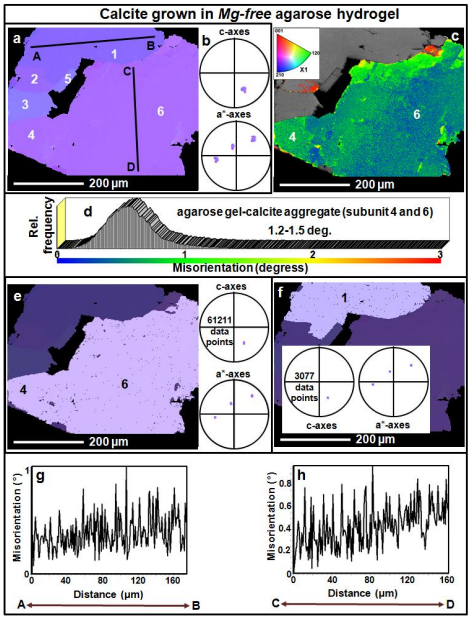

Figure 11. EBSD crystallographic co-orientation results for a calcite-Mg-free agarose hydrogel composite aggregate obtained in a Mg-free growth medium: (a) Color-coded EBSD orientation map of the entire aggregate, (b) Corresponding pole figure. The band contrast image is shown in Figure S3b. This aggregate is composed of two large (no. 1 and 6) and 4 small (no. 2 to 5) subunits as the pole figures in (e) and (f) show the subunits are single crystals. Internal overall misorientation for the subunits 4 and 6 is shown with the map in (c) and, in degrees, with a histogram in (d), respectively. These subunits have misorientation about 1.2 to 1.5 degrees. Local misorientation for the two large subunits 1 and 6 are shown in (g) and (h). For both subunits local misorientation is less than 1 degree. We do not observe any steps in the local misorientation patterns. Thus, within the subunits of the aggregate Mg-free agarose does not exert a major influence on crystal misorientation. However, it induces the formation of a radial aggregate composed of very few, quite similarly oriented, subunits (Figure S2b, e).

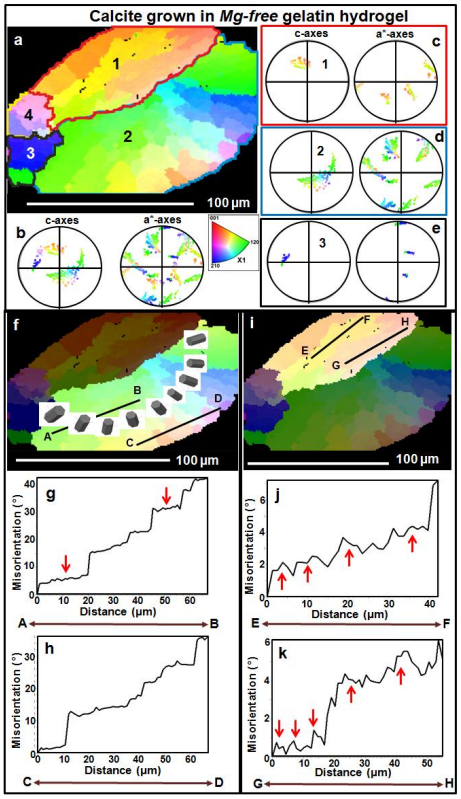

Figure 12. EBSD crystallographic orientation results for a calcite-gelatin hydrogel composite radial aggregate obtained in an Mg-free growth medium: (a) Color-coded EBSD orientation map of the entire aggregate, (b) Corresponding pole figure of measurements from the entire aggregate. The band contrast image of the aggregate is given in Figure S3c. This radial aggregate is composed of four large subunits (a), with these being internally further structured on different scale levels. Orientation patterns of individual subunits are shown in the pole figures (c), (d) and (e). Subunit 2 is a mosaic spherulite characterized by an even rotation in crystal orientation (f) and a misorientation between the entities of the spherulite of about 10 degrees (g, h). However as the pole figure in (d) shows and as indicated by the slight scatter of the misorientation graph within a unit of the spherulite (red arrows in g), the subunits of the spherulite are also mosaic crystals. Subunit 1 is an assemblage of a few large interlinked mesocrystals (a, pole figure in c, arrows highlighting the scatter in the diagram in k). The pole figures in (e) show that subunit 3 is a mesocrystal, with very minor tilt between the blocks of this subunit (very even color of subunit 3 in a).

spherulitic arrangement, the degree of misorientation between the subentities of the spherulites is between 5 and 10 degrees. The subunits are separated from each other by irregular incorporations of gelatin membranes (white stars in Figure 4b) but also contain an occluded dense network of gelatin hydrogel (Figure 4c). Although we always obtained mineral-gelatin hydrogel composites, the degree of mineralization of the subunits appears to differ. Some subunits show a higher mineralization (subunits I and II in Figure 4b), while others contain more of the dense, irregularly distributed gelatin hydrogel in the composite structure (subunit III in Figure 4b).

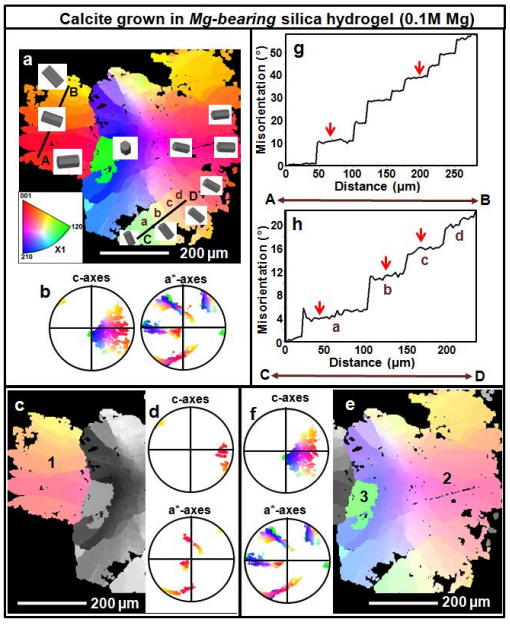

Figure 13. EBSD crystallographic co-orientation results for a calcite-silica hydrogel composite aggregate grown in a Mg-bearing growth medium: (a) Color-coded EBSD orientation map, (b) Pole figure, (S3) contrast image of the entire aggregate. This aggregate consists of two large and one small subunit (c, e). Calcite orientation patterns of subunits 1 and 2 are shown in the pole figures d and f. Subunits 1 and 2 are spherulites, subunit 3 is a single crystal. As the misorientation versus distance diagrams in Figures (g) and (h) show, subunits 1 and 2 are mosaic crystals (see the entities a, b, c, d in Figure a with a tilt of 5-6 degrees between them). In addition, the entities show an internal mesocrystalline arrangement of calcite (red arrow in g and h pointing to the scatter in the misorientation curve).

The addition of Mg to the hydrogel highly influences the morphology of the aggregate (Figures S2), its microstructure on several scalelevels (Figure S3) but also the mode of calcite co- and misorientation in the aggregate and in its subunits (Figures 13, 14). The aggregates that formed in Mg-bearing silica hydrogel are composed of three, to each other irregularly oriented, subunits (Figures 13c to f). The subentities of the subunits are clearly mesocrystals (see red arrows pointing to the slight scatter in the misorientation versus distance graph of a co-oriented unit in Figure 13h), that are bundled in an overall mosaic structure (large angle boundaries between co-oriented units Figure 13g) and are arranged in a spherulitic type arrangement (see the schematic crystal orientations in Figure 13a).

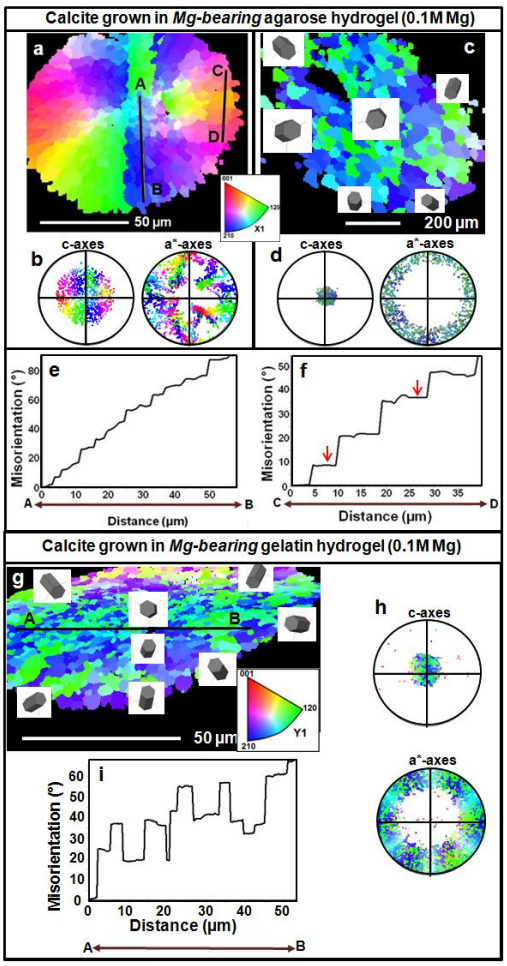

Figure 14. EBSD crystallographic co-orientation results for a calcite-agarose and calcite-gelatin hydrogel composite aggregate grown in a Mg-bearing growth medium: (a, c, g) Color-coded EBSD orientation maps, (b, d, h) Pole figures and (S3) band contrast image of the calcite-agarose and calcite-gelatin aggregate. The aggregates (a) and (c) have radial spherulitic microstructure, are mosaic crystals (see the large-angle tilt between the spherulites in e, f) but do not show a mesocrystalline substructure within the spherulites (see the absence of scatter within a spherulite unit (red arrow in f) in the misorientation curves shown in Figures (e) and (f)). The subentities of the spherulites are single crystals. The aggregate (g) is a radial spherulite, however, without clear-cut spherulitic subunits. These subunits are further structured into single crystal entities. As the misorientation diagram in (i) shows, large-angle boundaries are present between co-oriented subunits. Thus, this aggregate is a spherulite with a mosaic substructure.

Aggregates that form in Mg-bearing agarose hydrogels are cylindrically textured spherulites

(Figures 14a to f) assembled from co-oriented calcite rhombohedra. The aggregate in Figure 14a and c have been sectioned in two positions: (a) Within its middle and center part and (c) at the top of the aggregate. Depending on the position where the aggregate is cut, calcite c- and a*- axes are differently inclined to the plane of view. Is the aggregate cut at its top (Figure 14c), then calcite c-axes are about 80-90 degrees out (Figure 14d) and the a*-axes are more or less within the plane of view (Figure 14d), respectively. Is the aggregate cut in its median portion (Figure 14a), then the orientation of the c-axes is 50 to 90 degrees out (Figure 14b) and the a*-axes 40 to 90 degrees within the plane of view (Figure 14b), respectively. In comparison to the aggregate grown in Mg-bearing silica hydrogel we do not see any sign of mosaicity in the rhombohedra composing the spherulites grown in Mg-bearing agarose (compare Figure 13h to Figure 14f).

The aggregate that formed in Mg-bearing gelatin hydrogel (Figure 14g, h, i) is also a cylindrically textured spherulite with calcite c-axes being highly co-oriented and, in this cut, pointing 70 to 90 degrees out of the plane of view (Figure 14h). The a*-axes also show some systematic co-orientation, we observe a twin arrangement. As the misorientation versus distance curve shows, a mesocrystallinity in the subunits cannot be detected, the large angle boundaries point to a mosaic structure (Figure 14i).

DISCUSSION

Hydrogel incorporation into calcite. Incorporation of silica hydrogel into calcite was reported as early as 1969.[54] Recently the incorporation of both, gelatin and agarose hydrogels in amounts as high as ~4 wt% for crystals grown in gelatin (10 wt% gelatin solid content) and ~0.9 wt% for crystals grown in agarose, respectively (1 wt% agarose solid content) has been confirmed.[27,31,40-44,55] Estroff's group, following the force completion model for crystallization,[56-59] stated that growth rate and hydrogel strength are the main factors that control hydrogel incorporation into crystal aggregates during growth [31,40-42] and demonstrated that high growth rates lead to high amounts of incorporated hydrogel.[41] In addition, a positive relationship has been observed between growth rate and crystallization pressure, the pressure that is exerted by a growing crystal against the hydrogel network. The ability of this network to resist the crystallization pressure without breaking or being pushed away is defined as the hydrogel strength.[31,41] Strong hydrogels that resist high crystallization pressures are easily incorporated into the growing crystal while weak hydrogels are pushed away.[41,60-62] For a given hydrogel its strength increases with increasing hydogel solid content.[19,32-36] In agreement with Estroff's and coworkers' results on calcite crystals grown in agarose, we recently found a positive correlation between the amount of hydrogel incorporated into calcite crystals and the solid content of gelatin hydrogels.[44] Growth rate is also proportional to supersaturation.[59,63] Consequently, high amounts of hydrogel are expected to be incorporated when crystals grow under high supersaturation conditions. In calcite-agarose composites formed under high supersaturation conditions, it was found that the amount of incorporated hydrogel corresponded to ~100% when agarose fibers constitute the hydrogel network.[31]

Calcite-hydrogels composites formed in Mg-free hydrogel media. Irrespective of the type of hydrogels used and the presence or absence of Mg in the growth medium, all calcite crystals and crystal aggregates that were obtained in this study incorporated hydrogels. The morphologies of calcite crystals and crystal aggregates obtained in Mg-free hydrogels point to them forming under high supersaturation conditions. This interpretation is supported by the rough surfaces and hopper developments of calcite aggregates grown in Mg-free gelatin hydrogels and the radial crystal aggregates with curved edges and surfaces obtained from Mg-free agarose hydrogels. Under these conditions the high growth rate effect will dominate over possible effects contributed from the incorporated hydrogels and their strength.[32,33,64]

The high crystal co-orientation that is a characteristic feature of silica-calcite composites can be explained according to the model proposed by Estroff and collaborators.[31,40-42] The hydrogel membranes between the subunits of calcite/agarose and calcite/gelatin hydrogels are created as the hydrogel networks are pushed aside by the growing crystal. No evidence of these membranes can be found in SEM images of agarose or gelatin hydrogels prior to crystallization (Figures 1c to f). Therefore, we conclude that these membranes form during crystallization, as a result of the crystal growth process itself (Figure S5). Indeed, as explained above, Estroff and collaborators' model derives from the force completion model for crystallization in the presence of particles,

which proposes that between a foreign particle and an approaching growth front "a disjoining force" forms.[56-59] This "disjoining force" originates from repulsion of the van der Waals forces and disfavours particle incorporation into the crystal. It is opposed by a hydrodynamic force which is considered to be proportional to the growth rate and promotes particle incorporation. If the "disjoining force" predominates, the growth front pushes the particle ahead and incorporation will not occur (Figure S5). While the incorporation of Mg-free silica hydrogel into calcite hardly seems to have any effect on any characteristics of calcite crystals, Mg-free agarose and gelatin hydrogels appear to be responsible for the development of specific microstructural features of the mineral. In the presence of agarose and gelatin hydrogels (without Mg in the growth medium) calcite aggregates consist of subunits that are separated from each other by hydrogel membranes. These are thinner membranes in Mg-free agarose hydrogel (Figure 3b) than those in Mg-free gelatin hydrogel (Figures 4b, c). In the case of calcite grown in Mg-free agarose hydrogel, the subunits are few in number, they are co-oriented, and they have a very low internal misorientation (0.5º). The incorporated hydrogel network is evenly distributed within the subunits. On the contrary, calcite aggregates grown in Mg-free gelatin hydrogel consist of numerous subunits which are further sub-structured. The subunits can be very different from each other in both internal misorientation (differences can be as high 10 degrees) and in the amount of incorporated hydrogel.

The hydrogel membranes between the subunits of calcite-agarose and calcite-gelatin hydrogels are created as the hydrogel networks are pushed aside by the growing crystal. No evidence of these membranes can be found in SEM images of agarose or gelatin hydrogels prior to crystallization (Figures 1c to f). Therefore, we conclude that these membranes form during crystallization, as a result of the crystal growth process itself. Indeed, as explained above, Estroff and collaborators' model derives from the force completion model for crystallization in the presence of particles, which proposes that between a foreign particle and an approaching growth front "a disjoining force" forms.[56-59] This "disjoining force" originates from repulsion of the van der Waals forces and disfavors particle incorporation into the crystal. It is opposed by a hydrodynamic force which is considered to be proportional to the growth rate and promotes particle incorporation. If the "disjoining force" predominates, the growth front pushes the particle ahead and incorporation will not occur.

Under the conditions established in this work the silica hydrogel porous network is built up by coalescence of silica nanoparticles. If the hydrogel is able to plastically deform, as it is the case for gelatin and agarose hydrogels, hydrogel fibers will displace and become squeezed together in between those crystals. The hydrogel polymers hence become concentrated in areas between crystals and rearrangements occur in the structure of the network and the membranes such as those observed between calcite subunits grown in gelatin and agarose hydrogels. It stands to reason that the thickness of these membranes will depend on the density of hydrogel fibers in a particular hydrogel. The very different thickness of hydrogel membranes in calcite-agarose and calcite-gelatin composites can, thus, be explained by a high solid concentration in the dense gelatin (10 wt% solid in the hydrogel) compared to that of the agarose hydrogel (1 wt% hydrogel solid content). Since the dipolar forces involved in the co-orientation of crystal sub-blocks strongly decrease with distance, it can be expected that the formation of thick hydrogel membranes in dense hydrogels leads to less co-oriented aggregates composed of a large number of subunits. These classifications agree well with the features that we find when we compare the calcite microstructure obtained in different hydrogels. Is a brittle hydrogel locally broken, membranes will not form and the porous network will appear. The microstructure of calcite-silica composites evidences this disruption of the silica hydrogel porous network at the calcite-silica hydrogel interface, where broken pore walls can clearly be observed (Figure 5c).

The formation of membranes has a two-fold effect on the characteristics of the hydrogel network: on the one hand, since hydrogel strength is concentration dependent, hydrogel membranes are stronger than the rest of the hydrogel network. On the other hand, since diffusivity through a porous medium is strongly affected by pore size and pore wall thickness, the formation of hydrogel membranes locally alters diffusivity, hindering mass transfer and leading to local decreases in supersaturation and, consequently, in growth rates. The complex balance between these two effects, one, which favours hydrogel incorporation and the other that makes it less likely, can explain the uneven distribution of hydrogel in adjacent subunits that are separated by a hydrogel membrane. In turn,

this uneven hydrogel incorporation determines internal structuring, with adjoining subunits being mesocrystals or mosaic crystals, depending on the amount of incorporated hydrogel.

Calcite-hydrogel composites formed in Mg-bearing hydrogel media. Calcite-hydrogel aggregates formed in the presence of Mg show major differences with respect to their counterparts grown in Mg-free hydrogels. Irrespective the hydrogel considered these differences include more complicated mineral microstructure and morphologies; higher number of subunits constituting the aggregates and larger misorientation within and between subunits are the results. These differences are less marked in aggregates that formed in Mg-bearing silica hydrogel but become important in aggregates grown in Mg-bearing agarose hydrogel and, more so, in aggregates that grew in Mg-bearing gelatin hydrogels. It is interesting to observe, that the amount of Mg incorporated into calcite follows the same trend, with the lowest $MgCO_3$ contents (up to 3 mol%) detected in aggregates formed in silica hydrogel and the highest $MgCO_3$ contents (up to 28 mol%) found in aggregates grown in gelatin hydrogel. It has frequently been argued that high supersaturation[39] promotes the incorporation of impurities into crystals structures. Although the characteristics of all the aggregates formed in this work point to them forming under high supersaturations, we have no evidence that would allow us to assign the differences in $MgCO_3$ contents of calcite grown in different hydrogels to differences in supersaturation during crystal growth. In a recent paper, we proposed an active role of the acidic groups of gelatin in promoting Mg desolvation and facilitating its incorporation into the calcite structure to explain the very high $MgCO_3$ contents detected in calcite-gelatin composites.[39] The role of Mg in the formation of calcite-gelatin composites is two-fold. On the one hand, there is overwhelming evidence that Mg significantly inhibits calcite growth.[65-69] On the other hand, Mg incorporation into the calcite structure substituting Ca requires a tilting of the planar carbonate groups, thereby inducing structural disorder.[70,71] Moreover, due to their different geometries, Mg incorporates differently into kink sites on parallel $\langle \bar{4}41 \rangle$ growth steps on calcite (104) surfaces (obtuse "+", more open, step edges and acute "-", less accessible, step edges). This induces misfit strain into the system.[72-75] Mg inhibition of the calcite growth rate could lead to a reduction in the amount of hydrogel incorporated into the calcite-gelatin composites, an effect not supported by our observations. On the contrary, the comparison between Figure 2 and Figure 5 evidences that a similar amount of network is incorporated in silica-calcite composites, irrespective whether Mg was present in the growth medium or not. A similar conclusion can be derived for calcite-agarose and calcite-gelatin composites from the comparison of Figure 3 to Figure 6 and Figure 4 to Figure 7. The absence of hydrogel membranes is striking and two Mg-related effects might cause this feature: (i) possible changes in rheological properties of both hydrogels (when Mg is present) and (ii) changes in crystallization pressure due to the growth inhibiting effect of Mg. Although the second effect more likely plays a role, a modified mechanical response of Mg-bearing gelatin and agarose hydrogels to crystallization pressure cannot be entirely disregarded. Indeed, changes in gelatin fibers structuring related to the presence of specific ions in the growth medium have been previously proposed by Tlalik et al. (2006)[95] to explain differences in the characteristics of gelatin-fluorapatite-gelatine nanocomposites.

The lattice strain that is induced by Mg incorporation into the calcite structure can play a cooperative role in hydrogel incorporation and to some degree explains the higher misorientations within and between the subunits of the aggregates formed in any of the hydrogels in the presence of Mg in the growth medium. This interpretation is in good agreement with the degree of misorientation correlating the $MgCO_3$ content of the different aggregates. Aggregates that grew in silica hydrogel have the lowest Mg contents and show a low degree of misorientation between subunits, while aggregates that grew in gelatin hydrogel incorporated the highest amount of Mg and show the highest degree of misorientation within the aggregate. To explain the frequent small angle boundaries in Mg-calcite, in a previous paper we proposed the formation of dislocations at regular intervals that release the misfit strain associated with the differential incorporation of Mg.[39] This mechanism can lead to the formation of spherulites through accumulative split growth and can, to a certain extent, explain the morphological characteristics of the aggregates formed in agarose and gelatin hydrogels in the presence of Mg.

The comparison with nature: Biopolymer membrane and network structures in natural skeletons. Biological hard tissues are complex hierarchical structures that consist of a large variety of design concepts that extend over several scale levels.[76-78] On small structural scales biological hard tissues are composites of a compliant matrix that is reinforced by stiff components, often minerals. For example plant tissues consist of micrometer sized cellulose fibers embedded in an amorphous hemicellulose matrix,[79] arthropods with a mineralized cuticle contain nanometer sized chitin fibers that are surrounded by a proteinaceous matrix[80-82] and mineralized tissues such as shells and are assembled by stacks of mineral platelets or arrays of mineral fibers embedded in a protein-polysaccharide matrix.[83-86]

The compliant component of gastropod, bivalve and brachiopod shells is an insoluble silk-like protein that forms the basic matrix structure for the assemblage of soluble polyanionic proteins and calcium carbonate minerals.[83-86] While the silk-like proteins form membranes and provide the scaffold, polyanionic proteins mainly control crystal nucleation and orientation and formation of carbonate crystal entities such as platelets, prisms and fibers.[84,85] Figure 15 shows organic matrices in bivalve and gastropod shells that were made visible by complete decalcification of the carbonate hard tissue. These membranes are a few nanometers thick, subdivide space and envelope aggregations of carbonate nanoparticles (Figures S4a, b). In biological hard tissues these interlamellar (interfiber) membranes are always porous (Figures 15b, d) since they have to facilitate the transfer of carbonate mineral and crystallographic orientation information from one compartment-fiber to the other.[87,88] Within the compartments-fibers, a biopolymer network of fibrils can be distinguished (Figure 16). These infiltrate the space between the nanoparticles of a compartment or fiber and cause misorientation between the nanopartlicles. For example in nacre tablets misorientation between crystallites in a tablet is between 2 to 4 degrees.[9] For carbonate biomimetic systems Nindiyasari et al. 2014 have shown that gelatin is incorporated in the subunits of a carbonate-gelatin hydrogel aggregate.[44] An increase in gelatin content of the hydrogel from 2.5 to 10 wt% leads to an increase in misorientation between crystallites in the subunit of the composite aggregate from two to six degrees.

Organic matrix formation was investitgated by Nakahara and Bevelander 1969[89], Weiner and

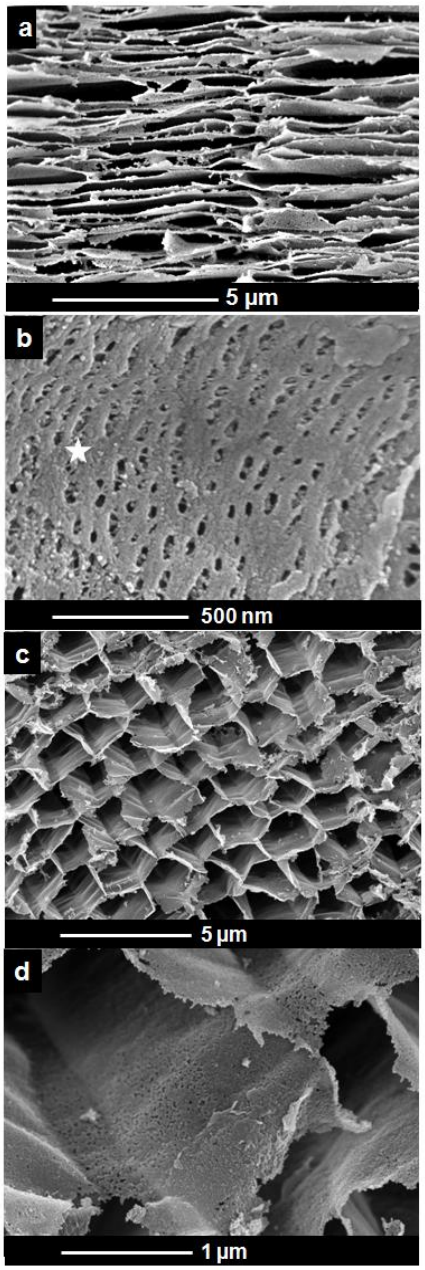

Figure 14. FE-SEM micrographs of microtome cut, polished, etched, decalcified and critical point dried biopolymer membranes. (a) A completely demineralized aragonitic shell portion of the gastropod *Haliotis assinina*. The mineral is entirely etched away and the remaining biopolymer membranes are stabilized and visualized (a). Well traceable in (a) are the former locations of columns composed of aragonitic tablets. (b) Biopolymer membranes showing the porous structure of the membranes (star in b) obtained from modern carbonate shells of aragonitic shell portion of the gastropod *Haliotis assinina*. (c, d) Biopolymer membranes in the bivalve *Mytilus edulis* as membranes surrounding calcite fibers (c, d) in the calcitic part of the shell.

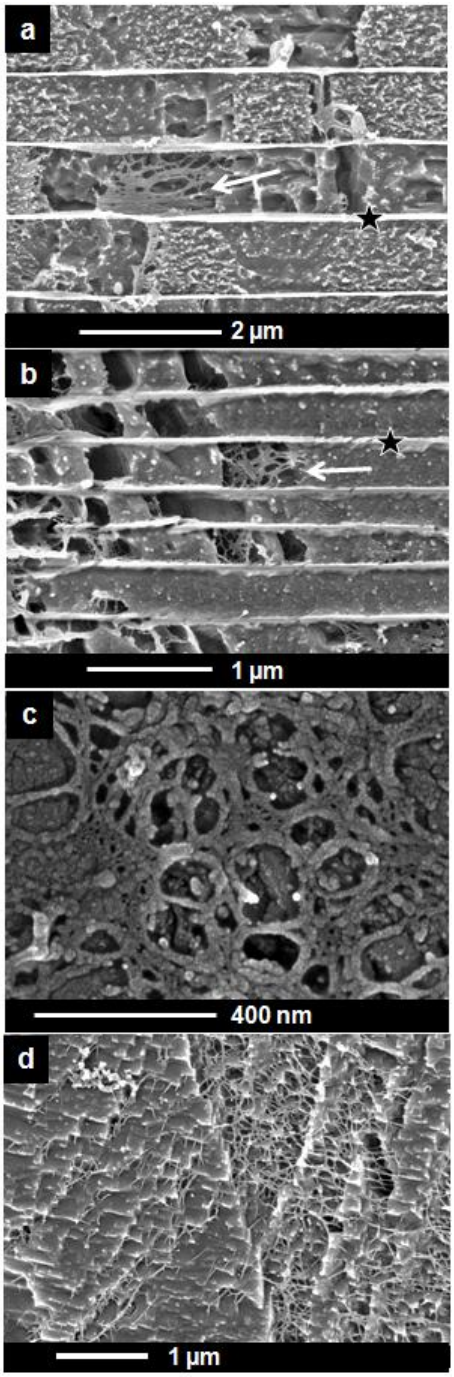

Figure 15. FE-SEM micrographs of microtome cut, polished, etched and critical point dried surfaces highlighting dense biopolymer networks that are present in modern carbonate skeletons. Within the aragonitic shell portions of the bivalve *Mytilus edulis* (arrow in a) and the gastropod *Haliotis assinina* (arrow in b), respectively, between the cells of the corraline red algae *Clathromorphum compactum* (c). The shell portion of the modern gastropod *Haliotis laevigata* shows a delicate biopolymer network of fibers that permeates the calcitic part of the shell (d).

Traub 1980[90], Fritz and Morse 1998[91], Addadi et al. 2006[92], Nudelmann et al. 2006[93], Checa et al.2005[87], Cartwright and Checa 2007[94], Checa et al. 2011[88], Gries et al. 2011[86]. Cartwright and Checa2007[94] propose that organic matrix formation starts with the self-assembly of liquid-crystalline core consisting of chitin fibers assembled through self-organization. These fibers are not bonded closely together to each other, thus, this fibrous structure is not yet strong enough to form the scaffold. According to Cartwright and Checa 2007[94] proteins with an affinity for chitin cover the chitin layer. This yields a chitin fiber-polymer composite that is strong enough to act as the supporting matrix for the carbonate hard tissue. Hydrogels are regarded to model biogenic matrix environments, due to their ability to confine space and to determine diffusion rates, local concentrations and supersaturation of solutes. However, hydrogel fiber organization lacks any order, unlike cholesteric liquid phases, e.g. chitin. Figure S5 shows the fabric of gelatin and agarose hydrogels after complete decalcification of the hydrogel-calcite aggregates. We observe some co-alignements of hydrogel fibers, however, we do not find any membranes in the decalcified hydrogel-calcite composites resembling those present in carbonate hard tissues. An increase in hydrogel solid content concentration will increase local hydrogel fiber co-alignements that will mimic organic matrices in biologic hard tissues to some extent. Furthermore, the presence of specific ions and molecules in the aqueous solution filling the hydrogel porous network will also introduce a certain degree of organization in the fiber arrangement.[95] Differences in fiber structuring will affect the mechanical properties of the hydrogels and will control their ability to deform under crystallization pressure. Thus, hydrogels can be fine tuned for the reproduction of some organization patterns of organic components in biological hard tissues, however, due to their high chemical complexity biological systems will never be fully reproduced by biomimetic counterparts. Further research is needed using hydrogels where both, proteins together with oligo- and polysacharides are simultaneously present,[55] a situation that can be attained by using combinations of different hydrogels and chitin. In addition to membranes we observe in carbonate hard tissues also the presence of fibril networks (Figure 16). These show similarities to the network present in the inorganic hydrogel counterparts.

CONCLUSIONS

The main feature of the mineralization environment of biological carbonate hard tissues is an extracellular-matrix that consists of a three-dimensional assembly of proteins, polysaccharides and glycoproteins. Hydrated networks of these biopolymers compartementalize space and thus control morphology, functionalities, which are the template for carbonate crystal nucleation and induce misorientation between nanoscale units which assemble to biocrystals such as nacre tablets or calcite fibers.

Hydrogels mimic to some extent biological extracellular matrices, since the local crystallization microenvironment in the hydrogel is distinguished from that in solution by confinement of solutes in the pores of the hydrogel network. In this study we investigated the influence of silica, agarose and gelatin hydrogels on carbonate crystal assembly and co-orientation and carbonate aggregate formation for a better understanding of both, biomimetic carbonate formation as well as the assembly of matrix-mediated carbonate biological hard tissues. From our study we deduce the following conclusions:

1. While the hydrogel fabric of agarose and gelatin hydrogels is comparable to each other, it is significantly different from that of silica hydrogel. In the case for the first two gels the fabric consists of a 3D network of fibres, whereas silica gel is a three-dimensional agglomeration of nanometric spherical particles.
2. All three hydrogels are occluded into the mineral, however, when the growth medium is free of Mg silica hydrogel does not impose a marked effect on mineral co-orientation and aggregate formation. Agarose gel and especially gelatin hydrogel impose a strong influence on aggregate formation. In magnesium-free environments either single crystals or radial aggregates with very few misoriented subunits are formed.
3. Is magnesium added to the growth medium the amount of internal boundaries in the crystal aggregates increases drastically and the number of subunits in an aggregate increases accordingly. In the case of silica gel very few subunits form an aggregate, and the individual subunits are partial spherulites. The subcrystals of the partial spherulite are further structured and are mesocrystals.
4. In the case of agarose and gelatin gels the addition of Mg to the growth medium drastically induces the formation of small and large angle boundaries and we obtain in both cases complete spherulites. In a radial profile the small angle boundaries are below 10 degrees, while in tangential profiles through the spherulite grain boundary misorientations form major steps in the order of 8 to 15 degrees. We do not see mesocrystallinity in the individual subunits of the spherulites. We attribute this growth process to accumulative split growth related to Mg incorporation.
5. In weak hydrogels such as Mg-free gelatine or agarose gels, growing crystals push gel matrix ahead of their growth front, such that gel accumulates to form membranes between crystals which nucleate in proximity and abut against each other after growth. In strong hydrogels such as Mg-bearing gelatine or agarose the gel becomes more incorporated than pushed ahead of the growing crystals, and consequently the membranes between abutting crystals are less pronounced.

Acknowledgements. This research is part of the German-Spanish joint Acciones Integradas program (AIB2010 DE-0008), DAAD-50749739. F.N. is grateful for a stipendium by KAAD. E.G. is supported by Deutsche Forschungsgemeinschaft, DFG grant number GR-1235/9-1. This research was partially funded by project CGL2010-20134-C02-01 (MECC-Spain). We sincerely thank the staff of the National Microscopy Centre (ICTS) of the Complutense University (UCM) for technical support and assistance.

REFERENCES

1. Lowenstam, H.A. and Weiner, S. (Eds) (1989) On Biomineralization. Oxford University Press, Inc., New York, 324 pp
2. Mann, S. Biomineralization: Principles and concepts of in biorganic materials chemistry. Oxford University Press, New York, 2001.
3. Robach, J. S.; Stock, S. R.; Veis, A. *J. Struct. Biol*. 2005, *151*, 18-29.
4. Robach, J. S.; Stock, S. R.; Veis, A. *J. Struct. Biol*. 2009, *168*, 452-466.
5. Alvares, K.; Dixit, S.N., Lux, E.; Veis, A. *J. Biol. Chem.* 2009*, 284*,26149-26160.
6. Li, H.; Xin, H.L.; Kunitake, M.E.; Keene, E.C.; Muller, D.A.; Estroff, L.A. *Adv.*

Funct. Mater. 2011, *21*, 2028–2034.
7. Griesshaber, E.; Schmahl, W. W.; Neuser, R.; Pettke, T.; Blüm, M.; Mutterlose, J.; Brand, U. *Am. Mineral.* 2007, *92*, 722-734.
8. Goetz, A. J.; Steinmetz, D. R.; Griesshaber, E.; Zaefferer, S.; Raabe, D.; Kelm, K.; Irsen, S.; Sehrbrock, A.; Schamhl, W. W. *Acta Biomaterialia* 2011, *7*, 2237–2243.
9. Griesshaber, E.; Schmahl, W. W.; Ubhi, H. S.; Huber, J.; Nindiyasari, F.; Maier, B.; Ziegler, A. *Acta Biomaterialia* 2013, *9*, 9492-9502.
10. Goetz, A. J.; Griesshaber, E.; Abel, R.; Fehr, Th.; Ruthensteiner, B.; Schmahl, W. W. *Acta Biomaterialia* 2014, *10*, 3885-3898.
11. Kim, Y.-Y.; Schenk, A. S.; Ihli, J.; Kulak, A. N.; Hetherington, N. B. J.; Tang, C. C.; Schmahl, W.; Griesshaber, E.; Hyett, G.; Meldrum, F. C. *Nat. Comms.* 2014, *5*, 1-14.
12. Raz, S.; Weiner, S.; Addadi, L. *Adv. Mater*. 2000, *12*, 38-42.
13. Erez J. *Rev. Mineral. Geochem.*, 2003, *54*, 115-149.
14. Bentoz, S.; Erez, J. *Geochem. Geophy. Geosy*. 2006, *7*, 1-11.
15. Ma, Y.; Aichmayer, B.; Paris, O.; Fratzl, P.; Meibom, A.; Metzler, R. A.; Politi, Y.; Addadi, L.; Gilbert, P. U. P. A.; Weiner, S. *Proc. Natl. Acad. Sci. U.S.A.* 2009, *106*, 6048–6053.
16. Lenders, J. J. M.; Dey, A.; Bomans, P. H. H.; Spielmann, J.; Hendrix, M. M. R. M.; de With, G.; Meldrum F. C.; Harder, S.; Sommerdijk, N. A. J. M. *J. Am. Chem. Soc*. 2011, *134*, 1367-1373.
17. Carpenter, S .J.; Lohmann, K.C. *Geochim. Cosmochim. Ac.* 1992, *56*, 1837-1849.
18. Sancho-Thomas, M.; Fermani, S.; Durán-Olivencisa, M. A.; Otálora, F.; Gómez-Morales, J.; Falini, G.; García-Ruiz, J. M. *Cryst. Growth Des.* 2013, *13*, 3884-3891.
19. Henisch, H. K. *Crystals in Gels and Liesegang Rings*; Cambridge University Press: Cambridge, 1988.
20. McCauley, J. W.; Roy, R. *Am. Mineral.* 1974, *59*, 947-963.
21. García-Ruíz, J. M.; Amorós, J. L. *J. Cryst. Growth* 1981, *55*, 379-383.
22. Prieto, M.; Putnis, A.; Arribas, J. ;Fernández-Díaz, L. *Min. Mag*. 1992, *56*, 587-598.
23. Fernández-Diaz, L.; Putnis, A.; Prieto, M.; Putnis, C. V. *J. Sediment Res*. 1996, *66*, 482-491.
24. Helbig, U. *J. Cryst. Growth* 2008, *310*, 2863-2870.
25. Falini, G.; Fermani, S.; Gazzano, M.; Ripamonti, A. *Chem. Eur. J.* 1997, *3*, 1807-1814.
26. Sancho-Thomas, M.; Fermani, S.; Goffredo, S.; Dubinsky, Z.; García-Ruiz, J. M.; Gómez-Morales, J.; Falini, G.; *Cryst. Eng. Comm.* 2014, *16*, 12571267.
27. Grassmann, O.; Muller, G.; Löbmann, P. *Chem. Mater.* 2002, *14*, 4530-4535.
28. Grassmann, O.; Neder, R. B.; Putnis, A.; Löbmann, P. *Am. Mineral.* 2003, *88*, 647-652.
29. Grassmann, O.; Löbmann, P. *Chem. Eur. J.* 2003, *9*, 1310-1316.
30. Dorvee, J.R.; Boskey, A.L.; Estroff, L.A. *CrystEngComm.*, 2012,*14*, 5681-5700.
31. Asenath-Smith, E.; Li, H.; Keene, E. C.; She, Z. W.; Estroff, L. A. *Adv. Funct. Mater*. 2012, *22*, 2891-2914.
32. Normand, V.; Lootens, D. L.; Amici, E.; Plucknett, K. P.; Aymard, P. *Biomacromolecules* 2000, *1*, 730-738.
33. Van den Buckle, A. I.; Bogdanov, B.; de Rooze, N.; Schacht, E. H.; Cornelissen, M.; Berghmans, H. *Biomacromecules*, 2000, *1*, 31-38.
34. Lee, K. Y.; Mooney, D. J. *Chem. Rev.* 2001, *101*, 1869-1879.
35. Dorvee, J. A.; Boskey, A. L.; Estroff, L.A. *CrystEngComm*. 2012, *14*, 5681–5700.
36. Hoffman, A. S. *Advanced Drug Delivery Reviews* 2002, *54*, 3-12.
37. Lefaucheux, F.; Robert, M. C. *Handbook of Crystal Growth*, Vol. 2, Ed: D. T. J. Hurle; Elsevier Science: Amsterdam 1994 .
38. Warren, B. E. *Chem. Rev.* 1940, *26*, 237-255.
39. Nindiyasari, F.; Griesshaber, E.; Fernández-Díaz, L.; Astilleros, J. M; Sánchez-Pastor, N.; Ziegler, A.; Schmahl, W. W. *Cryst. Growth Des*. 2014, 14, 4790-4802.
40. Li, H.; Estroff, L. A. *CrystEngComm*. 2007, *9*, 1153-1155.
41. Li, H.; Estroff, L. A. *Adv. Mat.* 2009, *21*, 470-473.
42. Li, H.; Fujiki, Y.; Sada, K.; Estroff, L. A. *CrystEngComm.* 2011, *13*, 1060-1062.
43. Simon, P.; Carrillo-Cabrera, W.; Huang, Y. X.; Buder, J.; Borrmann, H.; Cardoso-Gil, R., Roseeva, E.; Yarin, Y.; Zahnerty, T.; Kneip, R. *Eur. J. Inorg. Chem.* 2011, *35*, 5370-5377.
44. Nindiyasari, F.; Fernández-Díaz, L.; Griesshaber, E.; Astilleros, J. M; Sánchez-Pastor, N.; Schmahl, W. W. *Cryst. Growth Des*. 2014, *14*, 1531-1542.
45. Elhadj, S.; De Yoreo, J. J.; Hoyer, J. R.; Dove, P. M. *Proc. Natl. Acad. Sci. U.S.A*.

2006, *103*, 19237.
46. Boedtker, H.; Doty, P. *J. Phys. Chem*. 1954, *58*, 968−983.
47. Zhang, Z. K.; Li, G. Y.; Shi, B. *J. Soc. Leather Technol. Chem*. 2006, *90*, 23−28.
48. Fabritius, H.; Walther, P.; Ziegler, A. *J. Struct. Biol.* 2005, *2*, 190-199.
49. Moor, H. Riehle, U. *Proceedings 4th European Reg. Conf. Electron Microsc.* 1968, *2*, 33-34.
50. Müller, M. Moor, H. *Proceedings of the 42nd Ann. Meet. Electron Microsc. Soc. Am.* (ed. By G. W: Bailey), 1984, 6-9.
51. Walther, O.; Ziegler, A. *J. Microsc.* 2002, *208*, 3-10.
52. Walther, P. *J. Microsc.* 2003, *212*, 34-43.
53. Walther, P. *J. Microsc.* 2008, *232*, 379-385.
54. Nickl, H. J.; Henisch, H. K. *J. Electrochem. Soc.* 1969, *116*, 1258-1260.
55. Huang, Y.; Buder, J.; Cardoso-Gil, R.; Prots, Y.; Carrillo-Cabrera, W.; Simon, P.; Kniep, R. *Angew. Chem. Int. Ed.* 2008, *47*, 8280-8284.
56. Chernov, A. A.; Temkin, D. E. in *Current Topics in Materials Science* , Vol. 2 (Ed: E. Kaldis), North-Holland, New York 1977, 3-77.
57. Chernov, A. A., Temkin, D.E., Melnikova, A. M. *Sov. Phys. Crystallogr.* 1976, *21*, 369-74.
58. Chernov, A. A., Temkin, D. E., Melnikova, A. M. *Sov. Phys. Crystallogr*. 1977, *22*, 656-58.
59. Chernov, A. A. *Modern Crystallography III: Crystal Growth*. Springer: Berlin, Heidelberg, New York, Tokyo, 1984.
60. Pötschke, J.; Rogge, V. *J. Cryst. Growth* 1989, *94*, 726–738.
61. Gavira, J. A.; García-Ruiz, J. M. *Acta Crystallogr. Sect. D-Biol. Crystallogr*. 2002, *58*, 1653-1656.
62. Khaimov-Mal'kov, V. I. *Sov. Phys.: Crystallogr.* 1958, *3*, 487-493.
63. De Yoreo, J. J.; Vekilov, P. G. *Rev. Mineral. Geochem.* 2003, *54*, 57-93.
64. Ross-Murphy S.B. *Polymer* 1992, *33*, 2622-2627.
65. Davis, K. J., Dove, P. M., De Yoreo J. J. *Mat. Res. Soc. Symp*. 2000, *620*, M9.5.1-M9.5.7.
66. Davis, K. J., Dove, P. M., De Yoreo, J. J. *Science* 2000, *290*, 1134–1137.
67. Astilleros, J. M., Pina, C. M., Fernández-Díaz, L. Putnis, A. *Surf. Sci.* 2003, *545*, 767-773.
68. Astilleros, J. M., Fernández-Díaz, L., Putnis, A. *Chem. Geol.* 2010, *271*, 52–58.
69. Nielsen, L.C., De Yoreo, J. J., De Paolo, D. J. *Geochim Cosmochim Ac.* 2013, *115*, 100-114.
70. Bischoff, W.D., Sharma, S.K ., Mackenzie, F.T. *Am. Min.* 1985, *70*, 581-589.
71. Urmos, J., Sharma, S. K., Mackenzie F. T. *Am. Min.* 1991, *76*, 641-646.
72. Staudt, W.J.; Reeder, R.J.; Schoonen, W. A. A. *Geochim. Cosmochim. Ac.* 1994, *58*, 2087-2098.
73. Paquette, J., Reeder, R. J. *Geochim. Cosmochim. Ac.* 1995*, 59*, 735-749.
74. Jordan, G., Rammensee, W. *Geochim. Cosmochim. Ac.* 1998, *62*, 941-947.
75. Davis, K. J.; Dove, P. M.; Wasylenki, L.E.; De Yoreo, J. J. *Am.Min.* 2004, *89*, 714–720.
76. Fratzl, P.; Weinkammer, R. *Prog. Mater. Sci.* 2007, 52, 1263-1334.
77. Dunlop, J. W. C.; Fratzl, P. *Scripta Mater.* 2013, 68, 8-12.
78. Bar-On, B.; Wagner, H. D. *Ac. Biomater.* 2013, 9, 8099-8109.
79. Bungert, I.; Fratzl, P. *Phil. Trans. R. Soc. A.* 2009, 367, 1541-1557.
80. Hild, S.; Neues, F.; Znidarsic, N.; Struts, J.; Epple, M.; Marti, O.; Ziegler, A. *J. Struct. Biol.* 2009, 168, 426-436.
81. Seidl, B.; Huemer, K.; Neues, F.; Hild, S.; Matthias, E.; Ziegler, A. *J. Struct. Biol.* 2011, 3, 512-526.
82. Huber, J.; Fabritius, H.-O.; Griesshaber, E.; Ziegler, A. *J. Struct. Biol.* 2014, 188, 1-15.
83. Blank, S.; Arnoldi, M.; Khoshnavaz, S.; Treccani, L.; Kuntz, M.; Mann, K.; Grathwohl, G.; Fritz, M. *J. Microscopy 2003,* 112, 280-291.
84. Marin, F.; Luquet, G. *C. R. Palevol.* 2014, 3, 469-492.
85. Marin, F.; Luquet, F.; Marie, B.; Medakovic, D. *Curr. Top. Dev. Biol.* 2008, 80, 209-276.
86. Gries, K.; Heinemann, F.; Gimmick, M.; Ziegler, A.; Rosenauer, A.; Fritz, M. *Cryst. Growth Des.* 2011, 11, 729-734.
87. Checa, A. G.; Rodríguez-Navarro, A. B.; Esteban-Delgado, J. *Biomaterials* 2005, 26, 6404-6414.
88. Checa, A. G.; Cartwright, J. H. E.; Willinger, M.-G. *J. Struct. Biol.* 2011, 176, 330-339.
89. Nakahara, H.; Bevelander, G. *Tex. Rep. Biol. Med.* 1969, 101-109.
90. Weiner, S.; Traub, W. *FEBS Letters* 1980, 111, 311-316.
91. Fritz, M.; Morse, D. E. *Curr. Opin. Cell. Biol.* 1998, 3, 55-62.
92. Addadi, L.; Joester, D.; Nudelman, F.; Weiner, S. *A European J.* 2006, 12, 981-987.

93. Nudelman, F.; Gotliv, B. A.; Addadi, L.; Weiner, S. *J. Struct. Biol.* 2006, 153, 176-187.
94. Cartwright, J. H. E.; Checa, A. *J. Royal Interface* 2007, 4, 491-504.
95. Tlatlik, H.; Simon, P.; Kawska, A.; Zhan, D.; Kniep, R. *Angew. Chem. Int. Ed.* 2006, 45, 1905 –1910.

Supplementary Information

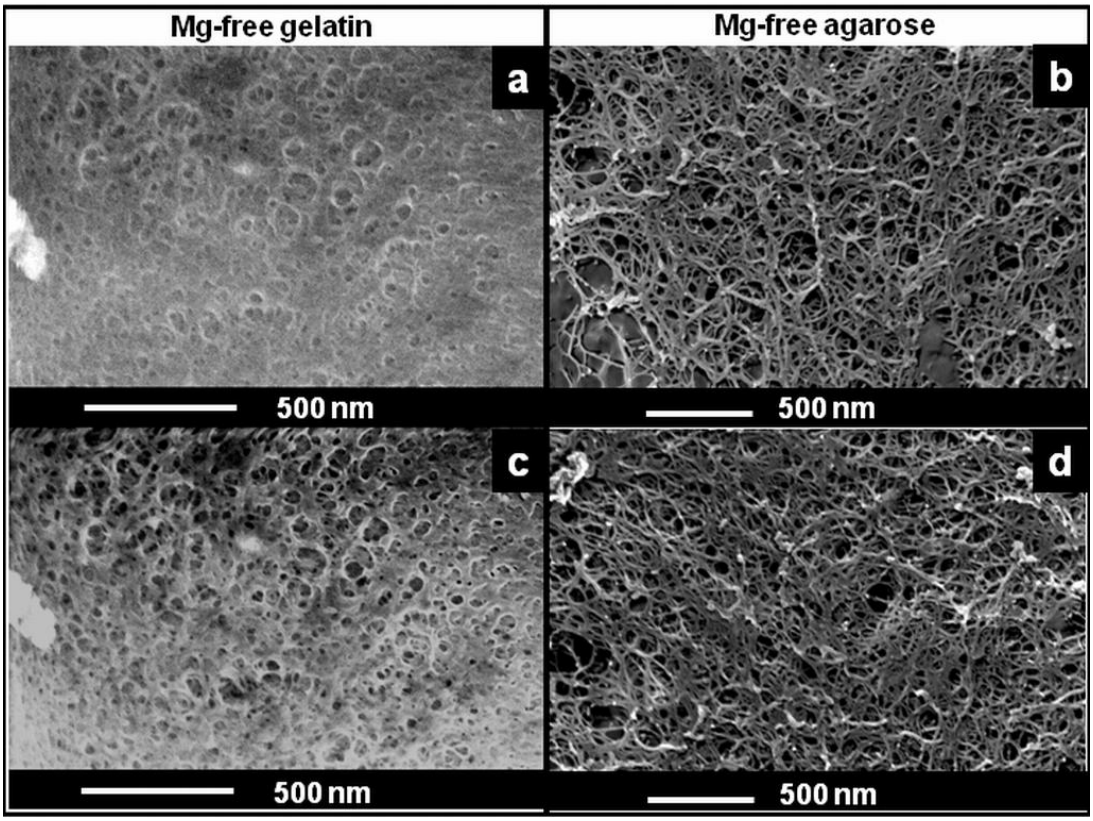

Figure S1. Cryo-FE-SEM images of fracture surfaces showing the fabrics of high-pressure frozen, Mg-free hydrogels that were not treated with isopropanol: (a, c) Gelatin, (b, d) Agarose. The fabrics of the isopropanol treated hydrogel samples are shown in Figure 3. We observe a good correspondence between the hydrogel microstructures in samples treated with and without isopropanol. Thus, the gel specific fabrics and mesh sizes are not caused or distorted by ice crystal formation.

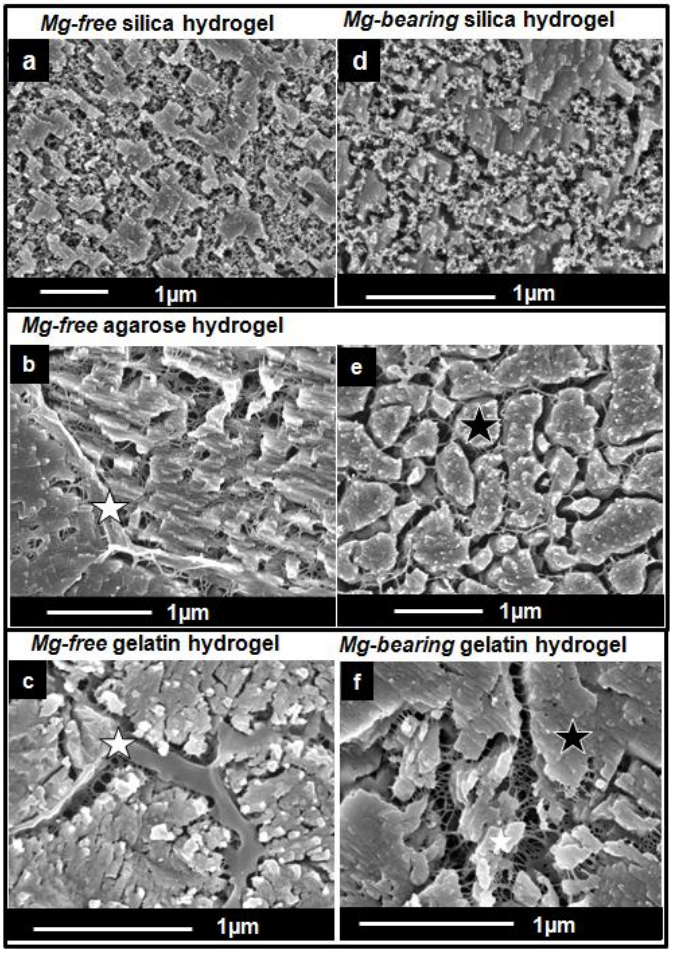

Figure S2. FE-SEM images of microtome cut, polished, etched and critical point dried surfaces of hydrogel-calcite composite aggregates: (a, d) Gelatin, (b, e) Agarose, (c, f) Silica. Depending on the presence or absence of Mg in the growth medium, we observe distinct morphological and microstructural characteristics of both, the mineral and the hydrogel fabrics. Gelatin hydrogel- calcite composites show in a Mg-free environment thick incorporations of gelatin membranes (white star in c) that is complemented with a low amount of gelatin network. In a Mg-containing environment gelatin hydrogel in the composite is only present as a dense network that connects bulky calcite crystal entities (black stars in f). Mg-free agarose hydrogel is incorporated into the hydrogel-calcite composite as both, a thin film of hydrogel (white star in b) but also as a pronounced network (b). Is Mg added to the growth medium only the agarose hydrogel network remains (e) and connects elongated mineral entities with rounded outer shapes (white star in e). In both, Mg-free (c) and Mg-bearing (f) silica hydrogel-calcite composites silica hydrogel is nestled between blocky calcite crystals.

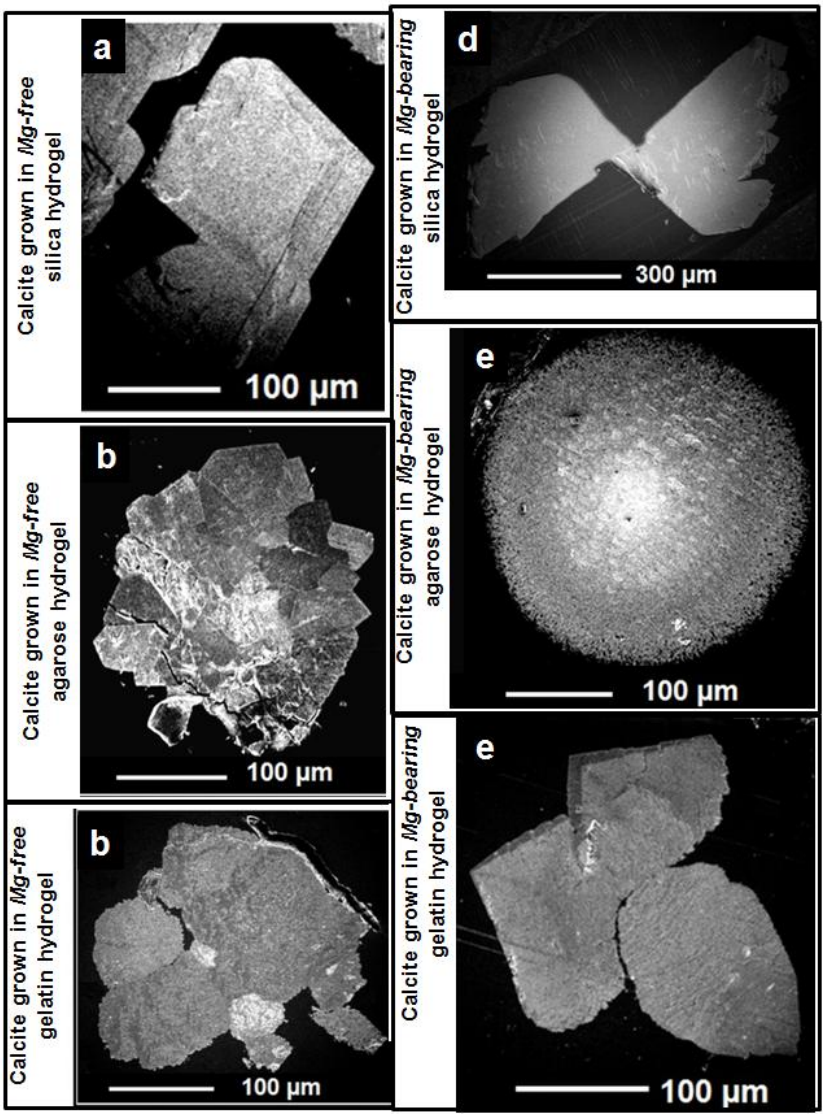

Figure S3. FE-SEM image of microtome cut, polished, etched and critical point dried surfaces of Mg-free and Mg-beaing hydrogel-calcite aggregates: Silica hydrogel (a, d), Agarose hydrogel (b, e), Gelatin hydrogel (c, f). As the morphologies of the aggregates show, the effect of Mg in the growth medium on calcite growth and aggregate formation is immense.

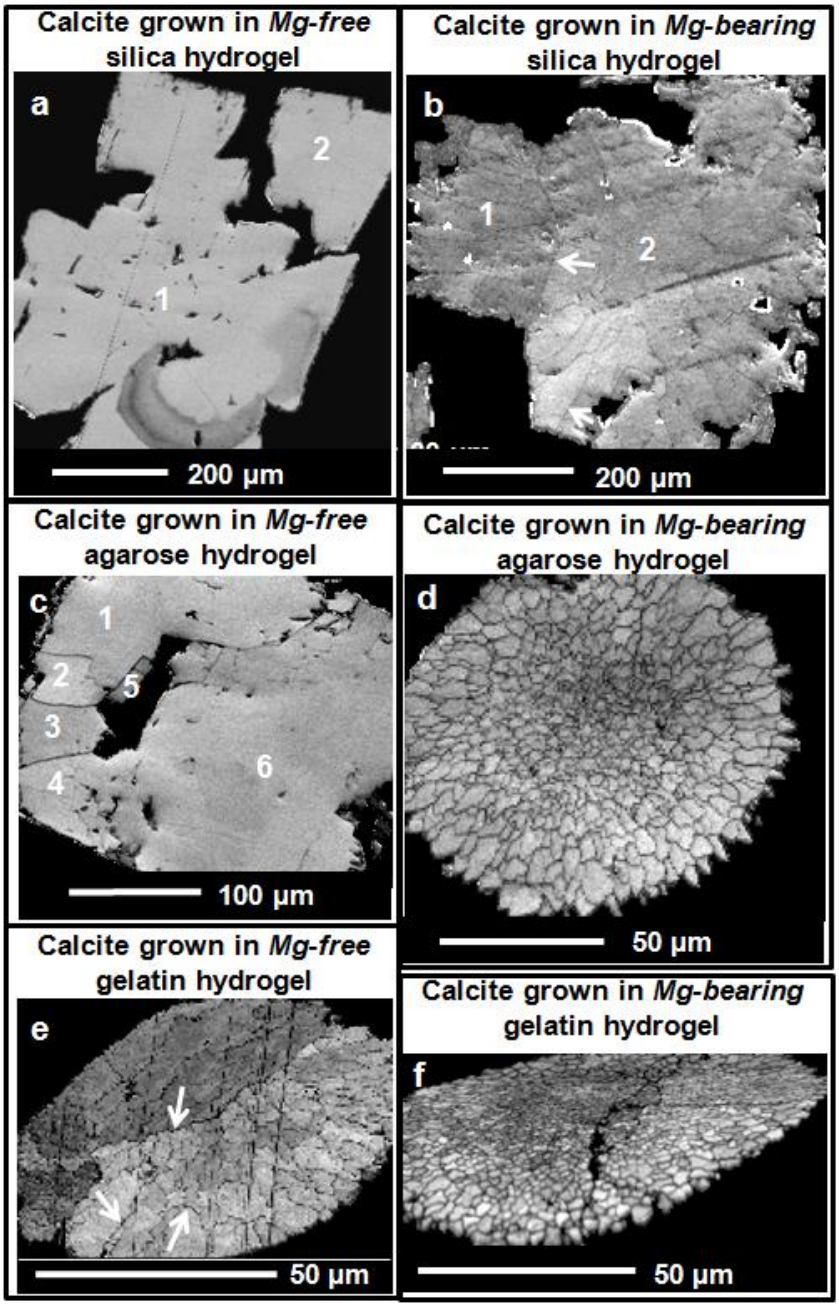

Figure S4. EBSD band contrast images that highlight internal features of the inveatigated single crystals and aggregates obtained from the three different hydrogels, in the presence and absence of Mg in the growth medium. We see the effect of the hydrogel on single crystal (a) and aggregate (c to f) formation and its occlusion within the aggregates as dark lines (see arrows in b, e) surrounding subunits and entities of calcite (c, d, e, f).

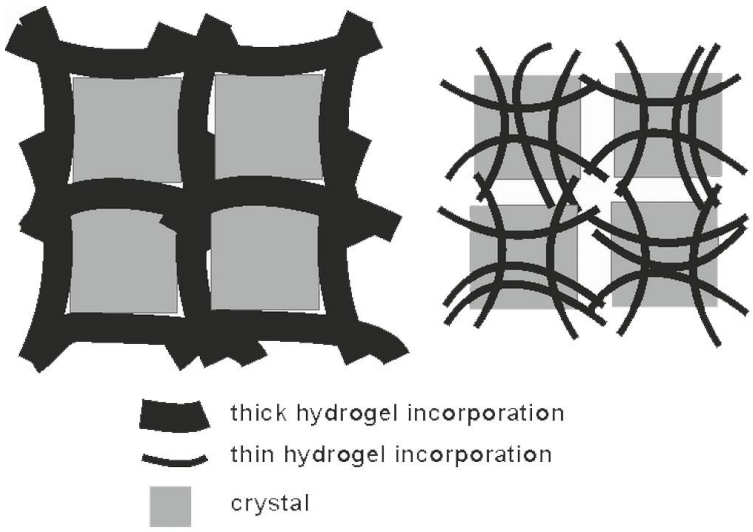

Figure S5. Sketch showing the formation of gel membranes assembling between crystals growing in proximity in weak hydrogels such as Mg-free gelatine or agarose. In strong hydrogels such as Mg-bearing gelatine or agarose the gel becomes more incorporated than pushed ahead of the growing crystals. Drawing inspired by Li and Estroff (2009).[41]

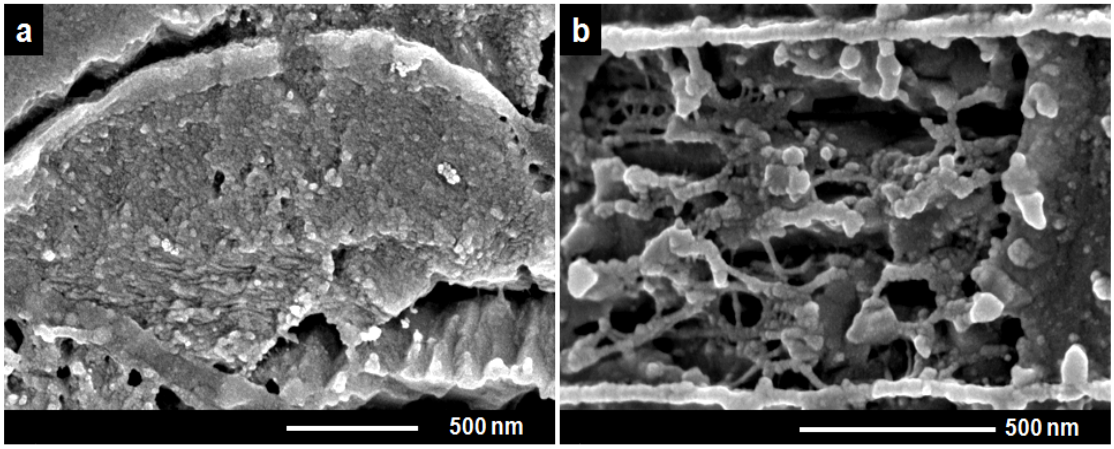

Figure S6. Assemblage of calcitic and aragonitic nanoparticles surrounded by proteinaceous matrices. (a) Calcite nanoparticles in a brachiopod fiber, (b) aragonite nanoparticles in a nacre tablet. Well visible are the membranes delimiting one specific tablet as well as the fiber network within the tablet and between the mineral nanoparticles.

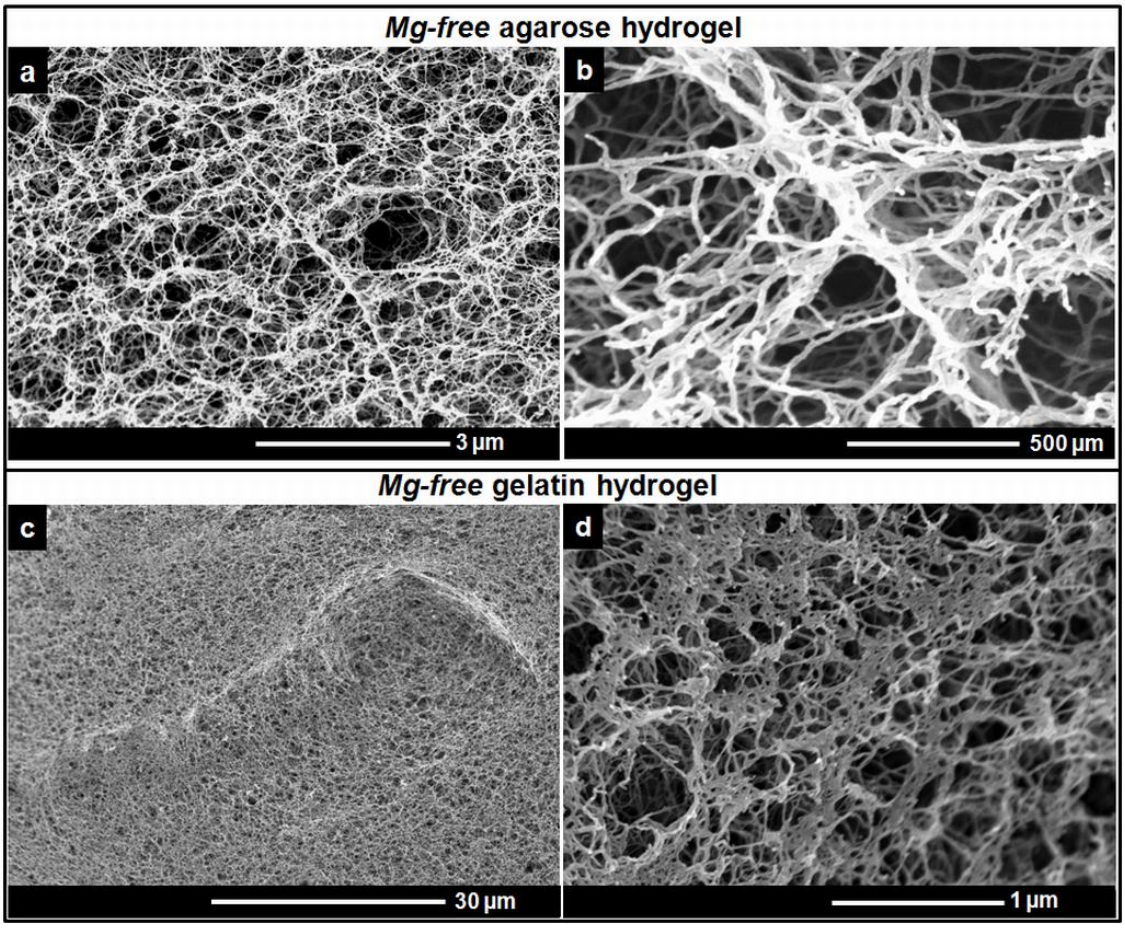

Figure S7. The fabric of gelatin and agarose hydrogels after complete decalcification of the hydrogel-calcite aggregate. Accumulation of hydrogel fibers are observable most probably due to crystallization pressure of the mineral.

2.5 Characterization and mechanical properties investigation of the cellulose/gypsum composite

Fitriana Nindiyasari[1,], Erika Griesshaber[1], Tanja Zimmermann[2], Avinash Pradip Manian[3], Clemens Randow[4], Rolf Zehbe[4], Lurdes Fernandez-Diaz[5,7], Andreas Ziegler[6], Claudia Fleck[4] and Wolfgang W. Schmahl[1]*

[1]Department für Geo- und Umweltwissenschaften, Ludwig-Maximilians-Universität München, München, Germany
[2]Department of Applied Wood Materials, Swiss Federal Laboratories for Materials Science and Technology (Empa,) Dübendorf, Switzerland
[3]Laboratory for Textile and Fiber Chemistry in Cellulosics, Research Institute for Textil Chemistry and Textile Physics, University of Insbruck, Dornbirn, Austria
[4]Department of Material Engineering, Technische Universität Berlin, Berlin, Germany
[5]Department of Crystallography and Mineralogy, Universidad Complutense, Madrid, Spain
[6]Central Facility for Electron Microscopy, University of Ulm, Ulm, Germany
[7]Institut of Geoscience, IGEO (CSIC, UCM), Madrid, Spain

Journal of Composite Material, 2015, DOI: 10.1177/0021998315580826

http://jcm.sagepub.com/content/early/2015/04/30/0021998315580826.abstract

Abstract
We synthesized cellulose/gypsum composites in the presence and absence of sodium alginate and investigated the interaction between the composite components as well as the mechanical properties of the final composites. Four different types of cellulose fiber materials were used: cellulose UFC100, cellulose B400, nanofibrillated cellulose (NFC) and Lyocell fiber. For all investigated composites the total amount of admixed cellulose was between 1 and 2 wt %, the amount of admixed sodium alginate was 0.5 wt %. We determined the morphology of the composites and observed that the particle and fiber dimensions of the admixed cellulose affect the mode of gypsum-gypsum interlocking and the total porosity of the composites. This in turn had a substantial influence on the mechanical properties of the final composite materials. The addition of sodium alginate resulted in an increase of ultimate strain values. The composite with Lyocell fiber, a synthetic fiber, also had a high Young's modulus.

Keywords
Gypsum; Hemihydrate; Sodium Alginate; Cellulose fiber; Mechanical properties; Porosity

1. Introduction

Gypsum is a well-known low cost material.[1] It is composed of interconnected needle-like calcium sulphate dihydrate crystals. These calcium sulphate dihydrate entangle and create a gypsum network. The main drawback of gypsum as a building material is due to its heaviness and brittleness. This drawback can be overcome by combining gypsum with mineral particles[2], natural fibers (waste paper[3], sisal fiber[4], stalk fiber[5], hemp fiber[6]), synthetic fibers (polyamide fiber[7,8], glass fiber[9-11]), or polymers.[12] Gypsum-based composites have a low cost production, a low thermal coefficient[5] and a low solid content. All these properties are good for insulating against heat and sound while the mechanical strength of the gypsum-based composites are still retained.[5,13]

The mechanical properties of the gypsum are correlated to its total porosity.[7,12-16] It turns out that the total porosity of the gypsum is influenced by the water/hemihydrate ratio[4,13-16] and the aging time.[4,14-17] It is well known that the total porosity increases when the water/hemihydrate ratio increases.[14-16] Moreover, the network structure, the intercrystalline interaction, the crystal sizes and the pores affect the mechanical properties.[13,16] The crystalline habits and the arrangement of the crystals influence the hardness of the gypsum, as explained by Amathieu (1986).[20] The hardness of the gypsum increases by a factor of two to three with reducing the crystal size from micrometer to nanometer scale level. This increase is attributed to the strong entanglement of the gypsum needle-like network.[21]

Cellulose is embedded into gypsum wallboard. Gypsum wallboard is an important construction material for building for example an interior wall.[22,23] The main drawback of wallboard is failure that occurs at the cellulose-

gypsum interface.[23] Cellulose is formed by sequences of glucose repeating units and has good mechanical properties such as high tensile strength and Young's modulus.[24-26] There are six different cellulose polymorphs, cellulose I, II, III_I, III_{II}, IV_I and IV_{II}.[27-31]

This paper focuses on the effect of natural (cellulose Arbocel UFC100, B400 and NFC) and synthetic (Lyocell) cellulose in the formation of gypsum crystals and entanglement of gypsum-gypsum needle-net network. De Maria Pinheiro Correia (2009) reported an increase in mechanical properties and a thermal conductivity of low porosity gypsum plates by an addition of nanofibril cellulose.[32] The addition of sodium alginate is expected to reduce the cellulose-gypsum interface failure by creating an intimate interlinkage of the components.[33]

2 Materials and material preparation

2.1 Materials

Chemical compounds such as sodium alginate and hemihydrate ($CaSO_4.1/2H_2O$) were obtained from Sigma Aldrich GmbH, Germany, while cellulose Arbocel was obtained from JRS Pharma GmbH & Co. KG, Germany. Lyocell fiber was obtained from Tencel® Lenzing AG, Lenzing, Austria.

Cellulose

Cellulose I or native cellulose is a polymorph that is found in nature. Cellulose I has two different polymorphs: cellulose Iα and Iß. Cellulose Iα and cellulose Iβ have the same conformation of the heavy atom skeleton but differ in hydrogen bonding patterns. Cellulose Iα is a metastable phase with a triclinic unit cell containing one chain, while cellulose Iβ has two chains in its monoclinic unit cell. Cellulose II, derived from cellulose I, has a similar unit cell as the unit cell of cellulose I. The main difference to cellulose I is that cellulose II has two cellulose chains that lie antiparallel to one another.[29,31]

Swelling agents such water or alkali treatments (NaOH up to 8 M) influence the degree of swelling, the degree of crystallinity and water retention value (WRV) of the cellulose fiber respectively. Water retention value is an ability of cellulose to uptake water.[34-37] In water or under alkali treatment of 2-4 M NaOH cellulose II can swell extensively in comparison to cellulose I.[36,37] On the other hand under strong alkali treatment, e. g. 5-8 M NaOH, cellulose I will swell more extensively than cellulose II.

As shown in Table 1, four different cellulose fibers were taken for the preparation of the composites: 1. Arbocel UFC100 an ultrafine cellulose powder with a particle size of 1 µm; 2. Arbocel B400 a fibrous cellulose with fiber lengths of about 900 µm and a fiber diameter of about 10 µm; 3. Lyocell fiber with a fiber length of 38 mm and a fiber fineness of 1.3 dtex. Dtex is the mass of fiber in grams per 10000 meter length. The higher the dtex value the thicker or coarser is the fiber;[34,36] 4. Nanofibrillated cellulose (NFC) with fiber lengths of 2 µm and a fiber diameter in the range of a few tens of nanometers.

Nanofibrillated cellulose production

Nanofibrillated cellulose (NFC) was prepared by dispersing 0.93 kg of Arbocel B1011 cellulose fiber in 9 L of water. First, the suspension was left in a thermo-static reactor at 10 ºC under continuous stirring for 4 days. Subsequently, the cellulose suspension was processed through a closed inline dispersing system equipped with an ultra-turrax for the disintegration of the fibers into smaller parts. The resulting suspension was treated in a high pressure homogenizer by pumping the resulting suspension with high velocities through fixed-geometry interaction chambers (Y or Z morphology) with diameters of 400, 200, and 75 µm. Pressures up to 1000 bar were applied to generate high shear-stresses to the cellulose fibers.[38] The NFC is prepared as a suspension to preserve the NFC structure with content of 1.5 wt % NFC (1.5 grams NFC in 100 mL water). The centrifugation and the heat appliance to reduce the water content yielded to the NFC content of 2 wt % (2 grams NFC in 100 mL water). Further heat appliance may lead to structure destruction of the NFC and centrifugation does not resolve to more water content reduction. This results to a problem in w_o/h_o ratio adjustment of the cellulose/gypsum composites. NFC, reported by some authors, has interesting properties such as high strength and high stiffness.[39-42]

Sodium alginate

Alginate is a natural polymer and is derived from cell walls of brown algae.[43] Alginate can be found as sodium alginate, calcium alginate and magnesium alginate salts within the cell walls and intercellular mucilage of seaweed.[44] It is a hydrophylic gelling of seaweed.[44] It is a hydrophylic gelling material that has interesting properties such as stabilizing emulsions, high capacity of holding water and improved viscosity.[43] The sodium alginate contributes to the mechanical strength and the flexibility of algae and is comparable to cellulose of land

plants.[45]

Sodium alginate is used in wide-range applications. Recently, some researchers investigated the application of sodium alginate in building and construction materials such as in cements,[46] clays[43] and soils.[47] An increase in compressive strength from 2.23 to 3.77 MPa by adding up to 19 wt % of sodium alginate to clay.[43]

Table 1. Bending and compressive strength of gypsum composites with the water/hemihydrate ratio (w_o/h_o), cellulose content (wt %) and sodium alginate content (wt %).

	w_o/h_o ratio	Cellulose content (wt %)	Sodium alginate content (wt %)	Compressive strength [MPa]	Bending strength [MPa]
Gypsum	0.50	-	-	9.25 ± 1.25	5.65 ± 1.15
Sodium alginate	0.50	-	0.5	6.04 ± 1.29	3.00 ± 0.58
Composite UFC 1a	0.50	1.0	-	17.82 ± 1.07	6.16 ± 0.94
Composite UFC 1b	0.50	1.0	0.5	9.02 ± 0.93	4.67 ± 0.74
Composite UFC 1c	0.50	2.0	-	5.98 ± 0.89	3.55 ± 1.09
Composite UFC 1d	0.50	2.0	0.5	10.51 ± 0.96	4.45 ± 0.71
Composite B400 2a	0.50	1.0	-	10.34 ± 0.44	4.49 ± 1.11
Composite B400 2b	0.50	1.0	0.5	7.76 ± 0.59	4.42 ± 0.38
Composite B400 2c	0.50	2.0	-	6.38 ± 0.72	2.78 ± 0.67
Composite B400 2d	0.50	2.0	0.5	6.62 ± 0.28	3.72 ± 0.23
Composite Lyo 3a	0.50	1.0	-	10.52 ± 0.79	5.40 ± 1.19
Composite Lyo 3b	0.50	1.0	0.5	7.94 ± 1.26	3.66 ± 0.47
Composite Lyo 3c	0.50	2.0	-	6.09 ± 0.69	4.00 ± 0.47
Composite Lyo 3d	0.50	2.0	0.5	5.71 ± 0.18	4.04 ± 0.80
Composite NFC 4a	0.50	1.0	-	10.95 ± 0.91	4.21 ± 0.70
Composite NFC 4b	0.50	1.0	0.5	10.11 ± 0.76	3.31 ± 0.83
Composite NFC 4c	0.97	2.0	-	3.17 ± 0.14	1.35 ± 0.34
Composite NFC 4d	0.97	2.0	0.5	4.21 ± 0.22	1.72 ± 0.36

2.2 Production of gypsum–cellulose composites

Several different composites were prepared from the four different cellulose types described above. The water/hemihydrate ratio (w_o/h_o), the cellulose and sodium alginate contents were adjusted to get the chosen value (Table 1). 1 M NaOH was added in order to produce well dispersed sodium alginate. This amount is well below the swelling maximum of cellulose fiber and does not influence the swelling degree of cellulose.

3 Methods

3.1 Microscope imaging

For scanning electron microscope (SEM), dried cellulose UFC100, B400, the Lyocell fiber and sodium alginate samples were mounted on the holder using carbon tape. They were then coated with carbon and gold. The morphology of the samples was imaged with a JEOL JSM-6500F SEM using an accelerating voltage of 10 kV. A drop of the nanofibrillated cellulose (NFC) was placed on a TEM grid and the cellulose was imaged with a Zeiss EM 10 TEM using an accelerating voltage of 80 kV.

3.2 X-ray diffraction (XRD)

The fine crystalline cellulose UFC100 and the thin film of nanofibrillated cellulose (NFC), were investigated using a Bragg-Brentano x-ray diffractometer (GE: XRD 3003 TT). XRD data were recorded in reflection mode using a 1-dimensional position sensitive semi conductor detector (Meteor 1D) with a step size of 0.01° (θ/θ). The thin film of nanofibrillated cellulose (NFC) was obtained by drying some amount of NFC inside an oven at a temperature of 60 °C for 24 hours. This diffractometer was also used to record diffraction patterns of hemihydrate, gypsum and the composite UFC 1a, in order to follow the transformation of hemihydrate to gypsum.

Both samples, the cellulose B400 and Lyocell fiber were packed into glass capillaries (ø = 0.5 mm). XRD data was collected in transmission mode on a single crystal diffractometer (Agilent, Gemini Ultra) equipped with a 2-dimensional charge-coupled detector (Atlas). All XRD data were collected using Cu

$K\alpha_1$ radiation.

The degree of crystallinity and the apparent crystallite size were estimated by deconvolution of the diffraction patterns in the range 10-40° (2θ) (Figure 1). The Gaussian profile function was applied for deconvolution intensities of the four reflections 110, $1\bar{1}0$, 120 and 200, respectively, for crystalline cellulose[27,30,35] and one broad peak at 2θ~18° for amorphous cellulose.[36,37] The crystallinity index was calculated according to $X_c = [A_{cr}/(A_{cr}+A_{am})]\ X\ 100\%$, where A_{cr} and A_{am} are the integrated intensities of the crystalline and amorphous phases, respectively.[38-40] The apparent crystallite size (L) was calculated according to the Scherrer equation $L = k\lambda/(\beta\ cos\ \theta)$, where the Scherrer constant k for an unknown crystal phase has been set to 0.9. λ stands for the applied x-ray wavelength, β is the FWHM of the reflections 200 for cellulose I and 020 for cellulose II in radian, and θ is the corresponding Bragg's angle.[48-52]

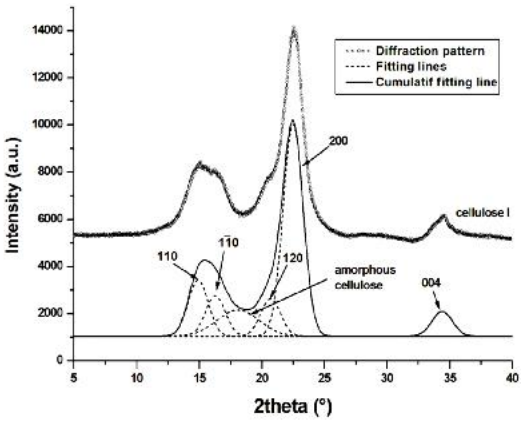

Figure 1. Diffraction pattern of cellulose I showing peak deconvolution. The diffraction pattern has five major reflections at 110, $1\bar{1}0$, 120, 200 and 004 of the crystalline phases. Amorphous cellulose is observed at 2θ ~18°.

3.3 Porosity measurement

The porosity was calculated from the water-to-stucco ratio, $p = (w-(w_o/h_o\ ratio))/(w+weight\ of\ cellulose)$ where w is the total weight of the gypsum composite. Following the Gibson-Ashby relation the strength of the composite scales with (1-porosity).[13]

3.4 Mechanical testing

For mechanical testing the samples were prepared by pouring the composite slurry into moulds with dimensions of 13.5 x 13.5 x 25 mm^3 for compression and 75 x 10 x 3.5 mm^3 for 4-point bending testing. The samples were dried within the moulds at room temperature for 7 days. The number of specimens for each composite was ~10 specimens for bending and ~ 10 specimens for compression testing. Bending testing was carried out with a UTS test system Typ 009, 3 kN and with a Zwick Universalprüfmaschine Typ Z005, 5 kN while compression testing was carried out with a Zwick Universalprüfmaschine Typ 1425, 100 kN and a Zwick Universalprüfmaschine Typ Z005, 5 kN. Measurment was stopped after the load dropped and the first cracks were observed. Some specimens failed at point of force transmission due to uneven surfaces and were excluded from data interpretation. The preload for bending and compression testing was 0.5 N. The velocity values of bending and compression testing were 0.02 mm/min and 0.12 mm/min, respectively. The strain rate values of bending and compression testing were $5.1x10^{-5}\ s^{-1}$ and $8x10^{-5}\ s^{-1}$, respectively. The strain is calculated by dividing the elongation by the original sample length. The Young's moduli are derived from the steep slope of stress-strain curve. The bending strength calculation is based on 4-points bending experiments. Thus, $\sigma = \frac{3Fd}{bh^2}$, where F is the applied load, d is the distance between the inner and the outer points of the bending machine, b is the sample width (10 mm) and h is the sample thickness (35 mm). The compressive strength is calculated by dividing the applied load by the surface area of the samples.

4 Results

4.1 Gypsum crystallization (formation)

Gypsum crystallization occurs as a result of a solvent mediated transformation that involves dissolution of hemihydrate and nucleation and growth of gypsum.[53] The driving force for this process is the different solubility of gypsum and hemihydrates, i.e. gypsum is less soluble in water than hemihydrate. As a consequence, in contact with water, the dissolution of hemihydrate leads to supersaturation of gypsum in the solution. At this point, gypsum can nucleate and, for the solute consumption involved, the system becomes again undersaturated with respect to hemihydrates. The coupling between hemihydrate dissolution and gypsum crystallization defines a feedback loop which guarantees that gypsum growth occurs under a constant supersaturation value that is controlled by the solubility difference between gypsum

and hemihydrate. This mechanism will operate while both water and hemihydrates remain available in the system.

Figure 2 shows SEM images of hemihydrate ($CaSO_4.1/2H_2O$) and gypsum ($CaSO_4.2H_2O$). Hemihydrate crystals have an irregular shape and are aggregates of small crystallites (Figure 2a). The single crystal size of β-hemihydrate is in the range of 1-10 µm. The entanglement of gypsum needle-like network (Figure 2c) creates pores with pore sizes in the range of 5-10 µm ((Figure 2b). As shown in Figure 2d small particles of β-hemihydrate appear indicating that some β-hemihydrate does not recrystallize to gypsum. This occurs due to an insufficient addition of water and/or a too short hydration time.

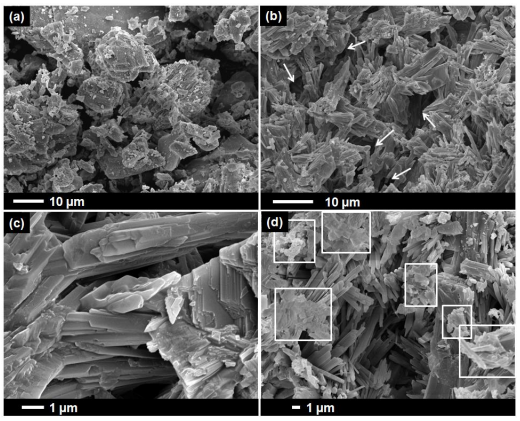

Figure 2. SEM images of **(a)** β-hemihydrate ($CaSO_4.1/2H_2O$) showing the irregular shape of β-hemihydrate aggregates and **(b)** fracture surface of gypsum (hydrated β-hemihydrate) with a water/hemihydrate (w_o/h_o) ratio of 0.5. Hydrated β-hemihydrate highlighted in **(c)** displays the mode of interlocking of gypsum-gypsum crystals**.** Interlocking of gypsum-gypsum crystals creates porous gypsum aggregates indicated by white arrows in **(b)** while white squares in **(d)** indicate chunks of hemihydrate that are remained.

4.2 Cellulose particle, fiber morphology and crystallinity characterisation

Diffraction patterns of the cellulose UFC100, B400 and NFC (Figure 3) resolve the presence of the cellulose polymorph I. Cellulose polymorph I has the following five major reflections: 110 at 2θ~15.12 °, $1\bar{1}0$ at 2θ~16.35 °, 120 at 2θ~20.57 °, 200 at 2θ~22.50 ° and 004 at 2θ~34.57 °. The diffraction patterns of cellulose II or Lyocell fibers reveals three peaks $\bar{1}01$, 101, 020 with reflections at 12.4, 20.6, and 21.4 ° (2θ), respectively (Figure 4).

The degree of crystallinity and apparent crystallite size calculations of cellulose UFC100, B400, Lyocell fiber as well as NFC cellulose are given in Table 2. The apparent crystallite sizes evaluated from XRD data are based on the line broadening of the reflection 200 for cellulose I and 020 for cellulose II.

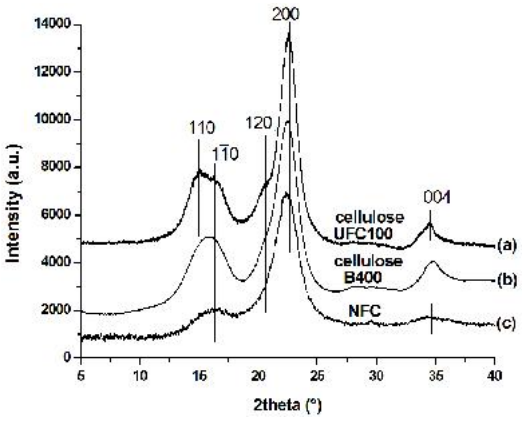

Figure 3. Diffraction patterns of the cellulose **(a)** UFC100, **(b)** B400, and **(c)** NFC show characteristic reflections of cellulose polymorph I. There are several overlapping peaks appear at 2θ~15 ° and 2θ~22 °.

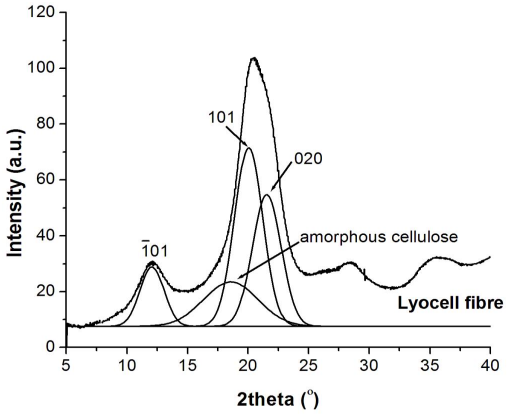

Figure 4. Diffraction pattern of Lyocell fiber and deconvolution of intensities of the reflection $\bar{1}$01, 101, and 020 of cellulose polymorph II along with a broad peak of an amorphous phase at 2θ ~18°.

These reflections are related to the thickness of the molecular sheets in the stacking direction of the a-axis of the cellulose unit cell. A reduction of the crystallite size can be assumed by a change in cellulose chains along the plane (200) or (020), resulting in an apparent crystallite size
of 4.28, 3.64 and 3.56 nm for UFC100, B400 and NFC, respectively. Cellulose UFC100 has a

degree of crystallinity of 75.5%, while cellulose B400 and NFC show a degree of crystallinity of 70.2% and 67.8 %, respectively. Lyocell fiber has the lowest crystallinity index and apparent crystallite size with a respective value of 52.3 % and 3.47 nm.

Table 2. The apparent crystallite size (L) and the degree of crystallinity evaluated from XRD using the Scherrer equation.

Samples	Apparent Crystallite size L (nm)	Degree of crystallinity X_c (%)
Cellulose UFC100	4.28	75.5
Cellulose B400	3.64	70.2
Lyocell	3.47	52.3
NFC	3.56	67.8

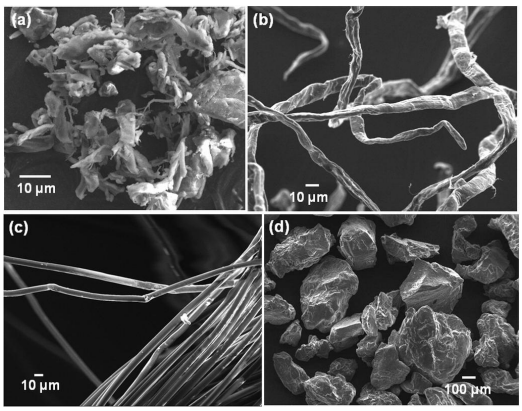

Figure 5. SEM images of the morphology of **(a)** cellulose UFC100, **(b)** cellulose B400, **(c)** Lyocell fiber and **(d)** sodium alginate. Cellulose UFC100 appears as aggregate of small cellulose particle while both cellulose B400 and Lyocell fiber are fibrous cellulose with diameter about 10 µm.

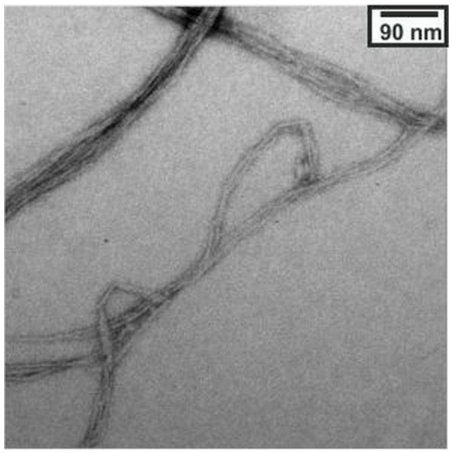

Figure 6. TEM image of fibril aggregates of NFC. Uranylacetate was added to increase the contrast of NFC.

Figure 5 shows the morphology of cellulose UFC100, cellulose B400, Lyocell fiber and sodium alginate. Cellulose UFC100 is an aggregate of irregular particles, while cellulose B400 and Lyocell fiber are entirely composed of cellulose fibers. Sodium alginate appears as an irregular particle with sizes ranging from about 100 µm to some hundred micrometers. Figure 6 shows the fiber structure of nanofibrillated cellulose showing cellulose nano-fibers with single nano-fiber diameters around ~10 nm.

4.3 The interaction of components in the composites

In hydration of hemihydrate, the gypsum crystals appear as needle-like that are interconnected to each other. An addition of biopolymers or other additives modifies the morphology and habit of growing gypsum crystals resulting in the change in microstructures and total porosity of the gypsum composites. It occurs as the presence of biopolymer or other additives changes the supersaturation of the solution and surface topography of the growing gypsum crystals.[16] During the growth gypsum crystals adopt a variety of habits created by differences in relative growth rates of faces of which the gypsum crystal is composed. Singh & Middendorf reported the adsorption on the step and kinks of gypsum crystal faces by retarder agents such as carboxyl groups. It results in the changes of morphology.[16]

The investigated composites were obtained by mixing cellulose (1 and 2 wt %) and hemihydrate in the presence and absence of sodium alginate. The presence of cellulose independent to the presence of sodium alginate changes the gypsum crystal morphology. This change is observed in the different gypsum-gypsum interlocking features (Figure 7). Gypsum crystals of the Composite UFC 1a (Figure 7a) are thinner and smaller than those precipitated in the absence of cellulose (Figure 2b). The interlocking of gypsum-gypsum crystals of the Composite UFC 1a is disoriented. The addition of B400 (Figure 7b) or Lyocell fiber (Figure 7c) produces composites with thick gypsum crystals while the addition of NFC (Composite NFC 4a) produces gypsum crystals with varied sizes (Figure 7d).

As shown in Figure 7, gypsum nucleation

can also occur on the cellulose surface, such as on cellulose B400 (Figure 7e) and the Lyocell fiber (Figure 7f) surfaces. The nucleation of gypsum on cellulose surfaces (heterogeneous nucleation) impacts the size and morphology of gypsum crystals. On both, B400 and Lyocell

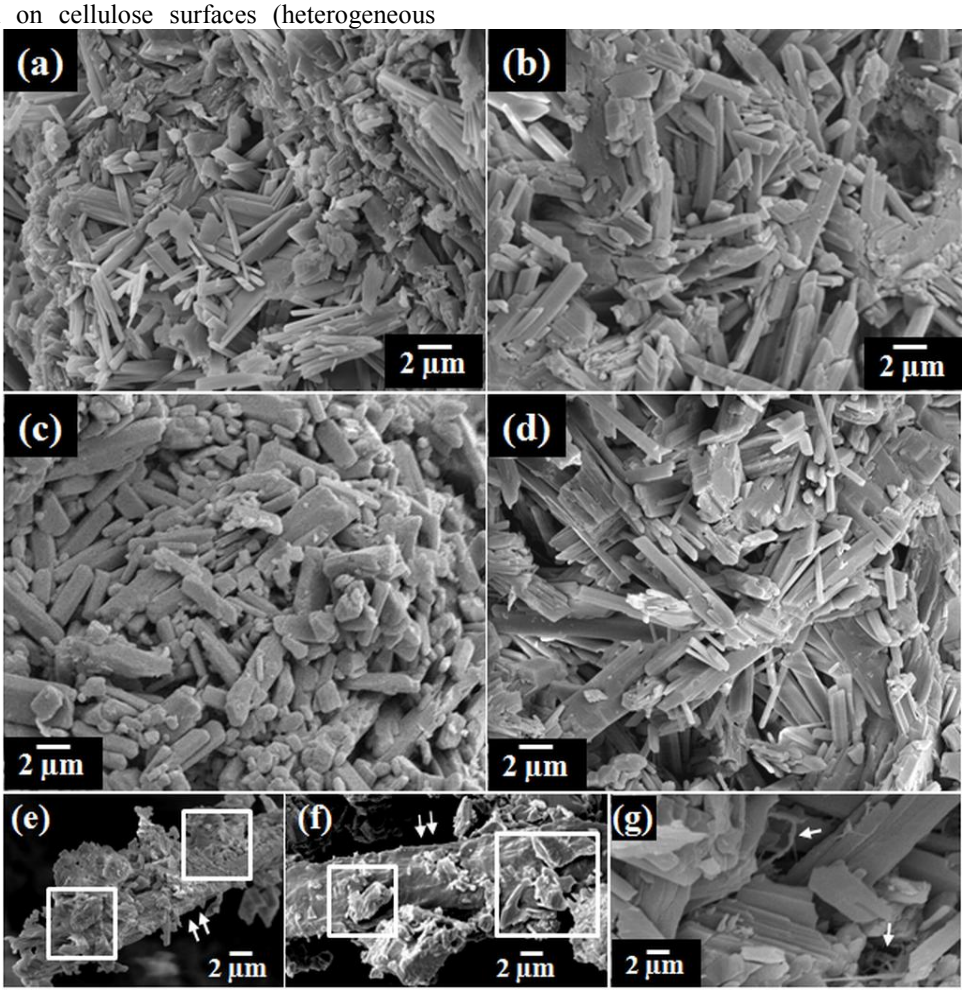

Figure 7. Scanning electron microscopy images of fracture surfaces of the composites. Gypsum crystals in Composite UFC 1a **(a)** are thinner and smaller than that precipitated in the pure state without any cellulose (Figure 2c). Composite B400 2a **(b)** and Composite Lyo 3a **(c)** have thicker and short gypsum crystals. Composite NFC 4a **(d)** has gypsum crystal with varied size. Figure **(e)** shows gypsum crystal grown on the surface of fibrous cellulose B400. Gypsum crystals grown on the surface of Lyocell fiber are shown in figure **(f)**. Figure **(g)** shows that no gypsum crystals are growing on NFC surface. Double arrows and white squares on figure **(e)** and **(f)** indicate the cellulose fiber and gypsum crystals on cellulose fiber surface, respectively. A white single arrow in figure **(g)** indicates the nanofibrillated cellulose.

fiber, the surficial gypsum crystals tend to form aggregates through the coalescence of individual crystals; marked by white squares in Figure 7e and f. This heterogeneous nucleation is not observed on the surface of nanofibrillated cellulose (Figure 7g) as small fibers absorb less water. Thus, the amount of water to support gypsum crystallization is lower. Cellulose fibers of B400 and Lyocell are marked with double arrows while NFC fiber is marked with single arrows (Figure 7e, f and g).

Diffraction patterns of β-hemihydrate (Figure 8a), hydrated hemihydrate (gypsum) (Figure 8b), and the Composite UFC 1a (Figure 8c) are used to follow the transformation of hemihydrate. The hemihydrate peak in the diffraction pattern of the Composite UFC 1a appears at 14.7 ° and 29.4 ° (2θ). The addition of 50% of water seems to be insufficient to convert all hemihydrate into gypsum. The peak at 29.2 ° (2θ) is due to gypsum. The anhydrite peak at 25.4 ° (2θ) is also seen in the diffraction pattern of β-hemihydrate (an initial ingredient and pure gypsum and the Composite UFC 1a. The appearance of anhydrite in hemihydrate indicates that anhydrite is formed

during the hemihydrate production process and is assigned to either anhydrite III or γ- $CaSO_4$.

4.4 Porosity of the composites

The total porosity (vol %) of each composite changes due to the presence of cellulose with or without sodium alginate (Figure 9, 10, 12, S1). The total porosity of pure gypsum is 47.96 vol % and increases to 51.31 vol % when 0.5 wt % sodium alginate is added. The decrease in the total porosity due to sodium alginate addition is a result of a gelation effect of sodium alginate that creates channels-like pores.[54,55] The composites with cellulose B400 follow a similar total porosity trend to that of composites with Lyocell fibers. The more cellulose is used the higher is the total porosity of the composites. Eve et al. (2002) observed the same trend when polyamide fiber was used.[7,8]

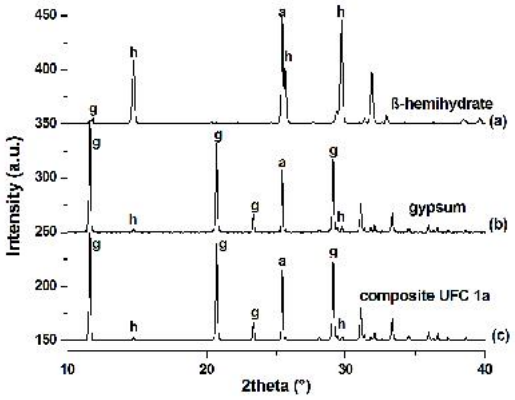

Figure 8. Diffraction patterns of **(a)** β-hemihydrate ($CaSO_4.1/2H_2O$), **(b)** hydrated β-hemihydrate (gypsum) with a water/hemihydrate (w_o/h_o) ratio of 0.5, and **(c)** Composite UFC 1a with a water/hemihydrate (w_o/h_o) ratio of 0.5. Anhydrite is formed and then remains intact. The intensity of hemihydrate peak decreases and replaced by the gypsum peaks along the formation of gypsum composites.

In the case of cellulose UFC100 a different trend was observed. The addition of 1 wt % cellulose UFC100 decreases the total porosity of the composite. Cellulose UFC100 has small particles with sizes less than 10 μm. These particles can fill the voids that occur from the entanglements of gypsums. The addition of 0.5 wt % sodium alginate indisputably increases the total porosity of the composite. The composite with 2 wt % cellulose IFC 100 has an increase in total porosity as a result of the increasing amount of cellulose UFC100. The total porosity decreases when 0.5 wt % sodium alginate is added having a similar total porosity value to that of the composite with 1 wt % cellulose and 0.5 wt % sodium alginate. This suggests that cellulose UFC100 fills only partly the holes created by sodium alginate.

The composite with 1 wt % of NFC has a similar total porosity value to that of the pure gypsum. The total porosity doesn't change when 0.5 wt % sodium alginate is added. It proves that NFC fills the holes created by sodium alginate. Composites with 2 wt % NFC has a high water/hemihydrates ratio resulting to a high total porosity. High water/hemihydrates ratio clearly influences the total porosity as seen in Figure S1.

4.5 Mechanical properties of the composites

The compressive and bending (flexural) strength values are presented as a function of the total porosity (Figure 9 and Figure 10). Box plots show maximum and minimum bars along with the median, the lower quartile (75^{th} percentile) and the lower percentile (25^{th} percentile) (Figure S2). The reference, the pure gypsum, has a compressive strength of 9.25 ± 1.25 MPa and a bending strength of 5.65 ± 1.15 MPa (mean ± standard deviation) (Table 1). The content of cellulose added to the composite is 1 and 2 wt % and that of sodium alginate is 0.5 wt %. Regarding their compressive and bending strength values, all composites differ from each other. The addition of 1 wt % cellulose UFC100 (Composite UFC 1a) increases the compressive strength of the composite up to 17.82 ± 1.07 MPa, almost twice the compressive strength of the pure gypsum reference. The compressive strength then decreases as 0.5 wt % sodium alginate is added (Composite UFC 1b), giving a compressive strength value similar to that of pure gypsum. The decrease of the compressive strength continues as 2 wt % cellulose UFC100 is added (Composite UFC 1c). Finally, the compressive strength value increases, slightly to value higher than that of the pure gypsum, when 0.5 wt % sodium alginate is added to the composite of 2 wt % cellulose UFC100 (Composite UFC 1d). Composites with cellulose B400 and Lyocell fiber show the similar trends. Composites with cellulose B400 (Composite B400 2) or Lyocell fiber (Composite Lyo 3) have the same decreasing trend as more cellulose B400 or Lyocell fiber is added, independent to the presence of sodium alginate. Composites NFC 4c and 4d have low compressive strength values due to the high porosity of the composite material as a result of the addition of a high amount of water (Figure S1). The addition of 1 wt % NFC, independent

of the addition of sodium alginate (Composite NFC 4a and 4b), gave a slight increase in compressive strength in comparison to that of the pure gypsum reference. The bending strength (Figure 10) follows a similar trend to that of the compressive strength.

Figure 11 shows stress-strain curves of the cellulose/gypsum composites tested in compression. As seen in Figure 11a the slope of the stress-strain curve of the Composite UFC 1a (C), up to a strain of 0.2 %, is more steep in comparison to that of the other composites. The Composites B400 2a (D), Lyo 3a (E) and NFC 4a (F) have a compressive strength that is similar to that of pure gypsum (A) with the strain values increase up to 0.38%, 0.18% and 0.25%, respectively. The composites with 1 wt % cellulose in the presence of 0.5 wt % sodium alginate such as Composite UFC100 1b (G), Composite B400 2b (H) and Composite Lyo 3b (I) have an almost constant load after the first observed load drop. These composites have ultimate strain values that are in the range of 0.4 - 0.8 % and are even higher than that of the sodium alginate (B). The addition of 0.5 wt % sodium alginate to 1 wt % NFC, Composite NFC 4b (J), does not give a big difference in the strain value in comparison to that of the Composite NFC 4a (F), composite without sodium alginate.

The Young's Moduli of investigated samples are presented as a function of the total porosity (Figure 12) and the box plot showing maximum and minimum bars along with the median, the lower quartile (75th percentile) and the lower percentile (25th percentile) (Figure S3). The Young's moduli of pure gypsum in the absence and presence of 0.5 wt % sodium alginate are shown as references. Composites with 1 wt % cellulose UFC or Lyocell fiber have significantly high Young's Moduli, almost as high as that of the pure gypsum reference. A slight increase of Young's Moduli is observed when 1 wt % cellulose B400 or NFC is added. The Young's Moduli of all composites drop when 0.5 wt % sodium alginate is added to the composites. Composite NFC 4b shows a slight increase of Young's Moduli when 0.5 wt % sodium alginate is added. Note the big scatter of the data shown in the box plot (Figure S3).

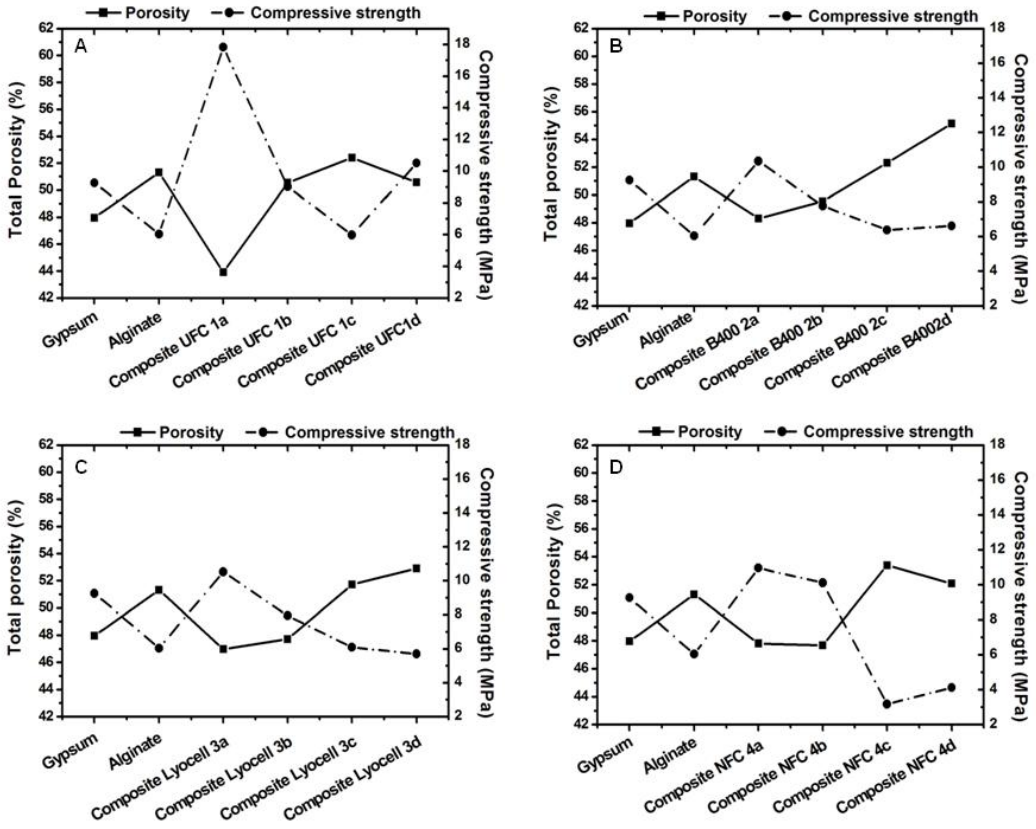

Figure 9. Total porosity of the cellulose/composites as a function of compressive strength: **(A)** composites UFC100, **(B)** composites B400, **(C)** composites Lyocell and **(D)** composites NFC. The graphs show that the total porosity influences the compressive strength of the final composites. Composites NFC

4c and 4d have w_o/h_o of 0.97 that influences the total porosity of the composites. The pure gypsum reference with w_o/h_o of 0.97 is shown in Figure S1.

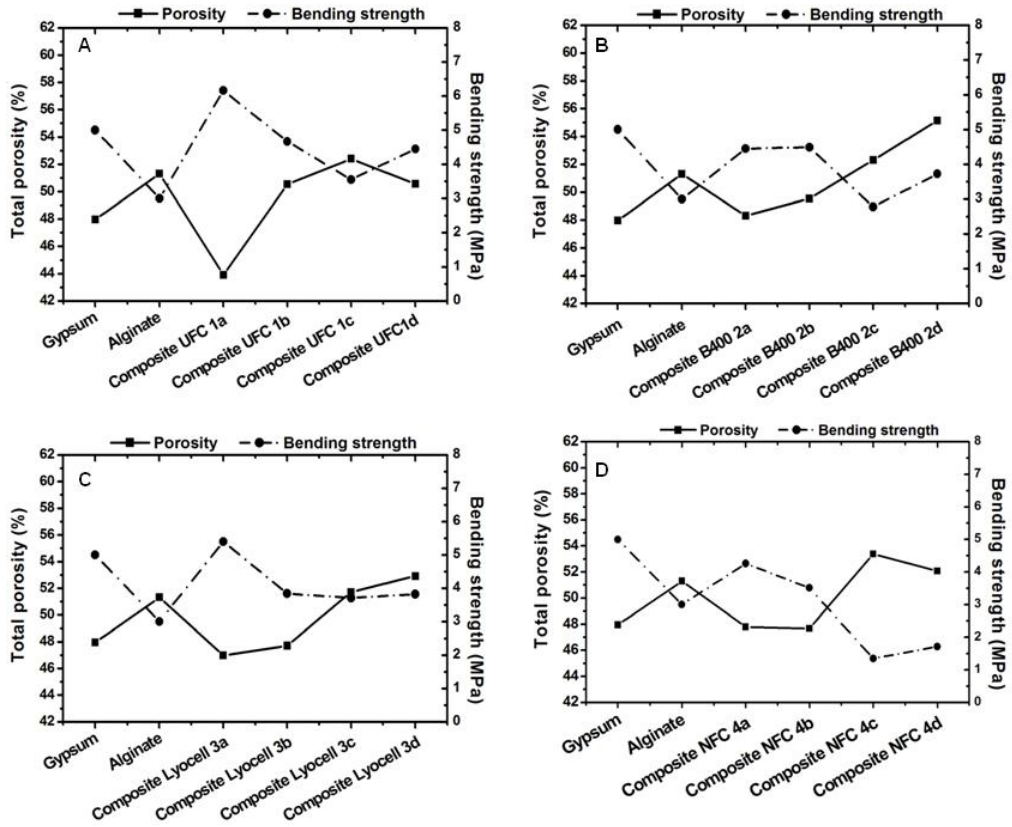

Figure 10. Total porosity of the cellulose/composites as a function of bending strength: **(A)** composites UFC100, **(B)** composites B400, **(C)** composites Lyocell and **(D)** composites NFC. The graphs show that the total porosity influences the bending strength of the final composites. The bending strength of the composites follows the same trend like the other mechanical property of the composites such as the compressive strength.

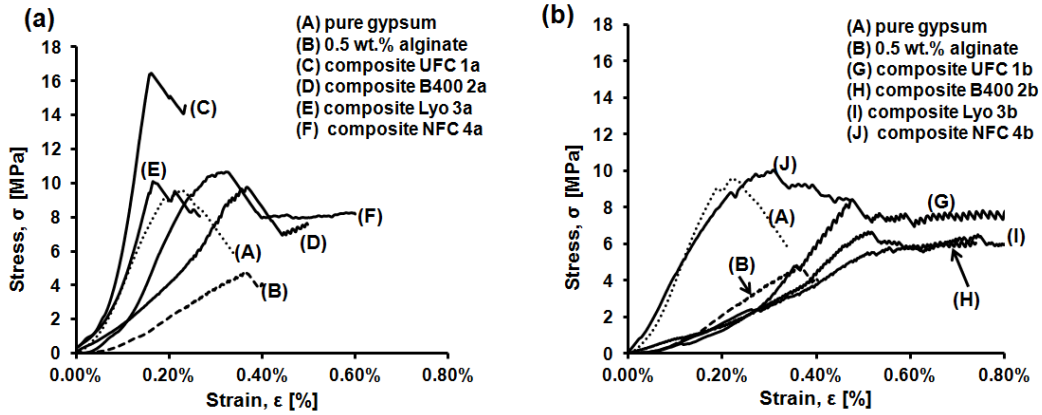

Figure 11. Stress-strain curves of **(a)** composites with 1 wt % of cellulose without sodium alginate and **(b)** composites with 1 wt % cellulose and 0.5 wt % sodium alginate. The stress-strain curves of pure gypsum in the presence and absence of sodium alginate are included as references

5 Discussion

5.1 The role of cellulose in the gypsum crystallization

Polyamide, hemp and cellulose fibers are commonly used to reinforce gypsum composites and are well-known to affect the properties of the composite materials. However, the role of cellulose during gypsum crystal formation, growth and gypsum-gypsum crystal interlocking has not yet been clearly explained. In this

contribution we try to point out this issue. In several composites heterogeneous gypsum nucleation occurs on the surface of cellulose. Such heterogeneous nucleation might be

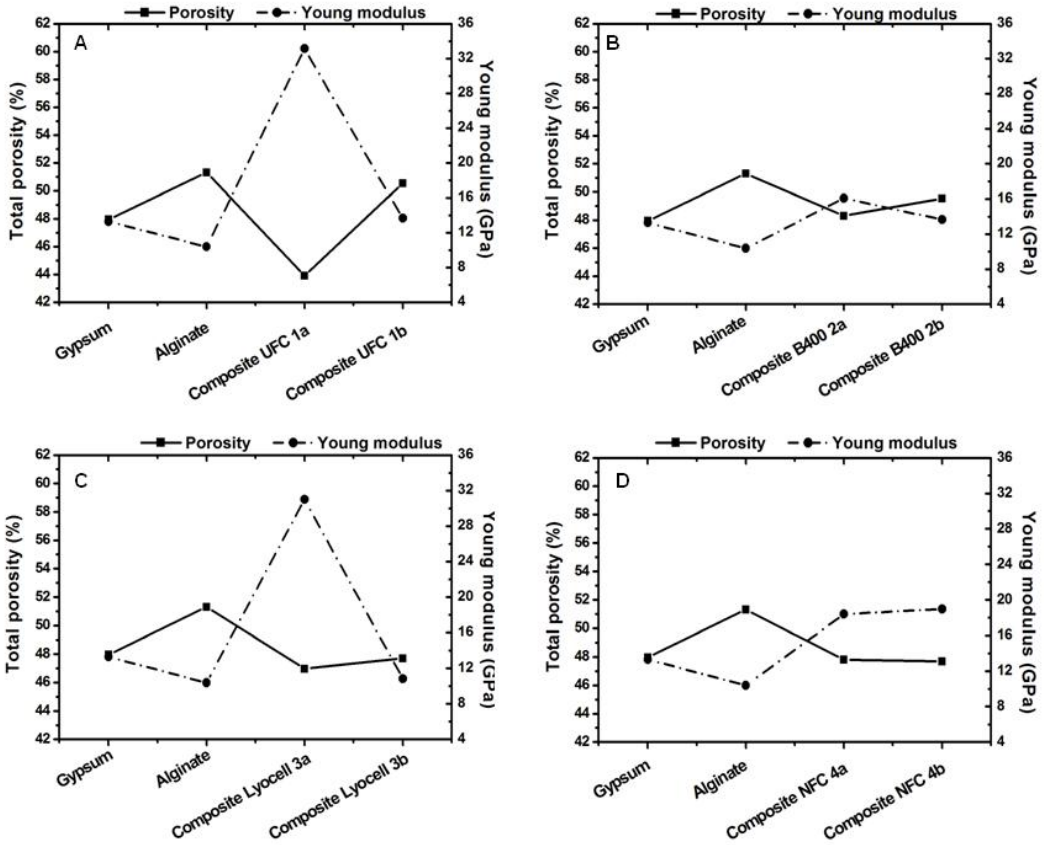

Figure 12. Total porosity of the cellulose/composites as a function of Young's modulus: **(A)** composites UFC100, **(B)** composites B400, **(C)** composites Lyocell and **(D)** composites NFC. The graphs show that the total porosity influences the Young's modulus of the final composites. Composite with an addition of 1 wt % cellulose UFC100 (UFC 1a) has the highest Young's modulus as an effect of low total porosity.

favored by a good matching interface between the structures of gypsum and the different characteristics of the celluloses materials such as the ability of cellulose to absorb and provide water for gypsum crystallization. When gypsum nucleates heterogeneously on cellulose such as in the case of cellulose B400 and Lyocell fiber (Figure 7e and f), the crystal morphology as well as the interlocking features strongly differ from the case in the pure gypsum precipitates. Heterogeneous nucleation does not appear on the surface of NFC. With a decreasing size of the fiber less water is absorbed by the fiber. Thus, a smaller quantity will be released to support gypsum crystallization.

As seen in the SEM image of the composite where UFC100 1a is added (Figure 7a), cellulose UFC100 produces smaller gypsum crystals in comparison to gypsum crystals precipitated without any cellulose. The addition of UFC100 reduces the porosity of the gypsum composite, thus enhances the bending and compression strength of the Composite UFC 1a (Figure 9, 10, S2 and S3).

5.2 The effect of cellulose characteristics and sodium alginate on the mechanical properties of the composites

Cellulose is a complex organic material with unique properties. In this study two distinct cellulose polymorphs were used: Cellulose I (cellulose UFC100, cellulose B400 and NFC) (Figure 3), and cellulose II (Lyocell fiber) (Figure 4). Cellulose UFC100, B400 and NFC are natural fibers, while Lyocell is a synthetic fiber. Cellulose I shows a high degree of crystallinity (degree of crystallinity values of 75.5, 70.2 and 67.8% for UFC100, B400 and NFC, respectively) whereas cellulose II is more amorphous in comparison to cellulose I (degree of crystallinity value of 52.3 %) (Table 2). The degree of crystallinity is correlated to the arrangement of individual fibrils within a cellulose fiber. The degree of crystallinity further defines the degree of swelling and the water retention value (WRV). The degree of

swelling in water or NaOH (2-4M) is larger for cellulose II in comparison to that of cellulose I. Under strong alkali treatment (NaOH of 5-8M) cellulose I has a higher degree of swelling than that of cellulose II.[33] The small swelling degree of cellulose I in water and under alkali treatment (NaOH of 2-4M) is due to the fact that cellulose I has a high degree of crystallinity and contain less disordered interlayers between the crystallites of the elementary fibrils.[38] This results in a lower uptake of water by cellulose I in comparison to cellulose II.

The degree of swelling together with the WRV influence the total porosity[33]. The total porosity further influences the mechanical properties of the composite (compressive strength, bending strength and Young's modulus) (Figure 9, Figure 10 and Figure 12). Note the scatter of data in the box plots (Figure S2 and Figure S3). The significant increase in Young's modulus of the composite with UFC100 is due to a fact that cellulose UFC100 is an ultrafine cellulose powder that can penetrate the pores created by the gypsum needle-like matrix. This reduces the total porosity of the composite. The high Young's modulus of the composite with 1 wt % Lyocell proofs that Lyocell fiber (synthetic fiber) has a high stiffness. The composite with 1 wt % NFC has a Young's modulus value higher than that of composite with 1 wt % B400. NFC is reported by some authors[39-42] as having an increased stiffness.

Cellulose and sodium alginate act as biopolymers that influence the mechanical properties of cellulose/gypsum composites. The composites consist of the gypsum matrix enforced by cellulose fibers and sodium alginate. The gypsum matrix infiltrates the cellulose fibers and affects the mechanical property of the composites depending on the fiber characteristics. The presence of sodium alginate increases the total porosity of the composites by creating more pores (Figure 9, 10 and 12). Cellulose UFC 100, the cellulose with small particles, is able to impregnate the gypsum matrix, thus, decrease the total porosity of the composite (Composite UFC 1a). The decrease in total porosity correlates to an increase in the mechanical properties of the Composite UFC 1a (Figure 10). The stress-strain curve behavior that is observed after the first load drop, appears as a result of an intimate interlinkage between cellulose and sodium alginate so that an effective load transfer between the matrix and the fibers is achieved. This behavior is not observed when cellulose alone is added to gypsum (Figure 11). The addition of sodium alginate to the cellulose/gypsum composite with NFC does not affect the Young's modulus of the composites (Composites NFC 4a and 4b). This clearly explains that sodium alginate does not reduce the NFC-gypsum interface failure by creating an intimate interlinkage between NFC and gypsum interfaces.

6 Conclusions

We investigated the porosity and mechanical properties of cellulose/gypsum composites in the presence and absence of sodium alginate. Our results show that the morphology of cellulose not only affects the formation of gypsum crystals but also the microstructure and the mode of the interlocking of the gypsum crystals. It occurs as the presence of cellulose changes the supersaturation of the solution and surface topography of the growing crystals. A heterogeneous nucleation is affected by a good matching interface between the structures of gypsum and the different characteristics of the celluloses materials such as the ability of cellulose to absorb and provide water for gypsum crystallization.

The gypsum microstructure and mode of interlocking further influence the total porosity and the mechanical properties of the final composite material. The compressive strength, bending strength and Young's modulus increase with the addition of cellulose UFC100 due to the fact that UFC100 is a cut off fiber with an irregularly shaped unit and is able to fill the pores of the composites. A high stiffness of Lyocell fiber, a synthetic fiber, resulted in a high Young's modulus of the composite with the addition of 1 wt % Lyocell fiber. The addition of sodium alginate reduces the interface failure as it is seen in stress-strain curves showing a high ultimate strain value.

Acknowledgments

This work has been partially funded by projects **AIB2010 DE-00085, DAAD-50749739** and **KAAD.** We thank Markus Sieber and the staff of the workshop of Department of Earth and Environmental Sciences, Ludwig Maximilian University for technical support. We also thank Dr. Robin Beddoe from Centre of Building Material, Technische Universität Muenchen for his help with the porosity measurement.

References

1. Wirsching F. Calcium Sulfate. In: Pfefferkorn R, Rounsaville JF, editors. Ullmann's encyclopedia of industrial chemistry. Fifth, completely revised edition, Weinheim: VCH

Verlagsgesellschaft GmbH, 1985, pp 555-584.

2. Gmouh A, Samdi A, Moussa R, and Gomina M. Lightened plaster-based composite materials:Elaboration and mechanical properties. *Silicates Industriels Ceramics Science and Technology* 2001; 66: 61-66.

3. Coutts R. Wastepaper fibers in plaster products. *J Mater Sci Lett* 1991; 10: 77-78.

4. Olvares-Hernández F, Oteiza I and de Villanueva L. Experimental analysis of toughness and modulus of rupture increase of sisal short fiber reinforced hemihydrate gypsum. *Compos Struct* 1992; 22: 123-137.

5. Li G, Yu Y, Zhao Z, Li J, Li C. Properties stuy of cotton stalk fiber/gypsum composite. *Cement Concrete Res* 2003; 33: 43-46.

6. Dalmay P, Smith A, Chotard T, Sahay-Turner P, Gloaguen V and Krausz P. Properties of cellulosic fiber reinforced plaster: influence of hemp or flax fiber on the properties of set gypsum. *J Mater Sci* 2010; 45: 793-803.

7. Eve S, Gomina M, Gmouh A, Samdi A, Moussa R and Orange G. Microstructural and mechanical behavior of polyamide fiber-reinforced plaster composites. *J Eur Ceram Soc* 2002; 22: 2269-2275.

8. Eve S, Gomina M, Pernot JP, Ozouf JC and Orange G. Microstructure characterization of polyamide fiber/latex-filled plaster composites. *J Eur Ceram Soc* 2007; 27: 3517-3525.

9. Ali MA and Grimer FJ. Mechanical properties of glass fiber-reinforced gypsum. *J Mater Sci* 1969; 4: 389-395.

10. Wu YF and Dare MP. Axial and shear behavior of galss fiber reinforced gypsum wall panels. *J Compos Constr* 2004; 8: 569-578.

11. Wu YF. The effet of longitudinal reinforcement on the cyclic shear behavior of glass fiber reinforced gypsum wall panels. *Eng Struct* 2004; 11: 1663-1646.

12. El-Maghraby HF, Gedeon O and Khalil AAA. Formation and characterization of Poly(vinyl alcohol-co-vinyl-acetate-itaconic acid)/plaster composites, part 2. Composite formation and characterization. Ceramics *2007*; 3: 168-172.

13. Chen Z. Sucech S. Faber KT. A hierarchical study if the mechanical properties of gypsum. *J Mater Sc*i 2010; 45: 4444-4453.

14. Lewry AJ and Williamson J. The setting of gypsum plaster, part I: The hydration of calcium sulphate hemihydrates. *J Mater Sci* 1994; 29: 5279-5284.

15. Badens E, Veesler S and Boistelle R. Crystallization of gypsum from hemihydrate in presence of additives. *J Crys Growth* 1999; 198: 704-709.

16. Singh NB and Middendorf B. Calcium sulphate hemihydrates hydration leading to gypsum crystallization. *Prog Cryst Growth Ch* 2007; 53: 57-77.

17. Yu QL and Brouwers HJH. Microstructure and mechanical properties of β-hemihydrate produced gypsum: An insight from its hydration process. *Constr Build Mater* 2011; 25: 3149–3157.

18. Padevět P, Tesárek P, Plachý T. Evolution of mechanical properties of gypsum in time. *Int H Mech* 2011; 5: 1-9.

19. Singh NB, Vellmer C and Middendorf B. Effect of carboxylic acids on the morphology, physical characteristics and hydration of α-hemihydrate plaster. *Indian J Eng Mater Sci* 2005; 12: 337-344.

20. Amathieu L and Boistelle R. Improvement of the mechanical properties of set plasters by means of four organic additives inducing {101} faces. *J Cryst Growth* 1986; 79:169.

21. Osterwalder N, Loher S, Grass RN, Brunner TJ, Limbach LK, Halim SC and Stark WJ. Preparation of nano-gypsum from anhydrite nanoparticles*J Nanopart Res* 2007; 9: 275.

22. Singh M and Garg M. Gypsum-based fibre-reinforcement composites: An alternatice to timber. *Constr Build Mater* 1994; 8: 155-160.

23. Bastidas JC, Pawlak JJ, Venditti RA, Hetimann JA, Hubbe MA and Kadla JF. A colloidal probe microscopy study of cellulose/gypsum interactions. Mater Charact 2008; 59: 144-150.

24. Rusli R and Eichhorn J. Determination of the stiffness of cellulose nanowhiskers and the fiber-matrix interface in a composite using Raman spectroscopy. *Appl Phys Lett*

2008; 93: 033111.

25. Li Q and Renneckar S. Supramolecular structure characterization of molecularly thin cellulose I nanoparticles. *Biomacromolecules* 2011; 12: 650-659.
26. Tanpichai S, Quero F, Nogi M, Yano H, Young RJ, Lindström T, Sampson WW and Eichhorn SJ. Effective Young's Modulus of Bacterial and Microfibrillated Cellulose Fibrils in Fibrous Networks. *Biomacromolecules* 2012; 13: 1340-1349.
27. O'Sullivan AC. Cellulose: the structure slowly unravels. Cellulose *1997*; 4: 173-207.
28. Finkenstadt VL and Millane RP. Crystal sturcture of Valonia Cellulose Iß. *Macromolecules* 1998; 31: 7776-7783.
29. Wada M, Nishiyama Y and Langan P. X-ray Structure of Ammonia-Cellulose I: New Insights into the Conversion of Cellulose I to Cellulose IIII. *Macromolecules* 2006; 39: 2947-2952.
30. Wada M, Nishiyama Y, Chanzy H, Forsyth T and Langan P. Lyocell: The New Generation of Regenerated Cellulose, JCPDS-International Centre for Diffraction Data, 2008, pp138-144.
31. Langan P, Nishiyama Y and Chanzy H. X-ray structure of mercerized cellulose II at 1 Å resolution. *Biomacromolecules* 2012; 2: 410-416.
32. de Maria Pinheiro Correia C and de Souza MF. Mechanical strength and thermal conductivity of low-porosity gypsum plates. *Mat Res* 2009; 12: 95-99.
33. Paul UC, Manian AP, Široká B, Duelli H and Bechtold T. Sorption of anionic polysaccharide by cellulose. *Carbohyd Polym* 2012; 87: 695-700.
34. Özturk HB, Potthast A, Rosenau T, Abu-Rous M, MacNaughtan B, Schuster KC, Mitchell JR and Bechtold T. Changes in the intra- and inter-fibrillar structure of Lyocell (TENCEL®) fibers caused by NaOH treatment. *Cellulose* 2009; 16: 37-52.
35. Ehrhardt A, Groner S and Bechtold T. Swelling behavior of cellulosic fibers – Part I: Changes in physical properties. *Fibre Text East Eur* 2007; 15: 46-48.
36. Oztürk HB and Bechtold T. Effect of NaOH treatment on the interfibrillar swelling and dyeing properties of Lyocell (TENCEL ®) fibres. *Fibre Text East Eur* 2007; 15: 114-117.
37. Lenz J, Schutz J and Wrentschur E. Properties and structure of solvent-soun and viscose-type fibres in the swollen state. Colloid Polymer Sci 1993; 271: 460-468.
38. Zimmermann T, Bordeanu N and Strub E. Properties of nanofibrillated cellulose from different raw materials and its reinforcement potential. *Carbohyd Polym* 2010; 79: 1086-1093.
39. Zadorecki P and Michell AJ. Future-prospects for wood cellulose as reinforcement in organic polymer composites. *Polym Compos* 1989; 10: 69–77.
40. Yano H and Nakahara S. Bio-composites produced from plant microfiber bundles with a nanometer unit web-like network. *J Mater Sci* 2004; 39: 1635–1638.
41. Hubbe MA, Rojas OJ, Lucia LA and Sain M. Cellulosic nanocomposites: a review. *Bio Res* 2008; 3: 929–980.
42. Eyholzer C, Lopez-Suevos F, Tingaut P, Zimmerman T and Oksman K. Reinforcing effect of carboxymethylated nanofibrillated cellulose powder on hydroxypropyl cellulose. *Cellulose* 2010; 17: 793-802.
43. Marín-Galán C, Rivera-Gómez C and Petric J. Clay-based composite stabilized with natural polymer and fibre. Const. Build. Mater. 2010; 24: 1462-1468.
44. Hay ID, Rehman ZU and Rehm BH. Membrane topology of outer membrane protein Algae which is required for alginate production in pseudomonas aeruginosa: Identification of two aflatrem biosynthesis gene loci in aspergillus flavus and metabolic engineering of penicillium paxilli to elucidate their function. Am. Soc. Microbiol. 2010; 76: 1806–1812.
45. Andresen IL, Skipnes O, Smidsrod O, Ostgaard K and Hemmer PC. Some biological functions of matrix components in benthic algae in relation to their chemistry and the composition of seawater. ACS Symp. Ser. 1977; 48: 361–381.
46. Friedemann K, Stallmach F, Kärger F. NMR diffusion and relaxation studies

during cement hydration. Cem. Concr. Res. 2006; 36: 817–826.

47. Rivier-Gómez C, Galán-Marín C and Bradley F. Analysis of the influence of the fiber type in polymer matrix/fiber bond using natural organic polymer stabilizer. Polymers 2014; 6: 977-994.

48. Teeäär R, Serimaa R and Paakkari T. Crystallinity of cellulose, as determined by CP/MAS NMR and XRD methods. *Polymer Bulletin* 1987; 17: 231-237.

49. Terinte N, Ibbett R and Schuster KC. Overview on native cellulose and microcrystalline cellulose I structure studied by X-ray diffraction (WAXD): Comparison between measurement techniques. *Lenzinger Berichte* 2010; 89: 118-131.

50. Park S, Baker JO, Himmel ME, Parilla PA and Johnson DK. Cellulose crystallintiy index: measurement techniques and their impact on interpreting cellulose performance. *Biotechnol Biofuels* 2010; 3: 1-10.

51. Focher B, Palma MT, Canetti M, Torri G, Cosentino C and Gastaldi G. Structural differences between non-wood plant cellulloses: evidence from solid state NMR, vibrational spectroscopy and X-ray diffractomer. *Ind Corp Prod* 2001; 13: 193-208.

52. Kaushik A and Singh M. Isolation and characterization of cellulose nanofibril from wheat straw using steam explosion coupled with high shear homogenization. *Carbohyd Res* 2011; 346: 76-85.

53. Cardew PT and Davey RJ. The Kinetics of Solvent-Mediated Phase Transformations. *Proc R Soc Lond* 1985; A 398: 415-428.

54. Thumbs H and Kohler HH. Capillaries in alginate gels as an example of dissipative structure formation. *Chem Phys* 1996; 208: 9-24.

55. d'Ayala GC, Malinconico M and Laurienzo P. Marine derived polysaccharide for biomedical applications: Chemical modification approaches. *Molecules* 2008; 13: 2069-2106.

Supporting Information

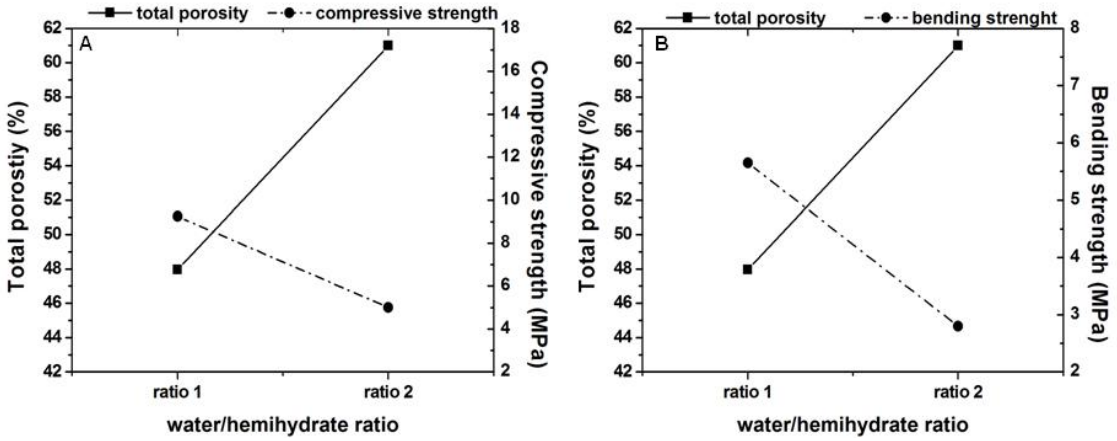

Figure S1. The total porosity as a function of mechanical properties: **(A)** compressive strength and **(B)** bending strength. Two different water/hemihydrate (w_o/h_o) are used: ratio 1 is 0.5 and ratio 2 is 0.97. The high w_o/h_o results to a high total porosity that further decreases the mechanical properties (bending strength, compressive strength and Young's modulus) of gypsum.

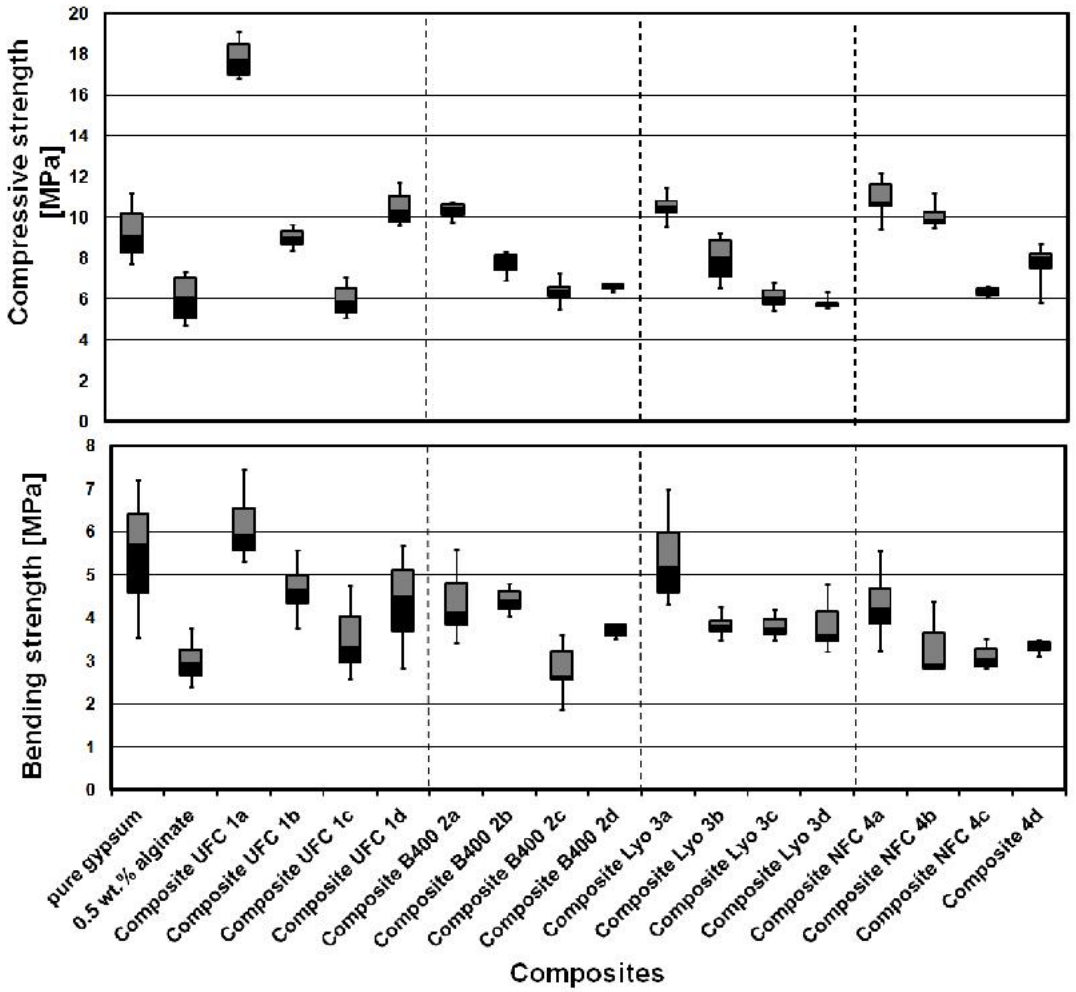

Figure S2. Box plots of compressive and bending strength of composites due to an addition of cellulose UFC100, cellulose B400, Lyocell fiber and NFC. The maximum and minimum bars are applied along with the median, the lower quartile (25th percentile) and the upper quartile (75th percentile). The upper box is defined as the upper quartile (75th percentile) and the bottom box is defined as the lower quartile (25th percentile). The median is defined as a border between lower the quartile box and the upper quartile box.

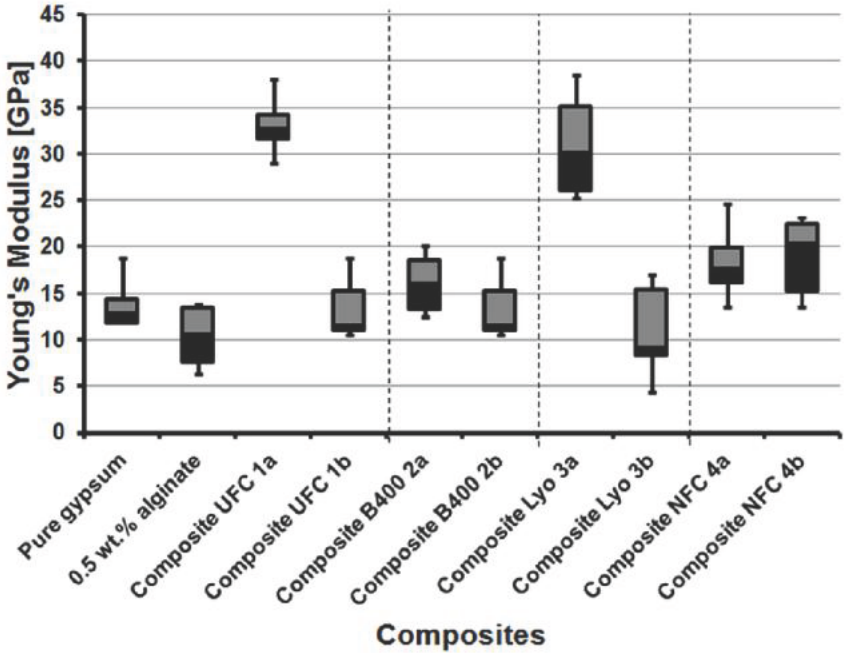

Figure S3. Young's moduli of composites with 1 wt % of cellulose in the presence and absence of sodium alginate. The samples are taken from Figure 11. The Composite UFC 1a and Lyo 1a have higher Young's moduli in comparison to the other composites. The maximum and minimum bars are applied along with the median, the lower quartile (25^{th} percentile) and the upper quartile (75^{th} percentile). The upper box is defined as the upper quartile (75^{th} percentile) and the bottom box is defined as the lower quartile (25^{th} percentile). The median is defined as a border between the lower quartile box and the upper quartile box.

3. Concluding Summary and Outlook

3.1 Concluding Summary

Chapter 2.1 summarized the characterization of *Mytilus edulis* shell as a biocomposite containing biocarbonate minerals and organic matrices using Electron Backscatter Diffraction (EBSD). *M. edulis* shell has two distinct layers, the outer layer is prismatic calcite and the inner layer is nacreous aragonite. In the interface between nacreous aragonite and prismatic calcite, a 1-2 micrometer wide granular aragonite band containing a high density organic matrix layer exists. By using EBSD, a misorientation of 2° full width half maximum is observed within the aragonite tablets confirming a presence of mesoscale crystallographic mosaic structure. The presence of organic network inside the aragonite tablets is observed after the etching procedure. The crystallographic lattice orientation spreads from tablet to tablet and across interlamellar matrix sheaths. The co-orientation comprises at least two adjacent tablets and stacks in a tower-like manner up to 20 tablets along c-axis and covers the area of 1-2 tablets in the a-b plane. Thus, it clearly explains that organic matrix membranes in nacreous aragonite become occluded into a growing hierarchical composite crystal.

The result shows that biominerals are nanocomposites with an intimate association of organic matrix and mineral in a hierarchical structure. In order to get better understanding of crystallization of biocomposite containing biocarbonate minerals and organic matrices, a reliable approach needs to be proposed. One of the approaches that can be applied to investigate the mechanisms that lead to the formation of this type of biocarbonate composite involves the use of hydrogels to mimic the organic matrix of the organism and the induction of the biomimetic crystallization of the carbonate mineral as a result of reagents counter-diffusion through the hydrogel.

Chapter 2.2-2.4 summarizes the characteristics of the crystallization of calcium carbonate in a biomimetic counter-diffusion system. Hydrogel systems have been widely used to reproduce the role of organic matrices during the formation of carbonate biominerals. There are a number of parameters of the hydrogels that can be adjusted to better mimic the characteristics of these organic matrices. Chapter 2.2 summarizes the crystallization of calcium carbonate minerals using gelatin hydrogels with different solid contents (2.5, 5 and 10 wt %). It is found that the increase of gelatin content decreases the hydrogel pore size, which further results in an increase of (i) the time delay between the beginning of experiments and the detection of the first optically visible crystals and (ii) the saturation index at the position of the nucleating crystals. By increasing the gelatin content, the hydrogel becomes stronger and is more able to resist the crystallization pressure, i.e. the pressure exerted against the hydrogel network by the growing calcite crystals. Both the high supersaturation in the system during crystallization and the high strength of the gelatin hydrogel explain the high amount of gelatin incorporated into the crystals as more gelatin solid content is used. Similarly to the case of biocomposites, the organic membranes occluded into the crystals formed in these experiments contribute to the formation of mesoscale crystallographic mosaic structures. The high amount of gelatin hydrogel occluded into calcite crystals grown in a 10 wt % gelatin hydrogel leads to crystals with internal structures with a high mosaicity and misorientations of up to 6° in the subunits constituting crystal aggregates. These characteristics coincide with some of those found in biocarbonate

composites in nature and reveal that calcite crystallization in hydrogels with a 10 wt % gelatin content can be used to mimic and investigate the crystallization of biocarbonate composites of organisms.

Magnesium is a common additive in calcium carbonate biological hard tissues, where it occurs in a wide range of concentrations, from 0 to 23 mol % $MgCO_3$ in the hard tissue of some organisms such as echinoderm skeletons, oktocorals and neritic benthic foraminifera, and up to 45 mol % $MgCO_3$ in the hard tissues of some other organisms, e.g. sea urchin teeth. Chapter 2.3 summarizes the effect of Mg in the crystallization of calcium carbonate in counter-diffusion systems using gelatin hydrogels with two solid contents, 2.5 and 10 wt % gelatin. The presence of Mg in the gelatin hydrogel has several effects on the crystallization of $CaCO_3$. The first effect is the inhibition of crystallization. This effect leads to an increase of the waiting time for the detection of the first optically visible crystal and a decrease of the number of crystal aggregates formed. The second effect refers to polymorph selectivity. The presence of Mg in 2.5 wt % gelatin hydrogels promotes the formation of aragonite, which is an alternative, metastable $CaCO_3$ polymorph that does not incorporate Mg^{2+}. However, Mg^{2+} does not promote the formation of any metastable polymorph in 10 wt % Mg-bearing gelatin hydrogels but leads to precipitates exclusively consisting of calcite. The range of incorporated Mg into calcite crystals varies depending on the gelatin content of the hydrogel; a high gelatin solid content promotes the likeliness of Mg incorporation. The calcite crystals precipitated from 2.5 wt % Mg-bearing gelatin have incorporated Mg that varies in the range from 0.2 – 9 mol % $MgCO_3$. Calcite crystal aggregates with the highest incorporated Mg are found in 10 wt % Mg-bearing gelatin hydrogels. These aggregates have $MgCO_3$ contents up to 26 mol %.

The presence of Mg in the hydrogel system strongly influences the characteristics of the incorporated polymeric network, such as the arrangement of polymeric intercalations and the fabrics of the hydrogels. The amount of Mg incorporated into calcite also influences the characteristics of the crystal aggregates. Crystals precipitated in Mg-bearing gelatin tend to produce aggregates that are built up by small subunits with sizes of hundred nanometers. In the experimental set used in our study crystallization occurs in a small region of the hydrogel. In that region a certain variation of the physicochemical conditions, including supersaturation, pH, Mg/Ca ratio will occur due to the mass transfer process. To this variation, the effect of reagents consumption due to crystal growth is superimposed, leading to locally altered conditions. The growing crystals exert a pressure against the polymeric walls that are bounded by pores in the hydrogel. Thus, this pressure promotes the rearrangement of the gelatin matrix. The combination of local differences in physichochemical condition and gelatin matrix characteristics explains the formation of crystal aggregrates that are constituted of subunits. These show a variety of features i.e. the formation of mosaic crystals and mesocrystal-like crystals in one aggregate. Moreover, the accumulation of small angle boundaries, formed as a mechanism to release the misfit strain associated to Mg preferential incorporation onto specific growth sites, leads to the formation of spherulites.

Several different hydrogels were used to investigate the crystallization of calcium carbonate (Chapter 2.4). Gelatin and agarose hydrogels have a fibrous structure with highly varying pore dimensions. In comparison to agarose, gelatin is more compact and has a characteristic mesh size in the order of 60 nm with occasional pores in the 150 nm size range. Smaller mesh sizes are very frequent, but they result from non-equatorial sectioning of large pores. While fiber thickness in agarose hydrogel is similar to that in gelatin, pore dimensions of

the agarose hydrogel are wider than those of gelatin hydrogel, with 100-200 nm pores. Silica hydrogel has an entirely different structure. It is composed of minute (less than 20 nm) spherical particles that do not appear to form a network. Each hydrogel acts differently in the formation and co-orientation of calcite crystals or aggregates. However, hydrogels only mimic biological extracellular matrices to some extent as the hydrogel fiber organization lacks any order, unlike in the case of cholesteric liquid crystal phase, e. g. chitin.

As it is explained above, hydrogels become increasingly important to mimic and investigate the crystallization of carbonate biominerals in the presence or absence of Mg. Carbonate hard tissues also have characteristic mechanical properties due the presence of organic matrices such as in aragonite nacre with fracture toughness higher than that of aragonite from chemical precipitation (Jackson et al., 1988).

Inspired by carbonate biocomposites gypsum/cellulose fiber composites were prepared (Chapter 2.5). Gypsum is chosen due to its importance in building materials. The addition of cellulose fiber as a biopolymer is expected to increase the ecological value and mechanical properties of the gypsum/cellulose composites.

Cellulose is a complex organic material with unique properties that are different for each cellulose polymorph. The main difference of each cellulose polymorph is due to a parallel or antiparallel stacking mode of cellulose chains and to the degree of crystallinity of each cellulose polymorph, low degree of crystallinity meaning that the cellulose contains more amorphous phase. The degree of crystallinity also correlates with the arrangement of individual fibrils within a cellulose fiber. This fibril arrangement defines the ability of the cellulose to swell under strong alkali treatment. This swelling behavior together with the oxidation process that occurs under strong alkali treatment defines the elasticity of the cellulose.

Gypsum/cellulose composites prepared in this study consist of gypsum matrix and cellulose fibers with or without addition of sodium alginate. The gypsum matrix infiltrates the cellulose fiber and affects the mechanical property of the composites depending on the fiber characteristics e.g. the nature of the cellulose (natural or synthetic), water retention value, swelling degree, etc. Sodium alginate reacts with cellulose and creates specific bonding that also affects the gypsum matrix. This intimate reaction between cellulose and sodium alginate is able to create an effective load transfer between the matrix and the fibers. Lyocell fiber, a synthetic fiber, is able to increase the Young's modulus of the final composites.

3.2 Outlook

The carbonate biomineralization process is a complex process that is not yet fully understood. Biomimetic crystallization experiments based on reagent counter-diffusion through a hydrogel define one of many approaches that can be used to investigate biomineralization of carbonate hard tissues. Although it has been possible to provide some answers, these experiments have open new research perspectives and left many questions unanswered.

1. Investigating of amorphous calcium carbonate by means of hydrogel counter-diffusion system.

The nature of hydrogel prevents the investigation of fine amorphous particles. The extraction of the precipitate formed in hydrogel counter-diffusion systems commonly involves dissolving the hydrogel (gelatin and agarose) in warm water. In the case of a fine amorphous calcium carbonate precipitate formed within the hydrogels, it would either dissolve or transform into a calcium carbonate crystalline phase during the extraction process. The use of other hydrogels, whose formation involves chemical reactions and cannot be reverted to the sol state by temperature changes, does not resolve the problem since difficulty of recovering the precipitate not only remains but increases. Thus, the investigation of the possible formation of amorphous phases as precursors to calcite or other $CaCO_3$ polymorphs in hydrogels remains unaccomplished. A possible approach is to focus a laser on the region of the hydrogel column where nucleation is expected to detect the exact moment when nucleation occurs by measuring the changes in the intensity of light scattered and immediately studying the Raman spectrum of that region. Since the spectrum of the hydrogel can be collected before nucleation, it can be subtracted to that after nucleation. The resulting spectrum should show the characteristics of ACC if it were forming in the system (Weiner et al., 2003; Wang et al., 2011)

2. Combining two different hydrogels to get a better reproduction of the characteristics of organic matrices in some organisms.

Some hydrogels, i.e gelatin and agarose, show features strikingly similar to organic matrices in bivalve' shells such as that of *Mytilus edulis* (Chapter 2.1). This similarity can be increased by combining both gelatin and agarose in the same hydrogel, as demonstrated by Simon et al. (2011). Further research to investigate the effect of hydrogels consisting of mixtures of gelatin and agarose on the characteristics of biomimetic calcium carbonate aggregates is, therefore, timely. Hydrogels with different proportions of each organic polymer would need to be explored to evaluate and discriminate possible influences of such combinations on polymorph selectivity, Mg incorporation and crystal shape (Li & Esttroff, 2009; Nindiyasari et al., 2014[a,b]). The characteristics of organic matrices created by combining two organic polymers in a hydrogel can be investigated with Cryo-SEM. Knowledge of these characteristics is crucial to interpret features of the crystals and crystal aggregates obtained.

3. The addition of organic and/or ionic compounds.

In the biomineralization of some carbonate hard tissue, the presence of specific organic compounds is thought to play crucial roles. Further research would involve the addition of

organics such as poly(L-aspartic acid) (Sethmann et al., 2005; Lam et al., 2007; Song & Cölfen, 2011), sodium dodecyl sulfate (SDS) or Tween 20 (You et al., 2009; Song & Cölfen, 2011) or ionic compounds such as sulfonic acid functional groups (Grassmann & Löbmann, 2003), carboxylate groups (Grassmann & Löbmann, 2004) or Mg^{2+} (Meldrum & Hyde, 2001) to the hydrogels to investigate by means of Electron Backscatter Diffraction (EBSD) the combined influence of these compounds and hydrogel characteristics on the polymorph selection and the crystal orientation features of the crystal aggregates obtained.

4. Investigation of Mg incorporation in gelatin-grown calcite crystals in relation to the presence of carboxyl groups in gelatin hydrogel.

Our previous results show that the incorporation of Mg in calcite crystals grown in gelatin can reach up to 26 mol % $MgCO_3$ (Nindiyasari et al., 2014[b]). A significant enhancement of Mg incorporation into calcite due to hydrophilic peptides was detected by Stephenson et al. (2008). Since gelatin is rich in hydrophilic peptides we have related the high Mg contents found in calcite crystal aggregates grown in gelatin hydrogels to the presence of different functional groups and interpreted that they provide a lower energy alternative pathway for Mg desolvation, which facilitates Mg incorporation into the calcite structure. However, the relationship between the existence of hydrophilic peptides in the hydrogel matrix and high amounts of Mg incorporating into calcite still needs to be unequivocally established. In order to check this relationship, new experiments need to be conducted. These experiments would involve the use of hydrogels in which hydrophilic peptides were absent and to modulate their presence through the addition of varying amounts of organic additives that contain carboxylate groups.

5. Investigation of the formation of membranes that limit subunits with different characteristics in a crystal aggregate.

Our previous results show that the growth of calcite crystal aggregates in both gelatin and agarose hydrogels is accompanied by the formation of hydrogel membranes that separate subunits with different structuring within these aggregates. Although the factors that control the formation of hydrogel membranes are not totally understood, the balance between growth rate and hydrogel strength seems to be crucial for their development. In order to shed light on the relative importance of both factors further research is needed. This research would involve:

(i) Characterizing the mechanical properties of different hydrogels (Li & Esttroff, 2009)

(ii) Conducting crystal growth experiments using hydrogels of known hydrogel strength and varying the concentration of the reagents so different growth rates are achieved.

Since it seems apparent from our results that the addition of Mg to the hydrogel can modify its strength, this research would have to be extended to Mg-bearing hydrogels. As it is summarized above, the crystallization of calcium carbonate by means of a hydrogel counter-diffusion system can significantly contribute to the understanding of biomineralization processes and the factors controlling the internal micro-organization of biominerals. This dissertation covers only a small range of possible applications of hydrogel counter-diffusion systems to mimic biomineralization.

Bibliography

Addadi, L., & Weiner, S. (2003). Taking Advantage of Disorder: Amorphous Calcium Carbonate and Its Role in Biomineralization. *Adv. Mat., 15*, 959-970.

Akiva-Tal, A., Kababya, S., Balazs, Y. S., Glazer, L., Berman, A., Sagi, A., & Schmidt, A. (2011). In Situ Molecular NMR Picture of Bioavailable Calcium Stabilized as Amorphous $CaCO_3$ Biomineral in Crayfish Gastroliths. *Proc. Natl. Acad. Sci. USA, 108*, 14763-14768.

Alberts, A., Johnson, J., Lewis, J., Raff, M., Roberts, K., Walter, P. (2007). *Molecular Biology of the Cell* (5th ed). Garland Science.

Alexander, R. B. (2001). Functional Morphology and Biomechanics of Articulate Brachiopods Shells. *The Paleontology Society Special Paper , 7*, 145-170.

Al-Sawamih, A. L., Siegel, S., Fabritius, H., Yi, S., Raabe, D., Fratzl, P., & Paris, O. (2008). Microtexture and Chitin/Calcite Orientation Relationship in the Mineralized Exoskeleton of the American Lobster. *Adv. Funct. Mater. , 18*, 3307-3314.

Asenath-Smith, E., Li, H., Keene, E. C., Seh, Z. W., & Estroff, L. A. (2012). Crystal Growth of Calcium Carbonate in Hydrogels as a Model in Biomineralization. *Adv. Funct. Mat., 22*, 2891-2914.

Astbury, W. T. (1933, 29). Some Problema in the X-ray Analysis of the Structure of Animal Hairs and Other Protein Fibres. *T. Faraday Soc.*, 193-211.

Beniash, E., Aizenberg, J., Addadi, L., & Weiner, S. (1997). Amorphous Calcium Carbonate Transforms Into Calcite during Sea Urchin Larva Spicule Growth. *Proc. R. Soc. Lond. B., 264*, 461-465.

Bochek, A. M. (2003). Effects of Hydrogen Bonding on Cellulose Solubility in Aqueous and Non Aqueous Solvent. *Russ. J. Appl. Chem., 76*, 1761-1770.

Borelli, G., Mayer-Gostan, N., Merle, P. L., De Pontual, H., Boeuf, G., Allemand, D., & Payan, P. (2003). Composition of Biomineral Organic Matrices with Special Emphasis on Turbot (*Psetta maxima*) Otolith and Endolymph. *Calcified Tissue Int. , 72*, 717-725.

Brooks, R., Clark, L. M., & Thurston, E. F. (1950). Calcium Carbonate and Its Hydrates. *Phil. Trans. R. Soc. Lond. A., 243*, 145-167.

Callister, W. D. (2007). *Material Science and Engineering: An Introduction* (7th ed.). New York: John Wiley & Son, Inc.

Cartwright, J. H., Checa, A. G., Gale, J. D., Gebauer, D., & Sainz-Díaz, I. (2012). Calcium Carbonate Polymorphism and Its Role in Biomineralization: How Many Amorphous Calcium Carbonates Are There? *Angew. Chem. Intl. Ed. , 51*, 11960-11970.

Chen, Z., Sucech, S., & Faber, K. T. (2010). A Hierarchical Study of the Mechanical Properties of Gypsum. *J. Mater. Sci., 45*, 4444-4453.

Chernov, A. A. (1984). *Modern Crystallogrpahy III: Crystal Growth.* Berlin, Heidelberg, New York, Tokyo: Springer.

Cölfen, H., & Antonietti, M. (2005). Mesocrystals: Inorganic Superstructure Made by Highly Parallel Crystallization and Controlled Alignment. *Angew. Chem. Int. Ed. , 44*, 5576-5591.

Cusack, M., & Freer, A. (2008). Biomineralization: Elemental and Organic Influence in Carbonate Systems. *Chem. Rev., 108*, 4433-4454.

Dalmay, P., Smith, A., Chotard, T., Sahay-Tumer, P., Gloaguen, V., & Krausz, P. (2010).

Properties of Cellulosic Fibre Reinforced Plaster: Influence of Hemp or Flax Fibre on the Properties of Set Gypsum. *J. Mater. Sci., 45*, 793-803.

Eve, S., Gomina, M., Gmouh, S., Samdi, A., Moussa, R., & Orange, G. (2002). Microstructural and Mechanical Behaviour of Polyamide Fibre-Reinforced Plaster Composites. *J. Eur. Ceram. Soc., 22*, 2269-2275.

Fengel, D. (1971). Ideas on Ultrrastructural Organisation of Cell-Wall Components. *J. Polym. Sci. Pol. Sym., 36*, 383-392.

Finkenstadt, V. L., & Millane, R. P. (1998). Crystal Structure of Valonia I-beta. *Macromolecus, 31*, 7776-7783.

Frey-Wyssling, A. (1953). Submicron Structure of Cellulose Microfibrils. *Science, 199*, 80-82.

Gago-Duport, L., Brioner, M. J., Rodríguez, J. B., & Covelo, B. (2008). Amorphous Calcium Carbonate Biomineralization in the Earthworm's Calciferous Gland: Pathways to the Formation of the Crystalline Phases. *J. Struc. Biol., 162*, 422-435.

Gebauer, D., & Cölfen, H. (2011). Prenucleation Clusters and Non-Classical Nucleation. *Nano Today, 6*, 564-584.

Gebauer, D., Gunawidjaja, P. N., Ko, J. Y. P. Bacsik, Z., Aziz, B., Liu, L. J., Hu, Y. F., Bergström, L., Tai, C. W., Sham, T. K., Edén, M., Hedin, N. (2010). Proto-Calcite and Proto-Vaterite in Amorphous Calcium Carbonate. *Angew. Chem. Int. Ed., 49*, 8889-8891.

Gebauer, D., Völkel, A., & Cölfen, H. (2008). Stable Prenucleation Calcium Carbonate Clusters. *Science, 322*, 1819-1822.

Goetz, A. J., Griesshaber, E., Abel, R., Fehr, Th., Ruthensteiner, B., Schmahl, W. W. (2014). Tailored order: The mesocrystalline nature of sea urchin teeth. *Ac. Biomater., 10*, 3885-3898.

Goussé, C., Chanzy, H., Cerrada, M. L., & Fleury, E. (2004). Surface Sylation of Cellulose Microfibril: Preparation and Rheological Properties. *Polymer, 45*, 1569-1575.

Gower, L. B. (2008). Biomimetic Model Systems for Investigating the Amorphous Precursor Pathway and Its Role in Biomineralization. *Chem. Rev., 108*, 4551-4627.

Grasby, S. E. (2003). Naturally Precipitating Vaterite (μ-$CaCO_3$) sphere: Unusual Carbonates Formed in an Extreme Environment. *Geochim. Cosmochim. Ac., 67*, 1659-1666.

Grassmann, O., & Löbmann, P. (2003). Morphogenetic Control of Calcite Crystal Growth in Sulfonic Acid Based Hydrogels. *Chem. Eur. J., 9*, 1310-1316.

Grassmann, O., & Löbmann, P. (2004). Biomimetic Nucleation and Growth of $CaCO_3$ in Hydrogels Incorporating Carboxylate Groups. *Biomaterials, 25*, 277-282.

Grassmann, O., Neder, R. B., Putnis, A., & Löbmann, P. (2003). Biomimetic Control of Crystal Assembly by Growth in an Organic Hydrogel Network. *Am. Min., 88*, 647-652.

Griesshaber, E., Kelm, K., Sehrbrock, A., Mader, W., Mutterlose, J., U., B., & Schmahl, W. W. (2009). Amorphous Calcium Carbonate in the Shell Material of the Brachiopod *Megerlia truncata*. *Eur. J. Mineral., 21*, 715-723.

Griesshaber, E., Schmahl, W. S., Ubhi, H. S., Huber, J., Nindiyasari, F., Maier, B., & Ziegler, A. (2013). Homoepitaxial Meso- and Microscale Crystal Co-Orientation and Organic Matrix Network Structure in *Mytilus edulis* nacre and Calcite. *Acta Biomater., 9*, 9492-9502.

Griesshaber, E., Schmahl, W. W., Neuser, R., Pettke, T., Blüm, M., Mutterlose, J., & Brand, U. (2007). Crystallographic Texture and Microstructure of Terebratulide Brachiopods Shell Calcite: An Optimized Materials Design with Hierarchical Architecture. *Am. Min., 92*, 722-

734.

Guillemet, B., Faatz, M., Göhn, F., Wegner, G., & Baptiste., G. (2006). Nanosized Amorphous Calcium Carbonate Stabilized by Poly(ethylene oxide)-b-poly(acrylic acid) Block Copolymers. *Langmuir, 22*, 1875-1879.

Han, T. Y.-J., & Aizenberg, J. (2008). Calcium Carbonate Storage in Amorphous Form and Its Template-Induced Crystallization. *Chem. Mater., 20*, 1064-1068.

Henisch, H. K. (1988). *Crystal Growth in Gels and Liesegang Rings*. Cambridge: Cambridge University Press.

Henisch, H. K., & García-Ruiz, J. M. (1986). Crystal Growth in Gels and Liesegang Ring Formation: I. Diffusion Relationships. *J. Cryst. Growth, 75*, 195-202.

Huang, S.-C., Naka, K., & Chujo, Y. (2007). A Carbonate Controlled-Addition Method for Amorphous Calcium Carbonate Spheres Stabilized by Poly(acrylic acid)s. *Langmuir, 23*, 12086-12095.

Humphreys, F. J. (2001). Grain and Subgrain Characterisation by Electron Backscatter Diffraction. *J. Mater. Sci., 36*.

Jackson, A. P., Vincent, J. F., & Turner, R. M. (1988). The Mechanical Design of Nacre. Proc. R. Soc. Lond. B., *234*, 415-440.

Jolivet, A., Bardeau, J.-F., Fablet, R., Paulet, Y.-M., & De Pontual, H. (2008). Understanding Otolith Biomineralization Process: New Insights into Microscale Spatial Distribution of Organic and Mineral Fractions from Raman Microspectrometry. *Anal. Bioanal. Chem., 392*, 551-560.

Jones, R.M., (1975) *Mechanics of Composite Materials*. Hemisphere Publishing Corporation, New York.

Kashiev, D. (2000). *Nucleation.* Butterworth-Heinemann.

Kim, Y.-Y., Schenk, A. S., Ihli, J., Kulak, A. N., Hetherington, N. B., Tang, C. C., Schmahl, W. W., Griesshaber, E., Hyett, G., Meldrum, F. C. (2014). A Critical Analysis of Calcium Carbonate Mesocrystals. *Nat. Commun., 5*, 1-4.

Kobayashi, I., & Samata, T. (2006). Bivalve Shell Structure and Organic Matrix. *Mater. Sci. Eng. , 26*, 692-698.

Lam, R. S., Charnock, J. M., Lennie, A., & Meldrum, F. C. (2007). Syntesis-Dependant Structural Variations in Amorphous Calcium Carbonate. *Cryst. Eng. Comm., 9*, 1226-1236.

Langan, P., Nishiyama, Y., & Chanzy, H. (2001). X-ray Structure of Mercerized Cellulose II at 1Å Resolution. *Biomacromolecules, 2*, 410-416.

Levi-Kalisman, Y., Falini, G., Addadi, L., & Weiner, S. (2001). Structure of the Nacreous Organic Matrix of a Bivalve Mollusk Shell Examined in the Hydrated State Using Cryo-TEM. *J. Struc. Biol., 135*, 8-17.

Levi-Kalisman, Y., Raz, S., Weiner, S., Addadi, L. Sagi, I. (2002) Structural Differences between Biogenic Amorphous Calcium Carbonate Phases Using X-ray Absorption Spectroscopy. *Adv. Funct. Mater*., 12, 43-48.

Li, H., & Esttroff, A. (2009). Calcite Growth in Hydrogels: Assessing the Mechanism of Polymer-Network Incorporation into Single Crystals. *Adv. Mat., 21*, 470-473.

Lippmann, F. (1973). *Sedimentary Carbonate Minerals*. Springer-Verlag.

Loste, E., Wilson, R. M., Seshadri, R., & Meldrum, F. C. (2003). The Role of Magnesium in Stabilising Amorphous Calcium Carbonate and Controlling Calcite Morphologies. *J. Cryst.*

Growth, 254, 201-218.

Lowenstan, H. A. (1988). Minerals formed by organisms. *Science*, 211, 1126-1131.

Lowenstam, H. A., & Weiner, S. (1989). *On Biomineralization.* New York: Oxford University Press.

Lowenstam, H. A., Abbot, D. (1975). Vaterite: A Mineralization Product of the Hard Tissues of a Marine Organism (Ascidiacea). *Science, 188*, 363-365.

Mahamid, J., Aichmayer, B., Shimoni, E., Ziblat, R., Li, C., Siegel, S., Paris, O., Fratzl, P. Weiner, S., Addadi, L. (2010). Mapping Amorphous Calcium Phosphate Transformation into Crystalline Mineral from the Cell to the Bone in Zebrafish Fin Rays. *PNAS, 107*, 6316-6321.

Maier, B. J., Griesshaber, E., Alexa, P., Ziegler, A., Ubhi, H. S., Schmahl, W. W. (2014). Biological control of crystallography architecture: Hierarchy and co- alignment parameters. *Ac. Biomater., 10*, 3866-3874.

Mann, S. (1983). Mineralization in Biological System. *Struct. Bonding, 54*, 125-174.

Mann, S. (2001). *Biomineralization: Principles and Concepts in Biorganic Materials Chemistry.* New York: Oxford University Press.

Marin, F., & Luquet, G. (2004). Molluscan Shell Protein. *C. R. Palevol., 3*, 469-492.

Marxen, J. C., Becker, W., Finke, D., Hasse, B., & Epple, M. (2003). Early Mineralization in *Biomphlaria glabrata*: Microscopic and Structural Results. *J. Mollus. Stud., 69*, 113-121.

Meldrum, F. C., & Cölfen, H. (2008). Controlling Mineral Morphologies and Structure in Biological and Synthetic Systems. *Chem. Rev., 108*, 4332-4432.

Meldrum, F. C., & Hyde, S. T. (2001). Morphological Influence of Magnesium and Organic Additives on the Precipitation of Calcite. *J. Cryst. Growth , 231*, 544-558.

Mullin, J. W. (2001). *Crystallization.* Oxford, United Kingdom: Butterworth-Heinemann.

Murayama, E., Okuno, A., Ohira, T., Takagi, Y., & Nagasawa, H. (2000). Molecular Cloning and Expression of an Otolith Matrix Protein cDNA from the Rainbow Trout, *Oncorhynchus mykiss*. *Comp. Biochem. Physio. B., 126*, 511-520.

Niederberger, M., & Cölfen, H. (2006). Oriented Attachment and Mesocrystals: Non-Classical Crystallization Mechanisms Based on Nanoparticle Assembly. *Phys. Chem. Chem. Phy., 8*, 3271-3287.

Nindiyasari, F., Fernández-Díaz, L., Griesshaber, E., Astilleros, J. M., Sánchez-Pastor, N., & Schmahl, W. (2014)[a]. The Influence of Gelatin Hydrogel Porosity on the Crystallization of $CaCO_3$. *Cryst. Grwoth Des., 14*, 1531-1542.

Nindiyasari, F., Griesshaber, E., Fernández-Díaz, L., Astilleros, J. M., Sánchez-Pastor, N., Ziegler, A., & Schmahl, W. W. (2014)[b]. The Effects of Mg and The Hydrogel Solid Content on the Crystallization of Calcium Carbonate in Biomimetic Counter-diffusion Systems. *Cryst. Growth Des., 14*, 4790-4802.

O'Sullivan, A. C. (1997, 4). Cellulose: The Structure Slowly Unravels. *Cellulose, 4*, 173-207.

Padevet, P., Tesárek, P., & Plachý, T. (2011). Evolution of Mechanical Properties of Gypsum in Time. *International Journal of Mechanics*, 1-9.

Paredes, A. M. (2000). Scanning Electron Microscopy. In. Carl A. Batt, *Encyclopedia of Food Microbiology* (pp. 695). Elsevier.

Pecharsky, V. K., & Zavalij, P. Y. (2005). *Fundamentals of Powder Diffraction and Structural*

Characterization of Materials. New York: Springer.

Plummer, L. N., & Busenber, E. (1982). The Solubility of Calcite, Aragonite and Vaterite in CO_2-H_2O Solution Between 0 and 90 °C, and An Evaluation of the Aqueous Model for the System $CaCO_3$-CO_2-H_2O. *Geochim. Cosmochim. Acta, 46*, 1011-1040.

Pokroy, B., Fitch, A. N., Lee, P. L., Quintana, J. P., Caspi, E. N., & Zolotoyabko, E. (2006). Anisotropic Lattice Distortions in the Mollusk-Made Aragonite: A Widespread Phenomenon. *J. Struc. Biol., 153*, 145-150.

Politi, Y., Levi-Kalisman, Y., Raz, S., Wilt, F., Addadi, L., Weiner, S., & Sagi, I. (2003). Structural Characterization of the Transient Amorphous Calcium Carbonate Precursor Phase in Sea Urchin Embryos. *Adv. Funct. Mater., 13*, 480-486.

Ponce, C. B., & Evans, J. S. (2011). Polymorph Crystal Selection by n16, An Intrinsically Disordered Nacre Framework Protein. *Cryst. Grwoth. Des., 11*, 4690-4696.

Prieto, M., Fernández-Dìaz, L., & López-Andrés, S. (1991). Spatial and Evolutionary Aspects of Nucelation in Diffusing-Reacting Systems. *J. Cryst. Grwoth, 108*, 770-778.

Prieto, M., Putnis, A., & Fernández-Diaz, L. (1990). Factors Controlling the Kinetics of crystallization: Supersaturation Evolution in a Porous Medium. Application to Barite Crystallization. *Geol. Mag., 27*, 485-495.

Prior, J., Boyle, A. P., Brenker, F., Cheadle, M. C., Day, A., Lopez, G., Peruzzo, L., Potts, G. J., Reddy, S., Spiess, R., Timms, N. E., Trimby, P., Wheeler, J., Zetterström, L. (1999). The Application of Electron Backscatter and Orientation Contrast Imaging in the SEM to Textural Problems in Rocks. *Am. Min., 84*, 1741-1759.

Putnis, A., Prieto, M., & Fernández-Dìaz, L. (1995). Fluid Supersaturation and Crystallization in Porous Medium. *Geol. Mag., 132*, 1-13.

Radha, A. V., & Navrotsky, A. (2013). Thermodynamics of Carbonates. *Rev. Min. Geochem., 77*, 73-121.

Rahman, M. A., & Isa, Y. (2005). Characterization of Protein from the Matrix of Spicules from the Alcyonarian, *Lobophytum crassum*. *J. Exp. Mar. Biol. Ecol., 321*, 71-82.

Rajan, K. (2000). Representation of Texture in Orientation Space. In A. J. Schwartz, M. Kumar, & B. L. Adams, *Electron Backscatter Diffraction in Material Science* (pp. 31-38). New York: Kluwer Academic/Plenum Publisher.

Randler, V. (2000). Theoretical Framework for Electron Backscatter Diffraction . In A. J. Schwartz, M. Kuamr, & B. L. Adams, *Electron Backscatter Diffraction in Materials Science* (pp. 23-26). New York: Kluwer Academic/Plenum Publisher.

Raz, S., Testeniere, O., Hecker, A., Weiner, S., & Luquet, G. (2002). Stable Amorphous Calcium Carbonate Is the Main Component of the Calcium Storage of the Crustacean *Orchestia cavimana*. *Biol. Bull., 203*, 269-274.

Reimer, L. (1998). *Scanning Electron Microscopy: Physics of Image Formation and Microanalysis* (2nd ed.). Berlin, Heidelberg: Springer.

Rodriguez-Blanco, J. D., Shaw, S., Benning, L. G. (2011). The Kinetics and Mechanism of Amorphous Calcium Carbonate (ACC) Crystallization to Calcite via Vaterite. *Nanoscale, 3*, 265-271.

Rudwick, M. J. (1970). *Living and Fossil Brachiopods*. Hutchinson, London, UK. ISBN: 0091030803.

Sato, A., Nagasaka, S., Furihata, K., Nagata, S., Arai, I., Saruwatari, K., Kogure, K., Sakuda, S., Nagasawa, H. (2011). Glycolitic Intermediates Induce Amorphous Calcium Carbonate

Formation in Crustaceans. *Nat. Chem. Biol. , 7*, 197-199.

Sawada, K. (1997). The Mechanism of Crystallization and Transformation of Calcium Carbonates. *Pure & Appl. Chem. , 69*, 921-928.

Schmahl, W. W., Griesshaber, E., Merkel, C., Kelm, K., Deuschle, J., Neuser, R. D., Goetz, A. J., Sehrbrock, A., Mader, W. (2008). Hierarchical Fibre Composite Structure and Micromechanical Properties of Phosphatic and Calcitic Brachiopods Shell Biomaterials- an Overview. *Min. Mag., 72*, 541-562.

Seidl, B. H., & Ziegler, A. (2012). Electron Microscopic and Preparative Methods for the Analysis of Isopod Cuticle. *Zookeys, 176*, 73-85.

Sethmann, I., Putnis, A., Grassmann, O., & Löbmann, P. (2005). Observation of Nano-Clustered Calcite Growth via a Transient Phase Mediated of Organic Polyanions: A Close Match for Biomineralization. *Am. Min., 90*, 1213-1217.

Seto, J., Ma, Y., Davis, S. A., Meldrum, F., Gourrier, A., Kim, Y.-Y., Schile, U., Sztucki, M., Burhammer, M., Maltsev, S., Jäger, C., Cölfen, H. (2012). Structure-property Relationship of a Biological Mesocrystal in the Adult Sea Urchin Spine. *PNAS, 6*, 3699-3704.

Simon, P., Carrillo-Cabrera, W., Huang, Y.-X., Buder, J., Borrmann, H., Cardoso-Gil, R., Rosseeva, E., Yarin, Y., Zahnert, T., Kniep, R. (2011). Structural Relationship Between Calcite-Gelatine Composite and Biogenic (Human) Otoconia. *Eur. J. Inorg. Chem.*, 5370-5377.

Singh, N. B., Vellmer, C., & Middendorf, B. (2005). Effects of Carboxylic Acids on the Morphology, Physical Characteristics and Hydration of αlpha-Hehimydrate Plaster. *Indian J. Eng. Mater. S., 12, 12*, 337-344.

Song, R.-S., & Cölfen, H. (2011). Additive Controlled Crystallization. *Cryst. Eng. Comm., 13*, 1249-1276.

Stephenson, A. E., De Yoreo, J. J., Wu, K. J., Hoyer, J., & Dove, P. M. (208). Peptides Enhance Magnesium Signature in Calcite: Insights into Origins of Vital Effects. *Science, 322*, 724-726.

Sunagawa, I. (2005). *Crystals: Growth, Morphology and Perfection.* Cambridge, United Kingdom: Cambridge University.

Towe, K. M., & Lowestam, H. A. (1967). Ultrastructure and Development of Iron Mineralization in the Radular Teeth of *Cryptochiton stelleri* (Mollusca). *J. Ultrastruc. Res., 17*, 1-17.

Wada, M., Nishiyama, Y., & Langan, P. (2006). X-ray Structure of Ammonia-Cellulose I: New Insights into the Conversion of Cellulose I to Cellulose II. *Macromolecules, 39*, 2947-2952.

Wang, D., Hamm, L. M., Bodnar, R. J., & Dove, P. M. (2011). Raman Spectroscopic Characterization of the Magnesium Content in Amorphous Calcium Carbonates. *J. Raman Spectrosc., 43*, 543-548.

Watanabe, N., Meenakshi, V. R., Blackwelder, P. L., Kurtz, E. M., Dunkelberger, D. G. (1976). *Mechanism of Calcification in Plants and Invertebrates.* In N. Watabe, K. M. Wilbur (Ed.). University of South Carolina Press, New York.

Weiner, S., & Addadi, L. (2011). Crystallization Pathways in Biomineralization. *Annu. Rev. Mater. Res., 41*, 21-40.

Weiner, S., & Dove, P. M. (2003). An Overview of Biomineralization: Process and the Problem of the Vital Effects. *Rev. Mineral. Geochem., 54*, 1-29.

Weiner, S., Levi-Kalisman, Y., Raz, S., & Addadi, L. (2003). Biologically Formed Amorphous

Calcium Carbonate. *Connective Tissue Research, 44*, 214-218.

Weiss, I. M., Tuross, N., Addadi, L., & Weiner, S. (2002). Mollusc Larva Shell Formation: Amorphous Calcium Carbonate Is a Precursor Phase for Aragonite. *J. Exp. Zool., 293*, 478-491.

Winklhofer, M., & Petersen, N. (2006). Paleomagnetism and Magnetic Bacteria. *Microbio., Monogr., 3*, 256-273.

Wirsching, F. (2005). Calcium Sulfate. In W. Gerhartz (Ed.), *Ullmann's Encyclopedia of Industrial Chemistry* (pp. 555-584). Weinheim: Wiley-VCH Verlag Gmbh & Co. KGaA.

Wischnitzer, S. (1988). *Introduction to Electron Microscopy* (Vol. 3rd ed.). New York: Pergamon Press.

Xu, A.-W., Yu, Q., Dong, W.-F., Antonietti, M., & Cölfen, H. (2005). Stable Amorphous $CaCO_3$ Microparticles with Hollow Spherical Superstructure Stabilized by Phytic Acid. *17*, 2217-2221.

You, C., Zhang, Q., Jiao, Q., & Fu, Z. (2009). Supernet Structure of Calcium Carbonate Mesocrystals Formed in a Blend System of Anionic/Nonionic Surfactants. *Crys. Growth Des., 9*, 4720-4724.

Zimmermann, T., Bordeanu, N., & Strub, E. (2010). Properties of Nanofibrillated Cellulose from Different Raw Materials and Its Reinforcement Potential. *Carbohyd. Polym., 79*, 1086-1093.

List of Figures

List of Tables

Appendix

Appendix I. Carbonate-Hydrogel Crystals Growth Procedure

I.1 Counter-Diffusion System for Crystal Growth Procedure

Fundamentals of Double Diffusion System

The use of hydrogels to support crystallization is a longstanding method (Henisch, 1988). In the double diffusion method a column of hydrogel separates two deposits of the reactants which diffuse through the column (Figure A-1). Mass transfer leads to the supersaturation being achieved and eventually nucleation and growth occur in a certain region of the diffusion column. Henisch & García-Ruiz (1986) investigated mass transfer through the gel column using finite analytical solutions that aim to explore the factors that control the position where in the column nucleation occurs. These authors concluded that the nucleation occurs where these requirements are fulfilled: (i) the system is supersaturated and (ii) the reagents concentration ratio is close to 1 (concentration equality range condition). Later, Prieto and coworkers (1990) experimentally evaluated the mass transfer through a silica hydrogel column in a number of systems (Ba^{2+}-CO_3^{2-}-H_2O, Sr^{2+}-CO_3^{2-}-H_2O, Ba^{2+}-SO_4^{2-}-H_2O and Sr^{2+}-SO_4^{2-}-H_2O) by considering different column lengths and different reagent concentrations. These authors found that the position where nucleation occurred coincided with that along the diffusion column where the supersaturation rate (R_β) was higher (Prieto et al., 1990). Moreover, they established a connection between R_β and the supersaturation at nucleation (threshold supersaturation, β_{th}) for a given phase. Both parameters depend on the length of the diffusion column and the initial concentration of the reagents in the deposits so that a short column length and a high reagent concentration lead to a high R_β and β_{th} (Prieto et al., 1991; Putnis et al., 1995). More importantly, these authors concluded a relationship between the solubility of the solid phase and β_{th}, so that the lower the solubility the higher the β_{th}.

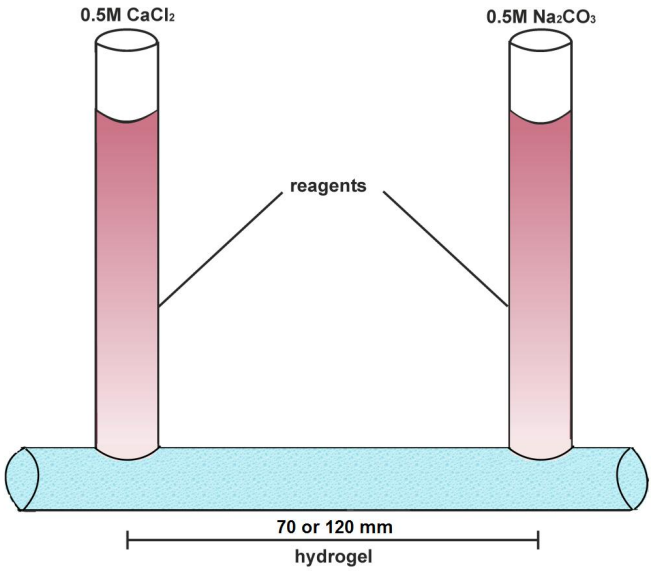

Figure A-1. Schematic of double diffusion system where two branches are filled with the reagents. The hydrogel occupies the horizontal branch of the U-tube. Modified after Henisch & García-Ruiz (1986).

Double Diffusion System for Calcium Carbonate Biomimetic

Experiments using the double diffusion method are carried out using a U-tube (Figure A-1). The hydrogel occupies the horizontal branch of the U-tube, while the reagents fill the vertical branches. Different types of hydrogel can be used. Gelatin and agarose hydrogels were prepared by dissolving porcine gelatin (Sigma Aldrich; Type A, Bioreagent) and agarose (Sigma Aldrich; Purified; Plant Cell Culture) in high purity deionized (MilliQ) water (18.2 MΩ) heated at 60 ºC. The hydrogel column was 70 mm and 120 mm long and had a diameter of 9 mm in all the cases. The gelatin and agarose were then cooled down to 4 °C. Silica gel was prepared by acidification of a sodium silicate solution (Merck, sp. gr.: 1.509 g/cm3; pH = 11.2) with 1N HCl to a pH = 5.5. The silica hydrogel contains ~ 96.5 wt % water filling its interconnecting pores. All hydrogels were set at 15 °C for 24 hours before aqueous solutions of calcium chloride (0.5M $CaCl_2$; Sigma Aldrich) and sodium carbonate (0.5M Na_2CO_3; Sigma Aldrich) were poured in the branches. Experiments were conducted at 15 ºC. The crystals were then extracted a week after the first optically visible crystals were observed.

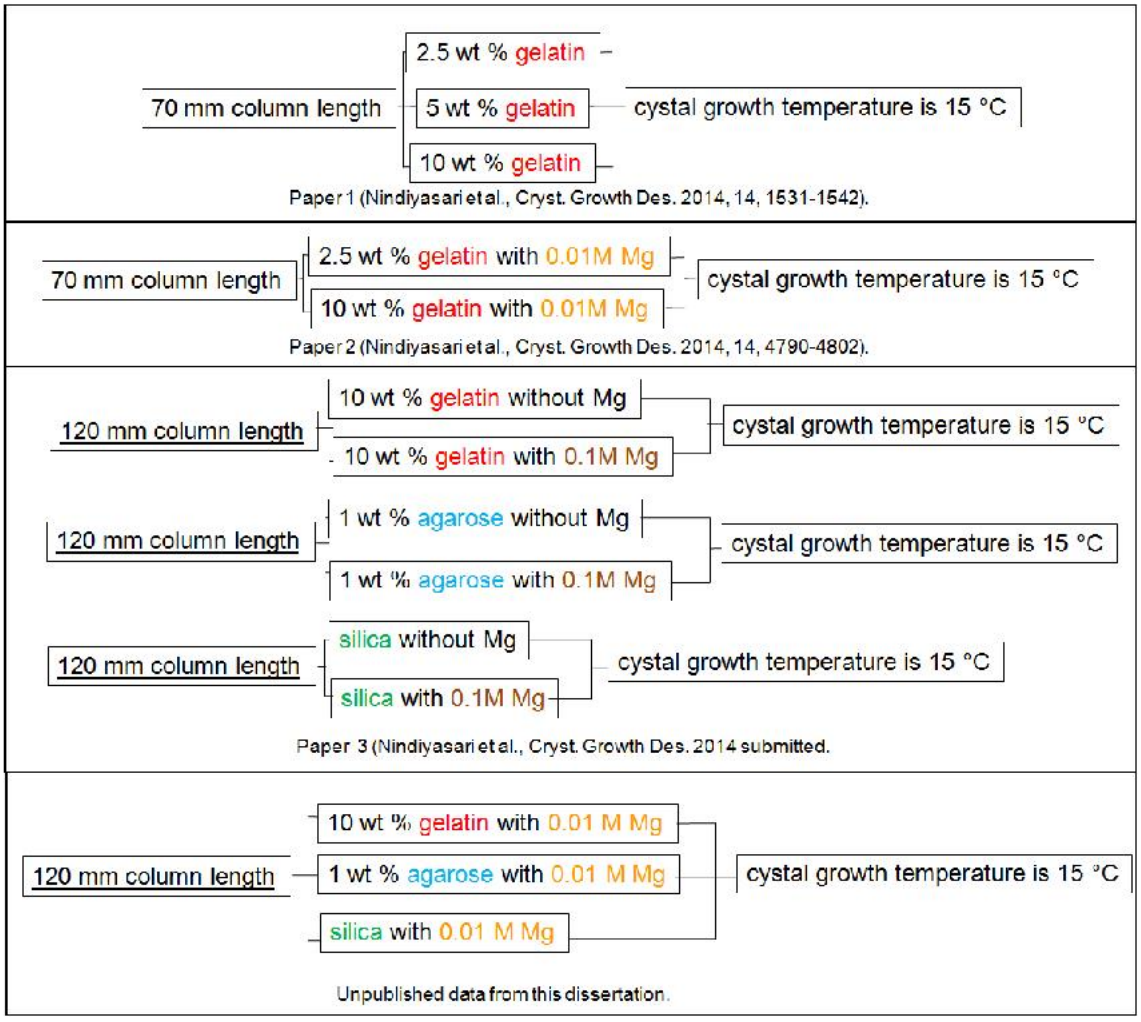

Figure A-2. Schematic of crystal growth experiments that have been carried out in order to study calcium carbonate biomineralization. The variations of hydrogels are used to get better understanding of biomineralization of calcium carbonate in different environment.

The double diffusion method is also applied to crystallize calcium carbonate in the presence of Mg. In this case the hydrogels were prepared using two solvents: water and an aqueous solution of 0.01M and 0.1M $MgCl_2$. The hydrogel preparation follows the previous procedure. All crystal growth experiments that were carried out are shown in Figure A-2. All experiments were conducted triplicate.

Appendix II. Sample Preparation Procedures

II.1 Chemical Procedure for Visualizing of the Etched Surface

The etching procedure is mainly applied to dissolve the mineral in order to expose the organic matrices. The calcite crystals obtained from the counter-diffusion experiments were embedded using EPON resin, trimmed with glass knife and polished with Diatome diamond knife. Etching solution was prepared from 27 mL of 0.1 M HEPES pH of 6.5 and 3 mL of 2.5% glutaraldehyde (Seidl & Ziegler, 2012). Etching procedure was carried out by gripping an EPON block with the gripper and dipping the specimens in etching solution for 90 seconds. This was followed by the washing procedure using 100% isopropanol for 10 seconds for three times. Afterwards, critical point drying process was applied. The procedure of critical point drying process is explained in appendix III.

II.2 Surface Preparation of EBSD Sample Measurement

EBSD measurements were performed on embedded and highly polished crystal surfaces. The required highly even surface of the samples was achieved by a final etch-polishing with colloidal silica in a vibratory polisher. Crystals with small size were glued on EPON blocks and polished using Ultracut ultramicrotome (Leica). The samples were coated with 4 nm of carbon. EBSD maps were obtained at 20 kV on an FEG-SEM (JEOL JSM 6400) equipped with an Oxford Instruments NordlysNano EBSD detector.

II.3 Isolation of Nanofibrillated Cellulose

Nanofibrillated cellulose (NFC) was prepared by dispersing 0.93 kg of Arbocel B1011 cellulose in 9 L of water. The suspension was left in a thermo-static reactor under continuous stirring at 10 ºC for 4 days. Subsequently the cellulose suspension was processed through a closed inline dispersing system equipped with an ultra-turrax for the disintegration of the fibers into smaller parts. The resulting suspension was treated in a high pressure homogenizer by pumping with high velocities through fixed-geometry interaction chambers (Y or Z morphology) with diameter of 400, 200, and 75 µm, respectively. Pressures up to 1000 bar were applied to generate high shear-stresses to the cellulose fibers (Figure A-3) (Zimmermann, et al., 2010).

II. 4 Sample Preparation for X-ray Diffraction Analysis of Cellulose

The measurement of cellulose samples was carried out using two different X-ray diffractometers. The fine crystallite samples, cellulose UFC100 and the thin film of nanofibrillated cellulose (NFC), were investigated using a Bragg-Brentano type X-ray diffractometer (GE: XRD 3003 TT) recorded in reflection mode using a 1-dimensional position sensitive semi conductor detector (Meteor 1D) with a step size of 0.01° (θ/θ). The cellulose B400 and Lyocell fiber were packed into glass capillaries (ø = 0.5 mm) to collect XRD data in transmission mode on a single crystal diffractometer (Agilent, Gemini Ultra) equipped with a 2-

dimensional charge-coupled detector (Atlas). All XRD data were collected using Cu $K\alpha_1$ radiation.

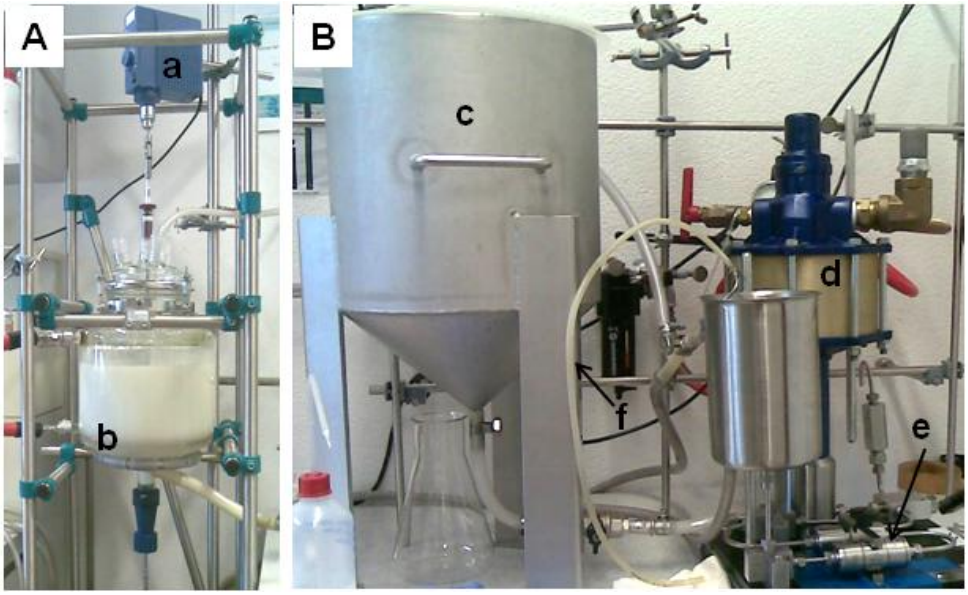

Figure A-3. (A) Lab-scale equipment for the mechanical pre-treatment of the cellulose. (a) Ultra-thorax used for dispersion of the cellulose. (b) Container of the dispersed cellulose. Figure (B) shows the microfluidizer lab-scale high-shear processor type M-110Y for isolation of nanofibrillated cellulose by mechanical disintegration and homogenization of the dispersed cellulose. (c) Container of the dispersed cellulose obtained after mechanical pre-treatment. (d) Air pump for the generation of high processing pressure (up to 1500 bar). (e) Patented interaction chambers (*Y*- and *Z*-type). (f) Cooling loop and product outlet.

II.5 Preparation of Cellulose/Gypsum Composites

For mechanical testing the samples were prepared by pouring the composite slurry into moulds with dimensions of 13.5 x 13.5 x 25 mm^3 (DIN EN 843-1) for compression and 75 x 10 x 3.5 mm^3 for 4-point bending testing, respectively. The samples were dried within the moulds at room temperature for 7 days. The number of specimens for each composite was ~10 specimens for bending and ~ 10 specimens for compression testing. Bending testing was carried out with a UTS test system Typ 009, 3 kN and with a Zwick Universalprüfmaschine Typ Z005, 5 kN while compression testing was carried out with a Zwick Universalprüfmaschine Typ 1425, 100 kN and a Zwick Universalprüfmaschine Typ Z005, 5 kN. Data log was stopped after the load dropped and the first cracks were observed. Some specimens failed at point of force transmission due to uneven surfaces. The preload for bending and compression testing was 0.5 N. The velocity values of bending and compression testing were 0.02 mm/min and 0.12 mm/min, respectively. The strain rate values of bending and compression testing were 5.1×10^{-5} s^{-1} and 8×10^{-5} s^{-1}, respectively. The strain is calculated by dividing the elongation by the original sample length, respectively. The Young's moduli are derived from the steep slope of stress-strain curve.

Appendix III. Applied Methods

III.1 Critical Point Drying Process

Critical point drying process (CPD) is a method that is normally used to dry biological specimens. Since biological specimens usually have contact with water, conventional drying process will destroy specimens' surface and structure by forcing water to evaporate with high surface tension. Critical point drying process reduces the surface tension by substituting water into another liquid. The specimen has to be dehydrated by replacing the water by intermediate fluid, such as isopropanol. The specimen is then transported to the critical point dryer and soaked with liquid CO_2. The temperature and pressure are controlled to get the critical point of the CO_2 (Figure A-4). The intermediate fluid is crucial as liquid CO_2 is miscible in water.

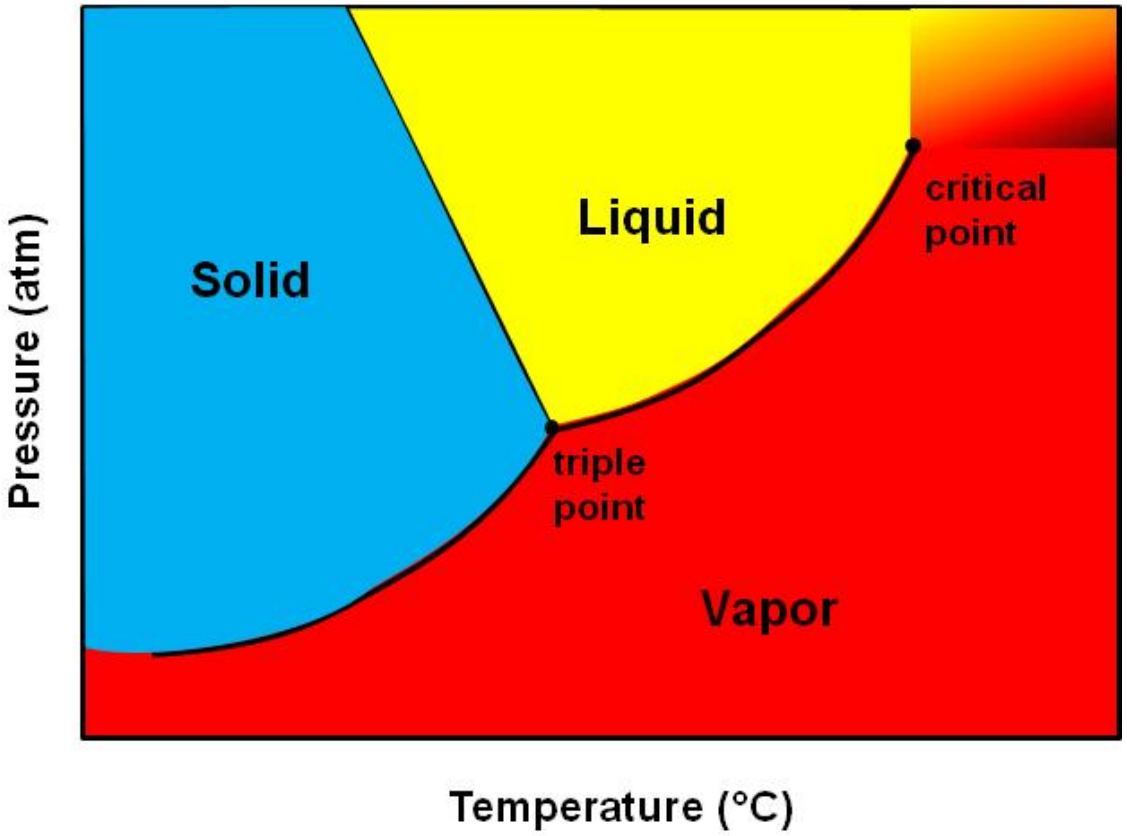

Figure A-4. Phase diagram of CO_2 showing the critical point of CO_2, from Paredes (2000). The critical point of CO_2 is reached approximately at pressure of 77 atm and temperature of 32 °C.

III.2 X-ray Diffraction

X-rays are generated using an X-ray tube where electron waves are generated from an impact of high energy electron with a metal target. The X-ray spectrum generated from a typical X-ray tube has three characteristic lines ($K_{\alpha 1}$, $K_{\alpha 2}$, and K_{β}) as a result of a transition of the upper level electron in the atom core to the vacant lower energy level. The vacant lower energy is created when the electron that occupies the lower energy is ejected due to the impact of

accelerated electron from the X-ray tube. The energy difference between energy levels in atoms is element specific. Thus, each chemical element has different characteristic X-ray wave lengths. A monochromator is applied to select one characteristic emission line ($K\alpha_1$) and to reduce the background due to white radiation. A collimator is applied to reduce the angular divergence. Interference of X-ray waves scattered from neighboring lattice planes creates a diffraction pattern with sharp peaks (Figure A-5). The angles at which these peaks occur can be calculated by Bragg's law (Figure A-5) (Pecharsky & Zavalij, 2005).

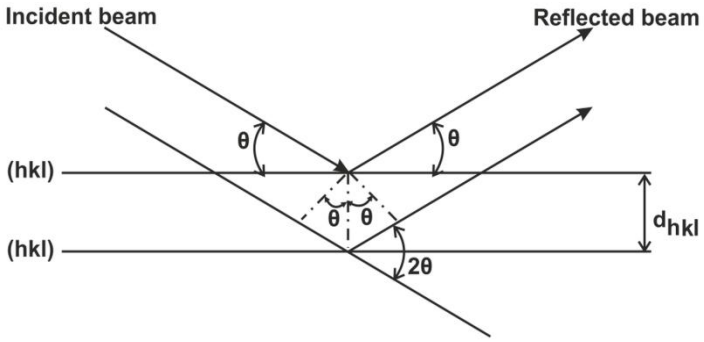

Figure A-5. Geometrical illustration of Bragg's law, from Pecharsky & Zavalij (2005).

The Bragg's law derived from the geometry is written as

$$n\lambda = 2d_{hkl}\sin\theta$$

where d_{hkl} is the spacing between the planes in the atomic lattice, λ is the wave length, n is the integer determined by the order given and θ is the angle between the incident ray and the scattering planes.

The intensity of the Bragg reflections is given by the square of the structure factor F,

$$F(G) = \sum_j f_j \exp(-iG \bullet x_j)$$

where G is 2π times the reciprocal lattice vector (hkl), the summation is over all atoms in the unit cell, f_j is the scattering power of the atom j, and x_j is its position. The x-ray diffraction line width (ΔΘ) increases both with decreasing particle size D according to Scherrer-equation as seen below,

$$L = \frac{k\lambda}{\beta\cos\theta}$$

where k is the Scherrer constant, λ is the applied x-ray wavelength, β is the FWHM, and θ is the corresponding Bragg's angle. The x-ray diffraction line width (ΔΘ) also increases with increasing mean square fluctuation of the lattice parameter (so called microstrain $<\varepsilon>$), seen below,

$$\Delta\Theta_{strain} = <\varepsilon>\tan\Theta$$

III.3 Electron Microscopy

Fundamental of Scanning Electron Microscopy

Scanning electron microscopy (SEM) is mainly used to observe the morphological characteristics of specimens. It uses an electron gun that bombards the specific point of the specimen as it scans the specimen in a predetermined regular pattern. There are mainly three different electron guns that are used in SEM. The first is tungsten filament cathode where the electrons are emitted by the filament or cathode and accelerated by the anode. The second electron gun is lanthanum hexaboride (LaB_6) cathode. The lanthanum hexaboride (LaB_6) cathode has high gun brightness due to its high emission current. The LaB_6 satisfactory operation can be maintained for several hundred hours. The last electron gun is a field emission gun that can produce a higher brightness than the other electron guns. The electron emission is produced by tunneling the electron through the potential barrier (Wischnitzer, 1980).

The formation of SEM images occurs in the following steps. The secondary electrons (SE) that are emitted from a specific point on the specimen are collected, converted and amplified to produce a signal voltage. This signal is then passed through cathode-ray tube (CRT) where it modulates the beam of the CRT, thus, SEM image is obtained (Figure A-6).

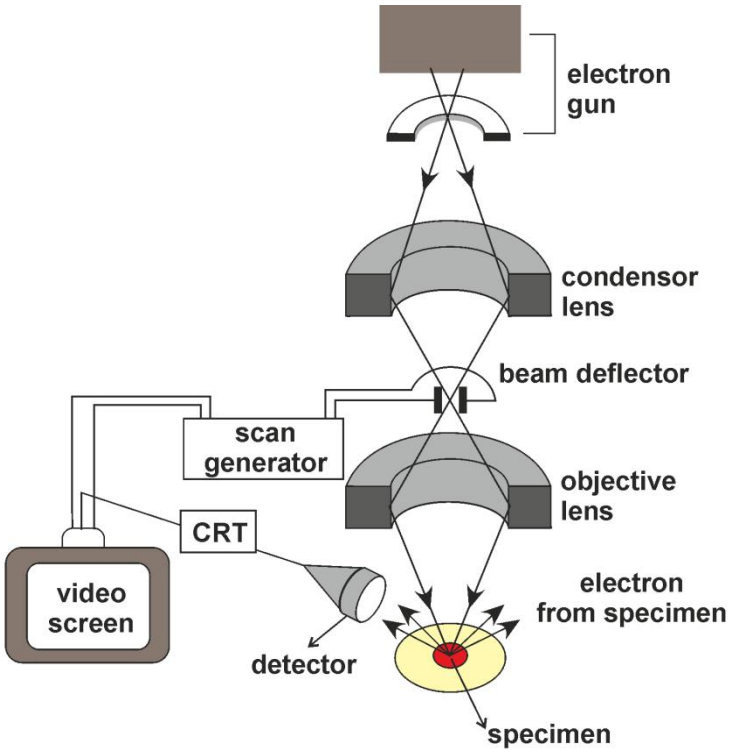

Figure A-6. Schematic of scanning electron microscopy. The electron is focused on the specimen by the electromagnetic coils that act as lenses. The scattered electron is measured by the detector and is used to build up image on the video screen. Modified after Albert et al. (2002).

Fundamental of Transmission Electron Microscopy

Instead of using backscatter or secondary electron like in the case of SEM, TEM looks at the amount of electron beam that goes through the sample onto the screen. The emitted electron from the electron gun irradiates the thin sample and the scattered beams are adjusted using the objective aperture (Figure A-7). The thicker the sample, the more the beam is scattered. The imaging system of TEM consists of at least three lenses; the objective lens, the intermediate lenses and the project lens. The intermediate lenses magnify the first intermediate image that is formed just in front of these lenses. When the excited transmission electrons are diffracted according to Bragg's Law ($n\lambda = 2d \sin\theta$), a diffraction pattern is created. The diffraction pattern gives information about periodicities in the lattice.

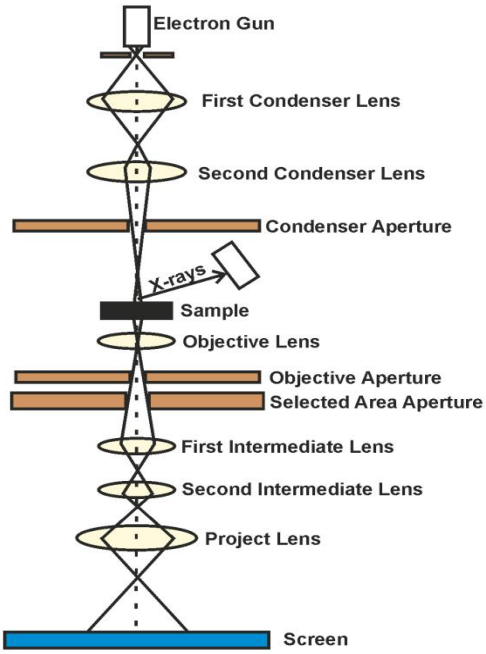

Figure A-7. Schematic of transmission electron microscopy. The sample is placed before the objective lens and the diffracted beam is adjusted using objective aperture to get bright or dark field image. Modified after Reimer (1989).

There are two different imaging modes in TEM; bright field (BF) and dark field (DF) imaging mode. The bright field imaging mode, the typical TEM mode, can be produced with objective aperture between 5 and 20 mrad. These aperture sizes allow only the direct beam to pass. In the dark field imaging mode, the direct beam is blocked by the objective aperture allowing the diffracted beam to pass through the objective aperture (Figure A-8).

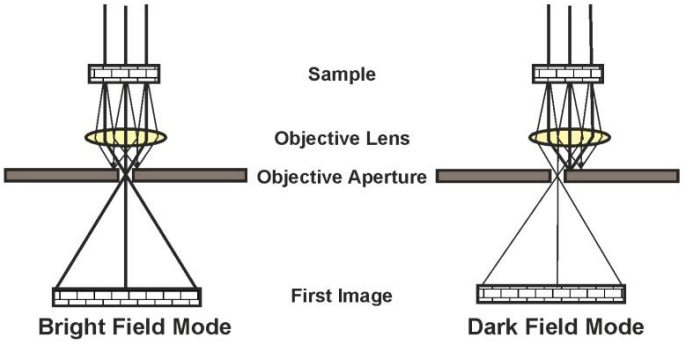

Figure A-8. Formation of bright and dark field images from the TEM. The bright field mode is created by placing the objective aperture so that the beam diffracted by the specimen can go through while the dark field mode is created by displacing the objective aperture to accept beam diffracted by the specimen. Modified after Reimer (1989).

III.4 Electron Backscatter Diffraction Analysis

The first observation of electron diffraction through thin mica that produced remarkable lines in the images as divergent diffraction pattern was done by Kikuchi in 1928. The further development has been done by Venables and Harland in 1973 when the first electron backscatter diffraction was applied in a scanning electron microscopy (SEM). The development of the electron backscattered diffraction (EBSD) had been going on until Dingley in 1984 used EBSD to investigate crystallographic orientation regularly for submicron crystals. Currently, EBSD, also known as backscatter Kikuchi diffraction, is regularly used for phase identification, determination of crystallographic orientation and thus texture, and strain measurement.

The basic requirement of EBSD system is a SEM or TEM that is complemented with an EBSD detector (Figure A-9). The EBSD acquisition hardware is mainly comprised as a sensitive CCD camera and an image processing system for pattern averaging and background subtraction (Humphreys, 2001).

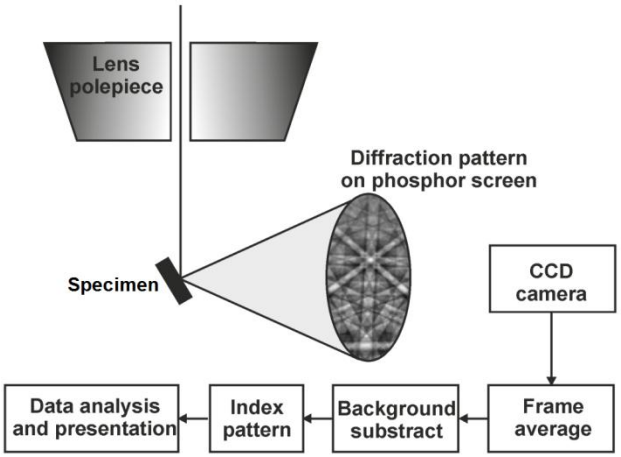

Figure A-9. Schematic diagram of a typical EBSD system installation, from Humphreys (2001). The electron beam hits a sample that is tilted 70 ° and the diffracted electrons are recorded by the CCD camera.

Backscatter electrons (BSE) are electrons from the incident beam that exit the samples after one or more scattering events. The EBSD mechanism uses the interference (Bragg-diffraction) of backscatter electrons to produce Kikuchi's lines. The electrons that arrive at the specimen are scattered from the specimen. Where the Bragg angle (θ) is fulfilled, Kikuchi-lines occur. Diffraction of these electrons through a Bragg angle defines a pair of cones (Figure A-10). As the electron wavelength is short the Bragg angle is small and the pair of parallel cones appears as a nearly straight band. Each pair of Kikuchi lines is known as Kikuchi band that has a distinct width and corresponds to a distinct crystallographic plane. The orientation of the pattern is evaluated by automatic indexing to identify the poles and bands in the patterns and calculating the relationship between these poles and bands and some reference axes (Randler, 2000).

The orientation data of the grains are then plotted on a single stereographic projection plane parallel. If the grains show completely random orientation, the poles on the pole figures will be distributed randomly over the projection. If preferred orientation is observed, the poles in the pole figures will tend to cluster together into certain areas of the projection. The inverse poles figures are usually applied to get orientation information with respect to a specific specimen coordinate, for example to investigate fiber texture when only one axis is strongly textured (Rajan, 2000). The orientation map will give information about the orientation difference in a given area that may contain several grains with each color representing different crystallographic orientation.

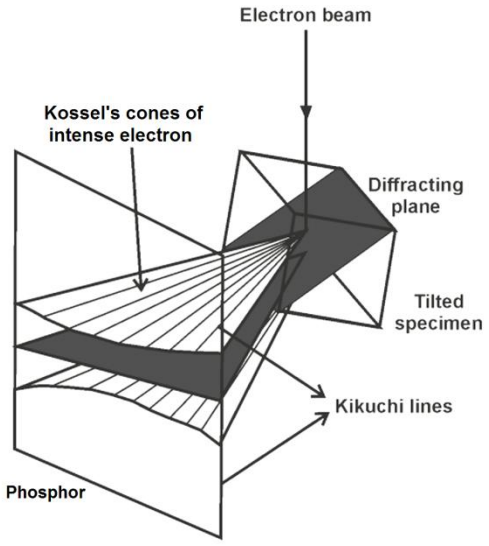

Figure A-10. Schematic diagram showing the formation of Kikuchi lines from diffraction cones that are related to diffraction from a single lattice plane (Kossel's cones). Modified after Prior et al. (1999).

III.5 Bending and Compressive Strength Tests

Bending tests can be performed in either three-point or four-point bending mode. At 3-

point bending, the load is applied from one point on top of the sample and two points at the bottom of the sample while at 4-point bending the load is applied at two different points on top of the samples and two different points at the bottom of the sample (Figure A-11).

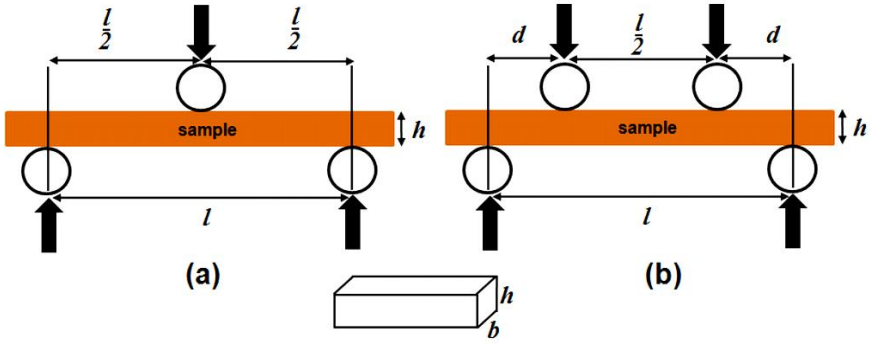

Figure A-11. Schematic of bending tests. Bending tests can be performed as three-point bending tests (a) or four-points bending tests (b), summarized from Jones (1975).

The three-points bending test will give compressive strength as follow

$$\sigma_f = \frac{3Fl}{2bh^2} \tag{1}$$

and the bending strength of four-points bending is given as

$$\sigma_f = \frac{3Fd}{bh^2} \tag{2}$$

where σ_f is the bending strength, F is the force, b is the width of the sample, h is the height of the sample, l is the distance between the lower point where the load is applied and d is the distance between the inner and the outer points (Figure A-11).

The Compression test is used to determine the strength of the sample under axial compressive load. Some materials, under compression load, have a linear relationship between stress (σ) and strain (ε) that is a physical manifestation of Hooke's law ($E = \frac{\sigma}{\varepsilon}$). Some materials have the elastic ability to return to their original form after the deformation. The stress-strain curve (Figure A-12) shows the elasticity of a material. At the beginning of the load the specimen will show an elastic deformation. Elastic deformation is accompanied by additional plastic deformation when the load reaches the so called yield point or yield strength. The compressive strength is calculated from the force at the yield point divided by the surface area of the specimen, $\sigma_c = \frac{F}{A}$ where σ_c is the compressive strength, F is the force and A is the surface area of the sample.

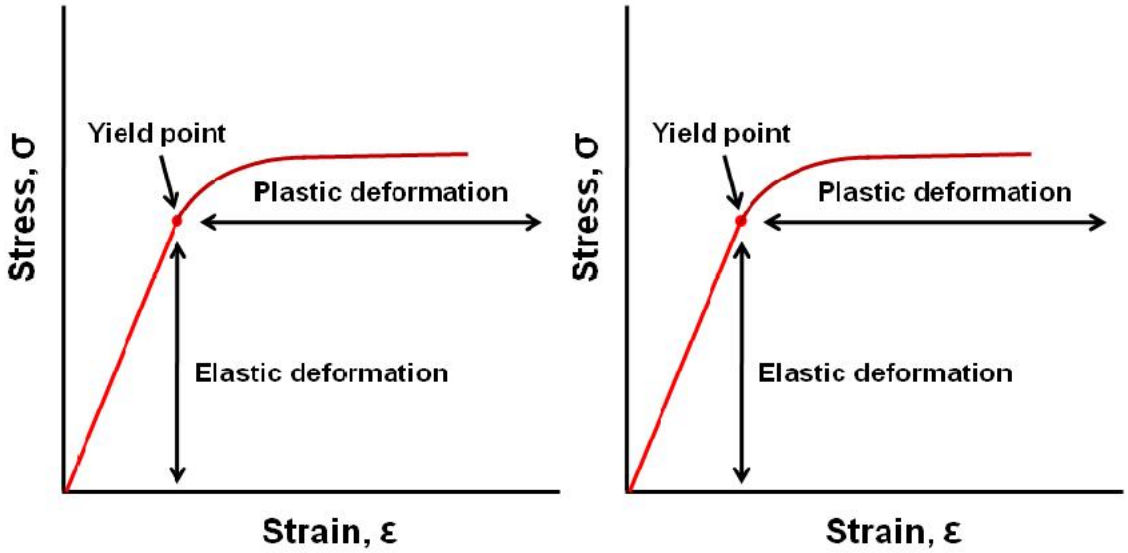

Figure A-12. Stress-strain curve showing the elastic deformation and the plastic deformation of a specimen. The curve is modified after Jones (1975).

Acknowledgements

A journey of a thousand miles must begin with a single step. My dissertation completion and subsequent Ph.D. has been a long and difficult journey. This process has been one of the most significant academic challenges I ever have to face.

First, I am deeply grateful for all the support, help, discussion and guidance from Prof. Dr. Wolfgang W. Schmahl. It has been a pleasure to work under his guidance.

I also am grateful for all the help and support from KAAD for the funding and Centre of Electron Microscopy (University of Ulm) for a valuable collaboration.

The great gratitude also goes to

- Dr. Erika Griesshaber for supporting me in every difficult situation and helping me through all them,
- Prof. Dr. Lurdes Fernandez-Diaz for all the discussion and guidance for completing this dissertation,
- Dr. Andreas Ziegler for such a nice cooperation and valuable lessons,
- Dr. Sohyun Park and Prof. Dr. Guntram Jordan for the help and guidance,
- Prof. Dr. Claudia Fleck and Dipl. Ing. Clemens Randow for the nice discussions and support
- Ismot Farjana Akter and Lucy Garcia Benitez Lara for proofreading my dissertation,
- Julia Huber for making everything easier and listening to all problems I faced during my research and completing my dissertation,
- Dr. Hsinyin Chiang, Dr. Kuhu Sarkar and Dr. Shuai Guo for keeping telling me that everything would be fine,
- all my friends and my family for all the support and making me believes that I can pass this long and difficult journey,
- all my PhD fellows (Laura Casella, Xiaofei Yin, Balasz Kocsis, Peter Kadletz, Ulf Gatermann, Benedikt Roska), all my students and colleagues for all the support and happy time during my research.

Finally, I would like to thank my husband, David Behal, for helping and supporting me during difficult time of completing my research and dissertation. Everything seemed easier with you by my side.

List of Publications

Griesshaber, E., Schmahl, W. W., Ubhi, H. S., Huber, J., **Nindiyasari, F.**, Maier, B., Ziegler, A. (2013): Homoepitaxial Meso- and Microscale Crystal Co-orientation and Organic Matrix Network Structure in *Mytilus edulis* Nacre and Calcite. Acta Biomaterialia, 9, 9492-9502.

http://www.sciencedirect.com/science/article/pii/S1742706113003681

Nindiyasari, F., Fernández-Díaz, L., Griesshaber, E., Astilleros, J. M, Sánchez-Pastor, N., Schmahl, W. W. (2014): Influence of Gelatin Hydrogel Porosity on the Crystallization of $CaCO_3$. Cryst. Growth Des., 14, 1531-1542.

http://pubs.acs.org/doi/abs/10.1021/cg401056t

Nindiyasari, F., Griesshaber, E., Fernández-Díaz, L., Astilleros, J. M, Sánchez-Pastor, N., Ziegler, A., Schmahl, W. W. (2014): The effect of Mg and the hydrogel solid content on the crystallization of calcium carbonate in biomimteic counter-diffusion systems. Cryst. Growth Des., 14, 4790-4802.

http://pubs.acs.org/doi/abs/10.1021/cg500938k

Nindiyasari, F., Ziegler, A., Griesshaber, E., Fernández-Díaz, L., Walther, P., Schmahl, W. W. (2015): The effect of hydrogels on calcite aggregate formation, morphology and crystal orientation. Cryst. Growth Des., 2015, **DOI:** 10.1021/cg5018483.

http://pubs.acs.org/doi/abs/10.1021/cg5018483

Nindiyasari, F., Griesshaber, E., Zimmermann, T., Manian, A. P., Randow, C., Zehbe, R., Fernandez-Diaz, L., Ziegler, A., Park, S.-H., Fleck, C., Schmahl, W. W. (2015): Characterisation and Mechanical Properties Investigation of the Cellulose/Gypsum Composite. J. Comp. Mater., 2015, DOI: 10.1177/0021998315580826.

http://jcm.sagepub.com/content/early/2015/04/30/0021998315580826.full.pdf+html

Huber, J., Griesshaber, E., Nindiyasari, F., Schmahl, W. W., Ziegler, A. (2015): Functionalization of biomineral reinforcement in crustacean cuticle: Calcite orientation in the partes incisivae of the mandibles of ***Porcellio scaber*** and the supralittoral species ***Tylos europaeus*** (Oniscidea, Isopoda). J. Struct. Biol. 190, 173-191.

http://www.sciencedirect.com/science/article/pii/S1047847715000696

Talks at Conferences

The improvement of material properties of gypsum-cellulose composite materials.

F. Nindiyasari, E. Griesshaber, T. Zimmerman, A. Manian, C. Randow, L. Fernandez-Diaz, A. Ziegler, S.-H. Park, C. Fleck, W. W. Schmahl.
Deutschen Gesellschaft für Kristallographie (DGK), Freiberg, Germany, March 19 - 22, 2013.

The influence of gelatin hydrogel porosity on the crystallization of $CaCO_3$.

F. Nindiyasari, L. Fernández-Díaz, E. Griesshaber, J. M. Astilleros, N. Sánchez-Pastor, W. W. Schmahl.
17th International Conference of Crystal Growth and Epitaxy (ICCGE), Warsaw, Poland, August 11 - 16, 2013.

How does the porosity of gelatin hydrogel matrices influence the crystallization of $CaCO_3$?

F. Nindiyasari, L. Fernández-Díaz, E. Griesshaber, J. M. Astilleros, N. Sánchez-Pastor, W. W. Schmahl.
12th International Symposium on Biomineralization (Biomin), Freiberg, Germany, August 27 - 30, 2013.

The effect of Mg and the hydrogel solid content on the crystallization of calcium carbonate in biomimetic counter-diffusion systems: 2. Calcite lattice orientation variation from single crystals to spherulites.

Nindiyasari, F., Griesshaber, E., Fernández-Díaz, L., Astilleros, J. M, Sánchez-Pastor, N., Ziegler, A., Schmahl, W. W.
Discussion Meeting on Crystal Growth and Biomineralization, Münster, Germany, November 27-28, 2014.

Poster Presented at Conference

The improvement of material properties of gypsum-cellulose composite materials.

F. Nindiyasari, E. Griesshaber, T. Zimmerman, A. Manian, C. Randow, L. Fernandez-Diaz, A. Ziegler, S.-H. Park, C. Fleck, W. W. Schmahl.
International school and conference on biological materials science (Bio-inspired Materials), Potsdam, Germany, March 18 – 27, 2014.